



Durham E-Theses

The role of obscured activity in galaxy formation

WARDLOW, JULIE,LOUISE

How to cite:

WARDLOW, JULIE,LOUISE (2010) *The role of obscured activity in galaxy formation*, Durham theses, Durham University. Available at Durham E-Theses Online: <http://etheses.dur.ac.uk/426/>

Use policy

The full-text may be used and/or reproduced, and given to third parties in any format or medium, without prior permission or charge, for personal research or study, educational, or not-for-profit purposes provided that:

- a full bibliographic reference is made to the original source
- a [link](#) is made to the metadata record in Durham E-Theses
- the full-text is not changed in any way

The full-text must not be sold in any format or medium without the formal permission of the copyright holders.

Please consult the [full Durham E-Theses policy](#) for further details.

The role of obscured activity in galaxy formation

Julie Louise Wardlow

A Thesis presented for the degree of
Doctor of Philosophy



Department of Physics

University of Durham

United Kingdom

September 2010

Dedicated to:

My Family

The role of obscured activity in galaxy formation

Julie Louise Wardlow

Abstract

In this thesis I investigate the formation and evolution of the galaxies that eventually form the colour-magnitude relation (CMR) in local galaxy clusters.

I survey galaxies that lie on the CMR in nine massive clusters at $z \sim 0.2$, environments in which the build-up of the faint end of the CMR is still underway. I show that there are relatively few dwarf galaxies on the CMR in the outer, low-density regions of clusters, but that their fraction increases towards higher-density regions as the cluster environment transforms infalling, blue, star-forming galaxies into red, passive, CMR galaxies. However, in the highest density regions, at the very centres of clusters the relative fraction of dwarf galaxies on the CMR is suppressed, evidence that, dwarf galaxies in the highest density regions at $z \sim 0.2$ are dynamically disrupted.

I then use 1.1-mm observations of a massive cluster at $z \sim 0.54$ to search for active, star-forming cluster galaxies, which would transform into CMR galaxies at lower redshifts as the star-formation terminates. I detect 36 sources in observations of 0.1 deg^2 of the cluster centre and identify counterparts to $\sim 50\%$ of these submillimetre galaxies (SMGs) using radio, 24- μm and IRAC data. Photometric redshifts suggest that at most two of the SMGs are potential cluster members. If this is the case they each have far-infrared luminosities of $\sim 5 \times 10^{11} L_{\odot}$ and star-formation rates (SFRs) of $\sim 50 M_{\odot}\text{yr}^{-1}$ – a significant fraction of the combined SFR of the cluster.

I next consider 126 SMGs detected in an 870- μm survey of the Extended *Chandra* Deep Field South (ECDFS). I derive a photometric redshift distribution of 74 robust radio, 24- μm and IRAC-identified counterparts that peaks at $z = 2.2$. An analysis of sources within the positional error circles of unidentified SMGs identifies a population of likely counterparts with a redshift distribution that peaks at $z = 2.5 \pm 0.3$ and likely comprises $\sim 60\%$ of the unidentified SMGs. The remainder are not detected in our IRAC imaging and likely lie at $z \gtrsim 3$. In total, I find that $\sim 30\%$ of all SMGs are at $z \gtrsim 3$, and the median redshift of all $S_{870\mu\text{m}} > 4 \text{ mJy}$ SMGs is $z = 2.5 \pm 0.6$. The contribution of SMGs to the global SFRD also peaks at $z \sim 2$ and SMGs with $S_{870\mu\text{m}} \gtrsim 4 \text{ mJy}$ and $S_{870\mu\text{m}} \gtrsim 1 \text{ mJy}$ provide $\sim 5\%$ and $\sim 50\%$ of the global total at $z \sim 2$, respectively.

Analysis of the projected real-space cross-correlation function of SMGs at $z = 1-3$ with IRAC-selected galaxies shows that SMGs are strongly clustered and reside in dark-matter halos of mass $(6_{-5}^{+12}) \times 10^{12} M_{\odot}$. This halo mass is comparable to that of quasars and the mass at which major mergers are most efficient at triggering starburst activity. I conclude that SMGs at $z \sim 2$ have star-formation rates, stellar masses and clustering properties that suggests that they are the likely progenitors of the massive CMR galaxies that dominate local clusters.

Contents

1	Introduction	1
1.1	Galaxy clusters	1
1.2	Submillimetre galaxies	5
1.3	Outline of this thesis	10
2	The effect of environment on the galaxy populations in rich clusters at $z \sim 0.2$	11
2.1	Introduction	11
2.2	Sample selection	13
2.3	Analysis and results	17
2.3.1	Colour-magnitude relation	17
2.3.2	Field correction	18
2.3.3	Evolution of the CMR from the luminosity function	20
2.3.4	Evolution of the CMR from the dwarf-to-giant ratio	24
2.3.5	Buildup of the CMR: radial dependence	26
2.3.6	Buildup of the CMR: density dependence	29
2.4	Discussion and Conclusions	33
3	A 1.1-mm survey for ULIRGs in the field of the galaxy cluster MS 0451.6–0305	35
3.1	Introduction	35
3.2	Observations and Data Reduction	37
3.2.1	AzTEC Observations	39
3.2.2	Multi-wavelength data	40
3.3	Analysis and Results	43
3.3.1	AzTEC catalogue	44

3.3.2	Identifying counterparts to AzTEC sources	48
3.3.3	Redshifts of MS 0451–03 AzTEC galaxies	54
3.3.4	Cluster and field SEDs	67
3.4	Conclusions	71
3.5	Appendix: Notes on Individual Sources	75
4	Calculating the photometric redshifts of SMGs	79
4.1	Introduction	79
4.2	Sample selection	80
4.2.1	Optical and infrared photometry	83
4.3	Analysis and results	88
4.3.1	Calibrating the photometry and templates	88
4.3.2	Improving photometric redshifts for galaxies at $z = 2-3$	90
4.3.3	Reliability of photometric redshifts	96
4.3.4	The effect of AGN on photometric redshifts	100
4.3.5	Reliability of SED parameters	103
4.4	Conclusions	106
4.5	Appendix: LESS SED fits	107
5	A photometric redshift survey of SMGs	116
5.1	Introduction	116
5.2	Sample selection	118
5.3	Results and Discussion	119
5.3.1	Redshift distribution of identified SMGs	119
5.3.2	Potential sample biases	122
5.3.3	Redshift distribution of unidentified SMGs	124
5.3.4	Simple redshift estimators for SMGs	128
5.3.5	Dust temperatures, far-infrared luminosities and star-formation history	133
5.4	Summary and Conclusions	140
5.5	Appendix: Discussion of individual sources	142
6	The physical properties of SMGs	154
6.1	Introduction	154
6.2	Results and Discussion	156

6.2.1	AGN	156
6.2.2	Typical SMG SEDs	163
6.2.3	Stellar masses	165
6.2.4	Specific star-formation rate	168
6.2.5	Volume density of SMGs	170
6.2.6	Clustering of SMGs	171
6.3	Conclusions	177
7	Conclusions	179
7.1	Summary of main results	179
7.1.1	The galaxy populations in rich clusters at $z \sim 0.2$	179
7.1.2	Searching for ULIRGs in a galaxy cluster at $z = 0.54$	180
7.1.3	Properties of 870- μm selected SMGs	180
7.2	Remaining questions and future research	182

List of Figures

1.1	“Tuning fork” diagram of galaxy classification	2
1.2	Galaxy cluster Abell 1689	3
1.3	The negative K-correction at submillimetre and millimetre wavelengths	5
1.4	Illustration of the proposed evolutionary sequence of SMGs and QSOs	9
2.1	Colour-magnitude plots for $z \sim 0.2$ galaxy clusters	19
2.2	Evolution of the CMR with redshift	20
2.3	Colour-colour plot highlighting CMR galaxies	21
2.4	Rest-frame V -band luminosity functions for the $z \sim 0.2$ galaxy clusters	23
2.5	Contours of χ^2 for Schechter function fits to the luminosity function of $z \sim 0.2$ clusters	24
2.6	Evolution of RDGR with redshift	26
2.7	Variation of RDGR with clustercentric radius	27
2.8	Variation of RDGR with local giant galaxy density	30
2.9	Luminosity functions for red-sequence galaxies with in regions of various local giant galaxy density	32
3.1	AzTEC 1.1-mm and Subaru R -band map of MS 0451–03	38
3.2	Catalogue detection limits at $z = 0.54$ compared to Arp 220 and M 82 SEDs	44
3.3	1.1-mm differential number counts in MS 0451–03	47
3.4	SMA observations of five SMGs in MS 0451–03	50
3.5	$S_{24\mu\text{m}}/S_{1.1\text{mm}}$ versus $S_{1.4\text{GHz}}/S_{1.1\text{mm}}$ for SMGs in the MS 0451–03 field	56
3.6	$B - z$ vs. $z - K$ colour-colour plot for SMGs in the MS 0451–03 field	57
3.7	Spectroscopic versus photometric redshifts for SMGs in the CDFN	60
3.8	Photometric redshift versus 1.1-mm flux and apparent K -band magnitude of SMGs in the field of MS 0451–03	63
3.9	Images of the potential cluster SMG MMJ 045421.55	65

3.10	Images of the potential cluster SMG MMJ 045431.35	66
3.11	Stacked mid-infrared to radio SEDs of 24- μ m, late- and early-type populations of MS 0451–03	68
3.12	Optical and infrared images of SMGs in the field of MS 0451–03	73
4.1	Colour-flux diagram showing the IRAC selection limits for SMG counterparts	82
4.2	Reliability of the initial photometric redshifts of LESS SMGs.	91
4.3	Effect of changing the VIMOS <i>U</i> -band zeropoint on the reliability of LESS SMG photometric redshifts.	94
4.4	Reliability of final photometric redshifts of LESS SMGs, and galaxies in the ECDFS.	97
4.5	Best-fit Burst and Im templates for two LESS SMGs	105
4.6	Photometry and best-fit SEDs for robust SMG counterparts	108
5.1	Redshift distribution of robust LESS SMG counterparts	120
5.2	Photometric redshift versus submillimetre flux for LESS SMGs	122
5.3	Comparison of the redshift distributions of robust and tentative SMG counterparts, and radio-, 24- μ m and IRAC-selected counterparts	123
5.4	Redshift distribution of unidentified SMGs	126
5.5	Photometric redshift distribution of all LESS SMGs	129
5.6	$(B - z)$ versus $(z - K)$ colour-colour plot of SMG counterparts	130
5.7	Submillimetre to radio and submillimetre to mid-infrared flux ratios versus redshift	132
5.8	The correlation between redshift and $S_8/S_{3.6}$ for SMGs	133
5.9	The characteristic dust temperature versus far-infrared luminosity for SMGs	135
5.10	Far-infrared luminosity functions of SMGs	137
5.11	Evolution of the SFRD of LESS SMGs	139
5.12	Optical and infrared images of LESS SMGs	145
6.1	Distribution of the effective X-ray photon index for X-ray detected LESS SMGs	159
6.2	Submillimetre flux against 0.5–8 keV X-ray flux	160
6.3	0.5–8 keV X-ray luminosity against 1.4 GHz radio luminosity for LESS SMGs	162
6.4	The average optical to near-infrared SED of SMGs	164

6.5	Photometric redshift against rest-frame H -band absolute magnitude for LESS SMGs	166
6.6	Specific star-formation rate versus redshift for the LESS SMGs	169
6.7	Autocorrelation function of IRAC galaxies in the ECDFS	174
6.8	Projected real-space cross-correlation of LESS SMGs and IRAC galaxies in the ECDFS	176

List of Tables

2.1	Details of the nine $z \sim 0.2$ galaxy clusters analysed.	14
2.2	Summary of the CFHT observations	16
2.3	Photometric corrections applied to the cluster fields.	17
2.4	Parameters of galaxies on the red-sequence and in the central 600 kpc radius of clusters at $z \sim 0.2$	22
3.1	Summary of observations of MS 0451–03	40
3.2	AzTEC galaxies in MS 0451–03	45
3.3	Radio and 24 μm counterparts of AzTEC galaxies in MS 0451–03	52
3.4	Optical and near-infrared photometry for the detected SMG counterparts in the MS 0451–03 field	53
3.5	Results of stacking 24- μm , 1.1-mm and radio imaged on 24- μm , late- and early-type populations of MS 0451–03	69
4.1	Summary of the number of LESS SMG counterparts identified from radio, 24- μm and IRAC observations	83
4.2	Summary of photometry employed for photometric redshift calculation of LESS SMGs.	85
4.3	Optical photometry of LESS SMG counterparts	87
4.4	Near-infrared photometry of LESS SMG counterparts	89
4.5	Photometric redshifts of LESS SMGs	101
5.1	Far-infrared luminosity function for radio-detected LESS SMGs	138
6.1	Signatures of AGN in LESS SMGs	157

Declaration

The work in this thesis is based on research undertaken between 2007 and 2010 at the Extragalactic Astronomy Group at the Department of Physics, Durham University, United Kingdom. No part of this thesis has been submitted elsewhere for any other degree or qualification, and unless referenced to the contrary here or in the text it is all my own work. Some of this work has been published in the following papers:

- **“An AzTEC 1.1-mm survey for ULIRGs in the field of the Galaxy Cluster MS 0451.6-0305”** Wardlow, J.L., Smail, Ian, Wilson, G.W., Yun, M.S., Coppin, K.E.K., Cybulski, R., Geach, J.E., Ivison, R.J., Aretxaga, I., Austermann, J.E., Edge, A.C., Fazio, G.G., Huang, J., Hughes, D.H., Kodama, T., Kang, Y., Kim, S., Mauskopf, P.D., Perera, T.A. & Scott, K.S. , 2010, Monthly Notices of the Royal Astronomical Society, Volume 401, Issue 4, pp. 2299-2317.
- **“The LABOCA survey of the Extended Chandra Deep Field South – the photometric redshift distribution of submillimetre galaxies”** Wardlow, J.L., Smail, Ian, Coppin, K.E.K., Alexander, D.M., Brandt, W.N., Danielson, A.L.R., Luo, B., Swinbank, A.M., Walter, F., Weiß, A., Xue, Y.Q., Zibetti, S., Bertoldi, F., Biggs, A.D., Chapman, S.C., Dannerbauer, H., Dunlop, J.S., Gawiser, E., Ivison, R.J., Knudsen, K.K., Kovács, A., Lacey, C.G., Menten, K.M., Padilla, N., Rix, H.-W., & van der Werf, P.P., astro-ph/1006.2137, Submitted to Monthly Notices of the Royal Astronomical Society

Chapter 3 notes –

§3.2: The AzTEC 1.1-mm data were reduced by G.W. Wilson, who contributed some text to this section regarding this reduction. The VLA data were reduced by R. J. Ivison, and the sources extracted by me from the radio maps he produced. R. J. Ivison also provided some text concerning the reduction of the radio data. The CFHT *U*-band data were reduced by C.-J. Ma and H. Ebeling; the *Spitzer* IRAC data was reduced by R.

Cybulski and I performed the source extraction on these reduced data. R. Cybulski also contributed contributed some text regarding the *Spitzer* IRAC data reduction.

§3.3: The AzTEC source extraction and number counts analysis was performed by G. W. Wilson and the SMA data reduction and source extraction was carried out by J. D. Younger.

Chapter 4 notes –

§4.2: The statistical identification of LESS SMG counterparts from radio and 24- μ m data was performed by A. Biggs. I undertook the analysis of the IRAC colours and fluxes of radio and 24- μ m identified SMGs, to search for potential IRAC counterparts, and A. Biggs performed the analysis on these galaxies to locate the robust and tentative IRAC counterparts.

§4.2.1: The ECDFS HAWK-I *J*- and *K*-band data were reduced by S. Zibetti, and the sources extracted by me. S. Zibetti contributed some text to this section regarding the data reduction.

§4.3.3: The derivation of photometric redshifts with ZEBRA, and the comparison to those from HYPERZ was performed by B. Luo and Y. Q. Xue and they contributed some text to this section describing the procedure.

Chapter 5 notes –

§5.3: Comparison data from the GALFORM semi-analytic model were provided by A. M. Swinbank.

Chapter 6 notes –

§6.2: Calculations of the X-ray flux limits of X-ray undetected SMGs were performed by D. Alexander, comparison data from the GALFORM semi-analytic model were provided by A. M. Swinbank and the calculations of the clustering of SMGs were performed by R. Hickox.

Copyright © 2010 by Julie Louise Wardlow

The copyright of this thesis rests with the author. No quotation from it should be published without prior written consent and information derived from it should be acknowledged.

Acknowledgements

First and foremost I would like to acknowledge the major role that my supervisor, Ian Smail, has had in this work. He believed in me from the start and has been willing to share his extensive knowledge in answer to the strangest of questions and at the busiest of times. I wholeheartedly thank you Ian for giving me this opportunity and supporting me throughout the journey.

Of course, there are many other Durham astronomers who have helped me along the way, and although I cannot mention everyone here, particular thanks go to Dave Alexander, Kristen Coppin, Alastair Edge, Jim Geach, Ryan Hickox and Mark Swinbank, who have each helped me out tremendously over the years, each with their own particular brand of expertise and breadth of knowledge. In addition, the numerous and varied coffee-time discussions have broadened my knowledge and made me stop and think on more occasions than I care to admit. For that I especially note Chris Done, Pete Edwards, Vince Eke, John Lucey, Tom Shanks and Russell Smith.

I have met many great friends here in Durham and I credit you all for keeping me sane! So thank you and best of luck to: Rob Crain, Alice Danielson, Nikos Fanidakis, Jeanette Gladstone, Andy Goulding, Mike Hill, Sarah Hutton, Elise Jennings, Bret Lehmer, Alex Merson, Jim Mullaney, Mark Norris, Alvaro Orsi, Tim Rawle, Nic Ross and Nok Tummuangpak.

Last, but by no means least, I wish to say thank you to my family, for their love, support and guidance over the years. Many years ago my parents somehow managed to instill in me a great sense of wonder of the Universe. Since then they have been there for me every step of the way, throughout years of study, and despite the miles of motorway between Poole and Durham. So, Mum, Dad and Vikki, thank you. I wouldn't have made it without you.

Chapter 1

Introduction

The Universe contains a plethora of galaxies of different colours, shapes, masses and star-formation activity. Astronomers have been classifying galaxies for many years, even before they were definitively shown to be “island universes” outside of our own Milky Way (Hubble 1929). Perhaps the most widely used scheme is based on that devised by Hubble (1926), commonly known as the “tuning fork” in which galaxies are classified as elliptical (early-type), spiral (late-type) or irregular galaxies (Fig. 1.1). We now know that there is much more variety in the Universe, and that galaxies of different types are not randomly distributed on the sky or in redshift space.

The reasons for many of the biases in the distributions of different types of galaxies are not well understood. In this thesis I use photometric observations of galaxy clusters and active star-forming galaxies to investigate the processes of galaxy evolution and the build-up of the populations of red, passive galaxies that are typically found in massive clusters at $z \sim 0$.

1.1 Galaxy clusters

The distribution of galaxies on the sky is not random and many regions are overdense, containing groups or clusters of galaxies. Galaxy clusters are massive, gravitationally-bound objects, which each contain large number of individual galaxies, hot intracluster gas, intracluster light and dark matter. Inflation and hierarchical structure formation theory suggests that galaxy clusters began as overdense primordial fluctuations in the early Universe, growing and accreting matter throughout cosmic history to become the massive structures we observe today.

The galaxy populations of local massive clusters are highly biased compared to the

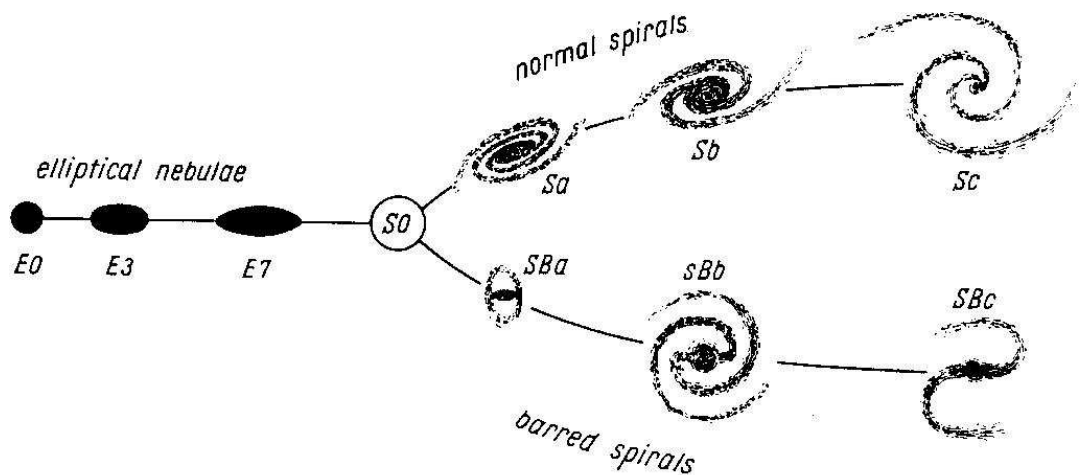


Figure 1.1: The traditional “tuning fork” diagram of galaxy classification (Hubble 1926), whereby galaxies are classed as elliptical (early-type), spiral (late-type) or irregular galaxies. Figure from Sandage et al. (1975).

field: galaxies in local clusters are typically passive early-types (see Fig. 1.2), yet the local field population hosts a significant fraction of late-type galaxies. This trend is described by the Morphology-Density relation (Dressler 1980) and is characterised by an increasing fraction of elliptical galaxies in regions of increasing local galaxy density (e.g. Oemler 1974; Dressler 1980). The passive early-type galaxies in local clusters are observed to have little scatter in their rest-frame colours, and define a tight colour-magnitude relation (CMR or “red-sequence”; Visvanathan & Sandage 1977; Bower et al. 1992). CMR galaxies in different clusters have very little scatter in their rest-frame UV-optical colours, indicative of a homogeneous population, and suggesting that the CMR consists of evolved galaxies with little ongoing star-formation (Ellis et al. 1997). Observations show that the Morphology-Density relation is caused by decreasing numbers of star-forming galaxies in the high-density regions of local clusters, and that the form of the red-sequence does not vary significantly as a function of local density (e.g. Pimblet et al. 2002; Baldry et al. 2006).

It has also been shown that the giant elliptical population in that dominates local cluster cores has been in place since at least $z \sim 0.6$ (Ellis et al. 1997), and possibly prior to $z \sim 1$ (Faber et al. 1997; Lubin et al. 1998), implying that they formed at high-redshifts. These elliptical galaxies are stable and have only undergone passive evolution in the recent past (van Dokkum & Franx 1996; Ellis et al. 1997; Barger et al. 1998). In

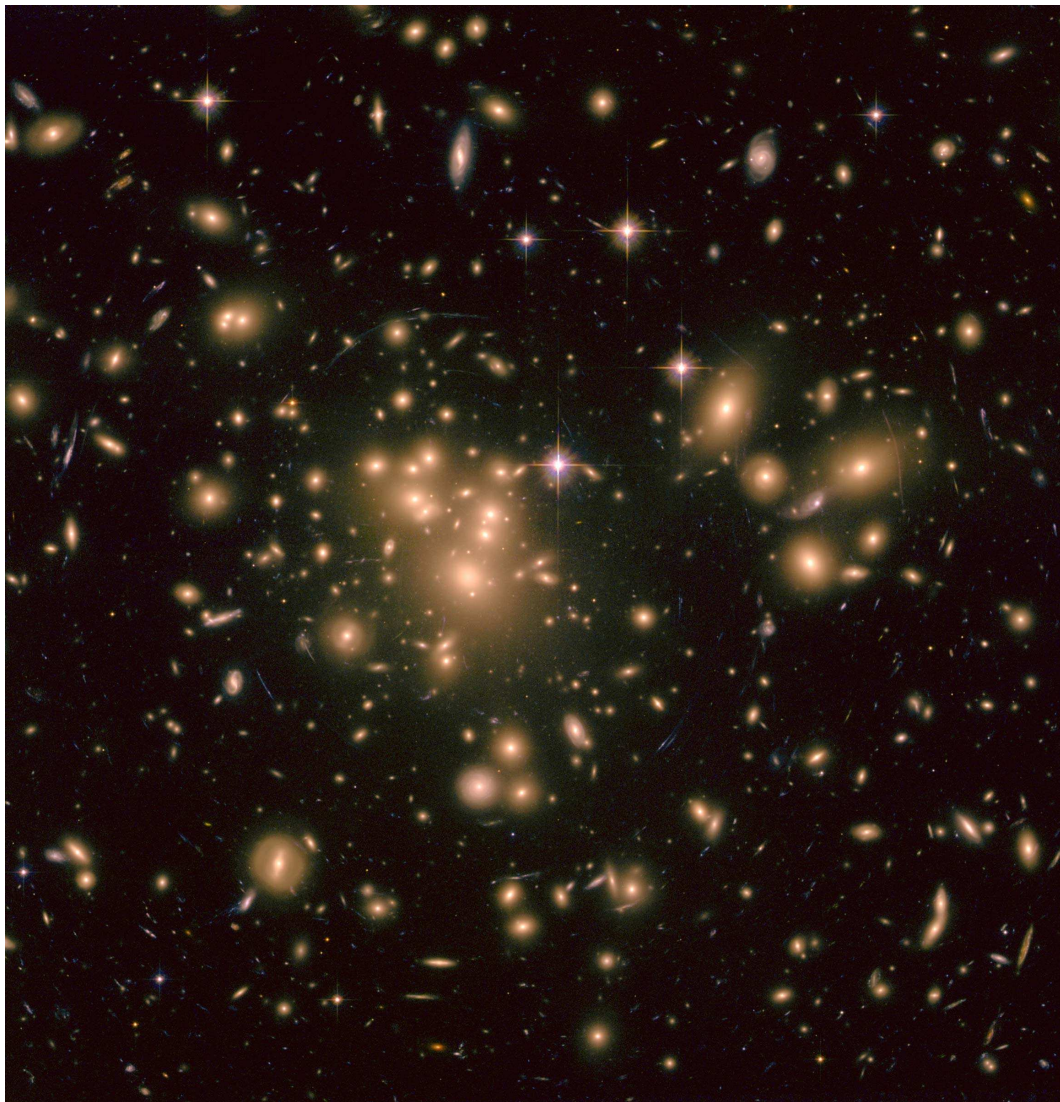


Figure 1.2: *Hubble Space Telescope* colour image of the galaxy cluster Abell 1689 showing the overdensity of red, early-type galaxies. Image credit and acknowledgements: NASA, ESA, E. Jullo (Jet Propulsion Laboratory), P. Natarajan (Yale University), and J.-P. Kneib (Laboratoire d’Astrophysique de Marseille, CNRS, France), H. Ford and N. Benitez (Johns Hopkins University), and T. Broadhurst (Tel Aviv University)

contrast S0 galaxies are rare in distant clusters ($z \gtrsim 0.5$; Dressler et al. 1997), indicating that the formation or transformation of S0 galaxies onto the CMR takes place at later times than the buildup of the elliptical galaxy population in clusters. There are also claims of an increasing deficit of faint CMR galaxies in clusters out to $z \sim 1$ (e.g. Dressler et al. 1997; Smail et al. 1998; De Lucia et al. 2004; Stott et al. 2007; Holden et al. 2009), suggesting that dwarf galaxies form at later times than giants (Tanaka et al. 2005) and that they move onto the CMR later than the cluster giants.

There is also evolution in the populations of blue, star-forming galaxies in clusters, with an increasing level of star-formation activity and an increasing fraction of blue, star-forming galaxies in clusters at increasing redshifts, at least out to $z \sim 1$ (e.g. Butcher & Oemler 1984). At high redshifts clusters are thought to accrete (typically blue star-forming) field galaxies as they grow via gravitational collapse. It has been suggested that these newly-accreted galaxies transform into passive populations with time (e.g. Smail et al. 1997) and build-up the faint end of the CMR. Thus, it appears that environmental processes in clusters transform infalling blue star-forming galaxies at high-redshifts into passive early-type galaxies that lie on the CMR at low-redshifts. Candidates for such processes include ram pressure stripping (Gunn & Gott 1972), strangulation (Larson et al. 1980), and galaxy-galaxy or galaxy-cluster interactions (Moore et al. 1996).

Studies also suggest that there are additional environmental processes at work in the central regions of local clusters. These central regions contain fewer dwarf galaxies than expected and the galaxies appear smaller than equivalent populations in the cluster outskirts (e.g. Lobo et al. 1997; Cypriano et al. 2006). Numerous low-surface-brightness tidal tails are also observed in the central regions of local clusters (Gregg & West 1998). Thus, it appears that the galaxies in the central regions of local clusters are disturbed by gravitational interactions, causing visible tidal tails, mass loss and reduction in the number of detectable low-luminosity galaxies. It has long been known that the centres of clusters contain a diffuse component of intracluster light (Zwicky 1951; Oemler 1976), which is composed of stars, supernovae and planetary nebulae (e.g. Arnaboldi et al. 1996; Theuns & Warren 1997; Gal-Yam et al. 2003) and it follows that galaxies in the central regions of local clusters are gravitationally disrupted and stripped of material that then contributes to the intracluster light. It is currently unknown whether galaxies in clusters at higher redshift are subject to the same destructive forces, but the existence of the intracluster light is well documented in $z > 0$ clusters.

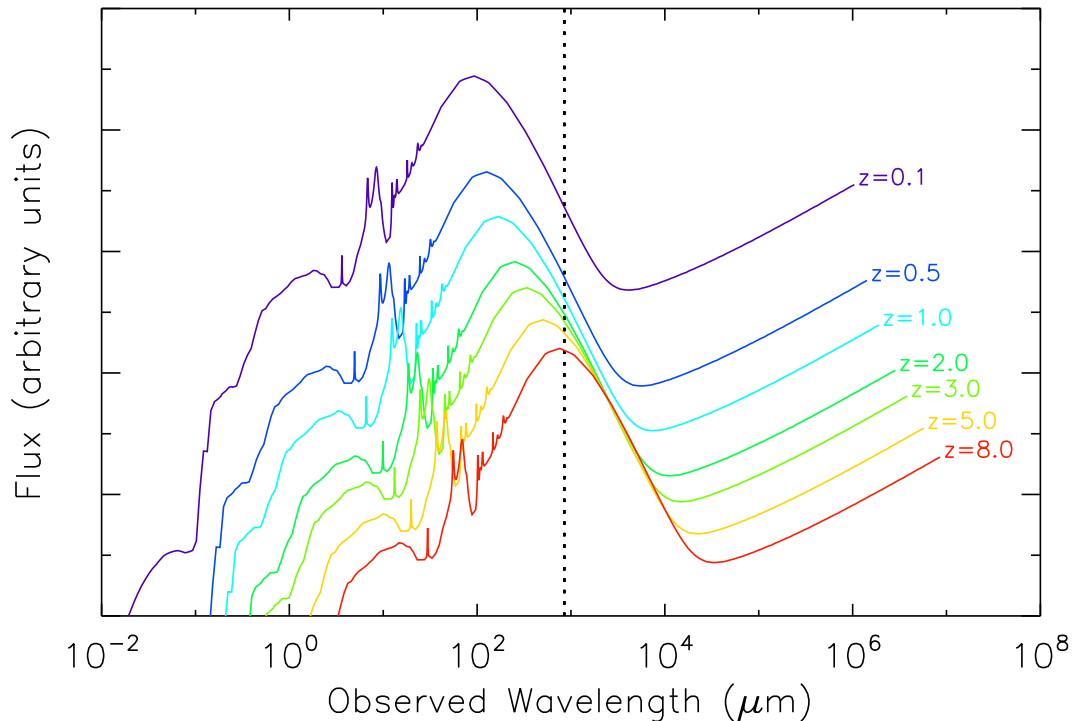


Figure 1.3: Example of the negative K-correction at submillimetre and millimetre wavelengths. We show the SED of Arp 220 (Silva et al. 1998) redshifted from $z = 0.1$ to $z = 8$, and highlight $850 \mu\text{m}$ with a vertical line. At $z \sim 1-8$ cosmological dimming is approximately negated by the redshifting of the SED due to the far-infrared dust peak, such that the observed flux at submillimetre wavelengths is approximately constant. However, we note that observations at radio wavelengths do not benefit from the negative K-correction, so the highest redshift SMGs may be amongst the faintest at radio wavelengths, making them difficult to identify.

1.2 Submillimetre galaxies

Thanks to the shape of the spectral energy distribution (SED) of rest-frame far-infrared dust emission, observations at submillimetre and millimetre wavelengths benefit from the negative K-correction (Blain & Longair 1993). The negative K-correction results in an almost constant apparent flux for sources with a fixed luminosity at $z \sim 1-8$ (Fig. 1.3). As such, surveys at submillimetre and millimetre wavelengths are able to efficiently select dusty active galaxies at high redshifts.

Since the first extragalactic submillimetre surveys 13 years ago detected a population

of dusty active sources (Smail et al. 1997; Barger et al. 1998), a series of ever larger surveys has exploited the negative K-correction at submillimetre and millimetre wavelengths to identify a population of sources with a surprisingly high surface density to mJy-flux limits (e.g. Smail et al. 1997; Barger et al. 1998; Hughes et al. 1998; Blain et al. 1999; Eales et al. 1999; Bertoldi et al. 2000, 2007; Coppin et al. 2006; Knudsen et al. 2008; Weiß et al. 2009; Austermann et al. 2010). These so-called submillimetre galaxies (SMGs) appear to lie at cosmological redshifts ($z \gtrsim 1$; e.g. Chapman et al. 2005), implying that they have far-infrared luminosities exceeding $10^{12} L_{\odot}$ and are therefore classed as Ultraluminous infrared galaxies (ULIRGs; Sanders & Mirabel 1996). The significant far-infrared luminosities of SMGs are typically powered by star-formation and not AGN (e.g. Alexander et al. 2005; Pope et al. 2008; Hill & Shanks 2010), suggesting that they have star-formation rates (SFRs) of $\gtrsim 1000 M_{\odot} \text{yr}^{-1}$, and are undergoing massive starbursts. The high surface density of SMGs suggests a strong evolution of the population: $\propto (1+z)^4$ (Smail et al. 1997; Blain et al. 1999), and therefore of starburst galaxies, indicating that a significant fraction of massive star-formation may be taking place in these galaxies – as such making them a good candidate for the progenitors of local massive cluster galaxies. The redshifts of SMGs are required to be able to reliably quantify the evolution, understand the physical processes that drive it and establish whether the density and clustering of SMGs is consistent with them being cluster progenitors.

SMGs are notoriously difficult to study in detail, and it has proved challenging to identify optical and near-infrared counterparts which can be used to measure spectroscopic or photometric redshifts. This is because single-disk submillimetre telescopes typically have beams of $\sim 15''$, which is too large to directly pinpoint the optical or near-infrared counterparts. In addition, the sensitivity of the current generation of submillimetre interferometers is such that the exposure times required means that they are unsuitable for identifying large numbers of SMGs. Finally, SMGs are typically optically faint due to dust obscuration and their typically high-redshifts. This makes identifying SMG counterparts for multiwavelength follow-up observations challenging.

The observed submillimetre and millimetre emission from SMGs corresponds to the rest-frame far-infrared emission, so the far-infrared-radio correlation (Helou et al. 1985; Condon 1992; Garrett 2002) and the relatively low spatial density of radio sources can be exploited to identify SMG counterparts (e.g. Ivison et al. 2002, 2005, 2007; Chapin et al. 2009). The dust emission that causes the high far-infrared luminosities in SMGs also means that they are typically bright at mid-infrared wavelengths. Therefore, 24- μm

sources, which also have relatively low spatial density, can also be used to identify SMG counterparts (e.g. Ivison et al. 2004; Pope et al. 2006; Ivison et al. 2007; Chapin et al. 2009). The reliability of radio and mid-infrared potential counterparts is typically calculated using the corrected Poissonian probability (p ; Downes et al. 1986) – the probability that potential counterparts lie within the vicinity of the submillimetre source by chance. The calculation takes into account the separation between the submillimetre centroid and the radio (or 24- μm) position, the density of radio (or 24- μm) sources, and the flux of the proposed counterpart. Typically only identifications with $p \leq 5\%$ or $p \leq 10\%$ are considered to be related to the SMG emission, yielding reliable counterparts to 60–80% of SMGs. Thus, excluding a handful of sources identified using submillimetre interferometry, only the 60–80% of SMGs with radio or mid-infrared counterparts have been studied in detail.

The optical faintness of SMGs makes measurement of their spectroscopic redshift distribution difficult and time-intensive (e.g. Barger et al. 1999; Chapman et al. 2003a, 2005), so photometric techniques based on the optical/near-infrared or far-infrared/radio SEDs are often employed to estimate SMG redshifts (e.g. Carilli & Yun 1999; Smail et al. 2000; Ivison et al. 2004; Pope et al. 2005, 2006; Ivison et al. 2007; Aretxaga et al. 2007; Clements et al. 2008; Dye et al. 2008; Biggs et al. 2010). The 60–80% of SMGs with reliable counterparts have a redshift distribution that peaks at $z \sim 2.2$ (Chapman et al. 2005), although there is significant variation between different studies (see e.g. Chapman et al. 2005; Clements et al. 2008; Dye et al. 2008), which may be partially due to the different levels of incompleteness and selection biases in the different studies. The infrared luminosity functions of SMGs with identified counterparts confirms the inferred evolution of the population, with SMGs at $z = 2\text{--}3$ have typically higher luminosities and luminosity density than those at $z = 1\text{--}2$. Similarly, the star-formation rate density (SFRD) of SMGs appears to peak at $z \sim 2$. However, the concern is that the 20–40% of SMGs that are unidentified could include the highest-redshift members of the population (see Fig. 1.3) and thus the derived evolution may be biased.

Optical and near-infrared SED fitting can provide estimates of the stellar masses of SMGs. Analysis of this kind suggests that SMGs have stellar masses of $\gtrsim 7 \times 10^{10} M_{\odot}$ (e.g. Borys et al. 2005; Dye et al. 2008; Hainline et al. 2010), although there are significant differences between studies, which is likely to be due to a combination of sample bias and systematic errors. Despite the differences between the different works the consensus is that SMGs have large stellar masses, which potentially could evolve into cluster red-sequence

galaxies. The claim that SMGs are massive is supported by observed dynamical masses of $\sim 5 \times 10^{10} M_{\odot}$ from integral-field spectroscopy (Swinbank et al. 2006), and $\sim 10^{11} M_{\odot}$ from observations of CO emission lines, which also yields gas masses of $\sim 3 \times 10^{10} M_{\odot}$ (e.g. Genzel et al. 2003; Greve et al. 2005).

In addition to being massive galaxies the progenitor population of low-redshift cluster CMR galaxies are expected to be strongly clustered, and reside in massive dark-matter halos. Unfortunately, the typically small samples of SMGs, which often do not have redshift information has hampered efforts to measure SMG clustering. Several authors (e.g. Webb et al. 2003; Blain et al. 2004; Scott et al. 2006; Serjeant et al. 2008; Weiß et al. 2009) find tentative evidence that SMGs are not randomly distributed in the sky and are likely to be strongly clustered. Blain et al. (2004) did manage to detect the clustering of a sample of SMGs with redshift information, and derived a correlation length of $r_0 = 6.9 \pm 2.1 h^{-1} M_{\odot}$, corresponding to a dark-matter halo mass of $\sim 3 \times 10^{12} M_{\odot}$ at $z = 2$. We also note that Cooray et al. (2010) recently investigated the angular correlation function of *Herschel* sources selected at 250- μm and with far-infrared colours similar to those expected of “classic” $\sim 850\text{-}\mu\text{m}$ selected $z \sim 2$ SMGs, and calculated that they reside in dark matter halos of mass $> (5 \pm 4) \times 10^{12} M_{\odot}$.

It is also now widely accepted that all galaxies contain a supermassive black hole (SMBH) in their centre; locally, the SMBH mass is observed to follow a well-defined relationship with the mass of the bulge (Magorrian et al. 1998; Gebhardt et al. 2000). Therefore, if SMGs are the progenitors of local elliptical galaxies it could be expected that the build-up of stellar mass is associated with co-eval or subsequent growth of the SMBH – observed as an AGN. Although the bolometric and far-infrared luminosities of SMGs are typically dominated by star-formation emission (e.g. Alexander et al. 2005; Pope et al. 2008), up to $\sim 40\%$ of SMGs are also found to contain AGN signatures (e.g. Alexander et al. 2005; Takata et al. 2006; Pope et al. 2008; Coppin et al. 2009; Hainline et al. 2010). However, due to the requirements for radio or 24- μm counterparts, and often spectroscopic redshifts, many surveys for AGN in SMGs are subject to significant selection biases, which makes it difficult to accurately constrain the AGN fraction in SMGs and thus investigate the evolution of the SMBHs in SMGs.

It has been postulated that SMGs and QSOs are closely related and are part of the same evolutionary sequence (Fig. 1.4; e.g. Sanders et al. 1988a,b; Hopkins et al. 2008a,b; Hickox et al. 2009). In this theory gas-rich galaxies form in the high-redshift Universe and slowly grow through cold-gas accretion or minor mergers. If two massive gas-rich

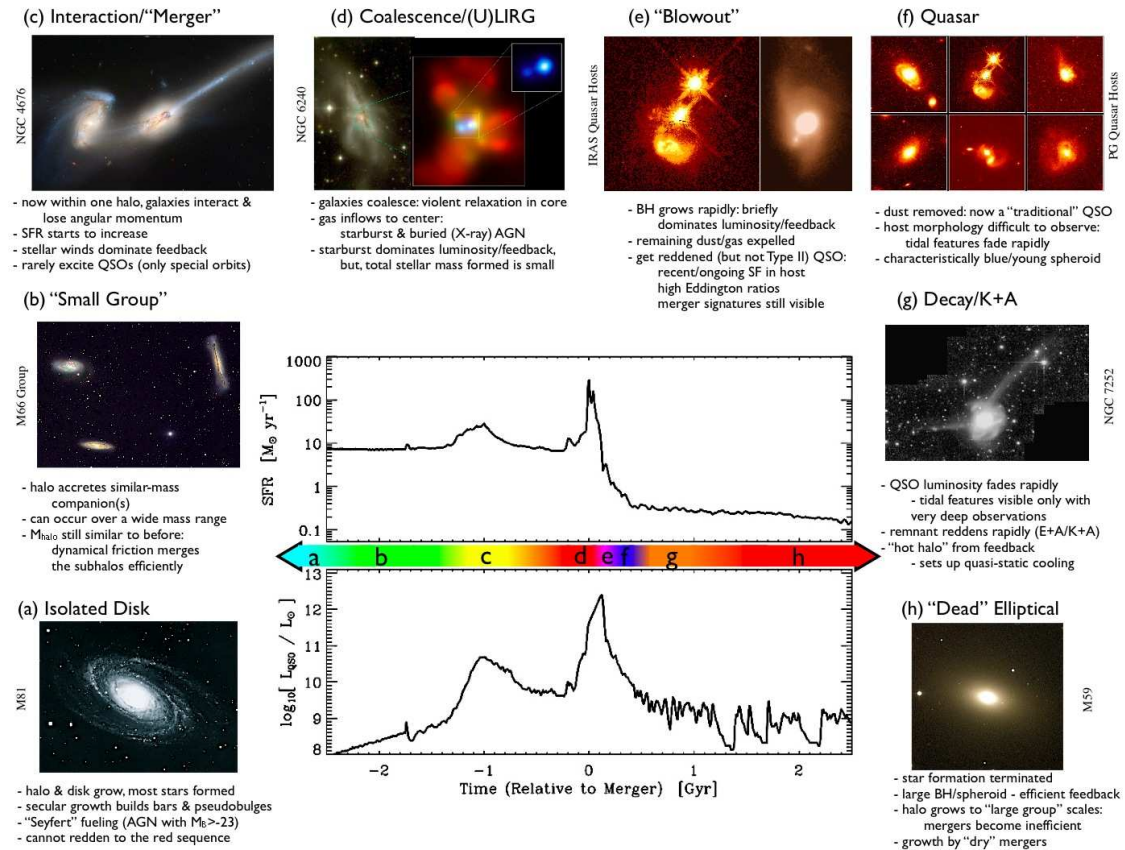


Figure 1.4: Schematic illustration of the proposed evolutionary sequence of SMGs and QSOs. When galaxies in the massive halos at high redshifts undergo major mergers (or are otherwise destabilised) a burst of dusty star-formation is triggered, which is observed as a SMG. The starburst is followed by (or perhaps concurrent with) a QSO phase, which becomes visible as the obscuring dust is blown off (or dissipates). At the end of the SMG and QSO activity the resulting galaxy fades to become a massive, passive early-type galaxy. Figure from Hopkins et al. (2008b). Image credits: (a) NOAO/AURA/NSF; (b) REU program/NOAO/AURA/NSF; (c) NASA/STScI/ACS Science Team; (d) Optical (left): NASA/STScI/R. P. van der Marel & J. Gerssen; X-ray (right): NASA/CXC/MPE/S. Komossa et al.; (e) Left: J. Bahcall/M. Disney/NASA; Right: Gemini Observatory/NSF/University of Hawaii Institute for Astronomy; (f) J. Bahcall/M. Disney/NASA; (g) F. Schweizer (CIW/DTM); (h) NOAO/AURA/NSF.

galaxies merge, a dusty starburst is triggered (ULIRG) and observed as a SMG. The same event also causes gas to be accreted onto the SMBH and black-hole growth to take place. As the gas and dust from the starburst are blown-off (or dissipate) we observe a QSO. It is currently unclear whether the black-hole and stellar mass growth phases coexist and dust prevents observations of the QSO, or whether the QSO phase only begins at the end of the star-burst phase. Eventually, all activity ceases and the merger remnant passively evolves into a massive early-type galaxy. The peak era of star-formation activity in SMGs is at $z \sim 2$, corresponding to the era of peak QSO activity, which also occurs at $z \sim 2$ (Hopkins et al. 2007). In addition, QSOs appear to reside in dark-matter halos of mass $\sim 3 \times 10^{12} M_{\odot}$ (e.g. Croom et al. 2005; Ross et al. 2009), in agreement with early estimates of the dark-matter halo masses of SMGs. These observations add credence to the idea that the evolution of SMGs and QSOs are related, although definitive evidence is currently lacking.

1.3 Outline of this thesis

In Chapter 2 we begin our investigation into galaxy evolution by considering the CMR population in clusters at $z \sim 0.2$. We use photometry to isolate red-sequence galaxies and study the build-up of the CMR in with clustercentric radius and local galaxy density. We next search for potential progenitors of a fraction of these CMR dwarf galaxies using 1.1-mm observations to identify potential LIRGs in a cluster at $z = 0.54$ (Chapter 3).

We then calculate and extensively test optical/near-infrared photometric redshifts of SMGs detected in an 870- μm survey of the ECDFS in Chapter 4, and in Chapters 5 and 6 we use these photometric redshifts to investigate whether SMGs could be the progenitor population of local CMR cluster galaxies. Chapter 5 focuses on the redshift distribution, infrared luminosity function and star-formation evolution of SMGs and finally, in Chapter 6, we consider the clustering of SMGs, and their stellar and dark-matter halo masses.

Chapter 2

The effect of environment on the galaxy populations in rich clusters at $z \sim 0.2$

2.1 Introduction

Galaxy clusters are highly biased environments in which galaxies potentially evolve more rapidly than in the field. The galaxy populations of local massive clusters contain mainly passive early-type galaxies which define a colour-magnitude relation (CMR; or “red-sequence”; e.g. Visvanathan & Sandage 1977; Bower et al. 1992). However, studies of clusters out to $z \sim 1$ suggest that they contain increasing star-formation activity at higher redshifts associated with a growing fraction of blue, star-forming galaxies (e.g. Butcher & Oemler 1984). Over the same redshift range there have been claims of a growing deficit in the CMR population at faint magnitudes, as well as a claimed decline in the numbers of S0 galaxies, in the sense that there are fewer faint red galaxies on the CMR as well as fewer S0 galaxies in clusters at higher redshifts (Dressler et al. 1997). It has been suggested that the blue, star-forming galaxies, accreted from the surrounding field, may be transforming into these passive populations with time (e.g. Smail et al. 1998). Evidence also suggests that the fraction of dwarf galaxies in clusters (as measured by the dwarf-to-giant ratio or M^*) on the CMR increases with decreasing redshift. Since the giant population was established by at least $z \sim 0.5$ (Ellis et al. 1997) this implies that increasing numbers of dwarf galaxies are transformed into red-sequence galaxies at low redshifts (De Lucia et al. 2007; Stott et al. 2007; Holden et al. 2009, although see Andreon

et al. 2006). Thus, it appears that environmental processes (e.g. ram pressure stripping, Gunn & Gott 1972; strangulation, Larson et al. 1980; galaxy-galaxy or galaxy-cluster interactions, Moore et al. 1996) in clusters transform infalling star-forming field galaxies into passive early-type galaxies lying on the CMR.

Furthermore, studies of local clusters suggest that there are additional changes happening in the properties of galaxies in the highest density regions. Cypriano et al. (2006) showed that the bright elliptical galaxies in the regions of highest galaxy density in clusters at $z = 0.015\text{--}0.08$ are $\sim 5\%$ smaller than those of equivalent brightness in lower density regimes, indicative of loss of stellar mass from galaxies in cluster centres. The faint-end slope of the luminosity function in local clusters is also found to be suppressed in the highest density domains (e.g. Lobo et al. 1997). This suggests that there are fewer faint galaxies in these high density regions of clusters than in areas of lower galaxy density. Additionally, numerous low-surface-brightness tidal tails are present in the same high-density regions of local galaxy clusters (e.g. Gregg & West 1998). Thus, at least locally, it appears that the galaxies in the centres of clusters are disturbed by gravitational interactions, causing visible tidal tails, mass loss, and a reduction in the number of low-luminosity galaxies. Indeed, the central regions of galaxy clusters have long been known to contain a diffuse component of intracluster light (Zwicky 1951; Oemler 1976), which consists of stars, supernovae, and planetary nebula (e.g. Arnaboldi et al. 1996; Theuns & Warren 1997; Gal-Yam et al. 2003). It follows that locally the intracluster light is most likely formed from material lost from galaxies in the highest density regions of clusters.

Current technology limits detailed study of the intracluster light at higher redshifts and to date there have been few studies into the evolution of cluster galaxies across a wide range of environments at $z \gtrsim 0.1$. Such studies could provide evidence of the buildup of the intracluster light from galaxies and information about the transformation of galaxy onto the red-sequence. Andreon (2002), Mercurio et al. (2003), Pracy et al. (2004) and Banados et al. (2010) each studied individual clusters at $z \sim 0.2\text{--}0.3$ and each found that the fraction of dwarf galaxies decreases in the central (or equivalently highest density) regions of the clusters. However, these studies either did not consider CMR and blue galaxies separately, or the areal coverage was insufficient to examine the buildup of galaxies onto the red-sequence out to the virial radius or beyond. Barkhouse et al. (2009) studied ~ 60 Abell clusters at $z = 0.02\text{--}0.2$ out to radii of $0.9r_{200}$ (where r_{200} is the cluster virial radius) and did examine the red and blue galaxy populations separately. However, they were unable to detect the transformation of galaxies onto the CMR.

In this work we utilise wide-field imaging of nine galaxy clusters at $z \sim 0.2$ to investigate the evolution of the red-sequence luminosity function and red-sequence dwarf-to-giant ratio (RDGR; Ferguson & Sandage 1991) as a function of clustercentric radius and local galaxy density – from the highest density, central regions out to the virial radii. The narrow redshift range and the well-defined cluster selection criteria enables us to simply combine the clusters to provide an ensemble average with correspondingly better precision, and our wide-field imaging enables us to study the cluster populations out to r_{200} . We also examine red-sequence galaxies within a fixed radius and, by comparing to previous surveys at $z \sim 0.1$ – 1 , track the build-up of the CMR with redshift. Later, in Chapter 3, we examine a cluster at $z = 0.54$ and search for active galaxies, which may be forming stars at a rate of hundreds of solar masses per year, and may be the progenitor population of the red-sequence galaxies studied here.

We describe the sample selection and available data in § 2.2 and in § 2.3 analyse the buildup of the cluster red-sequence and discuss our results. Finally, in § 2.4, we present our conclusions. Throughout this Chapter we use J2000 coordinates, Λ CDM cosmology with $\Omega_M = 0.3$, $\Omega_\Lambda = 0.7$ and $H_0 = 70\text{kms}^{-1}\text{Mpc}^{-1}$, and Vega magnitudes.

2.2 Sample selection

In this paper we study nine galaxy clusters selected from the X-ray Brightest Abell Clusters (XBACs; Ebeling et al. 1996) and observed with the CFH12k wide-field camera on the Canada-France-Hawaii Telescope (CFHT). XBACs is a flux-limited sample of galaxy clusters which contains 242 Abell clusters that are detected in the ROSAT All-Sky Survey data. Our sample of nine clusters with $L_X > 4 \times 10^{44} \text{ ergs}^{-1}$ is listed in Table 2.1 and is limited to those clusters with redshift $0.17 < z < 0.26$ (the selection of relatively narrow redshift range means that the evolution between the clusters is negligible), declination $-20^\circ < \delta < 60^\circ$ (for observability), Galactic latitude $|b| > 15^\circ$ (to minimize stellar contamination) and hydrogen column density $N_H < 10 \times 10^{20} \text{ cm}^{-2}$ (to minimise photometric errors introduced by galactic reddening). The clusters were observed in the B , R and I filters using the CFH12k wide-field ($42 \times 28 \text{ arcmin}^2$) camera during observing runs in November 1999 and May/June 2000 (Bardeau et al. 2007). The data were reduced using standard techniques (described in detail Czoske 2002), astrometrically calibrated to the Digitized Sky Survey (DSS) and photometrically calibrated using observations of Landolt (1992) and Stetson (2000) standard stars (Bardeau et al. 2007). We employ the CFH12k

Table 2.1: Details of the nine $z \sim 0.2$ galaxy clusters analysed.

Cluster	RA ^a	Dec ^a	z	$L_{X,\text{bol}}^b$ (10^{44}ergs^{-1})	r_{200}^c (Mpc)	M_{200}^d ($10^{14}M_{\odot}$)
Abell 1689	13 ^h 11 ^m 30 ^s .1	−01°20′28″	0.184	21.4 ± 1.0	2.25 ± 0.14	19.7 ± 3.4
Abell 1763	13 ^h 35 ^m 20 ^s .1	+41°00′04″	0.228	15.9 ± 1.4	1.93 ± 0.14	13.9 ± 2.6
Abell 209	01 ^h 31 ^m 52 ^s .6	−13°36′40″	0.206	13.2 ± 1.1	1.57 ± 0.17	7.2 ± 2.0
Abell 2218	16 ^h 35 ^m 49 ^s .3	+66°12′44″	0.171	12.2 ± 0.9	1.81 ± 0.14	9.7 ± 2.2
Abell 2219 ^e	16 ^h 40 ^m 19 ^s .9	+46°42′41″	0.228	...	2.25 ± 0.18	20.9 ± 4.4
Abell 267	01 ^h 52 ^m 42 ^s .0	+01°00′26″	0.230	6.6 ± 0.7	1.15 ± 0.23	2.7 ± 1.5
Abell 383	02 ^h 48 ^m 03 ^s .4	−03°31′45″	0.187	4.6 ± 0.5	1.32 ± 0.17	4.2 ± 1.5
Abell 68	00 ^h 37 ^m 06 ^s .9	+09°09′24″	0.255	10.1 ± 0.9	1.49 ± 0.18	6.2 ± 2.0
Abell 963	10 ^h 17 ^m 03 ^s .6	+39°02′50″	0.206	10.2 ± 0.9	1.33 ± 0.10	3.7 ± 0.9

^a Coordinates are those of the central galaxy (Bardeau et al. 2007).

^b The bolometric X-ray luminosity is derived from *XMM-Newton* observations and excludes the central $0.1r_{500}$ to avoid potential contamination by cool cores (Bardeau et al. 2007; Zhang et al. 2008).

^c r_{200} , is the cluster virial radius (Bardeau et al. 2007).

^d M_{200} , the virial mass, is the total mass included in a sphere of radius r_{200} as derived from weak gravitational lensing (Bardeau et al. 2007).

^e *XMM-Newton* observations of Abell 2219 suffered from flaring, so the equivalent $L_{X,\text{bol}}$ as the remaining sample is unavailable.

B -, R - and I -band imaging and catalogues described in Bardeau et al. (2007). Details of the B -, R - and I -band observations are given in Table 2.2. Source catalogues from each filter are extracted independently using SExtractor with the sources required to have be $> 1.5\sigma$ above the background level in a minimum of five $0.2'' \times 0.2''$ connected pixels. Magnitudes are measured in apertures of $3''$ radius and the B -, R - and I -band catalogues are combined using a matching radius of $1''$.

We apply corrections for galactic extinction to the photometric catalogues, employing values derived from Schlegel et al. (1998) by the NASA/IPAC Extragalactic Database (NED)¹. One of the three CFHT observing runs was affected by cirrus and was not photometric. Bardeau et al. (2007) performed some simple photometric calibration to account for this, but photometric accuracy between the clusters is critical for our work so we perform further checks and calibration as we now describe.

We select unsaturated stars in the fields of the clusters on the basis of their bright R -band magnitudes and unresolved sizes (full-width at half-maximum); each field contains > 200 stars selected this way. Stars follow well-defined tracks in colour-colour space (Landolt 1992) and we can use a two-dimensional KS-test to compare the $B - R$ and $R - I$ colour-colour tracks of the stars in all the cluster fields to identify, and hence correct, offsets in the photometry. Cross-testing shows that Abell 209, 267 and 963 have consistent star colours, suggesting that they are well calibrated and we next combine the stars from these three fields to create a catalogue of 936 stars with precise and consistent photometry: the photometric catalogue. The zeropoints of the catalogues of the remaining six clusters are then adjusted in steps of 10^{-3} mag, and a two-dimensional KS-test performed against the photometric catalogue at each step, to determine the optimum $B - R$ and $R - I$ offsets for each cluster. Based on these colour offsets we can determine which band the has largest photometric error and correct it. The magnitude of the colour-colour offsets and the photometric corrections applied are listed in Table 2.3. After the application of these offsets we expect the relative photometry of our cluster catalogues to be good to < 0.03 magnitudes.

¹The NASA/IPAC Extragalactic Database (NED) is operated by the Jet Propulsion Laboratory, California Institute of Technology, under contract with the National Aeronautics and Space Administration.

Table 2.2: Summary of the CFHT observations (Bardeau et al. 2007).

Cluster	B				R				I			
	T_{exp} (ks)	Seeing ^a ($''$)	Limiting ^b mag	A_B^c (mag)	T_{exp} (ks)	Seeing ^a ($''$)	Limiting ^b mag	A_R^c (mag)	T_{exp} (ks)	Seeing ^a ($''$)	Limiting ^b mag	A_I^c (mag)
Abell 1689	3.6	0.9	24.9	0.115	3.0	0.8	24.3	0.071	3.0	0.9	23.0	0.052
Abell 1763	3.6	1.0	24.9	0.039	6.0	0.9	24.4	0.024	3.0	0.8	23.2	0.018
Abell 209	7.2	1.0	25.0	0.083	6.6	0.7	24.5	0.052	3.6	0.7	23.3	0.037
Abell 2218	3.4	1.1	24.5	0.106	6.9	1.0	24.4	0.065	3.0	0.8	22.9	0.048
Abell 2219	5.4	1.0	25.0	0.108	6.3	0.8	24.6	0.067	3.0	0.8	23.3	0.048
Abell 267	3.0	1.0	24.2	0.106	4.8	0.7	24.1	0.066	0.9	0.7	22.7	0.048
Abell 68	8.1	1.1	25.2	0.393	7.2	0.7	24.3	0.244	3.6	0.6	23.3	0.177
Abell 383	7.2	0.9	24.6	0.140	6.0	0.9	24.1	0.087	3.6	0.7	22.7	0.063
Abell 963	7.2	0.9	25.2	0.066	4.8	0.8	24.3	0.041	1.1	1.1	22.8	0.030

^a Seeing is measured as the FWHM of stars on the final stacked image of each cluster (Bardeau et al. 2007).

^b 50% completeness limit (Bardeau et al. 2007).

^c Galactic extinction (Schlegel et al. 1998).

Table 2.3: Photometric corrections applied to the cluster fields. Abell 209, Abell 267 and Abell 963 are not included because they are deemed to already have accurate photometry and are used as the comparison sample.

Cluster	N_{star}^a	B-R offset ^b (mag)	R-I offset ^b (mag)	Filter to adjust	Filter correction (mag)
Abell 1689	416	-0.08 ± 0.01	0.07 ± 0.01	R	0.075
Abell 1763	316	0.01 ± 0.03	0.04 ± 0.01	I	-0.040
Abell 2218	434	-0.02 ± 0.02	0.07 ± 0.02	I	-0.070
Abell 2219	643	0.03 ± 0.01	0.46 ± 0.01	I	-0.460
Abell 383	348	0.05 ± 0.03	-0.02 ± 0.01	R	-0.035
Abell 68	264	-0.03 ± 0.02	0.02 ± 0.02	R	0.025

^a N_{star} is the number of stars employed for the photometry correction.

^b Colour offsets are the change that is applied to the colours of the stars in each cluster field to match to the stars in the photometric sample (see text for details).

2.3 Analysis and results

The CMR is composed of early-type (E and S0) galaxies, which appear to support little ongoing star-formation, and may represent the evolutionary end-point of galaxy formation (e.g. Visvanathan & Sandage 1977; Bower et al. 1992), although they can be formed via various processes. Therefore, by investigating the galaxies which lie on the CMR in different environments and at different redshifts we can study the physical processes that influence star-formation and hence drive galaxy evolution.

2.3.1 Colour-magnitude relation

In Fig. 2.1 we present the $B-R$ versus R colour-magnitude diagrams for the central 1 Mpc of each of the nine $z \sim 0.2$ galaxy clusters. At $z = 0.2$ the B - and R -bands approximately correspond to the rest-frame U - and V -bands, hence these colour-magnitude diagrams represent rest-frame $U-V$ versus V . For each cluster we identify the CMR for galaxies with $R = 16-22$ through a procedure in which the first estimate of the location of the CMR is performed by eye and then galaxies within ± 0.25 mags of the estimated CMR are linearly fitted using an iterative biweight procedure to derive the best-fit linear relation to the CMR. The colour-magnitude diagrams and CMR fits for each cluster are shown in

Fig. 2.1.

The galaxy clusters studied here cover a small range in redshift ($\delta z = 0.084$) and hence lookback time ($\delta t_L = 0.87$ Gyr), such that the evolution across the sample is expected to be negligible. Therefore, we can combine the data from all nine clusters to reduce the errors from field contamination and shot noise, and increase the significance of our statistics. In Fig. 2.2 we show the equivalent $B - R$ colour at $R = 20$ magnitudes for CMR in each of the nine clusters in our sample and compare this with a “no-evolution” model for the colours of elliptical and S0 galaxies at $z = 0$ from King & Ellis (1985). The model provides an adequate description of the mean colour of the CMR for all the clusters, except Abell 1689. It is unclear why the colours of CMR galaxies in Abell 1689 are offset, although it is most likely that the photometric corrections derived from the star colours (§ 2.2) are insufficient and that more than just the R -band was significantly affected by cirrus during the observations. Therefore, for Abell 1689 we use the observed value of $B - R$ at $R = 20$ to transform the colours of galaxies on the CMR to $z = 0.21$, the median redshift of the sample. This correction should minimise any remaining photometric errors between the Abell 1689 and the other clusters. The remaining eight clusters are transformed to $z = 0.21$ using the expected values from the model. We show the colour-magnitude diagrams of the resulting composite cluster in Fig. 2.1. The CMR of the composite cluster is fitted using the same iterative biweight procedure as the individual clusters, using a constant width ($\Delta(B - R) = 0.5$ magnitudes) colour slice.

In Fig. 2.3 we show the $B - R$, $R - I$ colour-colour plot of sources in the cluster fields that were detected in the B , R and I bands. We have highlighted the red-sequence galaxies (Fig. 2.2) with $R \leq 20.73$, which corresponds to the limit of our dwarf selection (§ 2.3.4). The red-sequence galaxies, selected from their $B - R$ colours, also typically have red $R - I$ colours, similar to those expected from the models of King & Ellis (1985). The small number of red-sequence galaxies that have very red or very blue $R - I$ colours suggests that there is minimal foreground and background contamination in the CMR galaxy sample, although in § 2.3.2 we further quantify the field contamination.

2.3.2 Field correction

The CMRs presented in Fig. 2.1 are not corrected for field contamination and will contain a contribution from foreground and background galaxies. The wide-field nature of the CFH12k imaging means that the data extends out to the periphery of the clusters, and we can use these regions to statistically estimate the field contamination and so correct for

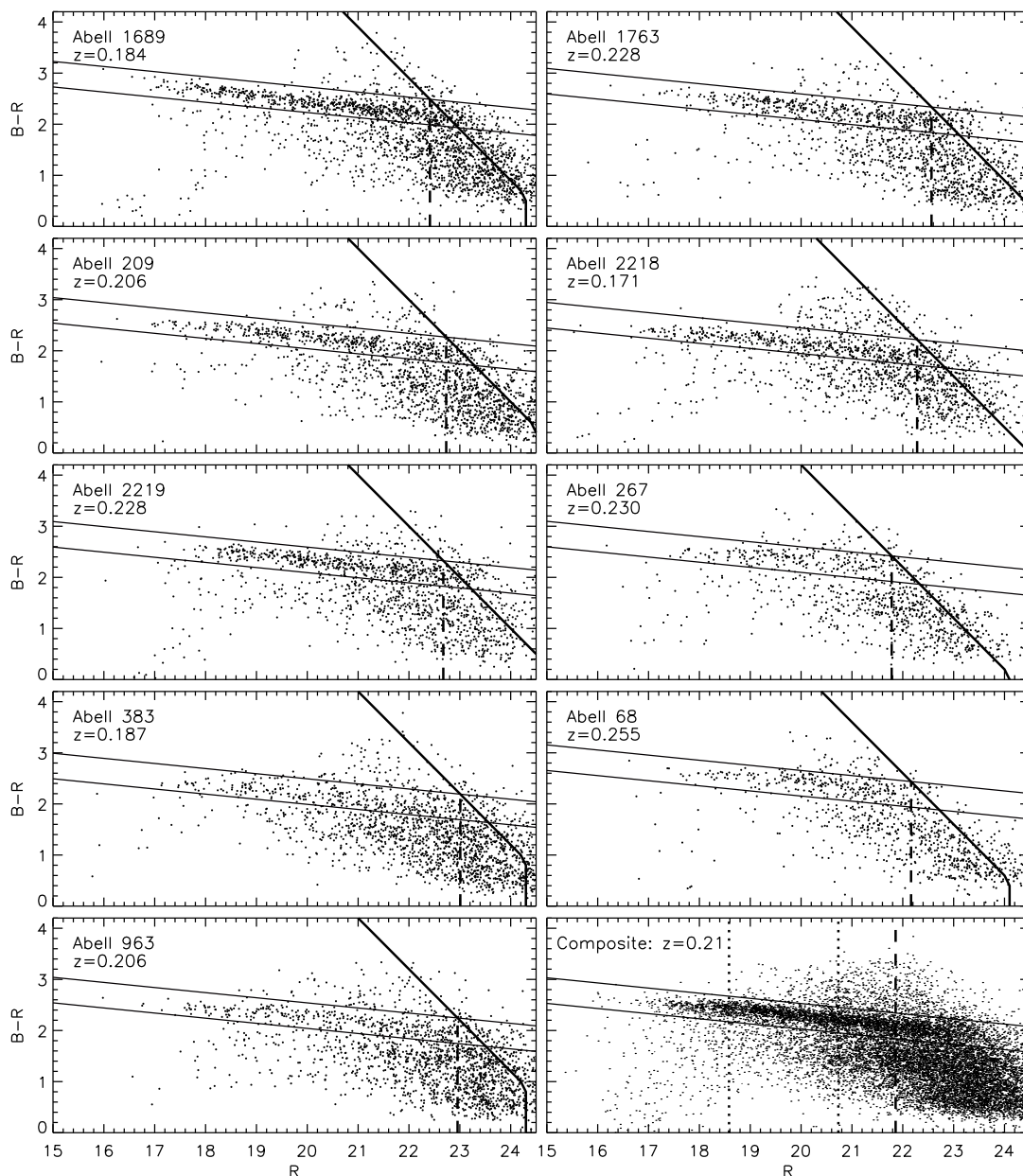


Figure 2.1: Colour-magnitude plots for the inner regions of the individual $z \sim 0.2$ galaxy clusters and the composite cluster, which is constructed at $z = 0.21$ as described in the text. The linear CMR is visible in all the individual clusters and the composite cluster, albeit with varying contrast. The 50% completeness limits of the photometry of the individual clusters are represented by solid black lines (Bardeau et al. 2007) and the dashed vertical lines highlight the observed R -band magnitude which represents the 50% completeness limit for galaxies on the CMR. Similarly the dashed line in the composite CMR represents the brightest 50% completeness limit on the CMR of the individual clusters, transformed to $z = 0.21$. On the composite CMR the dotted lines show the division between giants and dwarfs and the faint limit of our dwarf classification (§ 2.3.4) while the solid lines show our CMR selection. We note that the faint limit of our analysis lies ~ 1 magnitude above the 50% completeness limit, corresponding to $\sim 100\%$ completeness.

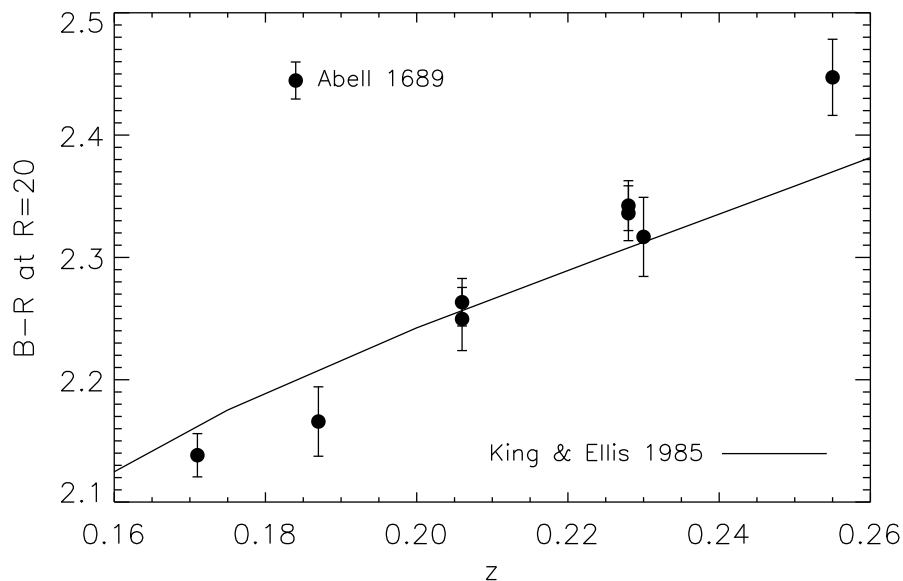


Figure 2.2: Plot of redshift against $B - R$ colour for galaxies with a characteristic brightness of $R = 20$ magnitudes on the CMR, compared to the “no-evolution” model of King & Ellis (1985) for elliptical and S0 galaxies. The model is normalised to the observed value in clusters at $z = 0.21$. The model and observed values are in good agreement for all the clusters except Abell 1689. Therefore, with the exception of Abell 1689, the models are used to transform the clusters to $z = 0.21$. For Abell 1689 we use the observed value.

this. For each cluster we identify 10 regions at the edge of the field, each with an area of 1.13 Mpc^2 , equivalent to a circle of 600 kpc radius, which is the area of the clusters that we study in § 2.3.3 and § 2.3.4 (to match previous studies). We use the mean and standard deviation of the number of galaxies in the 10 fields as a measure of the field contamination and its uncertainties in the clusters. The errors are propagated throughout and we scale the values for areas of different sizes when necessary.

2.3.3 Evolution of the CMR from the luminosity function

Having defined the cluster CMRs and selected red-sequence galaxies we next investigate and fit the luminosity distribution of CMR galaxies to explore the evolution of red-sequence dwarf and giant galaxies. In Fig. 2.4 we show the field-corrected rest-frame V -band luminosity functions for galaxies on the CMR and within 600 kpc of the centres of the composite cluster and the nine individual $z \sim 0.2$ galaxy clusters. The observed R -band magnitudes are converted to rest-frame absolute V -band magnitudes using the

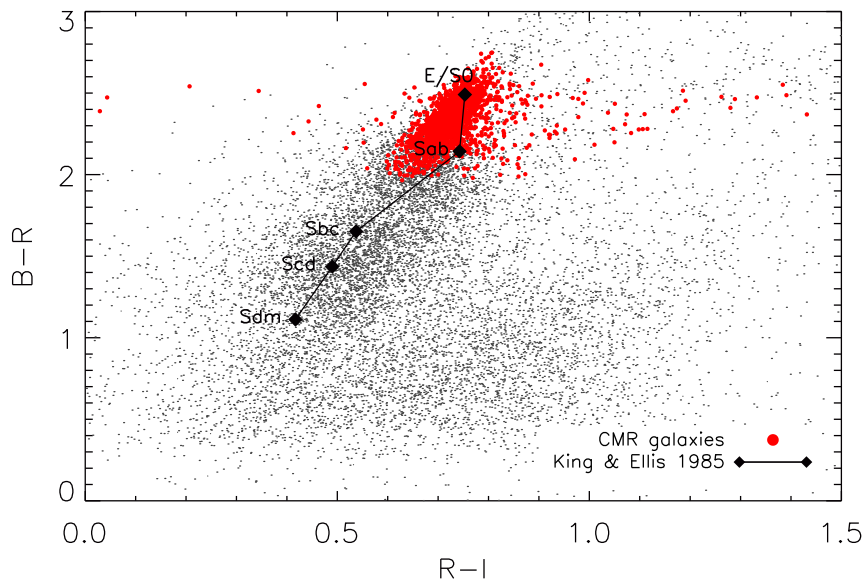


Figure 2.3: $B - R$, $R - I$ colour-colour plot for sources in the fields of the nine $z \sim 0.2$ clusters, K-corrected to $z = 0.21$. We highlight CMR galaxies, selected on the basis of $B - R$ colour and R -band magnitude (Fig. 2.2), and show the predicted colours of galaxies of different star-formation histories at $z = 0.21$ (King & Ellis 1985). The red-sequence galaxies typically have the colours expected for E/S0 galaxies, which indicates that the selection is reliable. The limited scatter in the $R - I$ colours of the CMR galaxies suggests that there is minimal field contamination in the sample.

Table 2.4: Field-corrected parameters of galaxies on the red-sequence and in the central 600 kpc radius.

Cluster	α^a	M^{*a}	Φ^{*a}	N_{giant}^b	N_{dwarf}^c	RDGR
Abell 1689	-1.0 ± 0.2	-20.5 ± 0.5	37 ± 18	35 ± 6	122 ± 12	3.5 ± 0.7
Abell 1763	-0.5 ± 0.3	-19.7 ± 0.4	63 ± 16	25 ± 6	103 ± 11	4.1 ± 1.0
Abell 209	-1.2 ± 0.2	-21.1 ± 0.7	14 ± 10	26 ± 6	74 ± 10	3.0 ± 0.8
Abell 2218	-1.1 ± 0.2	-20.5 ± 0.4	30 ± 14	32 ± 6	109 ± 12	3.4 ± 0.7
Abell 2219	-0.8 ± 0.3	-20.0 ± 0.4	46 ± 16	34 ± 7	95 ± 11	2.8 ± 0.7
Abell 267	-0.5 ± 0.4	-19.8 ± 0.4	39 ± 14	20 ± 5	65 ± 10	3.3 ± 1.0
Abell 383	-1.3 ± 0.5	-21.3 ± 2.4	7 ± 14	10 ± 4	48 ± 9	4.6 ± 2.1
Abell 68	-1.4 ± 0.2	-21.8 ± 0.9	6 ± 5	26 ± 6	82 ± 11	3.2 ± 0.8
Abell 963	-0.6 ± 0.4	-20.0 ± 0.5	31 ± 13	24 ± 5	54 ± 10	2.3 ± 0.7
Composite	-0.9 ± 0.4	-20.3 ± 0.5	305 ± 13	232 ± 17	753 ± 32	3.2 ± 0.3

^a α , M^* and Φ^* are from Schechter function fits to the CMR luminosity function (§ 2.3.3).

^b N_{giant} is the field-corrected number of galaxies with $M_V < -19.96$.

^c N_{dwarf} is the field-corrected number of galaxies with $-19.96 \leq M_V \leq -17.81$.

“no-evolution” K-corrections for E/S0 galaxies from King & Ellis (1985).

We use a χ^2 analysis to fit each luminosity function with the traditional single Schechter function (Schechter 1976), of the form:

$$\Phi(M_V) = 0.4 \ln(10) \Phi^* 10^{0.4(\alpha+1)(M_V^* - M_V)} \exp(-10^{0.4(M_V^* - M_V)}) \quad (2.1)$$

where Φ^* is the normalisation, α is the faint-end slope, and M_V^* is the magnitude at which the faint-end slope begins to dominate. To avoid incompleteness we only use galaxies with $M_V \lesssim -17.8$ magnitudes, corresponding to $R \sim 20.7$ magnitudes at $z = 0.21$. The fits and the parameters of each fit are shown in Fig. 2.4 and the parameters are presented in Table 2.4. We note that there is no correlation between redshift, r_{200} , M_{200} , X-ray luminosity, or the depth of the optical observations and the values of M_V^* or α .

Prior to using the parameters of the Schechter function fits of luminosity functions to investigate the evolution and the build-up of the CMR it is imperative that we understand any correlations in the parameters. In Fig. 2.5 we show contours of constant χ^2 for a range of values of M_V^* and α for Schechter function fits to the composite cluster luminosity function and highlight the locations of the best-fit M_V^* and α for each of the individual clusters. It is clear that M_V^* and α are highly correlated, and that their best-fit values

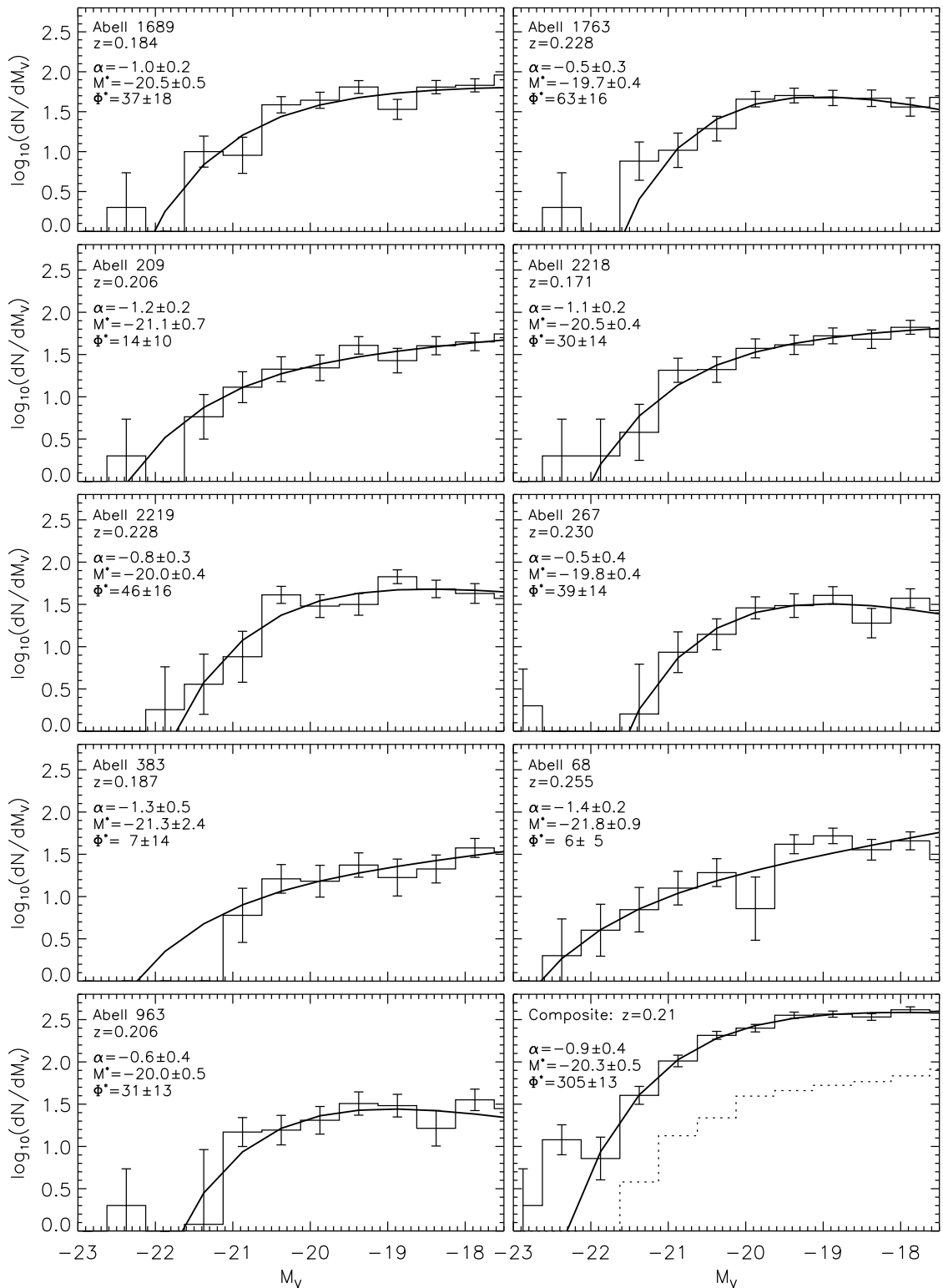


Figure 2.4: Field-corrected rest-frame V -band luminosity functions for galaxies in the central 600 kpc radius of the the nine individual $z \sim 0.2$ galaxy clusters and the composite cluster. Thick lines are the best-fit Schechter functions to each cluster, and the parameters of the Schechter function fits are presented. The dotted line in the panel of the composite cluster is the luminosity function for field galaxies and illustrates the size of the field correction.

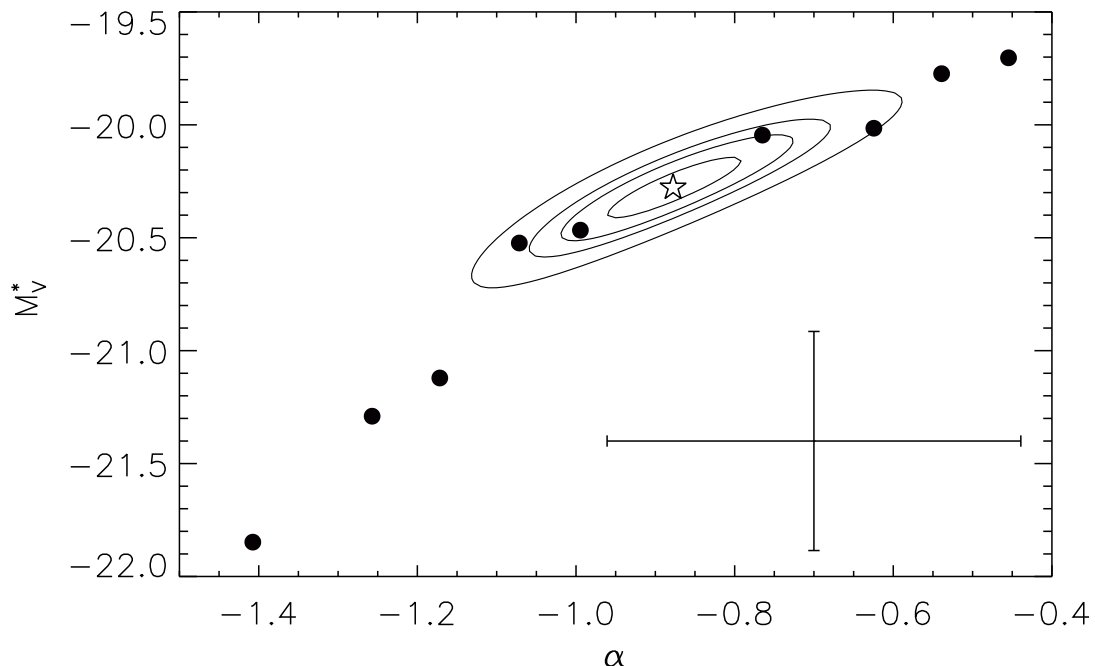


Figure 2.5: Contours of χ^2 as a function of M_V^* and α for Schechter function fits to the luminosity function of the composite cluster at $z = 0.21$. The star marks the position of the best-fit parameters for the composite cluster, and the points show the location of the best-fit M_V^* and α for the individual $z \sim 0.2$ clusters. The interdependency of M_V^* and α and the large scatter in values of the individual clusters suggests that it is difficult to interpret any evolution in luminosity functions using the parameters derived from these fits. Contour levels are $\chi_{\min}^2 + [1, 3, 5, 10]$, representing the 1, 3, 5 and 10σ levels. The median error bars are shown in the bottom right-hand corner.

vary widely even for this sample of clusters, which were selected for their homogeneity. We conclude that the evolution of the luminosity distribution along the CMR is difficult to interpret from M_V^* and α alone. Therefore, we next use an alternative parameterisation to investigate the evolution of the CMR.

2.3.4 Evolution of the CMR from the dwarf-to-giant ratio

As we showed in § 2.3.3 the evolution of the red-sequence is difficult to identify from the parameters of a Schechter function fit to the CMR luminosity function due to the coupled behaviour of α and M^* . Therefore, we next use the shape-independent, red-sequence dwarf-to-giant ratio (RDGR; Ferguson & Sandage 1991) to investigate the evolution and

build up of the cluster CMR. The RDGR (or its inverse RGDR) is straightforward to interpret because the single parameter quantifies the relative numbers of dwarf and giant galaxies on the red-sequence. Since the giant galaxy population is well established by $z \lesssim 0.5$ (e.g. Ellis et al. 1997) the RDGR provides a measure of the evolution of dwarf galaxies onto the CMR.

In calculating the RDGR we consider giant galaxies as those with $M_V < -19.96$, and dwarf galaxies as those with $-19.96 < M_V < -17.81$. These magnitude limits are the redshift-correct equivalent to those used by Stott et al. (2007), allowing us to directly compare to their results, although we note that our conclusions do not change if they varied slightly. The division between dwarf and giant galaxies was chosen by Stott et al. (2007) as the magnitude limit when the faint-end slope begins to dominate the luminosity function. As shown in Fig 2.1 the faint-end limit is ~ 1 mag brighter than the brightest 50% completeness limit of our catalogues and therefore we do not expect incompleteness to affect our results. The numbers of dwarf and giant galaxies in each cluster are corrected for field contamination as described in § 2.3.2.

In Fig 2.6 we show the RDGR for the central 600 kpc of the individual and the composite $z \sim 0.2$ galaxy clusters. The field-corrected number of giant and dwarf galaxies, and the RDGR for this region of the clusters are listed in Table. 2.4. The results are directly comparable with Stott et al. (2007), since the magnitudes limits and the areal coverage are equivalent. We also compare to the similar study of De Lucia et al. (2007) who examined galaxies within 740 kpc radius of the cluster centres and considered giants as those with $M_V < -19.96$ and dwarfs as those with $-19.96 < M_V < -18.16$. The evolution in the RDGR is apparent in Fig. 2.6, with relatively more dwarf galaxies on the cluster red-sequence at recent times, indicative of a build-up of the faint end red-sequence over the last ~ 8 Gyr (as seen by De Lucia et al. 2007; Stott et al. 2007).

With the aim of parameterising this evolution we determine a fit of the form $\text{RDGR} = k(1+z)^{-\beta}$ to the composite clusters from this work, Stott et al. (2007), and De Lucia et al. (2007). The best-fit has $\chi_{\text{red}}^2 = 0.84$, $k = 4.72 \pm 0.65$ and $\beta = 2.88 \pm 0.34$. Although this fit is statistically acceptable, we note that qualitatively the RDGR of $z \sim 0.1$ and $z \sim 0.2$ clusters are similar. Indeed, a KS-test of the RDGR in the individual $z \sim 0.1$ and $z \sim 0.2$ clusters yields a probability that the two samples are drawn from the same distribution of $P_{KS} = 38\%$ – indicating that the RDGR of these two samples are consistent with each other. For comparison, a KS-test between the RDGRs of the $z \sim 0.2$ and $z \sim 0.5$ clusters has $P_{KS} = 0.05\%$ – indicating that they are unlikely to be drawn from the same

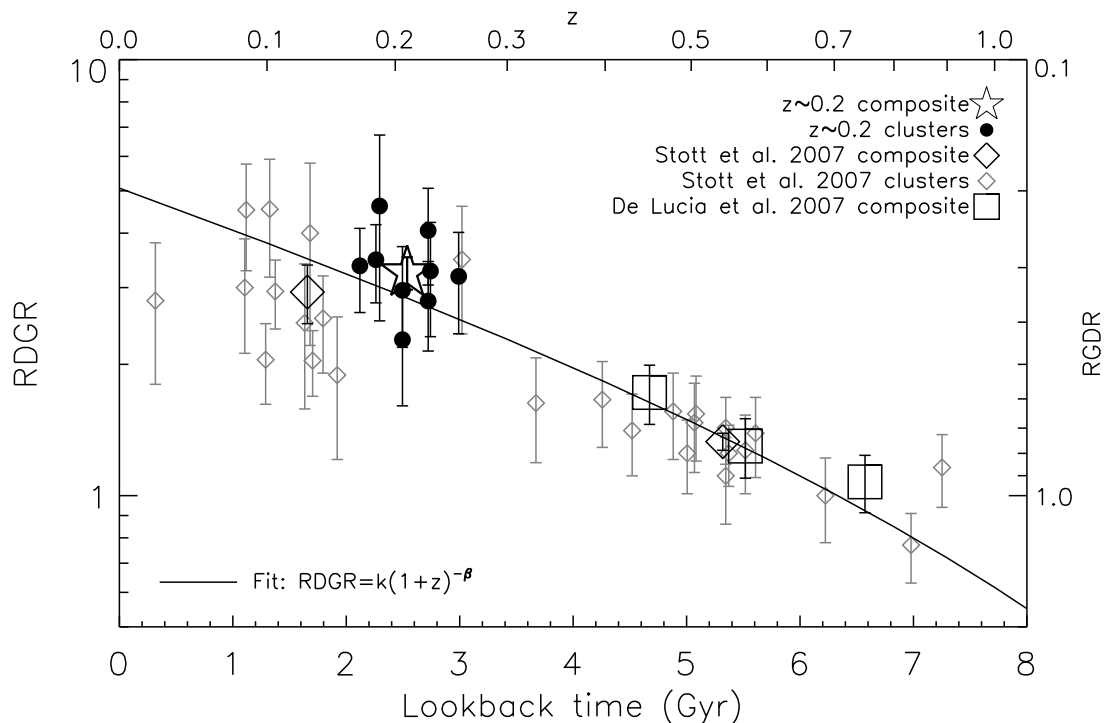


Figure 2.6: Evolution of the field-corrected red-sequence dwarf-to-giant ratio with redshift for the galaxies in the central 600 kpc of our $z \sim 0.2$ galaxy clusters. We compare to clusters from Stott et al. (2007) and De Lucia et al. (2007), which have similar galaxy selection criteria. A fit to the composite clusters of the form $\text{RDGR} = k(1+z)^{-\beta}$ has $k = 4.72 \pm 0.65$ and $\beta = 2.88 \pm 0.34$ and a reduced $\chi^2 = 0.84$.

distribution. We conclude that whilst there is strong evolution of the CMR of clusters between redshifts 0.5 and 0.2 is possible that this evolution is complete by $z \sim 0.2$, at least to within 600 kpc of the cluster centre. However, as discussed in § 2.4 it is possible that this result is biased by the use of a fixed 600 kpc radius for analysis at all redshifts, rather than considering galaxies within a fixed fraction of the cluster radius. We note that the values of the RDGR for the individual $z \sim 0.2$ clusters do not correlate with X-ray luminosity or M_{200} .

2.3.5 Buildup of the CMR: radial dependence

Having confirmed that the RDGR is redshift dependent we next utilise the full power of our wide-field imaging of all nine $z \sim 0.2$ galaxy clusters to investigate the evolution of the CMR and the dwarf galaxy population within the composite cluster.

We begin by studying the variation of the RDGR as a function of projected clus-

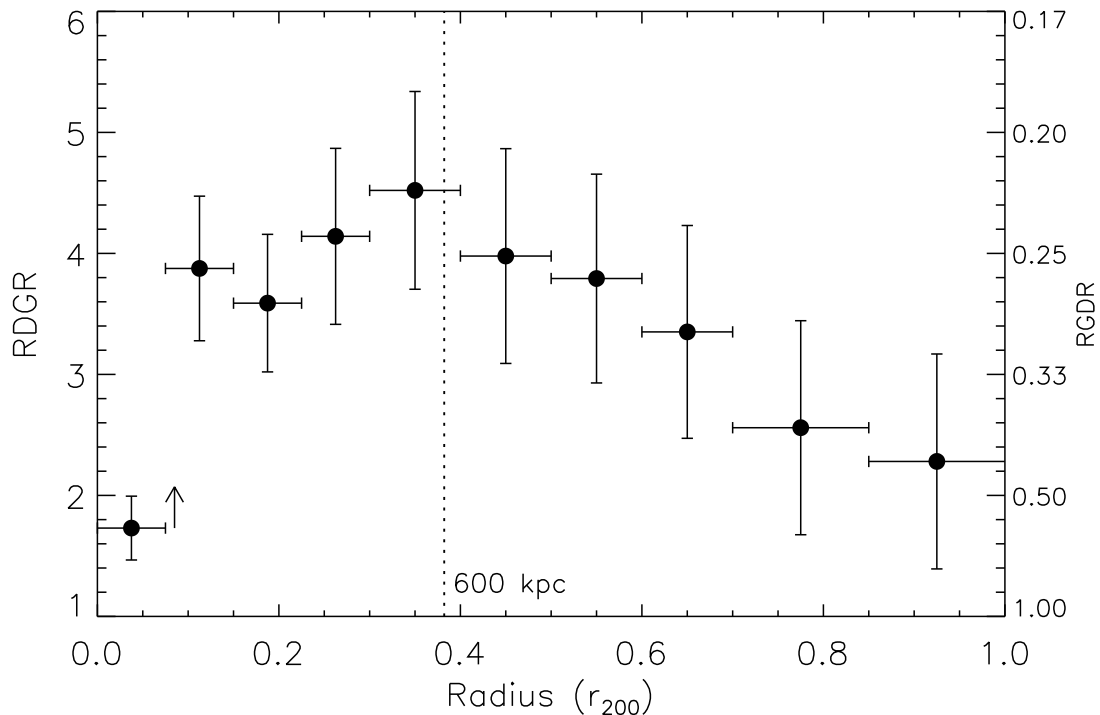


Figure 2.7: Variation of field-corrected RDGR with clustercentric distance for the composite $z \sim 0.2$ galaxy cluster. We see that the RDGR is low in the outer regions of the cluster and increases with decreasing radii and the RDGR in the innermost region of the clusters is depressed. We interpret this trend as the transformation of an increasing number of dwarf galaxies onto the CMR at mid-to-large clustercentric radii, and the disruption of dwarf galaxies in the inner regions of the clusters. Such disruption could destroy the dwarf galaxies or cause a reduction in surface brightness such that they no longer occupy our sample. It is also possible that our source extraction and deblending algorithms are less accurate in the cluster centres, where there is significant crowding of the images, potentially causing some galaxies not to be extracted. To test this we have examined the images and catalogues and estimated the number of dwarf and giant galaxies which were not included in the original catalogues. The effect of correcting this small bias in the innermost radial bin is shown by indicating with an arrow the maximum change in RDGR. For comparison to § 2.3.4 we identify the median radius corresponding to 600 kpc for our $z \sim 0.2$ clusters.

tercentric radius and in Fig. 2.7 we show the field-corrected RDGR as a function of clustercentric radius. We consider the radius scaled by r_{200} for each of the constituent clusters so that the effect of the variation in richness of the nine clusters is removed. We note that, if physical radius is instead considered, our conclusions do not change but the amplitude of the variation in RDGR is weakened.

We find that in the outskirts of the cluster the RDGR is low and, as expected, increases towards the cluster centre. However, the RDGR peaks at $\sim 0.4r_{200}$ and then plateaus until the innermost regions of the cluster where it declines. To test whether this effect could be a systematic error due to the source extraction algorithms failing to detect and deblend faint galaxies in the crowded cluster centres we examine the images of all the cluster centres and estimate the number of galaxies which are missing from the catalogues. Failure to extract galaxies due to crowding in the centres of the clusters is insufficient to explain the decrease in RDGR in the very centre of the clusters (Fig. 2.7).

Our sample of clusters are all massive and hence may (and indeed do) act as gravitational lenses, magnifying the image of all background galaxies. For our sample of $z \sim 0.2$ clusters gravitational lensing is most efficient within $\sim 1'$ radius ($\sim 0.1r_{200}$) and, due to flux boosting and magnification of the source plane, could affect the background counts in this region (Broadhurst et al. 1995). Therefore, we check whether the apparent reduction in the RDGR in the cluster centres is not a result to a systematic error in the field subtraction due to gravitational lensing. From Trentham (1998) we estimate that gravitational lensing boosts the dwarf galaxy field counts by a maximum of 12% and the giant galaxy field counts by a maximum of 8%. However, since the area in the central radial bins is small the overall effect is to increase the RDGR by $< 1\%$ in each of the $R < 0.1r_{200}$ and $R = 0.1-0.2r_{200}$ bins. We also repeat our calculations of RDGR for only the sub-sample of four clusters that show the weakest lensing signals (Abell 267, Abell 383, Abell 963 and Abell 209; Bardeau et al. 2007), alone and find no significant difference in our results, compared to when the full sample is employed. We conclude that gravitational lensing does not bias our analysis.

The observed low RDGR in the outer regions of the clusters is evidence that at these radii relatively few dwarf galaxies have evolved sufficiently to inhabit the red-sequence. The increase in RDGR from $R \sim 1-0.4r_{200}$ corresponds to increasing numbers of dwarf galaxies being transformed onto the CMR by the cluster environment. We note that Barkhouse et al. (2009) examined galaxy clusters at $z = 0.02-0.20$ and did not observe this decrease of RDGR in the outer regions of the cluster. This disparity is most likely

due to the large redshift range explored and could indicate that the radius at which the trend of RDGR flattens is redshift dependent.

We interpret the reduction in the RDGR in the very innermost regions of galaxy clusters at $z \sim 0.2$ is evidence of tidal forces stripping material from dwarf galaxies in these environments, in a similar process to that observed in locally. These tidal forces could destroy the dwarf galaxies or remove sufficient numbers of stars to cause them to fade below the magnitude limit of this survey – causing a reduction in the observed RDGR.

2.3.6 Buildup of the CMR: density dependence

We have shown that the relative number of dwarf and giant galaxies on the cluster red-sequence at $z \sim 0.2$ is dependent on the clustercentric radius. However, the clustercentric radius is only a proxy for galaxy density and it does not explicitly account for non-spherical clusters or those clusters with multiple high-density regions. Therefore, we next investigate variation in the form of the red-sequence with local galaxy density. Such analysis enables us to combine physically equivalent regions, in terms of local environment, in the nine clusters – without making assumptions about the relative richness of the clusters or the galaxy distribution within them.

In Fig. 2.8 we plot the dependence of the RDGR on the projected red-sequence giant density (Σ_{giant}). Σ_{giant} is field-corrected and is computed from the projected separation to the 10th nearest red-sequence giant galaxy. We use Σ_{giant} , instead of the density of all CMR galaxies, as a measure of the local galaxy density because unlike the CMR galaxy density Σ_{giant} is does not vary as dwarf galaxies evolve in the cluster environment. In addition, the field correction is lower for giant galaxies than for dwarfs so the using Σ_{giant} means that the errors on the density measurements are minimised. To calculate Σ_{giant} at the location of each of the dwarf galaxies we perform a two-dimensional interpolation of the values of Σ_{giant} at the positions of the giant galaxies. A measure of the area included in density bin is determined by using the median raw (i.e. not field corrected) Σ_{giant} and the observed number of giant galaxies in the bin. We use this value to appropriately scale the field correction (§ 2.3.2) and calculate the field-corrected RDGR for each Σ_{giant} . Each of the radial bins in Fig. 2.7 contains galaxies in a mixture of environments, such that the observed RDGR values are the average of each of those environments. This results in the observed range of RDGR in Fig. 2.8 to be larger than that in Fig. 2.7.

We find that in low-density regions regions with $\Sigma_{\text{giant}} \lesssim 10 \text{ Mpc}^{-2}$ the RDGR in-

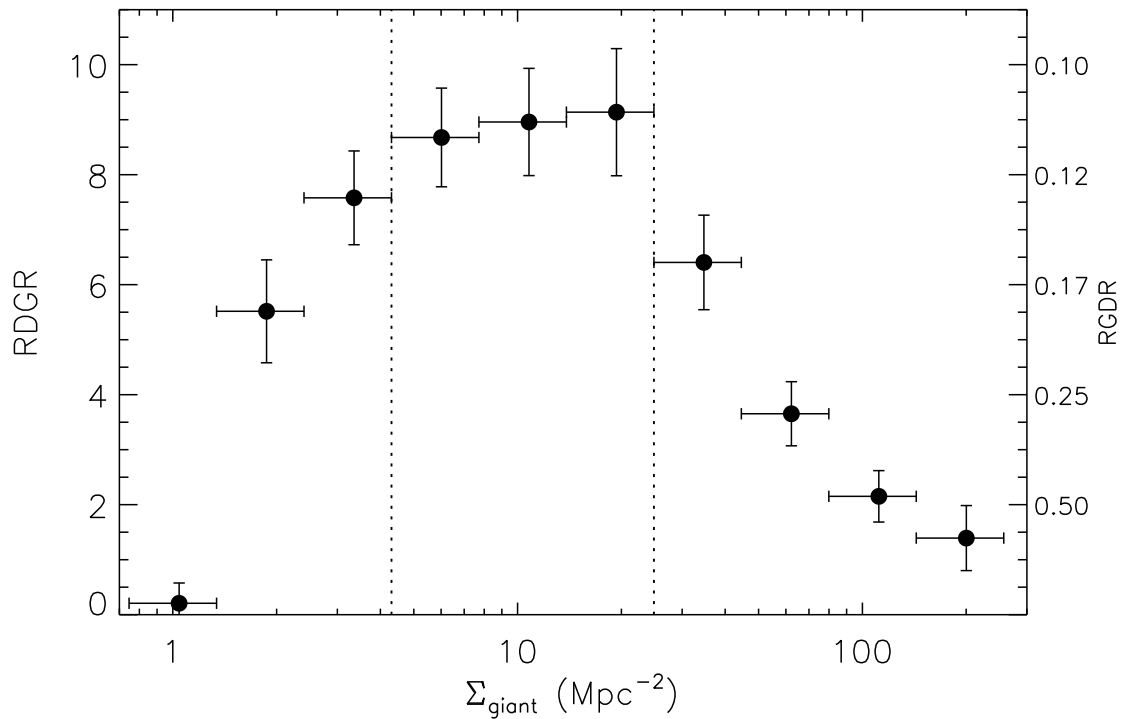


Figure 2.8: Variation of field-corrected RDGR with the local density of red sequence giant galaxies (Σ_{giant}) for the composite $z \sim 0.2$ galaxy cluster. The RDGR appears suppressed in the both the lowest and the highest density regions of the cluster, compared to intermediate density regions. The increase of RDGR from low to intermediate density regions is likely a result of the transformation of increasing numbers of dwarf galaxies onto the red-sequence by the cluster environment. We interpret the subsequent reduction in RDGR in regions with $\Sigma_{\text{giant}} \gtrsim 30 \text{ Mpc}^{-2}$ as evidence of dynamical interactions, which strip stars from the dwarf galaxies, causing them to fade below our selection limit. Dotted lines indicate the three Σ_{giant} regimes considered in Fig. 2.9.

creases with increasing giant density but at $\Sigma_{\text{giant}} \gtrsim 10 \text{ Mpc}^{-2}$ we observe a flattening in the RDGR, which then rapidly decreases at the very highest densities. The initial increase of RDGR with increasing Σ_{giant} is an indication that as dwarf galaxies enter progressively denser cluster regions increasing numbers are transformed onto the red-sequence. However, in regions with $\Sigma_{\text{giant}} \gtrsim 10 \text{ Mpc}^{-2}$ this process has been completed and at the very highest densities the dwarf galaxies may be dynamically disrupted in a process similar to that observed locally, such that they are destroyed or are stripped of enough stars to cause them to fade to below our selection limits. We note that in a study of Abell 2218 Pracy et al. (2004) found that the DGR of red and blue cluster galaxies was suppressed by a factor of five in the highest density regions of the cluster, similar to the relative reduction in the RDGR of our $z \sim 0.2$ clusters. This suggests that the mechanisms responsible for the depletion of the faint end of the CMR in the highest density regions in $z \sim 0.2$ clusters acts universally and is not specific to red-sequence galaxies – indicative of dynamical processes.

To confirm the observed trend of RDGR with local giant density we show in Fig. 2.9 the field-corrected red-sequence luminosity functions of the galaxies in low, intermediate and high density regions (indicated in Fig. 2.8), corresponding to $\Sigma_{\text{giant}} \leq 4.3 \text{ Mpc}^{-2}$, $\Sigma_{\text{giant}} = 4.3\text{--}25 \text{ Mpc}^{-2}$ and $\Sigma_{\text{giant}} \geq 25 \text{ Mpc}^{-2}$, respectively. The three luminosity functions in Fig. 2.9 are scaled such that they contain equal numbers of giant galaxies (i.e. at $M_V < -19.96$). The faint end of the luminosity function in both the low and high density environments appears less populated than in intermediate density environments. This confirms our findings from Fig. 2.8 and § 2.3.5 that in low to intermediate density regions (typically large to intermediate clustercentric radii) dwarf galaxies are transformed onto the red-sequence by the cluster environment, before being dynamically disrupted in regions of high giant galaxy density (typically low clustercentric radii).

We calculate the observed reduction in RDGR from intermediate to high density regions corresponds to typical fading of ~ 0.3 magnitudes per dwarf galaxy. This would result in $\sim 30\%$ reduction in the luminosity and stellar mass of each galaxy. Based on a V -band light-to-mass ratio of 2.1, derived from STARBURST99 (Leitherer et al. 1999) for a 1 Gyr old stellar population formed in an instantaneous burst, on average the stellar mass loss from disrupted dwarf galaxies into the centre each of the $z \sim 0.2$ clusters is $\sim 9 \times 10^9 M_{\odot}$, corresponding to $\sim 1\%$ of the intracluster light (Zibetti et al. 2005). Thus, although dynamical interactions in the highest density regions of $z \sim 0.2$ clusters are important for cluster populations they contribute only a small fraction to the intracluster

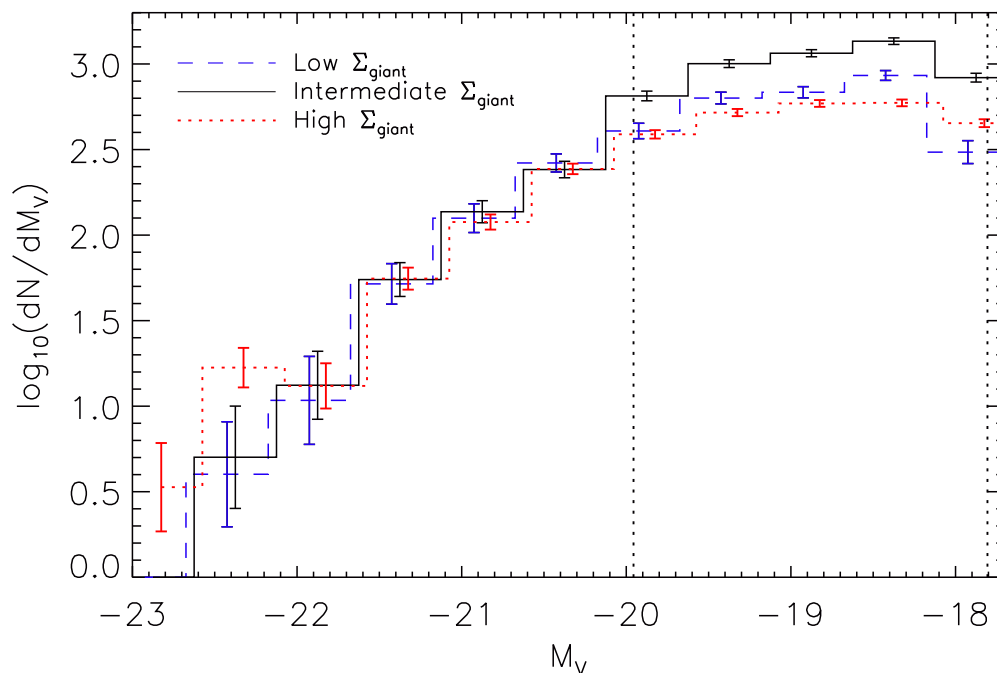


Figure 2.9: Rest-frame V -band luminosity functions for red-sequence galaxies in our $z \sim 0.2$ composite cluster. We separate galaxies into those with low, intermediate and high projected local red-sequence giant galaxy density (Σ_{giant}), as indicated in Fig. 2.8 and corresponding to $\Sigma_{\text{giant}} \leq 4.3 \text{ Mpc}^{-2}$, $\Sigma_{\text{giant}} = 4.3\text{--}25 \text{ Mpc}^{-2}$ and $\Sigma_{\text{giant}} \geq 25 \text{ Mpc}^{-2}$ respectively. The luminosity functions are scaled such that the number of giant galaxies in each is equal. The faint end of the luminosity function of red-sequence galaxies in low-density regions of the clusters is marginally suppressed compared to galaxies in intermediate density environments. We also find that the faint end slope of galaxies in high-density environments at $z \sim 0.2$ is significantly depressed, suggesting that in the highest-density environments dwarf galaxies are disrupted. This disruption would remove stars from the galaxies, causing them to fade below our selection limits, and contributing to the intracluster light. The low and high Σ_{giant} luminosity functions are offset slightly in M_V for clarity and the dotted lines highlight the dwarf and giant limits used throughout this chapter.

light at this epoch.

2.4 Discussion and Conclusions

In this study we have used wide-field imaging of nine $z \sim 0.2$ galaxy clusters to investigate the build-up of the red-sequence in these highly biased environments. We have shown that evolution in luminosity functions by parameterisation with Schechter function fits is difficult to interpret due to the interdependency of the parameters. We therefore use the RDGR as a single measure of the evolution of galaxies onto the red-sequence luminosity function that is straightforward to interpret.

We examined the RDGR within the central 600 kpc radius of $z \sim 0.2$ galaxy clusters in comparison with previous studies at $z \sim 0.1$ – 0.8 (Stott et al. 2007; De Lucia et al. 2007). There is a strong evolution in the RDGR from ~ 1 at $z \sim 0.8$ to ~ 3.5 at $z \sim 0.1$, although it appears that this evolution may be complete by $z \sim 0.2$. However, since we have also shown that the RDGR is a strong function of clustercentric radius, measured as a fraction of r_{200} , it is prudent to consider the effect of studying RDGR in a fixed physical radius.

For the sample of $z \sim 0.1$ clusters, r_{200} is, on average, 2.8 Mpc (Pimblet et al. 2006), and 600 kpc corresponds to $\sim 0.2r_{200}$. The clusters at $z \sim 0.2$ have typically smaller r_{200} , such that 600 kpc corresponds to $\sim 0.4r_{200}$, approximately the location of the maximum RDGR. The X-ray selected sample of $z \sim 0.5$ clusters from Stott et al. (2007), have similar r_{200} to the $z \sim 0.2$ sample (based on X-ray observations; Horesh et al. 2010). However, the EDisCS clusters ($z \gtrsim 0.5$) studied by De Lucia et al. (2007) are optically selected, and typically less massive – such that 600 kpc corresponds to $\sim 0.6r_{200}$ (Poggianti et al. 2006).

Therefore, on average, the RDGR in the central 600 kpc radius of the $z \sim 0.2$ and the Stott et al. (2007) $z \sim 0.5$ clusters are directly comparable. However, for the De Lucia et al. (2007) clusters 600 kpc incorporates a larger fractional area of the clusters (Fig. 2.7). This difference could potentially bias low the RDGR of the De Lucia et al. (2007) clusters than if equal fractional areas were compared. Although we note that the difference between the integrated RDGR within $0.4r_{200}$ and $0.6r_{200}$ for the $z \sim 0.2$ clusters is small so it is likely that this effect is minimal. The more significant difference is between the $z \sim 0.1$ and $z \sim 0.2$ clusters. 600 kpc radius for the $z \sim 0.1$ sample includes only $0.2r_{200}$ so the observed RDGR for these clusters is likely to be significantly lower

than if $\sim 0.4r_{200}$ was considered, as it is for the $z \sim 0.2$ clusters. It is therefore likely that the possible end-point of cluster evolution at $z \sim 0.2$ suggested by the minimal change in RDGR between $z \sim 0.2$ and $z \sim 0.1$ is actually due to the use of a fixed metric aperture.

By differentiating between regions of different local galaxy density we find that there are relatively few dwarf galaxies on the red-sequence in areas of the cluster with low giant density, typically corresponding to large clustercentric radii. The fraction of dwarf galaxies on the CMR increases towards the inner regions of the clusters and at higher Σ_{giant} , peaking at $R \sim 0.3 r_{200}$ and $\Sigma_{\text{giant}} \sim 10 \text{ Mpc}^{-2}$. This increase in RDGR is interpreted as evidence of the transformation of dwarf galaxies onto the red-sequence in high-density environments.

We also find that in the very centres of clusters ($R \lesssim 0.1 r_{200}$) and regions where $\Sigma_{\text{giant}} \gtrsim 25 \text{ Mpc}^{-2}$ the RDGR is significantly reduced. We interpret this as evidence that dwarf galaxies in high-density regions at $z \sim 0.2$ are dynamically disrupted in processes similar to those observed locally, where material is stripped from dwarf galaxies in the centres of clusters. We calculated that such interactions remove $\sim 30\%$ of the stellar mass from each dwarf, which when integrated over the whole sample is the equivalent of $\sim 1\%$ of the intracluster light of each cluster.

Having investigated the populations of CMR galaxies in clusters at $z \sim 0.2$, in Chapter 3, we next investigate the population of strongly star-forming galaxies in a cluster at $z = 0.54$. Such active galaxies, which are selected at 1.1 mm are likely forming stars at the rate of hundreds of solar masses per year, could be the progenitors of a fraction of the red-sequence galaxies in lower redshift clusters.

Chapter 3

A 1.1-mm survey for ULIRGs in the field of the galaxy cluster MS 0451.6–0305

3.1 Introduction

As discussed in Chapter 2, galaxy clusters are dense, biased environments in which galaxies may evolve more rapidly than the field. Local massive clusters contain mainly passive early-type galaxies (Visvanathan & Sandage 1977; Bower et al. 1992), although clusters at higher redshifts appear to support more star-formation activity (Butcher & Oemler 1984). Since the blue, star-forming populations within clusters are expected to be accreted from the surrounding field as the clusters grow via gravitational collapse, the evolution in the star-forming fraction in the clusters may simply track the increasing activity in the field population at higher redshifts.

This increasing activity in the field is reflected in an increasing number of the most luminous (and dusty) starburst galaxies with redshift (e.g. Le Floch et al. 2005; Magnelli et al. 2009; Goto et al. 2010; Rujopakarn et al. 2010): the Luminous Infrared Galaxies (LIRGs, with $L_{\text{FIR}} \geq 10^{11} L_{\odot}$) and their Ultraluminous cousins (ULIRGs, $L_{\text{FIR}} \geq 10^{12} L_{\odot}$). As the clusters grow these systems will also be accreted into the cluster environment along with the less-obscured and less-active population, and could transform into CMR galaxies observed at lower redshifts, such as those studied in Chapter 2. Mid-infrared surveys of clusters have identified a population of dusty starbursts whose activity increases with redshift (e.g. Geach et al. 2006, 2008; Haines et al. 2009). However, these

mid-infrared surveys can miss the most obscured (and potentially most active) galaxies which are optically thick in the rest-frame mid-infrared (as we show later). If they are present in clusters – even in relatively low numbers – such active galaxies will contribute significantly to the star formation rate (SFR) in these environments and the metal enrichment of the intracluster medium. Hence to obtain a complete census of the star formation within clusters we need to survey these systems at even longer wavelengths, in the rest-frame far-infrared, which is less sensitive to the effects of obscuration and which corresponds to the observed sub-millimetre and millimetre wavebands at $z \gtrsim 0.2$.

Over the past decade or more there have been a number of studies of rich clusters of galaxies in the sub-millimetre and millimetre wavebands (e.g. Smail et al. 1997; Blain et al. 1999; Zemcov et al. 2007; Knudsen et al. 2008). Many of these studies were seeking to exploit the clusters as gravitational telescopes to aid in the study of the distant sub-millimetre galaxy (SMG) population behind the clusters, while others focused on the detection of the Sunyaev-Zel’dovich (SZ) emission. Due to the limitations of current telescopes direct detection of millimetre sources is restricted to those with fluxes $S_{1100\mu\text{m}} \gtrsim 1$ mJy, or equivalently galaxies with SFRs $\gtrsim 300 M_{\odot} \text{ yr}^{-1}$ – much higher than expected for the general cluster populations based on optical surveys. Nevertheless these studies have serendipitously detected a number of cluster galaxies, although these are either atypical (e.g. central cluster galaxies, Edge et al. 1999) or are not confirmed members (e.g. Best 2002; Webb et al. 2005). More critically, with few exceptions these studies have all focused on the central 2–3 arcmin of the clusters, where the SZ emission and lensing amplification both peak, and have not surveyed the wider environment of the cluster outskirts where much of the obscured star formation is likely to be occurring (e.g. Geach et al. 2006). The two exceptions are the wide-field survey of the $z \sim 0.25$ cluster A 2125 by Wagg et al. (2009) and the survey of an overdense region of the COSMOS field by Scott et al. (2008) and Austermann et al. (2009). Wagg et al. (2009) detected 29 millimetre galaxies across a ~ 25 -arcmin diameter region centered on Abell 2125, at $z = 0.25$, of which none are claimed to be members. However, the only redshift estimates available are based on crude radio-to-millimetre spectral indices, which are sensitive to both dust temperature and redshift (Chapter 5; Blain et al. 2003). The AzTEC/COSMOS survey (Scott et al. 2008; Austermann et al. 2010) covered a number of structures, including an X-ray detected $z = 0.73$ cluster and concluded that the statistical overdensity of sources was most likely due to the gravitational lensing of background SMGs by these foreground structures.

To help to conclusively answer the issue of the obscured star-forming populations in

distant clusters, and potentially identify some of the progenitors of red-sequence galaxies in low redshift clusters, we have undertaken a wide-field 1.1-mm survey of the $z = 0.54$ rich cluster MS 0451.6–0305 (hereafter MS 0451–03) with the AzTEC camera (Wilson et al. 2008) on the James Clerk Maxwell Telescope (JCMT). This panoramic millimetre survey can also take advantage of the significant archival data available for this well-studied region. In particular the panoramic imaging of MS 0451–03 from *Spitzer* and uniquely, the *Hubble Space Telescope (HST)*, as well as extensive archival multiwavelength imaging and spectroscopy, which we employ for determining cluster membership of AzTEC-detected galaxies. Our survey probes the rest-frame $700\ \mu\text{m}$ emission of cluster galaxies – in search of examples of strongly star-forming but obscured galaxies – as well as identifying more luminous and more distant examples of the SMG population. We can compare our millimetre search for cluster members to the previous mid-infrared survey of this cluster by Geach et al. (2006) who uncovered a population of dusty star-forming galaxies which dominate the integrated SFR of the cluster of $200 \pm 100 M_{\odot} \text{yr}^{-1}$. Our AzTEC map covers ~ 60 times the area of the $850\ \mu\text{m}$ SCUBA observations of the central region of MS 0451–03 (Borys et al. 2004), while the depth of $\sigma \sim 1.1\ \text{mJy}$ is sufficient to identify ULIRGs individually and obtain stacked constraints on fainter far-infrared cluster members.

We describe our observations and the data reduction in §3.2; present 1.1-mm number counts, identify counterparts to the AzTEC galaxies, and use photometric techniques to determine cluster membership in §3.3. §3.4 contains our conclusions; individual AzTEC galaxies are presented in Appendix 3.5. Throughout this Chapter we use J2000 coordinates and ΛCDM cosmology with $\Omega_M = 0.3$, $\Omega_{\Lambda} = 0.7$ and $H_0 = 70\ \text{kms}^{-1}\text{Mpc}^{-1}$ and all photometry is on the AB system unless otherwise stated.

3.2 Observations and Data Reduction

Our survey focuses on MS 0451–03 – a massive galaxy cluster at $z = 0.54$. MS 0451–03 has been extensively studied over recent years and as such there is a plethora of data available in this field, including deep optical imaging, *Spitzer* and *HST* mosaics, X-ray observations and substantial spectroscopy. Details of the multiwavelength data employed in this survey are given in § 3.2.2.

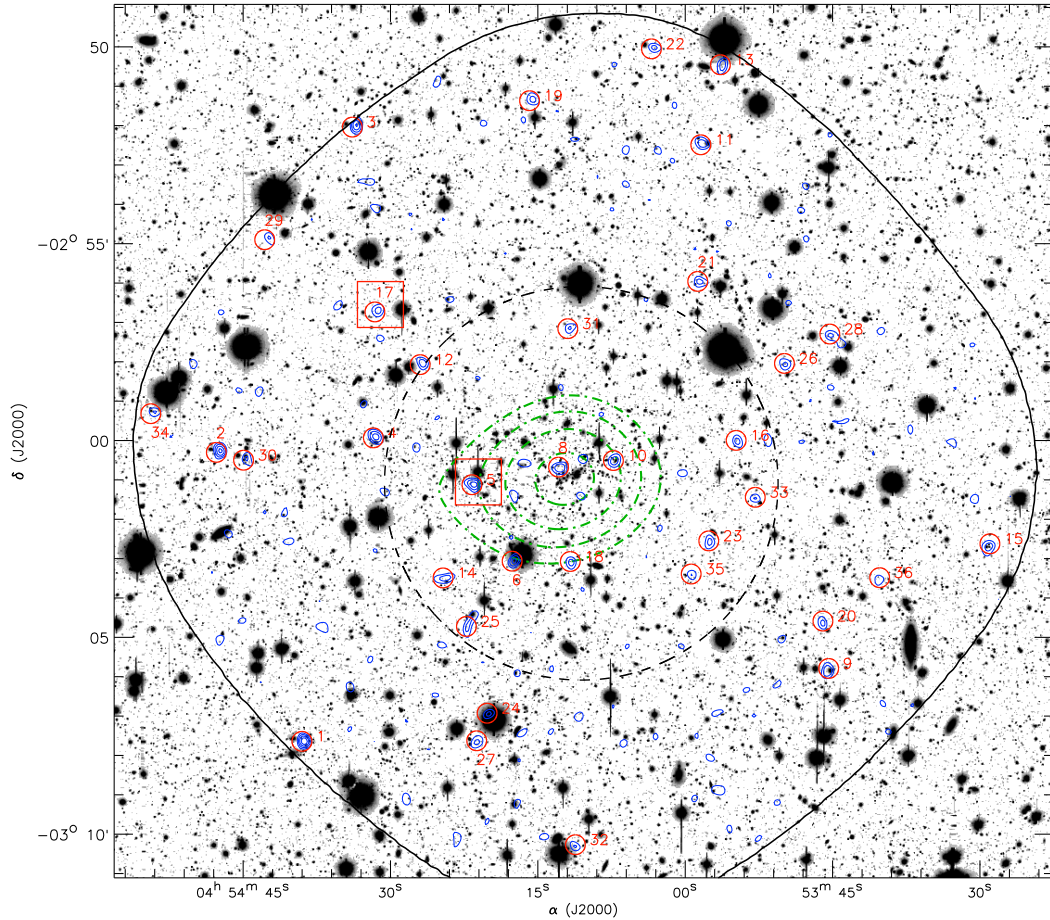


Figure 3.1: AzTEC S/N contours for the MS 0451–03 field shown over the corresponding Subaru *R*-band image; smoothed (dot-dashed) X-ray contours highlight the cluster centre. We also plot a 5-arcmin radius circle (dashed) illustrating the sub-region analysed in §3.3.1. The solid black line encircles the region with exposure coverage $\geq 50\%$ of the maximum value, where sources are extracted. In this region AzTEC contours shown are at 1σ intervals, starting at 2.5σ . 15 arcsec radius circles mark the 1.1-mm source detections labelled in order of decreasing S/N (Table 3.2) and squares highlight sources which are potential cluster members (§3.3.3.3). MMJ045413.35 is not shown because it lies outside of the area covered by the Subaru image. The 1.1-mm sources appear evenly distributed, with no obvious overdensity towards the cluster centre.

3.2.1 AzTEC Observations

The AzTEC millimetre camera (Wilson et al. 2008) was installed on the JCMT during November 2005 and operated nearly continuously until February 2006. On the JCMT AzTEC has a field-of-view of ~ 18 -arcmin² and a beam of 18-arcsec FWHM. For this project we observed a 0.23-deg² region centred on MS 0451–03 at 04^h54^m10^s.1, –03°01′07″.6, over a total of 24.5 hours between 2005 December 14 and 2006 January 6. Observations were carried out in raster-scan mode with 1200″ long scans in elevation separated by 9″ steps in azimuth (see Wilson et al. 2008 for details of our standard raster scan strategy). Scans were made at a fixed speed of 120″s^{–1}. Data from the turnarounds were excised for this analysis. Each observation took 35 minutes to complete and a total of 42 observations were made of the field. Over the set of observations the zenith opacity at 225 GHz, τ_{225} , was monitored with the Caltech Submillimeter Observatory’s opacity meter and ranged from 0.03 to 0.17. The average opacity for the set of observations was 0.09, equivalent to an atmospheric column of precipitable water vapour of ~ 2 mm.

The 42 individual AzTEC observations were reduced and combined using the publicly available AzTEC Data Reduction Pipeline V1.0 – a set of IDL code that is optimised for detecting point sources in blank-field AzTEC surveys. This is the same pipeline that has been used in previous blank-field AzTEC/JCMT analyses including Scott et al. (2008), Perera et al. (2008) and Austermann et al. (2010).

Since the reduction of these observations follows the same procedure and uses the same code as previous AzTEC studies, we refer the reader to Scott et al. (2008) for a thorough review of the reduction steps. Here we focus on the particulars of this field and the measured characteristics of the MS 0451–03 map.

Since we are interested in counterparts to our detected SMGs it is critical that we understand the pointing accuracy of the maps. In the reduction pipeline, fine corrections to the JCMT’s pointing model are applied to each observation based on regular observations of a nearby QSO ($\alpha = 04^{\text{h}}23^{\text{m}}15^{\text{s}}.8, \delta = -01^{\circ}20'33''.1$) in the same manner as described in Scott et al. (2008) and Wilson et al. (2008). The residual astrometric error for the field is measured by stacking the AzTEC map at the positions of radio sources in the field (see §3.2.2) and fitting for the centroid of the resulting image. The stacked radio sources are detected at $\sim 6\sigma$ and demonstrate an overall systematic astrometric shift in the AzTEC map of $\Delta\alpha = -3.0'' \pm 0.9'', \Delta\delta = 1.2'' \pm 1.5''$ with respect to the radio reference frame. This correction is negligible in Dec, but the significant RA offset is applied to the AzTEC

Table 3.1: Summary of the observations

Filter	Instrument	Detection Limit ^a	Reference
<i>U</i>	CFHT – MegaPrime	25.1 mag	Donovan (2007)
<i>B</i>	Subaru – Suprime-Cam	26.6 mag	Kodama et al. (2005)
<i>V</i>	Subaru – Suprime-Cam	25.8 mag	Kodama et al. (2005)
<i>R</i>	Subaru – Suprime-Cam	25.1 mag	Kodama et al. (2005)
<i>I</i>	Subaru – Suprime-Cam	24.2 mag	Kodama et al. (2005)
<i>z'</i>	WHT – PFIP	24.2 mag	This work
<i>K</i>	Palomar Hale – WIRC	20.1 mag	G. Smith et al., in prep.
3.6 μm	<i>Spitzer</i> – IRAC	23.0 mag	This work
4.5 μm	<i>Spitzer</i> – IRAC	23.2 mag	This work
5.8 μm	<i>Spitzer</i> – IRAC	21.4 mag	This work
8.0 μm	<i>Spitzer</i> – IRAC	22.1 mag	This work
24 μm	<i>Spitzer</i> – MIPS	120 μJy	Geach et al. (2006)
1.1 mm	JCMT – AzTEC	3.6 mJy	This work
1.4 GHz	VLA	51 μJy	This work

^a1.1 mm is the 3.5σ minimum catalogue limit in the roughly constant noise region of the map; in the other bands we quote 3σ limits.

data prior to further analysis and source extraction.

The AzTEC data are flux calibrated as described in Wilson et al. (2008) from nightly observations of Uranus over the JCMT run. The final calibration accuracy is $\sim 10\%$.

The primary products that come out of the AzTEC pipeline are a map representing the average filtered point source response, a map of the weight of each pixel in the sky flux map (representing the uncertainty in flux of each pixel), and a map of the signal to noise estimate in each pixel. All maps are made on the same $3'' \times 3''$ grid and all maps have been Wiener filtered to optimise sensitivity to point sources. The central ~ 0.10 deg² of the AzTEC map is relatively uniform, with all pixels having $\geq 50\%$ of the peak weight. Sources are extracted in the central region of the maps (§3.3.1) where the rms noise is ~ 1.1 mJy. Contours of ‘signal-to-noise’ (S/N), overlaid on the Subaru R-band image of the field are shown in Fig. 3.1.

3.2.2 Multi-wavelength data

Significant multiwavelength archival data exist for the MS 0451–03 field, which are summarised in Table 3.1 and described below.

3.2.2.1 *Spitzer* MIPS imaging

Geach et al. (2006) obtained *Spitzer* MIPS 24 μ m observations of a 0.23-deg² area of MS 0451–03, excluding the central 25-arcmin². The full details of the reduction and source extraction process are described in Geach et al. (2006). The central region of the cluster was part of Guaranteed Time Observations (*Spitzer* program 83) so these data were obtained from the archive and incorporated into the mosaic. The 5- σ catalogue detection limit corresponds to 200 μ Jy.

3.2.2.2 Radio Imaging

Archival observations of the MS 0451–03 field at 1.4 GHz were obtained using the National Radio Astronomy Observatory’s (NRAO¹) Very Large Array (VLA), combining 9 hours of data obtained in 2002 June in the VLA’s BnA configuration with 16 hours of A-configuration data taken in 2006 February (Project IDs AN109 and AB1199, respectively). The nearby calibrator, 0503+020, was used to track amplitude and phase, with absolute flux and bandpass calibration set via 0137+331. The now-standard 1.4-GHz wide-field imaging approach was adopted (Owen et al. 2005; Biggs & Ivison 2006), using spectral-line mode ‘4’ to acquire data with an integration time of 3 s (10 s in BnA) and using the IMAGR task in the Astronomical Image Processing System (AIPS) to map out the primary beam using a mosaic of 37 images, with 17 more distant radio sources covered by additional facets. Several iterations of self-calibration and imaging resulted in a noise level of 11 μ Jy beam⁻¹, with a 2.3'' \times 1.8'' synthesised beam at a position angle 0.0°.

Sources and corresponding fluxes are obtained from SExtractor (Bertin & Arnouts 1996), using the S/N map for detection and the flux map as the analysis image; sources are extracted where a minimum of 10 contiguous pixels (each is 0.16 arcsec²) have S/N \geq 2. The resulting catalogue has a 3- σ flux limit of 51 μ Jy and is corrected for bandwidth smearing. We verify the statistical properties of our catalogue by comparing source counts with Biggs & Ivison (2006). Notably, the source density is not significantly enhanced towards the cluster centre, allowing us to use the counts across the whole field in our statistical calculation of AzTEC counterparts (§3.3.2.2).

¹NRAO is operated by Associated Universities Inc., under a cooperative agreement with the National Science Foundation.

3.2.2.3 Optical and near-infrared imaging

Observations of MS 0451–03 in the U -band were taken with the MegaPrime camera on the Canada France Hawaii Telescope (CFHT) and reach a $3\text{-}\sigma$ detection limit of 25.1 mag in a 0.25-deg^2 field. Standard reduction techniques were employed, customised for MegaPrime data (C.-J. Ma & H. Ebeling, private communication), details of which can be found in Donovan (2007).

In addition we observed a 0.08-deg^2 area centered on the cluster core on 2007 October 09 through the z' filter with the Prime Focus Imaging Platform mounted on the 4.2-m William Herschel Telescope (WHT). A total integration time of one hour was obtained and reduced using standard techniques and calibrated using a Sloan Digital Sky Survey standard field, yielding a $3\text{-}\sigma$ limiting magnitude of 24.2 mag.

Finally, the $BVRI$ imaging employed here comes from the PISCES survey (Panoramic Imaging and Spectroscopy of Cluster Evolution with Subaru; Kodama et al. 2005). Detection limits are listed in Table 3.1. In addition K -band imaging to a $3\text{-}\sigma$ depth of 20.1 mag over 0.12-deg^2 centred on MS 0451–03 was obtained from the Wide-Field Infrared Camera (WIRC; Wilson et al. 2003) on the Palomar Hale telescope. Standard reduction methods were employed and are detailed in G. Smith et al. (in prep.). These data were used in the previous analyses of Geach et al. (2006) and Moran et al. (2007a,b).

3.2.2.4 *Spitzer* IRAC imaging

The *Spitzer* InfraRed Array Camera (IRAC; Fazio et al. 2004) observations of the $20' \times 20'$ field centered on the MS0451 field were obtained as a part of the Cycle 5 General Observer (program 50610, PI: M. Yun) on 2009 March 18. Each tile was observed for a total of 1500 seconds in each of the four IRAC bands (3.6, 4.5, 5.8, and $8.0\ \mu\text{m}$) in full array mode with a 15 position dither pattern with 100 second exposures at each position. The new data are combined with the archival IRAC data (program 83) to produce the final mosaic images using CLUSTER GRINDER (Gutermuth et al. 2009), which is an IDL software package that utilizes standard Basic Calibrated Data (BCD) products from the Spitzer Science Centre's standard data pipeline. The angular resolution of the final mosaic ranges between 2.0 and 2.5 arcsec depending on the observing band; the limiting depths are given in Table 3.1.

3.2.2.5 Cataloguing

To estimate redshifts photometrically we require that the photometry in all filters samples the same emission from the source so an accurate spectral energy distribution (SED) can be built. To meet this requirement we degrade all the optical images to match the worst seeing – the (V -band) in which the FWHM is 1.54 arcsec. Each seeing convolved image is astrometrically matched to the USNO catalogue with a set of unsaturated and unblended stars spread across the frames. We use SExtractor (Bertin & Arnouts 1996) on the R -band image to detect objects with a minimum of ten adjacent 0.2-arcsec pixels at least 1.5σ above the background to provide a source list and then use the APPHOT routine in IRAF to extract 3-arcsec diameter aperture photometry at these positions in each convolved image. These measurements are then aperture corrected assuming a point source, to yield total magnitudes. We report $3\text{-}\sigma$ detection limits in Table 3.1.

The resolution of the IRAC images is significantly lower than the optical so for source extraction we consider these data separately, although an equivalent procedure is followed. Sources are detected on the $8\mu\text{m}$ image with SExtractor (Bertin & Arnouts 1996) and are required to have a minimum of 4 adjacent 0.9-arcsec pixels at least 2σ above the background. The $8\mu\text{m}$ band is chosen so that we can use the IRAC colours to constrain counterparts for otherwise unidentified SMGs (§3.3.2.3 and Yun et al. 2008). This source list provides positions for the APPHOT routine in IRAF to extract 3.8-arcsec diameter fluxes. We also ensure that all SMGs which are identified in Submillimeter Array (SMA), radio or $24\mu\text{m}$ data and have IRAC counterparts in *any* bands are extracted, removing the requirement for an $8\mu\text{m}$ detection. The extracted fluxes are corrected for the aperture losses, employing the factors calculated by the SWIRE team (Surace et al. 2005), resulting in total magnitudes, which can be directly compared to our optical catalogue.

3.3 Analysis and Results

This study aims to identify 1.1-mm detected ULIRGs in the $z = 0.54$ galaxy cluster MS 0451–03. A priori, based on the space density of ULIRGs at $z \sim 0.5$ (Le Floc’h et al. 2005), and the overdensity of LIRGs in clusters at this redshift (Geach et al. 2006), we expect to find, at most, only a couple of cluster members in our survey. The large background population coupled with this small number of expected members makes this study challenging. Therefore, we focus on techniques to identify sources and confirm cluster membership. Similarly to other SMG studies, a fraction of our sources are unidentified

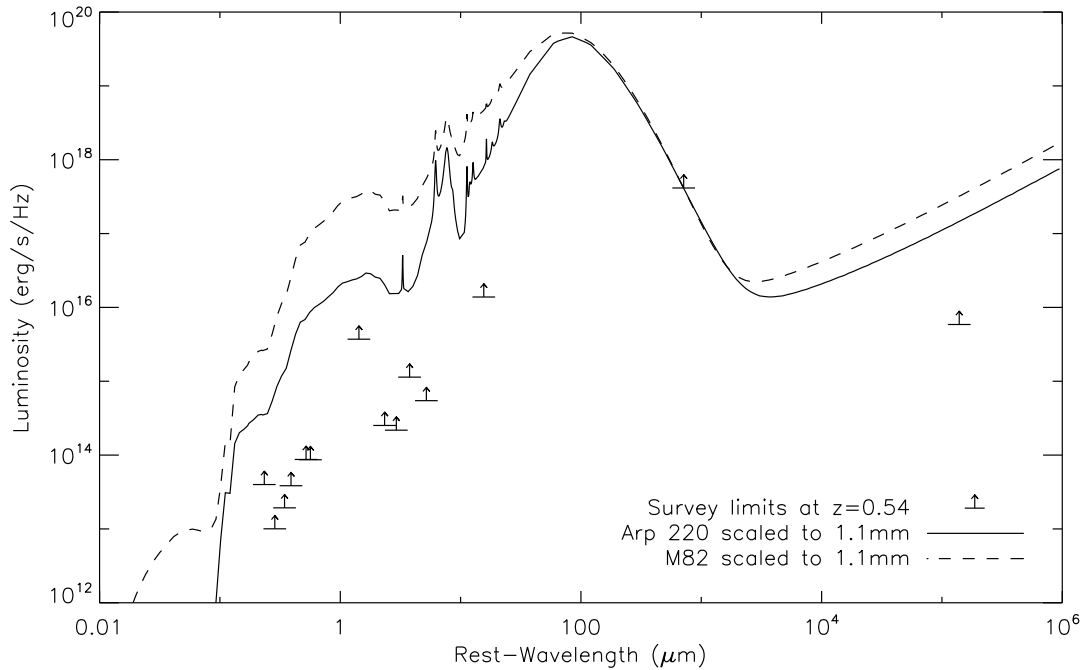


Figure 3.2: Catalogue detection limits (see Table 3.1) in each filter for a $z = 0.54$ galaxy overlaid with Arp 220 and M82 SEDs (Silva et al. 1998) scaled to our 3.5σ 1.1 mm catalogue limit. We expect to easily detect counterparts at this redshift suggesting that unidentified SMGs are most likely to be high redshift background galaxies and not cluster members.

in the radio, mid-infrared or optically. However, based on an Arp 220 SED, cluster members which are detectable above our 1.1-mm flux limit are also expected to be brighter than the catalogue limits in all other bands (Fig. 3.2). Therefore, any unidentified sources are likely to be part of the background population.

3.3.1 AzTEC catalogue

Millimetre sources are identified as local maxima with $S/N \geq 3.5$ and are selected in the roughly uniform noise ($\sigma \sim 1.1$ mJy, ~ 360 -arcmin²) region of the AzTEC signal-to-noise map (with weights of at least half of the maximum). In Table 3.2 we present the 36 detections in order of decreasing S/N . Measured source fluxes and their errors are given by the peak pixel value and corresponding noise value respectively; deboosted fluxes are calculated following the method of Perera et al. (2008). We determine the positions of sources on the sub-pixel level by calculating the centroid after weighting pixels close to the brightest pixel according to the square of their fluxes. Fig. 3.1 shows the Subaru R -band

Table 3.2: AzTEC galaxies in the MS 0451–03 field in order of decreasing S/N. Source names correspond to AzTEC positions in the J2000 epoch. SMGs with robust multiwavelength counterparts (§3.3.2 and Table 3.3) are shown in bold.

	Source	SNR	Flux (mJy)	Noise (mJy)	Deboosted flux (mJy)
1	MMJ 045438.96-030739.8^a	6.5	8.3	1.3	6.4^{+1.3}_{-1.4}
2	MMJ 045447.55-030018.8^a	5.8	6.2	1.1	4.7^{+1.1}_{-1.1}
3	MMJ 045433.57-025204.0^a	5.7	7.7	1.4	5.4^{+1.4}_{-1.5}
4	MMJ 045431.56-025957.8^b	5.1	5.2	1.0	3.7^{+1.0}_{-1.1}
5	MMJ 045421.55-030109.9	5.1	5.1	1.0	3.6^{+1.0}_{-1.2}
6	MMJ 045417.49-030306.6	4.9	5.0	1.0	3.5^{+1.1}_{-1.2}
7	MMJ 045413.35-031204.2^b	4.6	6.3	1.4	3.6^{+1.4}_{-2.0}
8	MMJ 045412.72-030043.7	4.5	4.5	1.0	2.9^{+1.0}_{-1.3}
9	MMJ 045345.31-030552.2	4.4	4.6	1.0	2.8^{+1.1}_{-1.4}
10	MMJ 045407.14-030033.9	4.3	4.3	1.0	2.6^{+1.0}_{-1.4}
11	MMJ 045358.12-025233.3	4.3	4.3	1.0	2.6 ^{+1.0} _{-1.5}
12	MMJ 045426.76-025806.5	4.2	4.2	1.0	2.6 ^{+1.0} _{-1.4}
13	MMJ 045356.09-025031.4	4.2	5.4	1.3	2.6 ^{+1.3} _{-2.2}
14	MMJ 045424.53-030331.7	4.1	4.2	1.0	2.4 ^{+1.0} _{-1.5}
15	MMJ 045328.86-030243.3	4.1	5.0	1.2	2.5^{+1.2}_{-2.0}
16	MMJ 045354.64-030004.0	4.0	4.0	1.0	2.1 ^{+1.0} _{-1.6}
17	MMJ 045431.35-025645.8	4.0	4.0	1.0	2.3^{+1.0}_{-1.4}
18	MMJ 045411.57-030307.5	4.0	4.1	1.0	2.3^{+1.0}_{-1.6}
19	MMJ 045415.53-025125.0	3.9	4.1	1.0	2.3 ^{+1.1} _{-1.6}
20	MMJ 045345.88-030440.0	3.9	4.0	1.0	2.2 ^{+1.0} _{-1.6}
21	MMJ 045358.49-025601.4	3.9	3.8	1.0	2.2 ^{+1.0} _{-1.5}
22	MMJ 045403.10-025006.8	3.9	4.7	1.2	2.2 ^{+1.3} _{-2.0}
23	MMJ 045357.46-030237.1	3.9	4.0	1.0	2.1 ^{+1.0} _{-1.6}
24	MMJ 045420.10-030658.2	3.8	4.0	1.0	2.2 ^{+1.1} _{-1.6}
25	MMJ 045422.17-030445.8	3.8	3.9	1.0	2.0 ^{+1.0} _{-1.7}
26	MMJ 045349.69-025807.1	3.8	3.8	1.0	2.0^{+1.0}_{-1.6}
27	MMJ 045421.17-030740.2	3.8	3.9	1.0	1.9^{+1.1}_{-1.7}
28	MMJ 045345.06-025722.6	3.7	3.7	1.0	1.9 ^{+1.0} _{-1.6}
29	MMJ 045442.54-025455.0	3.7	4.5	1.2	1.6 ^{+1.4} _{-1.6}
30	MMJ 045444.78-030030.9	3.7	3.8	1.0	1.9 ^{+1.1} _{-1.6}
31	MMJ 045411.73-025712.7	3.7	3.6	1.0	1.8 ^{+1.0} _{-1.6}
32	MMJ 045411.17-031019.2	3.6	4.1	1.1	1.8 ^{+1.2} _{-1.7}
33	MMJ 045352.72-030130.9	3.6	3.7	1.0	2.0 ^{+1.0} _{-1.6}
34	MMJ 045454.20-025919.3	3.6	4.6	1.3	1.5 ^{+1.5} _{-1.5}
35	MMJ 045359.27-030327.4	3.5	3.6	1.0	1.8 ^{+1.0} _{-1.6}
36	MMJ 045340.09-030334.2	3.5	3.6	1.0	1.7 ^{+1.0} _{-1.6}

^a These SMGs were observed with the SMA and detected (§3.3.2.1).

^b These SMGs were observed with the SMA but not formally detected (§3.3.2.1).

image with AzTEC contours of constant S/N and the detected 1.1-mm sources marked. Based on the analyses of AzTEC data in Scott et al. (2008) and Perera et al. (2008) we expect that 3–4 (8–10%) of the sources in our 3.5σ catalogue are false detections with only ~ 0.5 and 0 amongst those with $S/N \geq 4.5$ and 5 respectively.

To examine whether there is an overdensity of AzTEC galaxies in MS 0451–03 compared to similar field surveys – potentially indicating a significant number of obscured ULIRG cluster members – we calculate the number counts in MS 0451–03 compared to the AzTEC blank-field survey of the SHADES fields (Austermann et al. 2010). The source number counts and corresponding errors were calculated using the same bootstrap sampling methods as described in Austermann et al. (2010), employing the AzTEC/SHADES best fit Schechter parameters as a prior. Due to the effects of flux boosting, our catalogue, which is limited at an apparent S/N ratio of 3.5, corresponding to a typical apparent flux of 3.6 mJy, actually contains sources fainter than this limit, allowing us to statistically constrain counts fainter than 3.6 mJy. We also calculate number counts in the central 5 arcmin radius of the AzTEC MS 0451–03 map, by trimming the map to this area and repeating the calculations with the sky model, deboosting, and completeness estimates based on the full maps, since these are not expected to change across the field. The number counts for the whole MS 0451–03 survey area, and the central 5 arcmin (which represents a physical scale of ~ 1.9 Mpc at $z = 0.54$), compared to the AzTEC/SHADES survey are presented in Fig. 3.3.

Across the whole field MS 0451–03 does not exhibit a source excess at 1.1 mm compared to a blank field. This suggests that, as expected, there is not a dominant population of luminous obscured star-forming galaxies in MS 0451–03. Nevertheless, it is possible that a small number of the sources are still cluster members. Indeed, our number counts analysis (Fig. 3.3) suggests there may be a small overdensity of sources in the central 5-arcmin radius region of the AzTEC map. Based on integral number counts and their errors at 1.1 mm down to 1 mJy, derived from bootstrap sampling the Posterior Flux Densities of sources (as described in detail in Austermann et al. 2010) a very tentative overdensity is apparent at the $\sim 1.6\sigma$ level. If real this overdensity could arise from a combination of the Sunyaev-Zel’dovich effect (enhancing the background on which sources lie), the gravitational lensing of background sources by the cluster, and potentially 1.1 mm cluster members. To discover whether any of this excess is caused by 1.1-mm bright cluster galaxies we must first accurately locate the counterparts to the 1.1-mm emission.

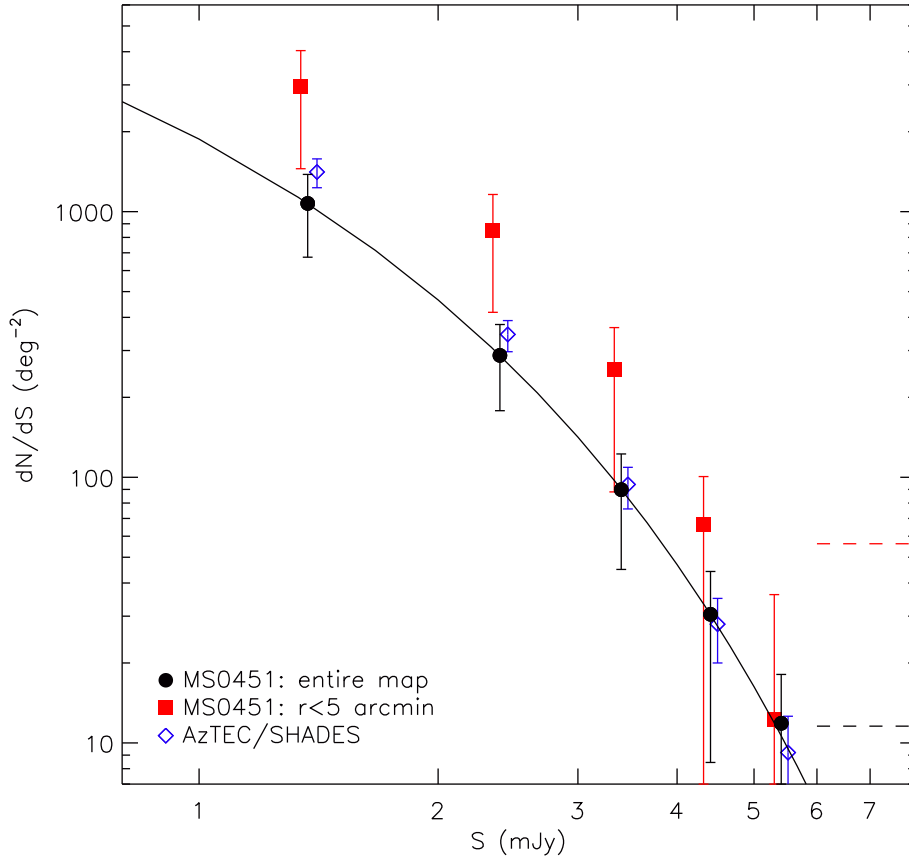


Figure 3.3: Differential number counts using deboosted fluxes from the AzTEC survey of MS 0451–03 compared to those from the AzTEC/SHADES survey (Austermann et al. 2010). We see that across the whole area of our survey there is no strong overdensity of 1.1 mm sources in MS 0451–03 compared to the AzTEC/SHADES blank-field survey; hence it is apparent that the majority, but not necessarily the entirety, of the millimetre sources in the cluster field are background galaxies. However, in the central 5 arcmin radius of the map (~ 1.9 Mpc at $z = 0.54$) there may be a slight overdensity of sources. This could be due to a combination of the Sunyaev-Zel’dovich effect, gravitational lensing of background sources by MS 0451–03, and potentially a contribution from 1.1 mm cluster members. The solid line is the Schechter function fit to the number counts in the entire AzTEC map, and the dotted lines represent the survey limits - the lower and upper lines represent the whole AzTEC MS 0451–03 field and the central 5 arcmin radius, respectively. For clarity number counts in the central 5 arcmin radius of MS 0451–03 and the AzTEC/SHADES survey are offset slightly in flux.

3.3.2 Identifying counterparts to AzTEC sources

The large AzTEC beam (18-arcsec FWHM on the JCMT), coupled with the high spatial density of optical sources makes identification difficult unless precise positions are determined for the SMGs. The observed mm/sub-mm emission from SMGs represents rest-frame far-infrared emission from dust-reprocessed starlight or AGN activity. Therefore, by exploiting the far-infrared–radio correlation (e.g. Condon 1992; Garrett 2002) and the low spatial density of radio sources, it is possible to employ deep ($\sigma \sim 10 \mu\text{Jy}$), high-resolution, interferometric radio observations to determine accurate source positions for ~ 60 – 80 per cent of SMGs (e.g. Ivison et al. 2002, 2005, 2007; Chapin et al. 2009). Similarly, 24- μm observations can be used for identification, a method which has proved useful in confirming tentative radio counterparts, or providing positions for a small number of the radio undetected SMGs (e.g. Ivison et al. 2004; Pope et al. 2006; Ivison et al. 2007; Chapin et al. 2009). In addition, mid-infrared colours have been used to isolate potential cluster SMGs (Chapter 4; Ashby et al. 2006; Pope et al. 2006; Yun et al. 2008; Biggs et al. 2010).

An alternative approach is submillimetre interferometry (e.g. Iono et al. 2006; Younger et al. 2007; Cowie et al. 2009), which is preferable to these traditional radio and mid-infrared identification methods because it samples the same part of the Spectral Energy Distribution (SED) as our AzTEC imaging. However, sources generally require individual observations due to the small field-of-views of such instruments, commanding prohibitive exposure times to accurately locate all sources in a catalogue.

We employ all three methods in this work, using millimetre interferometry where available, and radio and mid-infrared imaging as an alternative. The details of each of these identification methods is discussed in the following sections. In total we identify 18 AzTEC counterparts (50% of the sample; Table 3.3), of which 14 (39% of the total) also have optical counterparts (Table 3.4). In Fig. 3.2 we demonstrate that at $z \sim 0.5$ our multiwavelength observations are deep enough to detect galaxies above our AzTEC flux limit and hence provide counterparts, assuming SEDs typical of Arp 220 or M82. Therefore, our unidentified sample is not expected to contain cluster members. Of the optically-unidentified SMGs, one lies out of the field of the Subaru, CFHT and IRAC observations, two are contaminated by nearby saturated stars and one is fainter than our detection limits at all wavelengths. We discuss the AzTEC galaxies and corresponding counterparts on a source by source basis in Appendix 3.5.

3.3.2.1 SMA detections

The five brightest SMGs presented here were observed at 890 μm with the SMA in October and November 2007 (J. Younger, priv. comm.). On-source integration times of 5–6 hours were employed, yielding maps with $\sigma_{890\mu\text{m}} \sim 1.6$ mJy, which are presented in Fig. 3.4. The SMA configuration resulted in a beam of ~ 3 arcsec.

Of the five sources observed with the SMA MMJ 045438.96, MMJ 045447.55 and MMJ 045433.57 were detected with 870- μm fluxes of 8.4, 5.5 and 8.3 mJy respectively. The remaining two targets, MMJ 045431.56 and MMJ 045413.35, were undetected, but have AzTEC 1.1 mm detections with SNR = 5.1 and 4.6 respectively. The proposed radio identifications (§ 3.3.2.2) of MMJ 045438.96 and MMJ 045433.57 are coincident with their SMA positions. The other SMA detected galaxy, MMJ 045447.55, lies ~ 9 arcsec from an elliptical galaxy with bright radio and mid-infrared emission, which, due to the high fluxes is formally a ‘robust’ identification, but is unlikely to be the true source of the millimetre emission. MMJ 045431.56 and MMJ 045413.35 which were targeted but not detected with the SMA are identified through radio and mid-infrared counterparts respectively.

Unlike this MS 0451–03 study, previous SMA observations of AzTEC galaxies in the COSMOS field detected all seven targets (Younger et al. 2007). However, the faintest of the COSMOS SMGs has deboosted 1.1 mm flux of 5.2 mJy, compared to 3.7 and 3.6 mJy for MMJ 045431.56 and MMJ 045413.35 respectively. Therefore, based on the deboosted fluxes it is possible that MMJ 045431.56 and MMJ 045413.35 are too faint to be detected in our observations, although there are examples of bright SMGs that are undetected with the SMA (e.g. Matsuda et al. 2007). Alternatively, the lack of SMA counterparts could suggest that either the 890 μm to 1.1 mm flux ratios of these sources are lower than expected (i.e. the dust is colder, or they are higher redshift than spectroscopically identified SMGs), that these galaxies exhibit extended far-infrared emission on scales $\gg 2$ arcsec ($\gg 16$ kpc at $z = 2$; for example, from a merger-induced starburst), or that the AzTEC beam contains a blend of multiple SMGs. Our radio and SMA observations have similar resolutions, therefore, extended or multiple radio counterparts can indicate the extended or multiple nature of (sub)millimetre emission. Based on the radio emission it is likely that MMJ 045431.56 is composed of multiple (sub)millimetre sources, as discussed in Appendix 3.5. However, MMJ 045413.35 is more likely to be a single resolved (sub)millimetre source, with a lower 890-to-1100 μm ratio than expected. We use the positions of the three SMA detected SMGs in the following

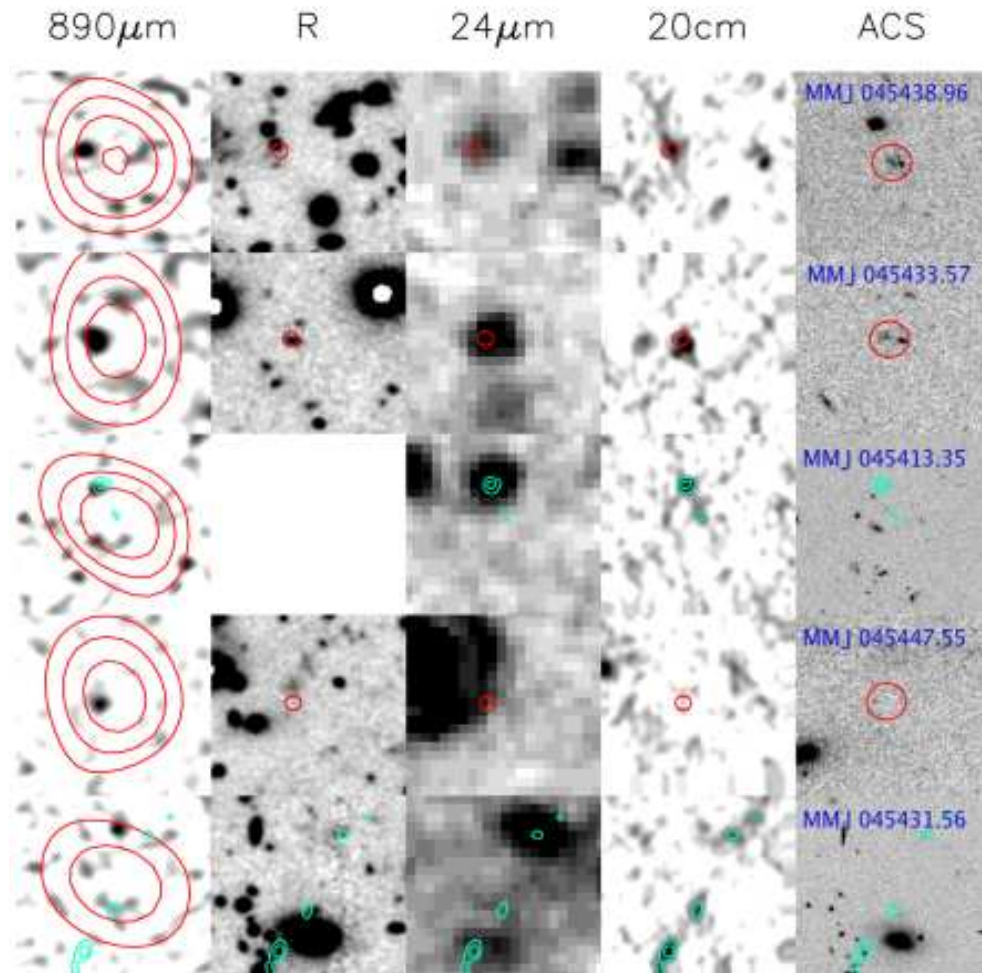


Figure 3.4: Images of the five SMGs in MS 0451–03 that were observed at 870- μm with the SMA (J. Younger, priv. comm.). The background figures are (from left to right) SMA 870- μm , Subaru *R*-band, MIPS 24- μm , radio and *HST* ACS F818W. North is up and east is to the left. The *HST* images of MMJ 045438.96, MMJ 045447.55 and MMJ 045433.57, which were detected with the SMA, are $10 \times 10''$; all other images are $25 \times 25''$. The red contours in the left-hand panel are at the 3, 4, 5, 6 σ levels from the AzTEC map and red $2''$ diameter circles show the position of the SMA detections. For MMJ 045431.56 and MMJ 045413.35, which were not detected with the SMA, cyan contours are radio 3, 5, 7 σ contours.

analysis.

3.3.2.2 Radio and mid-infrared identifications

In this Chapter we use both 1.4-GHz VLA and 24- μm *Spitzer* MIPS observations to locate the AzTEC galaxies in our sample. We identify SMG counterparts independently at radio and mid-infrared wavelengths before comparing these for each AzTEC source. In our maps the surface density of radio galaxies is lower than the mid-infrared, the positional accuracy is greater (~ 0.6 arcsec compared to ~ 1.8 arcsec), and the link from the radio emission to the far-infrared is tighter. Therefore, if the 24 μm and 1.4 GHz identifications disagree we consider the radio position as the more reliable counterpart.

To ensure that no genuine associations are missed we search up to 10 arcsec from each AzTEC position. This corresponds to a $\sim 3\sigma$ search radius for the lowest signal-to-noise ratio (SNR) sources, where σ is the error on AzTEC position, given by $0.6\text{FWHM}(\text{SNR})^{-1}$, and the FWHM is of the instrument beam (Ivison et al. 2007). We reject counterparts with more than 10 per cent probability of being chance associations using the P-statistic of Downes et al. (1986) (see also Pope et al. 2006; Ivison et al. 2007; Biggs et al. 2010, Chapter 4). Counterparts found with $p \leq 0.05$ are considered robust and those with $0.05 \leq p < 0.1$ tentative. We present all identifications in Table 3.3.

3.3.2.3 IRAC identifications

Yun et al. (2008) studied SMGs securely identified with SMA, radio, or 24 μm data and found that they typically have redder IRAC colours than the submillimetre-faint foreground galaxy population. They proposed a selection criteria for SMG counterparts, based on IRAC colours and found that the SMA detected galaxies in their sample, whether radio and mid-infrared identified or not, were all recovered by this method. We verify that this selection criteria for our SMA, radio and 24 μm -identified SMG counterparts and use it to search for counterparts to our otherwise unidentified AzTEC sources and identify two further galaxies. Unlike the Yun et al. (2008) result, MMJ 045447.55, our optically, radio and 24 μm faint, but SMA-detected SMG, is not detected in any of the IRAC wavebands to the depth of the survey listed in Table 3.1.

Later, in Chapter 4 (see also Biggs et al. 2010) we use the sample of 126 SMG in the ECDFS to further refine the IRAC-identification of SMGs by building on the analysis of Pope et al. (2008). We find that within the error circles of SMGs galaxies with $\log_{10}(S_{5.8\mu\text{m}}) \geq 0.75$ and $\log_{10}(S_{5.8\mu\text{m}}/S_{3.6\mu\text{m}}) \geq -0.05$ have a $\leq 10\%$ probability of

Table 3.3: Radio and 24 μm counterparts of AzTEC galaxies in MS 0451–03. All matches within 10-arcsec are listed, those secure identifications at 1.4 GHz or 24 μm with $P \leq 0.05$ are shown in bold and tentative associations ($0.05 < P \leq 0.10$) are also presented. Images and a discussion of each source are presented in Appendix 3.5.

	Source	1.4GHz position ^a		$S_{1.4\text{GHz}}^b$ (μJy)	1.1mm–1.4GHz Separation (arcsec)	$P_{1.4\text{GHz}}$	24 μm position ^c		$S_{24\mu\text{m}}^d$ (μJy)	1.1mm–24 μm Separation (arcsec)	$P_{24\mu\text{m}}$
		RA (J2000)	Dec				RA (J2000)	Dec			
1	MMJ 045438.96 ^e	04^h54^m39^s.01	−03°07′38″.5	98.0	1.51	0.003	04^h54^m38^s.97	−03°07′38″.0	157	1.3	0.023
2	MMJ 045447.55 ^f	04^h54^m47^s.46	−03°00′19″.2	< 51	-	-	-	-	< 120	-	-
		04 ^h 54 ^m 48 ^s .14	−03°00′14″.6	101	9.78	0.032	04 ^h 54 ^m 48 ^s .12	−03°00′14″.3	3396	9.56	0.009
3	MMJ 045433.57 ^e	04^h54^m33^s.55	−02°52′04″.6	93.5	0.71	0.0008	04^h54^m33^s.51	−02°52′06″.8	392	3.00	0.020
4	MMJ 045431.56 ^g	04^h54^m31^s.69	−03°00′07″.1	77.8	9.50	0.035					
							04 ^h 54 ^m 31 ^s .13	−02°59′51″.6	485	8.89	0.076
5	MMJ 045421.55	04^h54^m21^s.66	−03°01′08″.5	84.3	2.21	0.006					
							04^h54^m21^s.40	−03°01′07″.5	209	3.29	0.046
6	MMJ 045417.49	04^h54^m17^s.27	−03°03′03″.2	189	4.74	0.010	04 ^h 54 ^m 17 ^s .24	−03°03′03″.7	217	4.76	0.074
7	MMJ 045413.35	04^h54^m13^s.36	−03°11′58″.8	78.4	5.44	0.021	04 ^h 54 ^m 13 ^s .38	−03°11′58″.9	333	5.31	0.056
8	MMJ 045412.72	04^h54^m12^s.79	−03°00′43″.9	58.3	1.03	0.002	-	-	< 120	-	-
9	MMJ 045345.31	04^h53^m45^s.29	−03°05′53″.5	92.3	1.30	0.002	04^h53^m45^s.36	−03°05′52″.8	1393	0.86	0.0004
		04^h53^m45^s.07	−03°05′56″.6	76.9	5.62	0.022					
10	MMJ 045407.14	04^h54^m07^s.08	−03°00′37″.2	60.9	3.37	0.013	04^h54^m07^s.07	−03°00′37″.5	1120	3.76	0.007
12	MMJ 045426.76 ^h	04 ^h 54 ^m 26 ^s .86	−02°58′08″.0	< 51	-	-	-	-	< 120	-	-
15	MMJ 045328.86 ⁱ	-	-	~ 51	-	-	04^h53^m28^s.83	−03°02′45″.9	150	2.54	0.040
17	MMJ 045431.35	04^h54^m31^s.71	−02°56′45″.0	89.3	5.41	0.019	-	-	< 120	-	-
18	MMJ 045411.57 ⁱ	-	-	~ 51	-	-	04^h54^m11^s.66	−03°03′08″.0	185	1.55	0.016
26	MMJ 045349.69	-	-	< 51	-	-	04^h53^m49^s.80	−02°58′13″.9	530	7.03	0.049
27	MMJ 045421.17 ⁱ	-	-	~ 51	-	-	04^h54^m21^s.14	−03°07′46″.1	464	5.92	0.045
28	MMJ 045345.06 ^j	-	-	~ 51	-	-	04 ^h 53 ^m 45 ^s .33	−02°57′18″.1	226	6.00	0.095
29	MMJ 045442.54 ⁱ	04 ^h 54 ^m 42 ^s .62	−02°54′48″.2	< 51	-	-	-	-	< 120	-	-

^a1.4 GHz positions have typical uncertainties of ~ 0.6 -arcsec.

^b1.4 GHz fluxes have typical errors of 17 μJy .

^c24 μm positions have typical uncertainties of ~ 1.8 -arcsec.

^d24 μm fluxes have typical errors of 40 μJy .

^eThe radio and mid-IR positions agree with the SMA position (§3.3.2.1)

^fMMJ 045447.55 is identified from SMA observations (§3.3.2.1), but a bright elliptical galaxy ~ 9.6 arcsec from the AzTEC position is also a formal radio and mid-IR identification. We consider the radio and mid-IR galaxy to be a chance association – at $P = 0.05$ we expect 1–2 chance associations in our catalogue.

^gThere is an additional 176- μJy 24- μm source, with $P = 0.17$, coincident with the radio counterpart of MMJ 045431.56. It is considered related to the AzTEC detection due to the radio identification.

^hMMJ 045426.76 and MMJ 045442.54 have no radio or mid-IR counterparts but are identified on the basis of their IRAC colours (Yun et al. 2008).

ⁱThere is a $\sim 3\sigma$ radio peak coincident with the 24- μm counterpart.

Table 3.4: Optical and near-infrared photometry for the detected SMG counterparts with derived photometric redshifts. Potential cluster members are shown in bold (§3.3.3.3).

Source	U	B	V	R	I	z	K	$3.6\mu\text{m}$	$4.5\mu\text{m}$	$5.8\mu\text{m}$	$8\mu\text{m}$	z_{phot}
1 MMJ 045438.96	> 25.1	25.89±0.04	24.03±0.04	23.29±0.03	22.77±0.03	23.75±1.10	19.88±0.11	20.78±0.05	20.37±0.03	19.92±0.09	20.44±0.07	3.42 ^{+0.07} _{-0.05}
3 MMJ 045433.57	26.92±0.17	25.60±0.04	24.96±0.05	24.02±0.03	23.35±0.04	-	19.27±0.07	20.41±0.03	20.05±0.02	19.72±0.08	20.11±0.05	2.55 ^{+0.06} _{-0.09}
4 MMJ 045431.56	24.04±0.04	24.20±0.02	23.45±0.03	22.71±0.02	21.97±0.03	21.22±0.05	18.32±0.06	20.18±0.03	20.14±0.02	20.15±0.11	20.85±0.10	0.86 ^{+0.04} _{-0.03}
5^a MMJ 045421.55	24.92±0.08	24.50±0.03	23.37±0.03	22.31±0.02	21.44±0.03	21.31±0.09	18.81±0.12	19.70±0.02	19.96±0.02	19.43±0.06	20.54±0.08	0.50 ^{+0.05} _{-0.10}
8 MMJ 045412.72	> 25.1	> 26.6	> 25.8	> 25.1	> 24.2	> 24.2	> 20.1	19.48±0.01	19.03±0.02	18.61±0.03	19.40±0.03	1.85 ^{+0.31} _{-0.15}
10 MMJ 045407.14	22.83±0.03	22.23±0.02	21.69±0.02	21.23±0.02	20.80±0.02	20.64±0.04	19.67±0.08	20.78±0.05	20.37±0.03	19.92±0.09	20.44±0.07	0.35 ^{+0.05} _{-0.03}
12 MMJ 045426.76	> 25.1	27.32±0.11	27.71±0.57	25.53±0.08	23.83±0.05	26.80±4.24	22.39±0.34	21.95±0.13	21.77±0.10	21.37±0.36	21.25±0.15	0.89 ^{+0.10} _{-0.10}
15 MMJ 045328.86	> 25.1	> 26.6	> 25.8	> 25.1	> 24.2	> 24.2	> 20.1	21.08±0.06	20.83±0.04	20.48±0.15	21.48±0.19	1.87 ^{+0.62} _{-0.85}
17 MMJ 045431.35	24.45±0.05	24.37±0.03	24.23±0.03	23.72±0.03	23.31±0.04	25.94±1.40	21.13±0.17	22.21±0.17	21.97±0.12	22.37±1.21	22.07±0.33	0.60 ^{+0.11} _{-0.11}
18 MMJ 045411.57	24.83±0.05	24.65±0.03	24.23±0.03	23.53±0.03	22.82±0.03	22.68±0.11	22.27±0.37	22.37±0.20	21.78±0.10	21.41±0.37	21.80±0.25	0.74 ^{+0.06} _{-0.10}
26 MMJ 045349.69	26.41±0.14	26.25±0.06	27.72±0.38	26.04±0.10	24.58±0.09	24.35±0.40	> 20.1	-	-	-	-	1.33 ^{+0.03} _{-0.10}
27 MMJ 045421.17	25.42±0.10	25.51±0.04	24.46±0.04	23.56±0.03	23.11±0.04	23.68±0.22	18.82±0.07	20.07±0.02	19.83±0.02	19.15±0.05	20.52±0.08	1.80 ^{+0.25} _{-0.26}
28 MMJ 045354.06	25.61±0.08	25.19±0.03	24.83±0.05	24.68±0.04	24.35±0.07	24.36±0.34	21.63±0.43	-	-	-	-	1.89 ^{+0.35} _{-0.84}
29 MMJ 045442.54	25.00±0.09	26.16±0.05	25.71±0.12	24.61±0.04	23.86±0.05	> 24.2	20.65±0.13	21.59±0.10	21.42±0.07	20.49±0.16	21.31±0.16	1.09 ^{+0.15} _{-0.15}

^aThis is the combined photometry for C1 and C2 as discussed in §3.3.3.3

being chance associations. The analysis in this Chapter was performed and published prior to that refinement and calculation so it was not originally applied to the SMGs in MS 0451–03. However, we note that both the IRAC counterparts that were initially selected using the Yun et al. (2008) have $\log_{10}(S_{5.8\mu\text{m}}) \geq 0.75$ and $\log_{10}(S_{5.8\mu\text{m}}/S_{3.6\mu\text{m}}) \geq -0.05$ criteria would still be considered identifications. One additional SMG would have been identified with this methodology, had it been available at the time of this analysis: MMJ045444.75 is $\sim 4.5''$ from an IRAC source that satisfies these criteria and is discussed further in Appendix 3.5 but are not considered in the following analysis. There is also an IRAC source within $10''$ of MMJ045340.09 that formally meets the requirements, but examination of the data suggests that it is likely to be spuriously selected based on noise in the $8\text{-}\mu\text{m}$ image and as such this galaxy is not considered any further.

3.3.3 Redshifts of MS 0451–03 AzTEC galaxies

Our study seeks to identify potential millimetre sources in the cluster population of MS 0451–03. There are spectroscopic observations of 1639 galaxies within our field, but nevertheless none of the AzTEC galaxies have been spectroscopically observed. Therefore, we use photometric methods to separate any potential AzTEC detected cluster members from ‘typical’ $z \sim 2$ SMGs. We first apply two simple colour tests – the advantage of these is that it is easy to understand the biases in the sample – before applying a more sophisticated photometric redshift analysis. We use the $S_{24\mu\text{m}}/S_{1.1\text{mm}}$ and $S_{1.4\text{GHz}}/S_{1.1\text{mm}}$ flux ratios to estimate the redshifts of identified AzTEC galaxies and then also consider the BzK selection criteria of Daddi et al. (2004) to separate the higher redshift ($z > 1.4$) SMGs from potential cluster members. Finally, we use the spectroscopic redshifts and multi-wavelength photometry of the SMGs in Borys et al. (2005) to test the reliability of photometric redshifts for SMGs, and apply the findings to our AzTEC MS 0451–03 sources to obtain photometric redshifts for our SMGs.

3.3.3.1 Simple photometric redshift analysis

In Fig. 3.5 we plot $S_{24\mu\text{m}}/S_{1.1\text{mm}}$ versus $S_{1.4\text{GHz}}/S_{1.1\text{mm}}$ for AzTEC MS 0451–03 SMGs. For comparison we plot $850\text{ }\mu\text{m}$ sources from Ivison et al. (2007), extrapolated from the observed $850\text{ }\mu\text{m}$ to the equivalent 1.1mm flux assuming a power law spectrum of the form $S_\nu \sim \nu^{3.5}$. As expected both sets of SMGs lie broadly within the same region of colour-colour space, adding confidence to our detections and identifications. The redshift tracks of the local star-forming galaxy Arp 220, and the higher redshift HR10 ($z = 1.44$)

(based on the SEDs of Silva et al. 1998) suggest that the AzTEC galaxies have redshifts of $1 \lesssim z \lesssim 3.5$, in concordance with the SMG population (Chapter 5; Blain et al. 1999; Chapman et al. 2005). However, as we show in Chapter 5, degeneracy between redshift and dust temperature in the templates makes this method unreliable for identifying cluster galaxies.

We next determine whether any of the SMGs are likely to lie at low redshift and hence potentially be members of MS 0451–03 by using the *BzK* selection of Daddi et al. (2004) to separate $z > 1.4$ galaxies from those at $z < 1$. Of the ~ 70 SMGs with spectroscopic redshifts presented in Chapman et al. (2005) $\sim 80\%$, and $\sim 90\%$ of the LESS SMGs in Chapter 5, have $z > 1.4$, suggesting that the *BzK* selection should enable us to remove the majority of background sources from our sample. Fig. 3.6 shows the optically identified SMGs in MS 0451–03 which are covered by our *B*, *z* and *K* imaging, in addition to Daddi et al. (2004) selection criteria for high redshift ($z > 1.4$) galaxies; SMGs with $z_{\text{phot}} < 1.4$ are highlighted (§3.3.3.3). It is clear from Fig. 3.6 that from a *BzK* selection alone, at least two SMGs are low redshift and therefore potential cluster members; several additional galaxies lie close to the border or have photometric limits which could place them in the low redshift region. Therefore, we next carry out a full photometric redshift analysis of the whole sample using HYPERZ (Bolzonella et al. 2000a) to calculate redshifts for the SMGs, as in Chapter 4.

3.3.3.2 Photometric redshifts of SMGs

Having located the SMGs in this field we now use photometric redshifts to test whether any are potential cluster members. Photometric redshifts have been calculated for several sets of SMGs using various codes and spectral templates, generally designed for use on ‘normal’ low redshift galaxies (e.g. Clements et al. 2008). However, SMGs are located at high redshifts and powered by dusty starbursts which can be contaminated by AGN meaning that the stellar templates derived from low redshift galaxies may not be appropriate. Therefore, in this section we expand on previous analyses to examine how well redshifts can be constrained for a spectroscopically confirmed sample of SMGs, and whether they can be used to identify potential cluster members. In Chapter 4 we further build on this work and derive and test the photometric redshifts of a sample of 74 SMGs detected in the ECDFS (of which 30 have spectroscopic redshifts).

There are two main methods of calculating photometric redshifts – template fitting (e.g. HYPERZ, Bolzonella et al. 2000a; Easy and Accurate z_{phot} from Yale, EAZY, Bram-

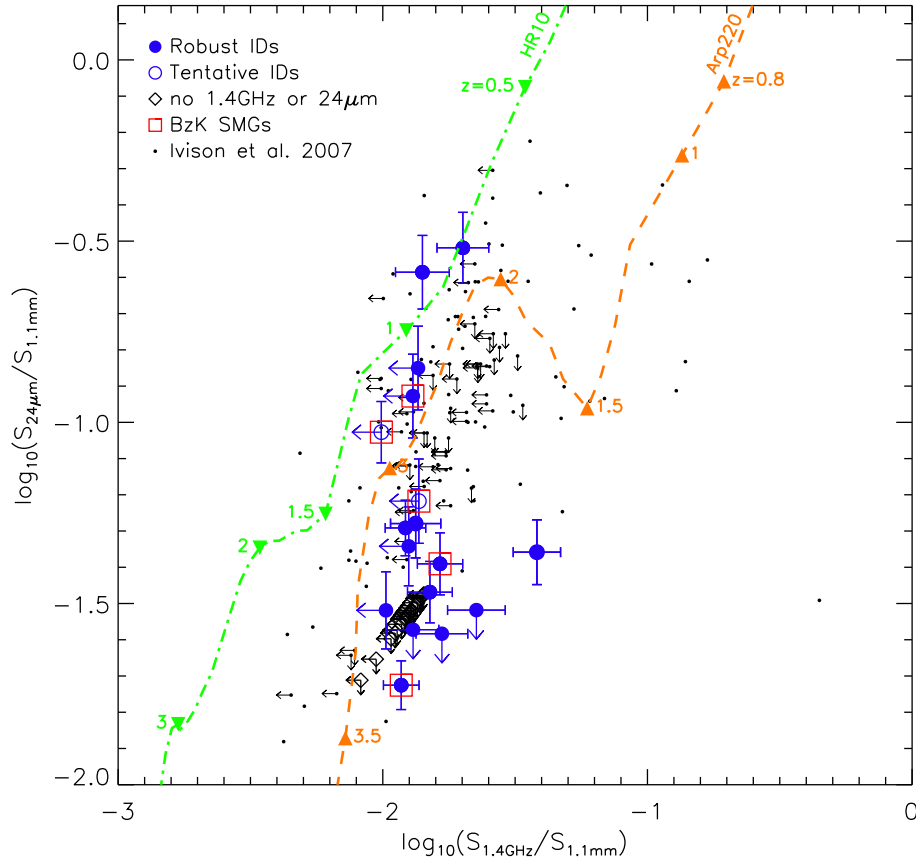


Figure 3.5: $S_{24\mu\text{m}}/S_{1.1\text{mm}}$ versus $S_{1.4\text{GHz}}/S_{1.1\text{mm}}$ for SMGs in the MS 0451–03 field. We differentiate between sources with robust ($p \leq 0.05$) and tentative detections ($0.05 < p \leq 0.10$), and highlight SMGs which satisfy the *BzK* selection criteria of Daddi et al. (2004) (Fig. 3.6). Sources without both mid-infrared and radio detections are plotted at the 3σ detection limit of the respective catalogues (Table 3.1). For comparison we also plot SHADES identifications (Ivison et al. 2007), converted to expected observed 1.1 mm fluxes as discussed in the text; error bars of this sample are omitted for clarity. Both sets of SMGs lie broadly within the same region of colour-colour space, providing confidence in our identifications. Redshift tracks of the $z = 1.4$ SMG HR 10 and local starburst Arp 220 (based on SEDs from Silva et al. (1998)) suggest that the AzTEC sources generally have $1 \lesssim z \lesssim 3.5$, in concordance with Chapman et al. (2005).

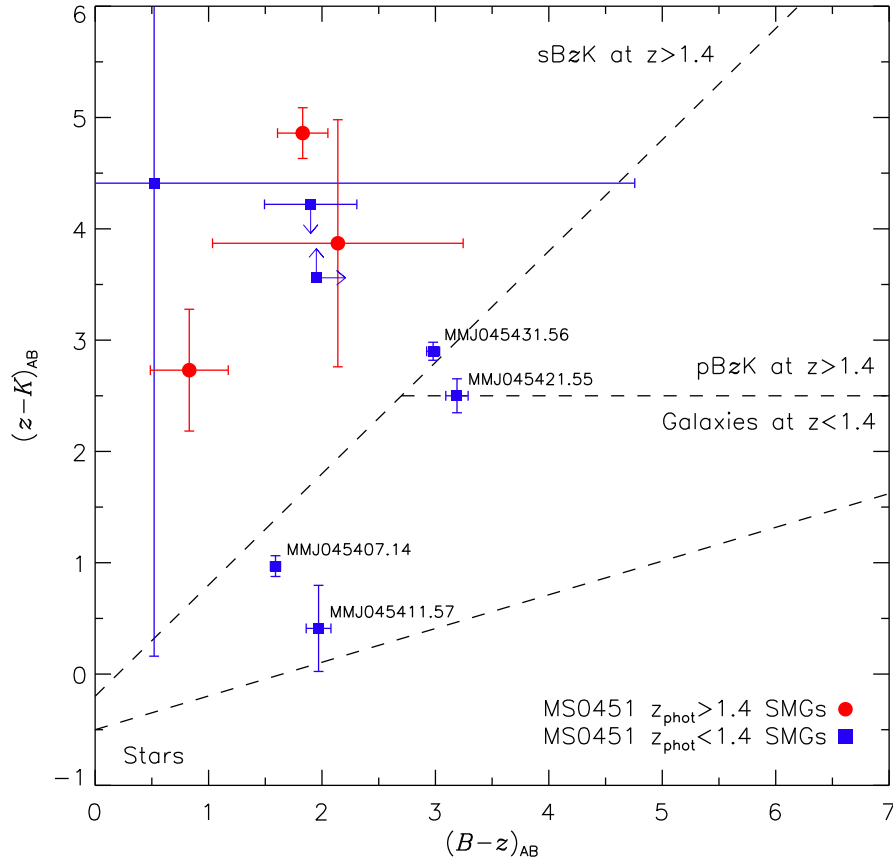


Figure 3.6: $B - z$ vs. $z - K$ colour-colour plot of the optically identified AzTEC galaxies in MS 0451–03 which lie within the field-of-view of our B , z and K observations. The lines of separation between passive and star-forming $z > 1.4$ BzK galaxies (pBzK and sBzK respectively), $z < 1.4$ galaxies, and stars (Daddi et al. 2004) are shown. Two SMGs occupy the $z < 1.4$ region, suggesting they are potential cluster members. Galaxies with BzK colours that indicate that they may be cluster members are labelled. We distinguish between galaxies with $z_{\text{phot}} > 1.4$ and $z_{\text{phot}} < 1.4$ based on the photometric redshifts calculated in §3.3.3.3. The BzK selection and full photometric analysis broadly agree as to the high and low redshift samples giving more confidence in our ability to isolate millimetre sources in the cluster from the dominant background population. As expected most SMGs are deemed to be actively star-forming by this criteria.

mer et al. 2008); and those that use sources with spectroscopic redshifts as training sets (e.g. ANNz, Collister & Lahav 2004). Some codes are now beginning to combine the two methods and incorporate training modes into template fitting codes (e.g. Zurich Extragalactic Bayesian Redshift Analyser, ZEBRA, Feldmann et al. 2006; Bayesian Photometric Redshift Estimation, BPZ, Benítez 2000; IMPZ, Babbedge et al. 2004).

We require a publicly available code and, since there are relatively few SMGs with spectroscopic redshifts (tens of SMGs compared to hundreds or thousands of sources in an ideal training set), we consider only template fitting codes. Therefore, throughout this work we use the HYPERZ² package (Bolzonella et al. 2000a) for our photometric redshift estimates. We note that Hildebrandt et al. (2010) recently performed extensive testing of the accuracy and reliability of 19 different photometric redshift codes on simulated and typical galaxies in GOODS, and found that HYPERZ produces reasonable results. However, as discussed, the typical redshifts and optical faintness of SMGs means that it is prudent to specifically test the reliability of photometric redshifts for this population.

HYPERZ calculates expected magnitudes in the observed filters for given SEDs of a library of model star-formation histories, with different ages, reddening and redshifts; the observed and expected magnitudes are compared in each filter to calculate the reduced χ^2 (χ_{red}^2). The photometric redshift is statistically the most likely redshift for the galaxy and is determined from the minimum χ_{red}^2 of best-fit SED at each redshift step. The star-formation history, age and reddening of the best-fit template at the photometric redshift are also returned, and in Chapter 4 we investigate whether these parameters are statistically reliable.

Unfortunately we do not have access to the IRAC photometry or images of the whole MS 0451–03 field so it is not possible to use the 1639 galaxies with available spectroscopy to test the reliability of photometry and photometric redshifts in this field. Therefore, for the purposes of photometric redshift testing we employ the sample of 12 SMGs analysed by Borys et al. (2005), which have spectroscopic redshifts from Chapman et al. (2003a, 2005) and Pope et al. (2008) and deep 12-band photometry: U , B , V , R , I , z' , J , K_S ³, and the IRAC 3.6, 4.5, 5.8 and 8 μm filters (Capak et al. 2004; Smail et al. 2004; Borys et al. 2005; Bundy et al. 2005). Of the 13 SMGs studied by Borys et al. (2005), we exclude SMM J123712.05 from our analysis as it is undetected at wavelengths shorter than 2- μm , and the power-law shape of the SED at longer wavelengths means that a

²We use HYPERZ version 10.0 (<http://www.ast.obs-mip.fr/users/rosier/hyperz/>).

³Two SMGs have HK' photometry instead of K_S

photometric redshift cannot be derived. We also note that SMM J123622.65 has a rest-frame UV/optical spectrum with $z = 2.466$ (Chapman et al. 2005; Swinbank et al. 2004) but mid-infrared spectroscopic analysis suggests $z = 1.79 \pm 0.04$ (Pope et al. 2008), therefore, we exclude it from the statistical analyses, but consider both spectroscopic solutions elsewhere.

Although eight different Bruzual & Charlot (1993) star-formation histories are available in the standard HYPERZ distribution (E, S0, Sa, Sb, Sc, Sd galaxies, a single burst (Burst) and a constant Star-formation rate (Im)) we initially consider the results if only four – E, Sb, Burst and Im – are employed. The full set of templates represents almost a continuum of star-formation histories, with only minimal differences between them. As suggested by Bolzonella et al. (2000b) the inclusion of many more templates can be redundant yet still cost significant processing time. E, Sb, Burst and Im star-formation histories are initially considered because these most likely to represent SMGs (which are known to be young starbursts) and are they cover the entire available range. SMGs are also known to be dusty systems, therefore, we initially allow reddening of $A_V = 0-5$, in steps of 0.2 using the Calzetti et al. (2000) reddening law. There are currently no known SMGs with $z_{\text{spec}} > 5.5$, and there are few candidate $z \sim 7$ galaxies of any type (e.g. Bouwens et al. 2008, 2010a,b), therefore, we conservatively consider photometric redshifts between 0 and 7 throughout. We note that highest redshift galaxies will “dropout” of our imaging at short wavelengths making the photometric redshifts increasingly difficult to accurately constrain. Ages of the galaxies are required to be less than the age of the Universe at the appropriate redshift. We also note that in Chapter 4 we examine the HYPERZ-derived SMG ages and find that they cannot be reliably determined, but that the requirement for SMGs younger than the Universe at the observed redshift does not significantly affect the derived photometric redshifts.

In Fig. 3.7, we compare the derived photometric redshifts, based on our nominal choice of parameters, with the spectroscopic redshifts of the Borys et al. (2005) SMGs. For our nominal choice of parameters we employ all available photometry, E, Sb, Burst and Im star-formation histories and $A_V = 0-5$. It is clear from Fig. 3.7 that the photometric redshifts do broadly agree with the spectroscopic redshifts for these SMGs. Indeed, the average scatter in $\Delta z = z_{\text{spec}} - z_{\text{phot}}$ is -0.27 ± 0.21 . We note that the average scatter in Δz is smaller for the $z \leq 1.5$ SMGs ($\Delta z = -0.15 \pm 0.13$) than for the more distant sample ($\Delta z = -0.32 \pm 0.22$), demonstrating that when testing photometric redshifts of these galaxies it is important to consider a comparison sample with the same redshift

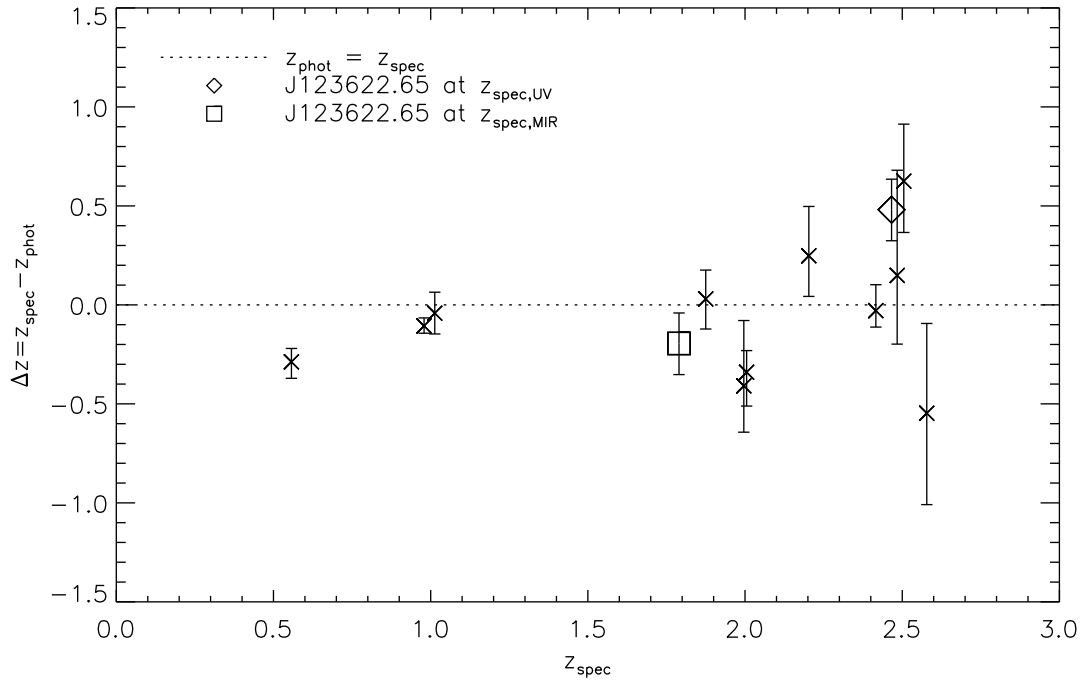


Figure 3.7: Spectroscopic versus photometric redshifts for Borys et al. (2005) SMGs. It is clear that the photometric redshifts broadly agree with the spectroscopic redshifts, and that they are sufficiently precise to allow the separation of typical high-redshift SMGs from the potential cluster population at low-redshifts. SMMJ 123622.65 has rest-frame UV/optical spectra with $z = 2.466$ (Chapman et al. 2005; Swinbank et al. 2004) but mid-infrared analysis places it at $z = 1.79 \pm 0.04$ (Pope et al. 2008), therefore, SMMJ 123622.65 is plotted at each redshift.

distribution as the population under study. We find that the HYPERZ quoted 68% confidence intervals for this sample typically underestimate the scatter and that the 99% error bars more realistically represent the 1σ limits on the redshifts. We interpret this as evidence that either there is some disparity between the models and the photometry or that the photometric errors are underestimated. Therefore, we quote the 99% confidence intervals throughout, with the understanding that these encompass the 1σ error range. We highlight that in Chapter 4 we find that for a larger sample of SMGs with 17-band photometry modified handling of Lyman- α absorption is required to remove a systematic bias in the photometric redshift of galaxies at $z \gtrsim 2$. However, this analysis was performed before that result, although in this Chapter we are interested in galaxies at $z \sim 0.5$, and not galaxies at $z \gtrsim 2$, so the exact choice of the strength of the Lyman- α absorption should not significantly affect our results.

Having established that photometric redshifts for SMGs can be reliable we next consider the effect of varying the parameters from the nominal case above to judge if these can improve the precision of the photometric redshifts. Firstly, we allow all the available star-formation histories: E, S0, Sa, Sb, Sc, Sd, Burst, and Im and we find that there is no significant change in the average Δz from when only the four nominal templates are included. When allowing all eight of the star-formation histories 10 of the 11 CDFN SMGs have best-fit templates of Burst and elliptical star-formation histories (with young ages), and one is best-fit by the Sa template. Since, only one of the SMGs is not best-fit by one of the four templates that were initially considered it is unsurprising that there is no gain in the reliability in the photometric redshifts by allowing more SED templates. If the available star-formation histories are restricted to only two – Burst and Im – we again find little change in the average Δz . We therefore find it unlikely that including additional stellar templates in the fitting procedure will improve the photometric redshift accuracy. Our results are also unchanged if we allow higher values of A_V , $A_V = 0-10$, or if we restrict to $A_V < 2.5$, although a tighter limit than this does affect the results and increases Δz .

AGN contamination at mid-infrared wavelengths, particularly in the $8\ \mu\text{m}$ filter, is a concern for SED modelling of SMGs (Hainline et al. 2009, 2010; Coppin et al. 2010b) yet the SED templates employed are based on pure stellar emission and do not include any AGN contribution. Therefore, in order to crudely assess the effect of AGN emission on the accuracy of our photometric redshifts we repeat the photometric redshift calculations as above but exclude the $8\ \mu\text{m}$ data from the analysis. For all the SMGs $\Delta z_{\text{no}8\mu\text{m}} \leq \Delta z_{\text{allbands}}$

yielding an average scatter $\Delta z = 0.23 \pm 0.22$ for the high redshift ($z > 1.5$) galaxies – consistent with the view that the $8\ \mu\text{m}$ fluxes are potentially contaminated (see also the SED plots in Hainline et al. 2010). In Chapter 4 we expand of this analysis and use the larger sample of LESS SMGs to further examine the effect of AGN on the accuracy of photometric redshifts of SMGs.

3.3.3.3 Photometric redshifts of the AzTEC galaxy sample

In this work we are interested in separating low redshift ($z \sim 0.5$; potential cluster members) from the typical high redshift ($z \sim 2$) SMG population. As we showed in § 3.3.3.2 this is possible based on the photometric redshift resolution so we next calculate the photometric redshifts of SMGs in MS 0451–03. As in § 3.3.3.2 we use HYPERZ to calculate the redshifts of the SMGs in the field of MS 0451–03 from our optical, near-infrared and mid-infrared photometry. The Bruzual & Charlot (1993) spectral templates included with HYPERZ are used and, as discussed in § 3.3.3.2, we consider only the Burst, Elliptical, Sb and constant star-formation rate (Im) models, limit reddening to $0 \leq A_V \leq 5$, and redshifts to $0 \leq z \leq 7$. Bright, resolved galaxies with uncharacteristically high primary photometric redshifts are considered to lie at the calculated secondary solutions.

The redshift estimate of each counterpart is presented in Table 3.4, and in Fig. 3.8 we show the SMG photometric redshifts versus AzTEC 1.1-mm fluxes. Although, most of the AzTEC sources are high redshift background galaxies, two – MMJ 045421.55 and MMJ 045431.35 – are possible cluster members, and are discussed further below. Our sample has a median photometric redshift of 1.2 and an interquartile range of $z = 0.6$ – 1.8 – lower than spectroscopic studies (e.g. $\langle z \rangle = 2.2$ Chapman et al. 2005) and our photometric analysis of SMGs in the ECDFS ($\langle z \rangle = 2.2 \pm 0.1$ Chapter 5). Similarly, the median photometric redshift for the sub-sample of 7 SMGs in the ECDFS with $870\ \mu\text{m}$ (for $S_\nu \sim \nu^{3.5}$) and radio or $24\text{-}\mu\text{m}$ fluxes sufficient to be detected in this survey of MS 0451–03 is $\langle z \rangle = 2.5 \pm 0.3$, suggesting that the brighter flux limits in this field are not the cause of the disparity in the redshift distributions. If we exclude the potential cluster members MMJ 045421.55 and MMJ 045431.35 from our analysis the median redshift of the field SMGs in this study is 1.6 and the interquartile range is $z = 1.1$ – 2.1 . We conclude that the cause of the lower median redshift of SMGs in MS 0451–03 compared to the ECDFS and Chapman et al. (2005) is likely to be that the SMGs with $z \gtrsim 2$ in MS 0451–03 have potentially underestimated photometric redshifts (see § 4.3.2 for details) and thus the results could be skewed. However, this study focuses on detected cluster-member SMGs

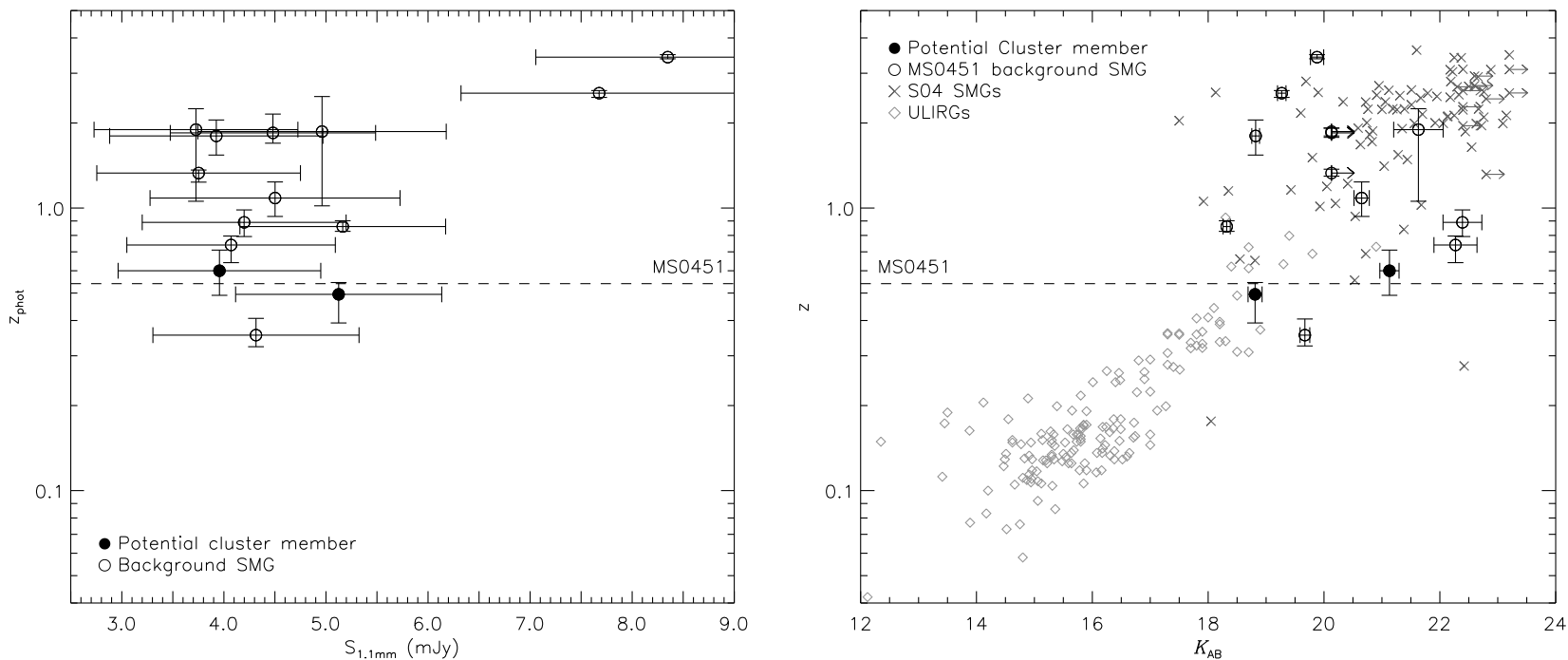


Figure 3.8: The left-hand panel shows photometric redshifts of SMGs against the 1.1 mm AzTEC fluxes. Two SMGs - MMJ045421.55 and MMJ045431.35 - have photometric redshifts consistent with being cluster members and are highlighted; we discuss these two sources in detail in §3.3.3.3. In the right-hand panel we show redshift versus K -band magnitudes of MS 0451–03 SMGs compared to the spectroscopic sample presented in Smail et al. (2004), and local ULIRGs from Kim et al. (2002) and Stanford et al. (2000). Both datasets occupy the same parameter space suggesting it is unlikely that any of our photometric redshifts are extreme outliers.

at $z = 0.54$, so any potential bias in the redshifts of SMGs at $z \gtrsim 2$ is not expected to affect our conclusions.

Although in § 3.3.3.2 we showed that the exclusion of $8\ \mu\text{m}$ information can sometimes improve the accuracy of photometric redshift estimates of SMGs, the redshifts reported in Table 3.4 include the $8\ \mu\text{m}$ photometry. This is because for the galaxies with only IRAC detections the resulting lack of information about the location of the $1.6\ \mu\text{m}$ stellar peak means that only weak redshift constraints are possible if we remove the $8\ \mu\text{m}$ photometry. Critically, the inclusion or exclusion of the $8\ \mu\text{m}$ information does not affect MMJ045421.55 and MMJ045431.35 which still both have photometric redshifts consistent with the cluster ($z = 0.54$).

In Fig. 3.6 we test our photometric redshifts by using the $B - z$ versus $z - K$ (BzK) selection criteria (Daddi et al. 2004), finding that both methods broadly agree. In Fig. 3.8 we show the redshifts and K -band magnitudes of MS 0451–03 SMGs in comparison to the spectroscopic sample of SMGs examined by Smail et al. (2004), and local ULIRGs from Kim et al. (2002) and Stanford et al. (2000). The apparent K -band magnitudes of our AzTEC sample are consistent with their estimated redshifts, when compared with spectroscopic SMG surveys and local ULIRGs, suggesting that our photometric redshifts are reasonable. The general agreement between our photometric redshift analysis, BzK and K -band magnitudes supports the derived redshifts of the AzTEC sources.

The potential cluster members, MMJ045421.55 and MMJ045431.35, are discussed in detail here. The other identified SMGs are examined in Appendix 3.5.

MMJ 045421.55 MMJ045421.55 is identified through radio emission 2.2 arcsec from the AzTEC centroid, which lies between two optical galaxies (2.1 and 1.6 arcsec from the northern (C1) and southern (C2) galaxies, respectively). There is also an IRAC source at the location of the radio emission, which appears slightly extended towards C2 (Fig. 3.9). The three possible explanations for this system are: C1 and C2 are interacting and both millimetre bright; C2 is the millimetre counterpart; or neither C1 nor C2 are responsible for the millimetre emission. Each of these possibilities is discussed below.

Individual photometric analysis of C1 and C2 (excluding the IRAC information) suggests that they are both potential cluster members, and with a separation of 2.6 arcsec - corresponding to ~ 17 kpc at $z = 0.54$ - they could be in the early stages of a merger. Although high-resolution (0.1 arcsec) archival *HST* F814W imaging shows no evidence of disturbance (Fig. 3.9), the expected tidal tails can be low surface brightness features,

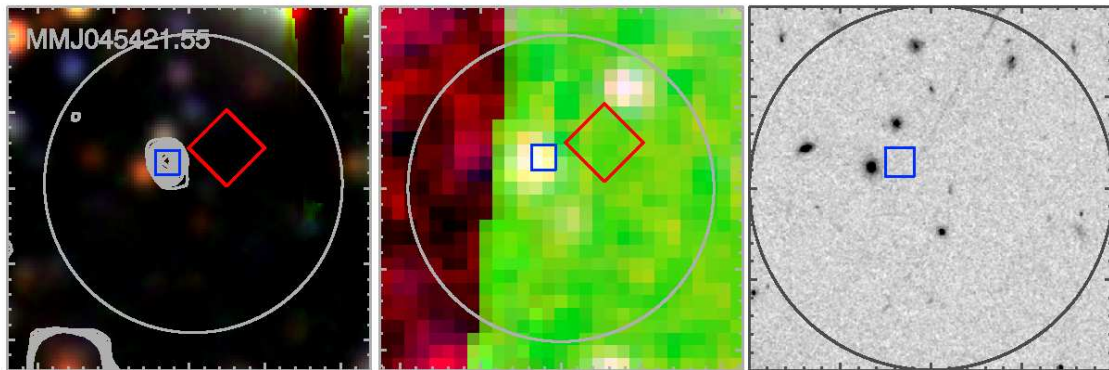


Figure 3.9: Images of the potential cluster SMG MMJ 045421.55; north is up and east is to the left. The left-hand and central panels are $25 \times 25''$, and the right-hand panel is $20 \times 20''$; radio contours are shown on the left-hand panel. The circle is $20''$ in diameter and centered on the AzTEC position; the square is the radio counterpart and the diamond shows the location of the $24\text{-}\mu\text{m}$ identification. C1 and C2 are visible to the north and east of the radio counterpart, respectively in the optical and *HST* images.

making them difficult to detect. Such interactions are widely known to trigger dusty starbursts in which the radio emission appears to be located between the optical nuclei (e.g. systems similar to VV 114; Frayer et al. 1999; Le Floch et al. 2002; Iono et al. 2004).

With the aim of measuring redshifts we targeted C1 and C2 with the ISIS long-slit spectrograph on the WHT during service time in 2009 February. The total integration time was one hour in $\sigma = 1.1\text{-arcsec}$ seeing and standard reduction techniques were employed. A faint continuum was observed (the two targets are blended), but no features suitable for redshift measurement were detectable. A possible faint ($\sim 2\sigma$) emission feature at 7852 \AA is visible, which, if real, is most likely to be [OIII] $\lambda 5007 \text{ \AA}$ at $z = 0.568$ – placing the galaxy in a small group that is known to exist just behind the cluster. However, the feature is tentative.

On the assumption that C1 and C2 lie at the same redshift, and that the millimetre, radio and IRAC fluxes are emitted from a merging system as described above, we combine the optical fluxes from C1 and C2. The optical to near-infrared photometric redshift of the whole system is $z = 0.50^{+0.05}_{-0.10}$ which, as shown in Fig. 3.8, agrees with the z versus K ULIRG trend. Therefore, if C1 and C2 are an interacting system, MMJ 045421.55 a possible cluster member.

The radio counterpart lies only 2.6σ from C2 (compared to 3.5σ from C1), and the

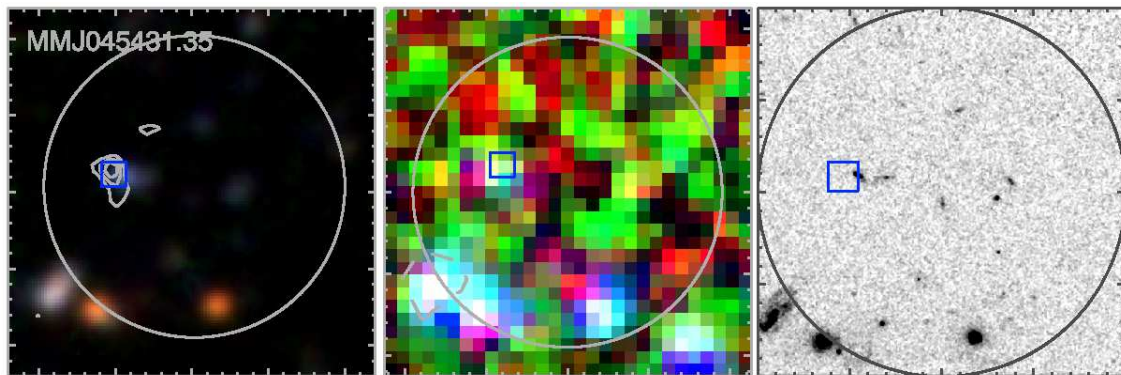


Figure 3.10: Images of the potential cluster SMG MMJ045431.35; layout and symbols as in Fig 3.9. Two, apparently merging, galaxies are resolved in the *HST* image and we suggest this interaction triggered a dusty starburst and consequently the millimetre emission.

IRAC emission of MMJ 045421.55 appears extended towards C2. Therefore, in the situation where C1 and C2 are unassociated we find it most likely that the C2 is the counterpart to the IRAC, radio and millimetre flux. In this case we obtain a photometric redshift of $z = 0.51^{+0.07}_{-0.05}$ – once again placing MMJ 045421.55 in the redshift range of MS 0451–03.

Based on the intrinsic faintness of many SMG counterparts it is feasible that the identified radio and IRAC emission arises from an optically faint background galaxy, unrelated to C1 and C2, and undetectable in our observations. Previous SMG surveys have confused low redshift galaxies with the source of sub-mm emission due to the lensing of the background source (e.g. Chapman et al. 2002). In these situations it is only possible to distinguish between a lensed background galaxy and a foreground cluster member through the detection of the faint optical counterpart in deeper imaging, or by the detection of CO emission lines.

MMJ 045431.35 The counterpart to MMJ 045431.35 is securely identified 5.4 arcsec from the AzTEC centroid through its radio emission. The source is detected in all our *Spitzer* and ground-based imaging and resolved in the *HST* F814W image into merging galaxies with centroids separated by ~ 1.6 arcsec (~ 10 kpc at $z = 0.54$) and tidal tails between them (Fig. 3.10). We suggest that a dusty starburst triggered by the interaction between the two galaxies is causing the millimetre emission from this system. The photometric redshift is calculated as $z = 0.60 \pm 0.11$, making MMJ045431.35 a possible cluster member.

If MMJ 045421.55 and MMJ 045431.35 are cluster members at $z = 0.54$ SED-fitting suggests they each have $L_{\text{FIR}} \sim 5 \times 10^{11} L_{\odot}$ and thus $\text{SFR} \sim 50 M_{\odot} \text{yr}^{-1}$. We also find that they are colder than typical $z \sim 2$ SMGs, with dust temperatures of $T_d = 15 \pm 4$ K (for $\beta = 1.5$), or $T_d = 30 \pm 5$ K (for $\beta = 1.1$), compared to $T_d \sim 40$ K and $\beta = 1.5$ for archetypal SMGs. Such properties are not unprecedented – both the spectroscopic survey of SMGs by Chapman et al. (2005), and our photometric survey of the SMGs in the ECDFS (Chapter 5) contain examples of sources with equivalent millimetre-to-radio flux ratios at $z \sim 0.5$, suggestive of galaxies containing cold dust. Similarly, in the SCUBA Local Universe Galaxy Survey (SLUGS) Dunne et al. (2000) surveyed local *IRAS*-bright galaxies with SCUBA at $850 \mu\text{m}$ and utilised the combined *IRAS* and SCUBA photometry for SED fitting. This sample of local galaxies has average $T_d = 35.6 \pm 4.9$ K, and $\beta = 1.3 \pm 0.2$. Indeed, cold low-redshift galaxies are easier to detect at $850 \mu\text{m}$ or 1.1-mm than their hotter counterparts. This is because colder dust produces emission which peaks at longer wavelengths than hot dust (Blain et al. 2002). Therefore, we do not find it unreasonable that one or both of MMJ 045421.55 and MMJ 045431.35 are cluster members at $z = 0.54$ with $T_d \sim 30$ K and $\beta = 1.1$.

If both MMJ 045421.55 and MMJ 045431.35 are members of MS 0451–03, their combined SFR is $\sim 100 M_{\odot} \text{yr}^{-1}$ – a significant fraction of the SFR of all the cluster galaxies within 2 Mpc ($200 \pm 100 M_{\odot} \text{yr}^{-1}$; Geach et al. 2006) MMJ 045431.35 lies ~ 2.6 Mpc from the cluster centre (about half of the turnaround radius), but MMJ 045421.55 is much closer to the centre: ~ 1 Mpc in projection. Notably, both of these systems are possible interacting pairs. Although not conclusive, if they are both cluster members, this suggests that the galaxy pairs could have been accreted into the cluster – suggesting that accreted galaxies can retain their gas reserves during infall into clusters (Geach et al. 2009).

3.3.4 Cluster and field SEDs

To better test the evolution of the star-forming population in galaxy clusters in relation to a growing passive population (e.g. Chapter 2) we also investigate obscured star-formation of the general galaxy population in MS 0451–03. We can study galaxies that are below the flux limit of our AzTEC map by stacking fluxes at the positions of known cluster galaxies. Optical galaxies in MS 0451–03 were morphologically classified by Moran et al. (2007a) using the scheme defined by Abraham et al. (1996), which we group into 148 early-types and 167 late-types for this analysis. We also define a mid-infrared sample

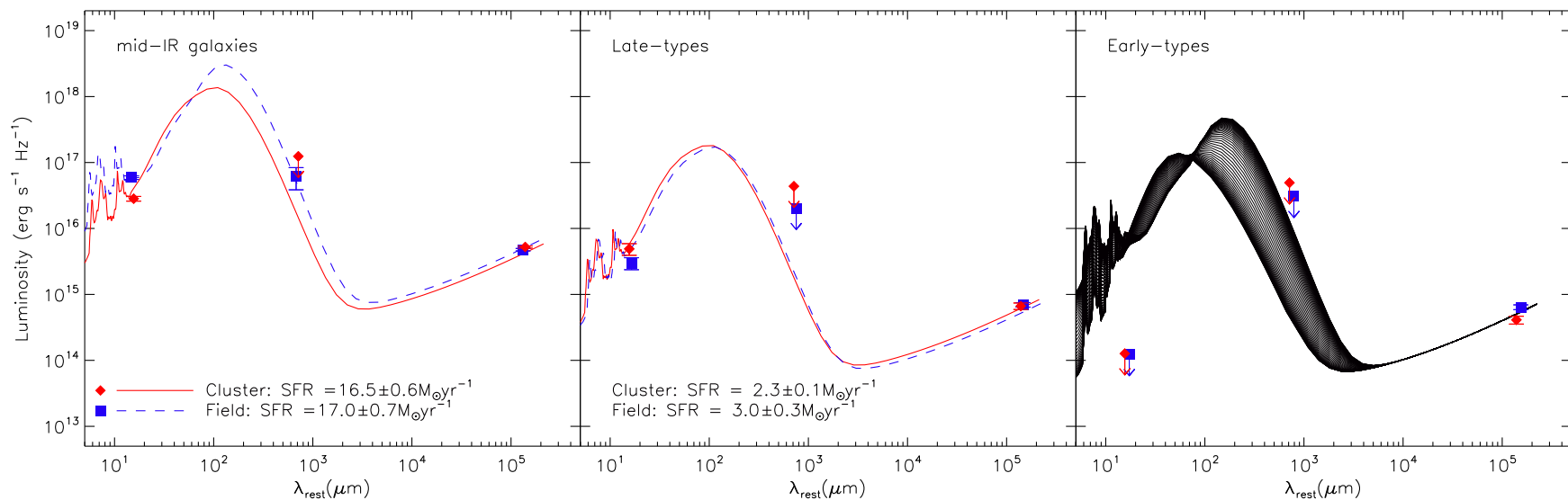


Figure 3.11: Clipped weighted-average SEDs of the $24\mu\text{m}$, late- and early-type populations of MS 0451–03 and the field. In the case of non-detections the 3σ noise limit is marked by arrows. The field populations are shown at their mean redshifts of 0.58, 0.46, and 0.39 for the mid-infrared galaxies, late- and early-types and respectively. We also show the best-fitting SEDs and corresponding SFRs (Kennicutt 1998) from Dale & Helou (2002) for the mid-infrared and late-type galaxies; since the early-type populations are only detected at 1.4 GHz we cannot select one best-fitting SED and instead display all the Dale & Helou (2002) SEDs on this panel. Although the observed populations have similar activity levels, in the late-type galaxies this is due to the flux limits of our observations and the different luminosity distances between the samples. If the cluster and field late-type populations were equivalent, the cluster should have $\text{SFR} \sim 3$ times higher than observed. We deduce that the cluster environment has caused a reduction in the SFR of this population, and that these galaxies are probably in the process of transformation onto the red-sequence, similarly to those discussed in Chapter 2.

Table 3.5: Parameters and results of stacking on known cluster and field galaxies in the 24 μm , 1.1 mm and 1.4 GHz maps. SFRs are based on SED fits, except for the early-type galaxies, which are based purely on 24 μm detection limits. Non-detections are represented by 3σ limits. Since the samples are flux limited and have various median redshifts we also present the expected observed SFR of the field mid-infrared and late-type samples were they to have $z_{\text{median}} = 0.54$ (§3.3.4). Differences between this value and the observed cluster SFR for the late-type galaxies suggests that the cluster late-type population is less active than the field late-type population.

Population	$N_{24\mu\text{m}}^a$	$S_{24\mu\text{m}}^b$	$N_{1.1\text{mm}}^a$	$S_{1.1\text{mm}}^b$	$N_{1.4\text{GHz}}^a$	$S_{1.4\text{GHz}}^b$	z_{median}	SFR	SFR
		(μJy)		(μJy)		(μJy)		($M_{\odot}\text{yr}^{-1}$)	($M_{\odot}\text{yr}^{-1}$)
									($z = 0.54$)
Cluster mid-IR galaxies	14	222 ± 18	14	< 970	15	41.1 ± 1.6	0.54	16.5 ± 0.6	16.5 ± 0.6
Field mid-IR galaxies	84	331 ± 21	94	340 ± 130	89	26.8 ± 1.1	0.58	17.0 ± 0.7	12.6 ± 2.8
Cluster late-type	167	38.4 ± 7.7	131	< 340	162	5.2 ± 0.6	0.54	2.3 ± 0.1	2.3 ± 0.1
Field late-type	315	34.4 ± 7.1	309	< 230	355	8.0 ± 0.6	0.46	3.0 ± 0.3	7.8 ± 1.1
Cluster early-type	148	< 1.0	106	< 390	144	3.2 ± 0.4	0.54	< 0.07	< 0.07
Field early-type	35	< 2.1	32	< 530	40	10.9 ± 0.9	0.28	< 0.03	< 0.19

^aThe number of galaxies used in the stacking – excluding those close to the edge, off-image, or near detected sources

^bClipped weighted-average flux

of 14 galaxies which are bright at $24\ \mu\text{m}$, based on the catalogue of Geach et al. (2006) with $S_{24\mu\text{m}} \geq 200\ \mu\text{Jy}$. To reduce contamination we consider only those galaxies with spectroscopic redshifts and to search for environmental dependencies we also examine spectroscopically identified field galaxies. The cluster members are required to have $0.52 < z < 0.56$ and the field population is outside this window. The field samples have median redshifts of 0.58, 0.46, and 0.28 with interquartile ranges of $z = 0.33\text{--}0.82$, $0.26\text{--}0.62$, and $0.20\text{--}0.51$ for the 84 mid-infrared galaxies, 315 late-types and 35 early-types respectively. For each of these six samples we stack the MIPS $24\ \mu\text{m}$, AzTEC 1.1 mm and VLA 1.4GHz fluxes. We note that the galaxy samples are optical magnitude limited due to the requirement for a spectroscopic redshift. Therefore, the stacked SEDs may not be representative of the entire population, in particular the most obscured galaxies are likely to fall below the optical magnitude limit. However, we expect such selection effects to equally affect the cluster and field samples allowing us to compare populations between the two environments.

Any galaxies within 9 arcsec (the radius of the AzTEC beam) of an AzTEC map pixel with $S/N \geq \pm 3.5$ are removed prior to stacking the AzTEC map. The contribution from each AzTEC-faint galaxy is weighted by the inverse of the squared noise at that pixel to calculate the weighted mean 1.1-mm flux of each population. Similarly we calculate the clipped weighted mean radio flux of each sample using our 1.4 GHz VLA map, correcting for bandwidth smearing, and also stack $24\ \mu\text{m}$ emission in the same way. The results of the stacking are given in Table 3.5 and the SEDs are presented in Fig. 3.11.

We fit the mid-infrared and late-type galaxies with template SEDs from Dale & Helou (2002) and calculate the corresponding SFRs based on the far-infrared luminosity (Kennicutt 1998). Mid-infrared cluster galaxies without bright AzTEC counterparts have $\text{SFR} = 16.5 \pm 0.6\ \text{M}_{\odot}\text{yr}^{-1}$ which is consistent the SFR estimate of $17.0 \pm 0.7\ \text{M}_{\odot}\text{yr}^{-1}$ for the mid-infrared field population. In contrast, the late-type galaxies in the field have $\text{SFR} = 3.0 \pm 0.3\ \text{M}_{\odot}\text{yr}^{-1}$, compared to $\text{SFR} = 2.3 \pm 0.1\ \text{M}_{\odot}\text{yr}^{-1}$ in the cluster. Both cluster and field early-type populations are undetected at 1.1 mm and $24\ \mu\text{m}$ and SED fitting to the $24\ \mu\text{m}$ limits suggest, on average, $\text{SFR} < 0.06\ \text{M}_{\odot}\text{yr}^{-1}$.

Since our samples are flux limited, the different redshift distributions will affect the derived SFR. The extent of this effect on our results is tested by calculating an observed SFR for each sample by fitting templates with $S_{24\mu\text{m}} = 200\ \mu\text{Jy}$ at the redshift of the galaxies included in the stacks. Due to the generally higher redshift of the field sample, we find that identical mid-infrared populations would be observed with $\text{SFR} = 0.74 \pm 0.16$

times lower in the cluster than the field. In fact the stacked cluster population is observed with SFR 0.97 ± 0.05 times lower than the field population, therefore, to within $\sim 1\sigma$ the mid-infrared samples are consistent. However, the equivalent test for late-type galaxies, where the field sample is, on average, lower redshift, suggests that, due to the different luminosity distance, identical populations in our analysis would appear 2.6 times more active in the cluster than in the field. In fact, the cluster late-type galaxies are less active than the field. Therefore, the cluster environment is suppressing star-formation activity in the late-type population, transforming galaxies onto the CMR as studied in Chapter 2.

Geach et al. (2006) estimated the total SFR within 2 Mpc of the core of MS 0451–03 as $200 \pm 100 M_{\odot}\text{yr}^{-1}$, based on converting 24 μm fluxes of colour-selected 24- μm detected galaxies to total IR luminosities with the *average* SED from Dale & Helou (2002). Our analysis presented in this paper includes radio and 1.1 mm data enabling us to better characterise the cluster populations, and by stacking we can probe a fainter population. Within 2 Mpc of cluster core we calculate $\text{SFR}_{>} 315 \pm 50 M_{\odot}\text{yr}^{-1}$ from the spectroscopically confirmed mid-infrared and late-type galaxies. To this we can then add $50 M_{\odot}\text{yr}^{-1}$ for MMJ 045421.55, the potential ULIRG within 2 Mpc of the cluster core.

3.4 Conclusions

In this study we have investigated the dust-obscured star-forming population of the galaxy cluster MS 0451–03; we utilise 1.1-mm observations to study obscured star-formation in MS 0451–03. We present a $\sigma \sim 1.1$ mJy AzTEC map of the central 0.1 deg^2 of MS 0451–03, within which 36 sources are detected at $S/N \geq 3.5$. We use radio, 24 μm , IRAC and SMA observations to precisely locate 18 of these SMGs.

We calculate the reliability of photometric redshifts for SMGs and find that they are able to remove the bulk of background contamination, We then use photometric redshifts to isolate potential cluster members using our optical, near- and mid-infrared photometry. Based on these redshifts we find two SMGs which are possible cluster members: MMJ 045421.55 and MMJ 045431.35. These systems are both resolved into close pairs of galaxies by our ground-based and *HST* imaging, suggesting that interactions have triggered their starbursts. If they are cluster members both of these SMGs contain cold dust with $T_d \sim 30$ K, for $\beta = 1.1$ (similar to SLUGS galaxies; Dunne et al. 2000) and have SFRs of $\sim 50 M_{\odot}\text{yr}^{-1}$ each, and will likely transform onto the cluster red-sequence as the starburst extinguishes.

Geach et al. (2006) compared obscured activity, based on 24 μ m emission, in MS 0451–03 and C10024+16 at $z = 0.39$, and found that C10024+16 has SFR ~ 5 times that of MS 0451–03 within 2 Mpc of the clusters centres. They show that, taking into account the slightly different redshifts and masses of these two structures, MS 0451–03 is underactive and C10024+16 overactive at 24 μ m. Therefore, it is likely the other galaxy clusters, including C10024+16, could contain ULIRGs in significantly larger numbers than we find in MS 0451–03. Indeed, since this work was undertaken BLAST (Braglia et al. 2010) and *Herschel* (Haines et al. 2010; Pereira et al. 2010; Rawle et al. 2010; Smith et al. 2010) observations at 100–500 μ m of clusters at $z \sim 0.1$ –0.3 have been published. All the clusters contain spectroscopically confirmed members that are bright at 100–500 μ m, although due to the shorter wavelength selection not all are LIRGs or ULIRGs. Indeed the majority appear to be late-type spirals and the remaining significant fraction are dusty red galaxies (Haines et al. 2010). It is suggested that the majority of the submillimetre-bright galaxies are located in the cluster outskirts, or in groups of infalling galaxies (Pereira et al. 2010).

To further investigate the obscured star-forming population which lies below the limit of our AzTEC observations we create composite SEDs of spectroscopically confirmed mid-infrared, early- and late-type cluster members and compare them to the corresponding field populations. As expected we find that both early-type populations are undetected at both 24 μ m and 1.1 mm and so are unlikely to be actively forming large numbers of stars ($< 0.1 M_{\odot}\text{yr}^{-1}$). The 24 μ m galaxies are significantly more active than the morphologically classified late-types with SFRs $\sim 15 M_{\odot}\text{yr}^{-1}$ versus $\sim 3 M_{\odot}\text{yr}^{-1}$ on average, although the late-type galaxies are more numerous and therefore overall represent a higher fraction of the clusters SFR. The typical brightness of these 24- μ m and late-type galaxies suggests that by $z \sim 0.2$ they could fade and transform into the red-sequence galaxies studied in Chapter 2. We find that the star-formation activity in the cluster late-type population, compared to a redshift-matched field population is quenched and ~ 3 times lower than expected. Mid-infrared galaxies do not show this trend suggesting the more intense activity in these systems is more robust to environmental influences. We find that the total SFR $> 315 \pm 50 M_{\odot}\text{yr}^{-1}$ in the central 2 Mpc of MS 0451–03. However, if MMJ 045421.55 is a cluster member it has SFR $\sim 50 M_{\odot}\text{yr}^{-1}$ and lies 1 Mpc from the cluster centre, taking the total SFR within 2 Mpc to $\gtrsim 360 M_{\odot}\text{yr}^{-1}$.

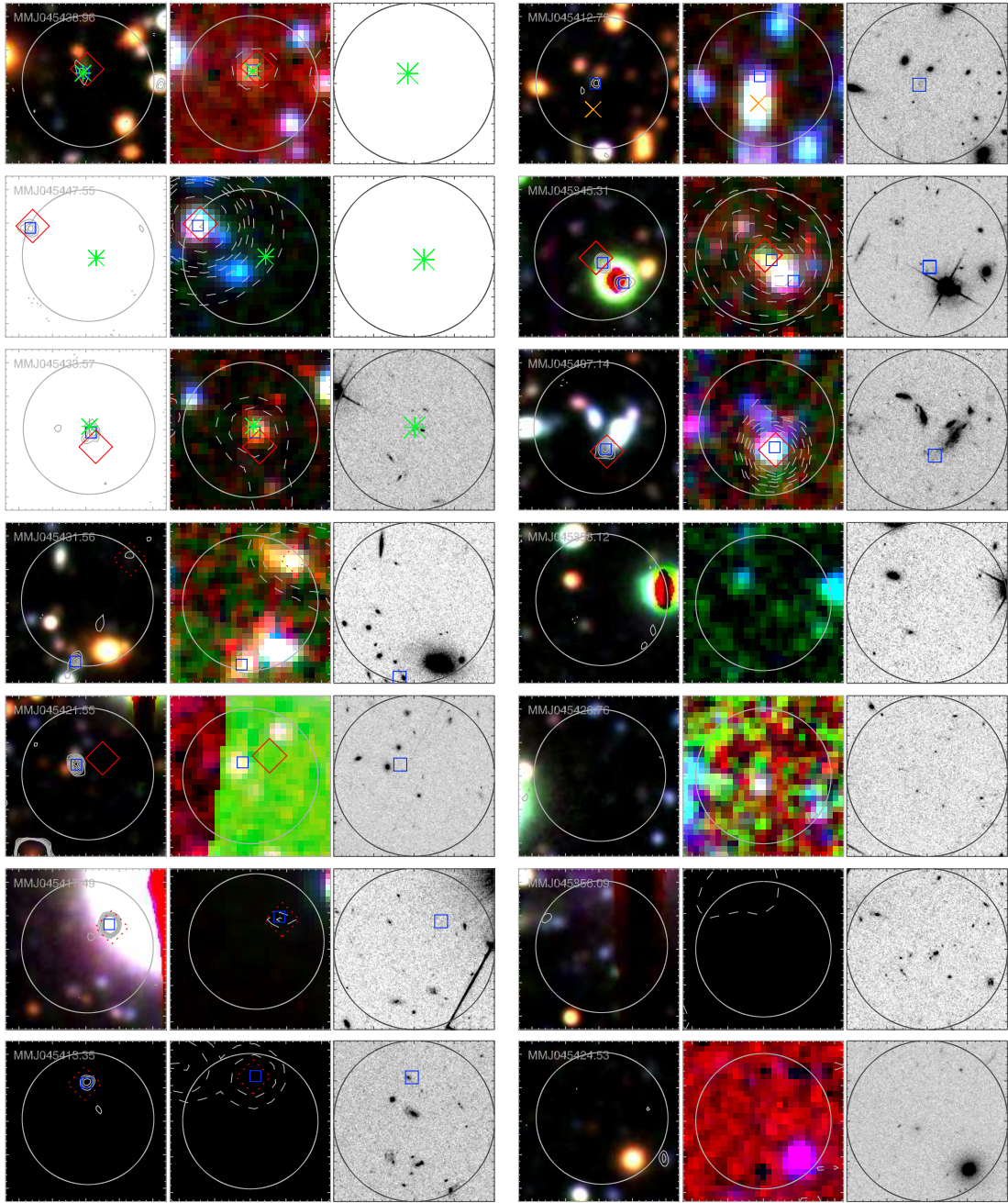
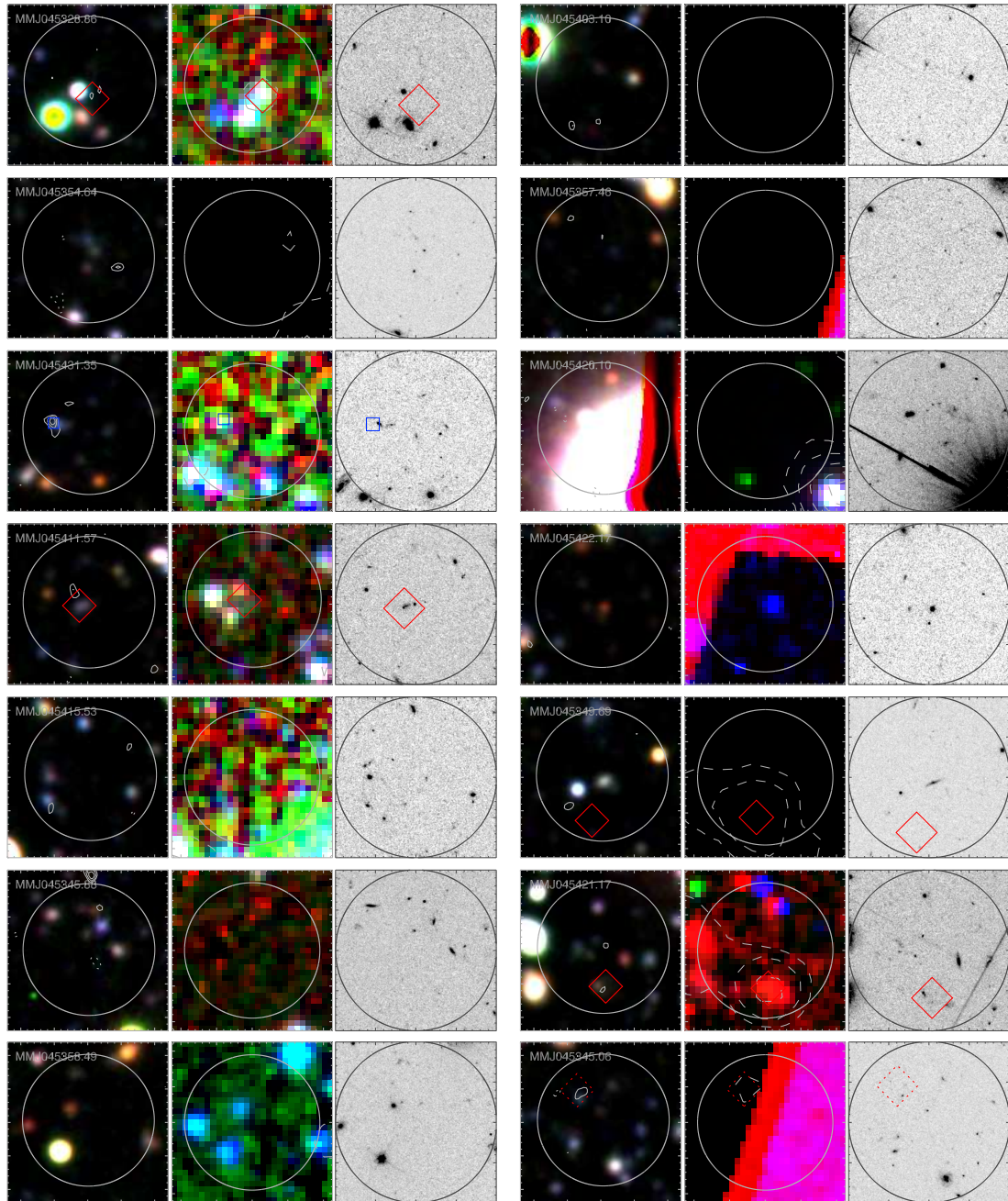
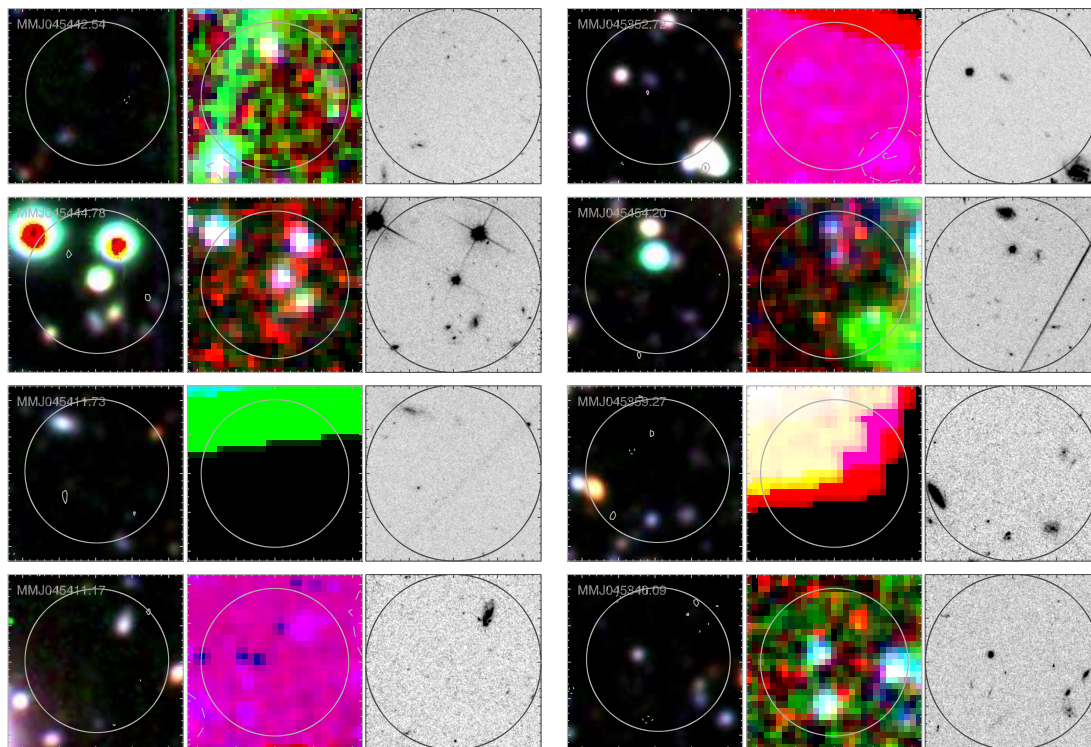


Figure 3.12: 25×25 arcsec images centred on each AzTEC galaxy are shown in the left-hand and middle panels; north is up and east is to the left. In the left-hand panel we show Subaru data: BVR colour images with solid radio contours at -3 (dotted), $3, 4, 5, 6, 7, 8, 9, 10 \times \sigma$ are overlaid. The middle panel contains true-colour images containing the IRAC $3.6 + 4.5$ (blue), 5.8 (green) and $8.0 \mu\text{m}$ (red) data; dashed contours present $24 \mu\text{m}$ flux at $5, 10, 20, 30, 40, 50, 100, 200, \dots, 1000 \times \mu\text{Jy}$ per pixel and the right-hand panel contains 20×20 arcsec *HST* F814W cutouts centered at the AzTEC position. In all images circles are centred on the AzTEC positions and have 20 arcsec diameter, corresponding to our radio and mid-infrared search radius. $24 \mu\text{m}$ and radio counterparts are highlighted with diamonds and squares respectively; dotted symbols represent tentative counterparts (with $0.05 < p \leq 0.10$) and the sizes of the symbols are representative of the typical astrometric errors of these data. We mark the positions of SMA detected sources with stars and X-ray sources (Molnar et al. 2002) with crosses.

Figure 3.12: – *continued*

Figure 3.12: – *continued*

3.5 Appendix: Notes on Individual Sources

In Fig. 3.12 we present images centered on each AzTEC source, in order of decreasing S/N. We show Subaru and IRAC colour, and *HST* images, with radio and 24 μm contours. Identified galaxies are labelled and discussed below.

1. MMJ 045438.96: SMA observations of this galaxy confirm the identified radio and 24- μm counterparts. The corresponding red optical and IRAC source at $z_{\text{phot}} = 3.42^{+0.07}_{-0.05}$ has a disturbed morphology in the *HST* image.

2. MMJ 045447.55: This galaxy has been located with the SMA but does not have any radio or 24 μm counterparts, or optical or IRAC galaxies at the SMA position. Therefore, MMJ0455447.57 could be one of a population of very distant SMGs, or be much cooler and more obscured than typical SMGs. In Chapter 5 we use SMGs in the ECDFS and the large number of sources with photometric redshifts in this field to statistically investigate the redshift distribution of unidentified SMGs, such as MMJ 045447.55.

3. MMJ 045433.57: SMA observations confirm the identified radio and 24- μm counterparts, corresponding to an optically faint but near-infrared bright galaxy with $z_{\text{phot}} = 2.55^{+0.06}_{-0.09}$. The *HST* image shows three components to this system, and their interaction is the likely cause of the ULIRG.

4. MMJ 045431.56: There is a robust extended radio counterpart 9.5 arcsec from the 1.1 mm centroid, which also corresponds to faint 24- μ m emission and the coincident red galaxy is at $z_{\text{phot}} = 0.86^{+0.04}_{-0.03}$. The *HST* image of this region shows a galaxy with a bright core and a low surface-brightness tail or edge-on spiral arm. However, the picture of this SMG is complicated by the presence of a statistically tentative 24- μ m counterpart 9.1 arcsec from the 1.1 mm centroid which is unassociated with the aforementioned radio emission. The 24 μ m position is coincident with an extended red IRAC galaxy, which is undetected in the optical. Further complexity arises from the SMA observation; MMJ045431.56 was targeted but not formally detected. However, the SMA data does contain two potential sources. One is close to an extended $\sim 3\sigma$ peak in the radio map and ~ 3.7 arcsec from the AzTEC centroid and unassociated with either the radio or 24 μ m counterparts previously discussed. There also appears to be red IRAC emission at this position, which may be from a nearby elliptical, but the geometry suggests that it is more likely to originate from one or both of two optical galaxies, which are unresolved in the *HST* image. The other potential SMA source is ~ 5 arcsec from the tentative 24- μ m counterpart and is coincident with part of the extended IRAC source at this position. The true origin of millimetre flux from MMJ045431.56 will likely only be identified in deeper interferometric (sub-)millimetre data than is currently available.

5. MMJ 045421.55: We find reliable coincident radio and 24 μ m counterparts, corresponding to two optical galaxies separated by 2.6 arcsec, which are possible interacting cluster members ($z_{\text{phot}} = 0.50^{+0.05}_{-0.10}$). The system is discussed in detail in §3.3.3.3.

6. MMJ 045417.49: Both 24- μ m and strong radio counterparts are detected although the presence of a nearby, bright star prevents optical and near-infrared study. Although the stellar halo is less extended in the *HST* image no counterpart is visible.

7. MMJ 045413.35: The radio and 24 μ m identification agrees with a 2–3 σ peak in the 890 μ m ‘dirty’ SMA map. Unfortunately this source lies outside of the IRAC and much of the ground-based optical coverage, although a galaxy is detected in the *U*-band and *HST* imaging, indicating that it is at $z \lesssim 3$.

8. MMJ 045412.72: This source is potentially part of the gravitationally lensed arc from Borys et al. (2004). Our optical imaging is too shallow to detect the ERO discussed in Borys et al. (2004), but radio and extended IRAC emission betrays the likely counterpart.

9. MMJ 045345.31: There are two secure radio and one 24 μ m counterparts. One of the radio galaxies corresponds to the 24 μ m position. The IRAC source is blended with

the emission from an optically saturated star making further conclusions difficult. It is unclear whether the one of the radio counterparts is actually emission from the star, or a background source.

10. MMJ 045407.14: We find coincident robust radio and 24 μm counterparts which are located in a red region at the edge of a bright, resolved galaxy which appears disturbed in the *HST* image and has $z_{\text{phot}} = 0.35^{+0.05}_{-0.03}$. The morphology of the galaxy suggests that a merger has triggered a dusty starburst region, causing the millimetre emission. The large size and optical brightness support the low redshift of this galaxy, although if the photometric redshift errors are underestimated it could potentially be a cluster member. Similarly, it is also possible that a background galaxy that is unrelated to the foreground galaxy is the source of the millimetre emission. The detection of CO emission lines is required to confirm either scenario.

12. MMJ 045426.76: There are no radio or 24- μm counterparts identified. However, an IRAC galaxy has colours consistent with those of SMGs.

15. MMJ 045328.86: A 24 μm counterpart is detected 3.8 arcsec from the AzTEC position, corresponding to an IRAC source, but there is no detectable optical flux. The IRAC photometry yields $z_{\text{phot}} = 1.87^{+0.62}_{-0.85}$. There is coincident faint radio emission ($\sim 3\sigma$) at the position of the 24 μm counterpart, increasing the likelihood that this is the correct identification.

17. MMJ 045431.35: A radio counterpart 4.8 arcsec from the AzTEC position coincides with a pair of merging galaxies which are resolved in the *HST* image and have $z_{\text{phot}} = 0.60 \pm 0.11$; this possible cluster ULIRG is discussed further in §3.3.3.3.

18. MMJ 045411.57: 24- μm emission betrays the source of the millimetre emission as a galaxy with $z_{\text{phot}} = 0.74^{+0.06}_{-0.11}$. This 24- μm source is resolved in the *HST* image as an interacting pair, separated by < 1 arcsec. The photometric redshift includes IRAC photometry from a red source with coincident radio emission that is ($\sim 3\sigma$) ~ 2.3 arcsec to the northeast of the 24 μm identification, although it is possible that the radio and IRAC source is unrelated to the optical emission, in this case we can only constrain the redshift to $z_{\text{phot}} > 1.14$.

26. MMJ 045349.69: A faint optical galaxy with $z_{\text{phot}} = 1.33^{+0.03}_{-0.10}$ corresponds to the robust 24- μm counterpart. The galaxy is undetected by *HST* and the region is not covered by our IRAC mosaic.

27. MMJ 045421.17: The 24- μm counterpart is coincident with both faint radio emission and a faint red galaxy at $z_{\text{phot}} = 1.80^{+0.25}_{-0.26}$, which the *HST* imaging resolves into a

bright nuclear region and some extended emission.

28. MMJ 045345.06: The galaxy is tentatively identified through its 24- μm emission, which is coincident with faint radio flux; our IRAC mosaic does not cover the counterpart, but optical and near-infrared photometry yields $z_{\text{phot}} = 1.89^{+0.35}_{-0.84}$.

29. MMJ 045442.54: Although there are no radio or 24- μm counterparts MMJ 045442.54 is identified from its unusual IRAC colours and the photometry of the corresponding faint galaxy yields $z_{\text{phot}} = 1.09 \pm 0.15$.

30. MMJ 045444.75: This SMG does not have any formal counterparts and is not included in the analysis in this work. However, based on the IRAC selection that is derived and verified in Chapter 4 (see also Biggs et al. 2010), there is a $> 90\%$ probability that the red optical galaxy $\sim 4.5''$ to the south-west of the AzTEC centroid is the likely counterpart.

Chapter 4

Calculating the photometric redshifts of SMGs

4.1 Introduction

In Chapters 5 and 6 we investigate the redshift distribution, star-formation evolution and clustering of dusty starburst galaxies that are identified through their submillimetre emission (termed submillimetre galaxies; SMGs). To be able to thoroughly and accurately investigate such properties a measure of their redshifts is required. However, as discussed in Chapter 3 SMGs contain significant quantities of dust, which reprocesses the emission from their starbursts and thus causes their characteristic large far-infrared luminosities, and simultaneously obscures the UV, optical and near-infrared light, making measuring the spectroscopic redshifts of SMGs challenging and expensive (e.g. Barger et al. 1999; Chapman et al. 2005). In place of spectroscopic redshifts various photometric techniques have been employed, including submillimetre-to-radio flux ratios (e.g. Carilli & Yun 1999; Smail et al. 2000; Ivison et al. 2004, 2007; Aretxaga et al. 2007; Biggs et al. 2010) and optical/near-infrared photometric redshifts (e.g. Chapter 3 Pope et al. 2005; Clements et al. 2008; Dye et al. 2008). However, redshifts inferred from submillimetre-to-radio flux ratios are unreliable because redshift and dust temperature are degenerate in submillimetre-to-radio flux ratio (Blain et al. 1999), and as we show in Chapter 5, this leads to significant errors on the derived redshifts. For this reason we focus here on the use of optical/near-infrared photometric redshifts.

Typically studies of SMGs do not have both spectroscopic and photometric information (e.g. Hainline et al. 2010) so the photometric redshifts of SMGs have not been

extensively tested. Often results from optical and near-infrared SED fitting codes, such as HYPERZ (Bolzonella et al. 2000a) and IMPZ (Babbedge et al. 2004), are compared to those from other, apparently cruder, methods of redshift estimation – such as the radio to far-infrared -(sub)-mm spectral indices (e.g. Carilli & Yun 1999; Yun & Carilli 2002; Aretxaga et al. 2003; Clements et al. 2008). There are two main problems with this approach – firstly, the comparison is made with a set of results which themselves are not known to be correct, and secondly, the errors on the comparison redshifts are typically large, such that a general agreement can be confirmed but nothing more. In cases where spectroscopic information has been obtained for a sub-sample of galaxies, typically the samples are small (e.g. Chapter 3; Dye et al. 2008), or the SMGs lie at unusually low redshifts (e.g. Pope et al. 2005).

In this Chapter we expand on our analyses in Chapter 3 to further test and refine photometric redshift estimates of SMGs. We test the photometric redshifts on a sample of 30 SMGs detected in an 870- μm survey of the ECDFS that have spectroscopic redshifts and then apply the same methods to derive photometric redshifts for SMGs from the same survey for which spectroscopic redshifts are currently unavailable. The ECDFS has deep 17-band photometry, so in addition to being a larger sample than that in Chapter 3, this sample has significantly more photometric information available for SED fitting. As in Chapter 3 we employ the HYPERZ photometric redshift code and investigate the optimum input parameters for the reliable determination of photometric redshifts of SMGs. In Chapters 5 and 6 we use the photometric redshifts derived in this Chapter to investigate the properties of SMGs detected in an 870- μm survey of the ECDFS.

The layout of this Chapter is as follows: in § 4.2 we introduce the sample and available data. In § 4.3 we determine the most reliable parameters for photometric redshift estimation of SMGs and calculate the photometric redshifts for 870- μm selected SMGs in the ECDFS. Our conclusions are presented in § 4.4 and the best-fit SEDs to the ECDFS SMGs are shown in Appendix 4.5.

4.2 Sample selection

Our parent sample is the 126 SMGs detected in the Extended *Chandra* Deep Field South (ECDFS) by the Large APEX BOlometer CAmera (LABOCA; Siringo et al. 2009) on the Atacama Pathfinder EXperiment (APEX; Güsten et al. 2006) 12-m telescope in the LABOCA ECDFS Submillimetre Survey (LESS; Weiß et al. 2009). LESS mapped the

full $30' \times 30'$ ECDFS at $870\text{-}\mu\text{m}$ to a noise level of $\sigma_{870\mu\text{m}} \approx 1.2 \text{ mJy beam}^{-1}$, for a beam with angular resolution of $19''.2$ and detected 126 SMGs at $> 3.7\sigma$ significance (equivalent to a false-detection rate of $\sim 4\%$, Weiß et al. 2009).

Radio and $24\text{-}\mu\text{m}$ counterparts to LESS SMGs were identified by Biggs et al. (2010) who (similarly to Chapter 3) used the corrected Poissonian probability (p ; Downes et al. 1986) to calculate the probability that sources within the vicinity of each SMG is unassociated with the submillimetre emission. A radius of 3σ (where σ is the error on the $870\text{-}\mu\text{m}$ position) is used to search for SMG counterparts. Since σ is a function of the deboosted submillimetre flux this formulation leads to a search radius that varies on a source by source basis.

We briefly describe the radio and $24\text{-}\mu\text{m}$ catalogues used for source identification here, and refer the reader to Biggs et al. (2010) for more details. The radio catalogue is extracted from the VLA 1.4-GHz map published in Miller et al. (2008), which is a mosaic of six separate points of ~ 5 hours each, and reaches $\sigma \sim 6.5 \mu\text{Jy beam}^{-1}$ at the deepest points. The catalogue published in Miller et al. (2008) only reaches 7σ ; since SMGs can be radio-faint we perform our own source extraction from the Miller et al. (2008) map, which reaches depths of 3σ . Similarly to submillimetre and millimetre observations, simulations show that flux boosting is important for the faintest radio sources, so a correction for flux boosting is applied to each radio source. The $24\text{-}\mu\text{m}$ data is obtained from the Far-Infrared Deep Extragalactic Legacy Survey (FIDEL; Dickinson et al. in prep.). Catalogues are created without priors and using the DAOPHOT package in IRAF; sources brighter than $\sim 30\mu\text{Jy}$ are found to be reliable, so we cut our catalogues are $30\mu\text{Jy}$.

Once radio and $24\text{-}\mu\text{m}$ counterparts are identified we use those with $p \leq 0.05$ to determine the photometric properties of typical SMG counterparts in an effort to identify additional counterparts in the IRAC imaging. We follow the example of Pope et al. (2006) and in Fig. 4.1 plot the IRAC $5.8/3.6\text{-}\mu\text{m}$ colour against the $5.8\text{-}\mu\text{m}$ flux (§ 4.2.1) for field galaxies, LESS radio and $24\text{-}\mu\text{m}$ selected counterparts, and galaxies within 3σ radius of SMGs without radio or $24\text{-}\mu\text{m}$ counterparts. We find that applying limits of $\log_{10}(S_{5.8}(\mu\text{Jy})) \geq 0.75$ and $\log_{10}(S_{5.8}/S_{3.6}) \geq -0.05$ simultaneously maximises the number of radio and $24\text{-}\mu\text{m}$ counterparts recovered whilst limiting the contamination from field galaxies to 10% . We apply these IRAC selection criteria to the error circles of SMGs without radio or $24\text{-}\mu\text{m}$ counterparts and then calculate p for the selected IRAC sources.

Following convention we consider robust counterparts as those with $p \leq 0.05$ in one

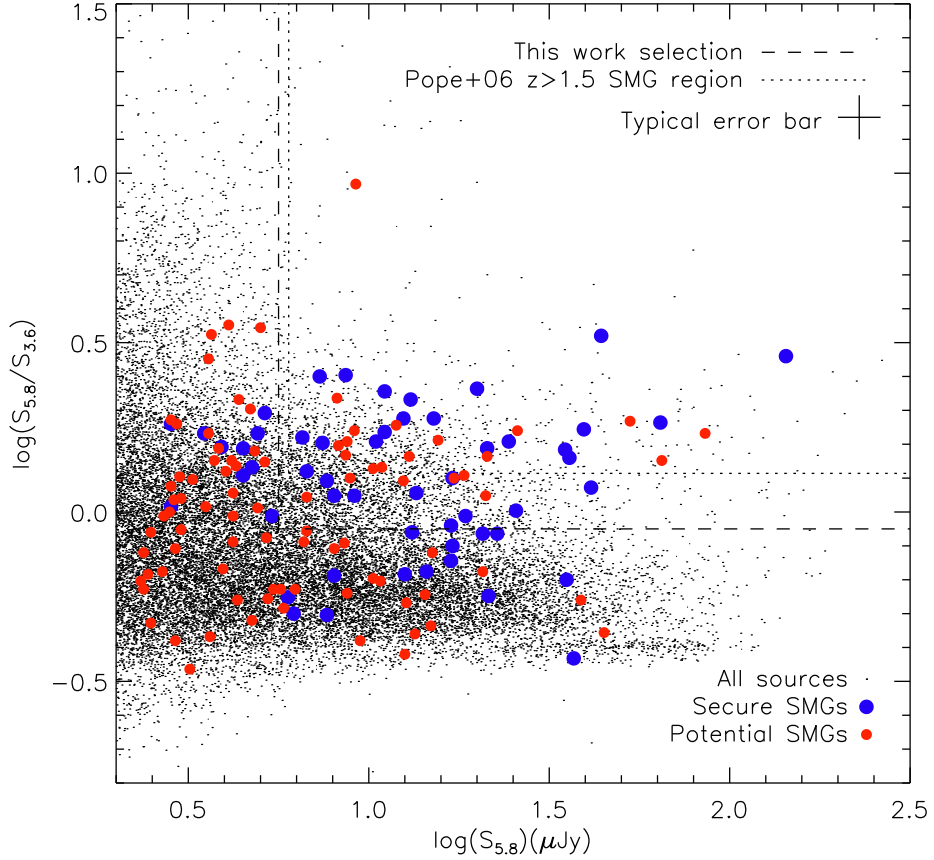


Figure 4.1: 3.6- and 5.8- μm colour-flux diagram for IRAC-selected galaxies in the ECDFS. We highlight secure radio and 24- μm SMG counterparts ($p \leq 0.05$) and potential SMG counterparts that lie within 3σ radius of SMGs without radio or 24- μm counterparts. Typically SMG counterparts are redder than the field population, and we show the IRAC counterpart selection region used in this work, compared to that from Pope et al. (2006). The selection criteria in this work maximises the number of counterparts returned whilst limiting the contamination from field galaxies to 10%, and corresponds to $\log_{10}(S_{5.8}(\mu\text{Jy})) \geq 0.75$ and $\log_{10}(S_{5.8}/S_{3.6}) \geq -0.05$.

Table 4.1: Summary of the number of LESS SMG counterparts identified from radio, 24- μm and IRAC observations. Note that some counterparts are SMGs identified at more than one wavelength, so the overall total are *not* simply the sum of the number of SMGs identified in each band.

	Robust	Tentative
Radio	46	19
24- μm	36	24
IRAC	12	16
Total ^a	68 ^b [74]	22 [25]

^a Numbers in square brackets are the number of optical/near-infrared counterparts to these identifications.

^b There are 71 robust radio, 24- μm and IRAC counterparts, but only 68 of them have detectable optical or near-infrared counterparts.

or more of the radio, 24 μm , or IRAC datasets, or $p = 0.05 - 0.10$ in two or more; tentative counterparts are those with $p = 0.05 - 0.10$ in only one of the three bands. In total robust or tentative radio, 24 μm or IRAC mid-infrared counterparts are identified to 93 (71 robust and 22 tentative) SMGs (Biggs et al. 2010). There are 74 robust and 25 tentative detectable optical and near-infrared counterparts to 91 of the identified SMGs in new and archival imaging of the ECDFS (§ 4.2.1) and these are the galaxies studied in this Chapter and in Chapters 5 and 6. Of the two counterparts that are not identified in our optical and near-infrared imaging one, LESS 35, lies beyond the extent of the imaging; the other, LESS 46, is undected in the optical images but lies outside of the extent of the IRAC data.

4.2.1 Optical and infrared photometry

SMGs typically have faint optical and near-infrared counterparts (e.g. Ivison et al. 2002) so we require deep photometry for accurate photometric redshift estimates. The ECDFS was chosen for the LESS survey because it is an exceptionally well-studied field, and as such we are able to utilise data from extensive archival imaging and spectroscopic surveys. A summary of our photometry is presented in Table 4.2. For completeness and uniformity we only consider surveys that cover a large fraction of the ECDFS rather than the smaller and deeper central CDFS region. Therefore, we utilise the MUltiwavelength Survey by

Yale-Chile (MUSYC; Gawiser et al. 2006) near-infrared survey for U to K -band imaging (Taylor et al. 2009b), and the *Spitzer* IRAC/MUSYC Public Legacy in ECDFS (SIMPLE) imaging for *Spitzer* IRAC data (Damen et al. 2010). We also include U -band data from the deep GOODS/VIMOS imaging survey of the CDFS (Nonino et al. 2009); although this covers only $\sim 60\%$ of LESS SMGs it is valuable for galaxies that are undetected at short wavelengths in the shallower MUSYC survey.

In addition, we have carried out deep near-infrared observations in the J and K_s bands with HAWK-I (Pirard et al. 2004; Casali et al. 2006; Kissler-Patig et al. 2008) at the ESO-VLT (ID: 082.A-0890, P.I. N. Padilla). The ECDFS was covered with a mosaic of 16 pointings in each band, with a total exposure time of 0.75 and 1.1 hours per pointing, in the J and K_s bands respectively. The median seeing is $0.7''$ in J and $0.5''$ in K_s . Data reduction has been performed using an upgraded version of the official ESO pipeline for HAWK-I, customized calibration has been obtained from observations of photometric standard stars. More details and catalogues will be published in Zibetti et al. (in preparation).

For accurate photometric redshifts we require consistent photometry in apertures which sample the same emitting area in each of the 17 filters. For consistency between surveys and to ensure that all detected SMG counterparts are included in this study we extract photometry from the available survey imaging rather than relying on the catalogued sources. SMGs are typically brighter at mid-infrared than optical wavelengths due to their high redshifts and extreme dust obscuration. Therefore, we use SExtractor (Bertin & Arnouts 1996) to create a source list from a combined image of the four IRAC channels, which is weighted such that a given magnitude receives equal contributions from all of the input images. Real sources are required to have at least four contiguous $0.6'' \times 0.6''$ pixels with fluxes at least 1.5 times the background noise. In addition, we visually check the area within $15''$ of each LABOCA source to ensure that no potential SMG counterparts are missed. We next use APPHOT in IRAF to measure the fluxes in $3.8''$ diameter apertures for each of the four IRAC bands. We then cut the catalogues to $\geq 3\sigma$ based on the background noise, and finally apply aperture corrections as derived by the SWIRE team (Surace et al. 2005) to obtain total source magnitudes.

The resolution in the U - to K -band imaging is better than IRAC (FWHM $\leq 1.5''$ compared to $\sim 2''$ for IRAC) and so we convolve each U - to K -band image to match the $1.5''$ seeing of the worst band. We next use APPHOT to measure photometry in $3''$ diameter apertures at the positions of the IRAC-selected sources. In all cases, we only allow APPHOT

Table 4.2: Summary of photometry employed for photometric redshift calculation of LESS SMGs.

Filter	$\lambda_{\text{effective}}$ (μm)	Detection limit (3σ ; mag)	Reference
MUSYC WFI <i>U</i>	0.35	26.9	Taylor et al. (2009b)
MUSYC WFI <i>U38</i>	0.37	25.4	Taylor et al. (2009b)
VIMOS <i>U</i>	0.38	28.4 ^a	Nonino et al. (2009)
MUSYC WFI <i>B</i>	0.46	26.8	Taylor et al. (2009b)
MUSYC WFI <i>V</i>	0.54	26.7	Taylor et al. (2009b)
MUSYC WFI <i>R</i>	0.66	25.8	Taylor et al. (2009b)
MUSYC WFI <i>I</i>	0.87	24.9	Taylor et al. (2009b)
MUSYC Mosaic II <i>z</i>	0.91	24.5	Taylor et al. (2009b)
MUSYC ISPI <i>J</i>	1.25	23.6	Taylor et al. (2009b)
HAWK-I <i>J</i>	1.26	25.7	Zibetti et al. (in prep.)
MUSYC SofI <i>H</i>	1.66	23.0	Taylor et al. (2009b)
MUSYC ISPI <i>K</i>	2.13	22.7	Taylor et al. (2009b)
HAWK-I <i>K_s</i>	2.15	25.3	Zibetti et al. (in prep.)
SIMPLE IRAC 3.6 μm	3.58	24.6	Damen et al. (2010)
SIMPLE IRAC 4.5 μm	4.53	24.4	Damen et al. (2010)
SIMPLE IRAC 5.8 μm	5.79	22.8	Damen et al. (2010)
SIMPLE IRAC 8.0 μm	8.05	23.5	Damen et al. (2010)

^aThe listed depth of the VIMOS *U*-band is that of the central region. The typical depth in the shallower outskirts is 28.0 mag.

to re-centroid the aperture if centroiding does not cause the extraction region to be moved to a nearby source, as flagged by IRAF's CIER parameter when the centroid shift is $> 0.5''$. We have not performed any deblending of the photometry but examination of the images suggests fewer than $\sim 10\%$ of the SMG counterparts are affected. We note here that the photometric extraction process is not restricted to SMGs and yields photometry (which allows us to calculate and test consistent photometric redshifts) for IRAC-selected sources throughout the ECDFS.

Finally, to ensure equivalent photometry between the IRAC and optical-to-near-infrared filters we create simulated IRAC images of point sources. Using these images we calculate that the correction between the measured IRAC total magnitudes and the photometry extracted from $3''$ diameter apertures on $1.5''$ seeing images is -0.014 ± 0.017 magnitudes, and as such we do not apply any systematic corrections to the IRAC magnitudes at this stage. In §4.3.1 we calibrate the photometry prior to photometric redshift calculation in a process which corrects for small residual offsets. The optical and infrared photometry of the SMGs is given in Tables 4.3 and 4.4, respectively.

The median number of photometric filters per SMG counterpart is 15 and we require detections in at least three photometric filters in order to calculate photometric redshifts. Our final sample therefore contains 74 optical counterparts to the 68 robustly identified SMGs with sufficient detectable optical-to-infrared emission. There are a further 25 tentative counterparts to 23 SMGs that we do not use for testing the photometric redshifts, but we do calculate the photometric redshift for use in Chapter 5.

30 of the robust SMG counterparts have available spectroscopic redshifts, which we use to test and calibrate the derived photometric redshifts for SMGs. There are an additional 1796 galaxies and AGN in the field with spectroscopic redshifts, which we employ to calibrate the photometry and test the reliability of the photometric redshifts of the field population. The spectroscopic redshifts are obtained from archival surveys of the ECDFS (Cristiani et al. 2000; Croom et al. 2001; Bunker et al. 2003; Dickinson et al. 2004; Le Fèvre et al. 2004; Stanway et al. 2004; Strolger et al. 2004; Szokoly et al. 2004; van der Wel et al. 2004; Zheng et al. 2004; Daddi et al. 2005; Doherty et al. 2005; Mignoli et al. 2005; Grazian et al. 2006; Ravikumar et al. 2007; Kriek et al. 2008; Vanzella et al. 2008; Popesso et al. 2009; Treister et al. 2009; Balestra et al. 2010, Kuposov et al. in prep.) and also an on-going spectroscopic survey of LESS sources with the VLT (PID: 183.A-0666, P.I. I. Smail), which will be published in full in Danielson et al. (in prep.).

Table 4.3: Observed optical photometry for robust counterparts to LESS SMGs. 3σ limiting magnitudes are presented where sources are observed but not detected; SMGs which are not observed a given filter have no photometry listed in that band. The VIMOS U , MUSYC U , $U38$, R , I and z band magnitudes have been corrected according to § 4.3.1.

Source ^a	MUSYC U	$U38$	VIMOS U	B	V	R	I	z
LESS 2a	25.67 ± 0.13	25.35 ± 0.32	25.19 ± 0.10	24.78 ± 0.05	24.65 ± 0.05	24.39 ± 0.09	24.08 ± 0.15	23.82 ± 0.17
LESS 2b	> 26.85	> 25.40	> 28.38	> 26.81	26.56 ± 0.29	> 25.79	> 24.94	> 24.48
LESS 3	> 26.85	> 25.40	...	> 26.81	> 26.68	> 25.79	> 24.94	> 24.48
LESS 6	26.57 ± 0.27	> 25.40	28.11 ± 0.23	25.95 ± 0.15	24.94 ± 0.07	24.00 ± 0.06	22.91 ± 0.05	22.75 ± 0.07
LESS 7	26.46 ± 0.25	> 25.40	26.29 ± 0.12	24.90 ± 0.06	24.08 ± 0.03	23.37 ± 0.04	22.22 ± 0.03	22.11 ± 0.04
LESS 9	> 26.85	...	> 28.38	> 26.81	> 26.68	> 25.79	> 24.94	...
LESS 10a	26.29 ± 0.21	> 25.40	25.74 ± 0.11	25.53 ± 0.11	25.60 ± 0.13	25.05 ± 0.16	24.61 ± 0.23	> 24.48
LESS 10b	> 26.85	> 25.40	27.45 ± 0.14	26.66 ± 0.28	25.79 ± 0.15	24.28 ± 0.08	22.63 ± 0.04	22.36 ± 0.05
LESS 11	> 26.85	...	27.86 ± 0.15	> 26.81	> 26.68	> 25.79	> 24.94	> 24.48
LESS 12	> 26.85	> 25.40	> 28.38	> 26.81	> 26.68	> 25.79	> 24.94	> 24.48
LESS 14	> 26.85	> 25.40	> 28.38	> 26.81	26.71 ± 0.32	> 25.79	> 24.94	> 24.48
LESS 15	> 26.85	> 26.81	> 26.68	> 25.79	> 24.94	> 24.48
LESS 16	25.04 ± 0.07	24.86 ± 0.21	24.83 ± 0.10	24.49 ± 0.04	24.01 ± 0.03	23.29 ± 0.03	21.79 ± 0.02	21.57 ± 0.02
LESS 17	25.15 ± 0.08	25.25 ± 0.29	24.83 ± 0.10	24.47 ± 0.04	24.26 ± 0.04	23.94 ± 0.06	23.27 ± 0.07	23.05 ± 0.09
LESS 18	26.11 ± 0.18	> 25.40	25.71 ± 0.11	25.52 ± 0.11	25.34 ± 0.10	25.30 ± 0.20	24.64 ± 0.23	24.41 ± 0.27
LESS 19	> 26.85	> 25.40	27.01 ± 0.12	27.04 ± 0.35	26.39 ± 0.25	26.79 ± 0.62	> 24.94	> 24.48
LESS 20	> 26.85	> 25.40	...	26.25 ± 0.20	25.66 ± 0.13	25.89 ± 0.33	> 24.94	> 24.48
LESS 22	> 26.85	> 26.81	26.20 ± 0.21	25.60 ± 0.26	> 24.94	> 24.48
LESS 24	> 26.85	> 25.40	...	25.53 ± 0.11	25.71 ± 0.14	25.15 ± 0.18	24.31 ± 0.18	24.71 ± 0.35
LESS 25	...	> 25.40	26.78 ± 0.13	26.02 ± 0.16	25.46 ± 0.11	25.04 ± 0.16	24.45 ± 0.20	24.25 ± 0.24
LESS 27a	> 26.85	> 25.40	...	> 26.81	> 26.68	> 25.79	> 24.94	> 24.48
LESS 27b	> 26.85	> 25.40	...	26.14 ± 0.18	25.88 ± 0.16	25.35 ± 0.21	> 24.94	> 24.48
LESS 29	> 26.85	> 26.81	> 26.68	> 25.79	> 24.94	> 24.48
LESS 31	> 26.85	> 25.40	...	> 26.81	> 26.68	> 25.79	> 24.94	> 24.48
LESS 34	24.98 ± 0.07	24.69 ± 0.18	24.39 ± 0.10	24.09 ± 0.03	23.67 ± 0.02	23.06 ± 0.03	21.87 ± 0.02	21.57 ± 0.02
LESS 36	> 26.85	> 25.40	...	> 26.81	...	> 25.79	> 24.94	> 24.48
LESS 37	> 26.85	26.19 ± 0.19	25.33 ± 0.10	24.18 ± 0.08	23.45 ± 0.08	...
LESS 39	25.44 ± 0.10	> 25.40	...	25.17 ± 0.08	24.77 ± 0.06	24.15 ± 0.07	23.91 ± 0.13	23.41 ± 0.12
LESS 40	24.82 ± 0.06	24.71 ± 0.19	24.54 ± 0.10	24.36 ± 0.04	24.07 ± 0.03	23.81 ± 0.05	23.36 ± 0.08	23.44 ± 0.12
LESS 41
LESS 43	> 26.85	> 25.40	28.17 ± 0.21	> 26.81	> 26.68	> 25.79	> 24.94	> 24.48
LESS 44	25.06 ± 0.07	24.77 ± 0.20	...	24.42 ± 0.04	24.32 ± 0.04	24.34 ± 0.09	24.58 ± 0.22	24.32 ± 0.25
LESS 47	> 26.85	> 25.40	27.05 ± 0.13	26.31 ± 0.21	25.58 ± 0.12	25.26 ± 0.19	> 24.94	> 24.48
LESS 48	> 28.38
LESS 49a	26.26 ± 0.21	> 25.40	...	25.30 ± 0.09	25.22 ± 0.09	24.59 ± 0.11	24.07 ± 0.14	24.25 ± 0.24
LESS 49b	> 26.85	> 25.40	...	24.85 ± 0.06	24.56 ± 0.05	24.37 ± 0.09	24.13 ± 0.15	24.38 ± 0.26
LESS 50a	24.34 ± 0.04	24.09 ± 0.11	23.95 ± 0.10	23.70 ± 0.02	23.38 ± 0.02	22.90 ± 0.02	22.19 ± 0.03	22.04 ± 0.03
LESS 50b	> 26.85	...	26.12 ± 0.12	26.17 ± 0.18	26.12 ± 0.20	25.90 ± 0.33	> 24.94	> 24.48
LESS 54	> 26.85	...	26.97 ± 0.13	26.08 ± 0.17	26.33 ± 0.24	> 25.79	> 24.94	> 24.48
LESS 56	> 26.85	> 25.40	> 28.38	> 26.81	> 26.68	> 25.79	> 24.94	> 24.48
LESS 57	> 26.85	> 25.40	26.57 ± 0.12	25.14 ± 0.08	25.38 ± 0.10	24.96 ± 0.15	> 24.94	> 24.48
LESS 59	> 26.85	> 25.40	27.66 ± 0.14	26.89 ± 0.33	26.67 ± 0.31	> 25.79	24.36 ± 0.19	> 24.48
LESS 60	25.50 ± 0.11	25.12 ± 0.26	24.98 ± 0.10	24.95 ± 0.06	24.59 ± 0.05	24.08 ± 0.07	23.18 ± 0.07	22.87 ± 0.07
LESS 62	26.55 ± 0.26	> 25.40	26.27 ± 0.12	25.55 ± 0.11	25.09 ± 0.08	24.44 ± 0.10	23.45 ± 0.08	23.56 ± 0.13
LESS 63	25.39 ± 0.10	> 25.40	...	25.05 ± 0.07	24.69 ± 0.06	24.25 ± 0.08	23.28 ± 0.07	22.92 ± 0.08
LESS 64	> 26.85	...	> 28.38	26.53 ± 0.25	25.52 ± 0.12	24.29 ± 0.08	24.17 ± 0.16	24.44 ± 0.28
LESS 66	21.03 ± 0.00	20.89 ± 0.01	...	21.18 ± 0.00	21.13 ± 0.00	20.79 ± 0.00	20.64 ± 0.01	20.23 ± 0.01
LESS 67	26.14 ± 0.19	> 25.40	25.37 ± 0.10	24.85 ± 0.06	24.52 ± 0.05	24.42 ± 0.09	23.80 ± 0.11	23.74 ± 0.16
LESS 70	25.19 ± 0.08	24.72 ± 0.19	24.56 ± 0.10	23.87 ± 0.02	23.78 ± 0.02	23.69 ± 0.05	23.61 ± 0.10	23.53 ± 0.13
LESS 73	> 26.85	> 25.40	> 28.38	> 26.81	> 26.68	25.82 ± 0.31	24.38 ± 0.19	> 24.48
LESS 74a	> 26.85	...	> 28.38	> 26.81	> 26.68	> 25.79	> 24.94	24.72 ± 0.35
LESS 74b	> 26.85	...	27.83 ± 0.15	> 26.81	> 26.68	> 25.79	25.04 ± 0.32	> 24.48
LESS 75	25.14 ± 0.08	24.80 ± 0.20	...	23.86 ± 0.02	23.60 ± 0.02	23.42 ± 0.04	23.38 ± 0.08	23.50 ± 0.13
LESS 79	26.37 ± 0.23	> 25.40	25.56 ± 0.11	25.16 ± 0.08	24.84 ± 0.06	24.54 ± 0.10	23.61 ± 0.10	23.74 ± 0.16
LESS 81	25.94 ± 0.16	> 25.40	...	24.18 ± 0.03	23.73 ± 0.02	23.39 ± 0.04	22.79 ± 0.05	...
LESS 84	26.42 ± 0.24	> 25.40	25.62 ± 0.11	25.10 ± 0.07	25.03 ± 0.08	24.89 ± 0.14	24.43 ± 0.20	> 24.48

Table 4.3: – *continued*

Source ^a	MUSYC <i>U</i>	<i>U</i> 38	VIMOS <i>U</i>	<i>B</i>	<i>V</i>	<i>R</i>	<i>I</i>	<i>z</i>
LESS 87	25.52 ± 0.11
LESS 88	26.78 ± 0.32	> 25.40	25.98 ± 0.11	25.42 ± 0.10	25.10 ± 0.08	24.98 ± 0.15	24.27 ± 0.17	24.43 ± 0.28
LESS 96	21.92 ± 0.00	21.73 ± 0.01	21.32 ± 0.10	20.82 ± 0.00	20.62 ± 0.00	20.40 ± 0.00	19.99 ± 0.00	19.72 ± 0.00
LESS 98	> 26.85	> 26.81	> 26.68	> 25.79	24.61 ± 0.23	24.64 ± 0.33
LESS 101	> 26.85	> 25.40	27.28 ± 0.13	26.70 ± 0.29	26.20 ± 0.21	25.58 ± 0.25	> 24.94	> 24.48
LESS 102	> 26.85	> 25.40	...	26.93 ± 0.34	26.24 ± 0.22	25.98 ± 0.35	24.97 ± 0.31	24.49 ± 0.29
LESS 103	> 26.85	> 26.81	> 26.68	> 25.79	> 24.94	> 24.48
LESS 106	> 26.85	> 25.40	...	> 26.81	> 26.68	> 25.79	24.51 ± 0.21	24.38 ± 0.27
LESS 108	21.25 ± 0.00	21.00 ± 0.01	20.82 ± 0.10	19.64 ± 0.00	19.11 ± 0.00	18.60 ± 0.00	18.02 ± 0.00	17.94 ± 0.00
LESS 110
LESS 111	25.06 ± 0.07	25.03 ± 0.25	...	23.82 ± 0.02	23.31 ± 0.02	22.79 ± 0.02	22.38 ± 0.03	22.27 ± 0.04
LESS 112	26.98 ± 0.15
LESS 114	25.31 ± 0.09	25.24 ± 0.29	24.98 ± 0.10	24.52 ± 0.04	24.21 ± 0.04	23.87 ± 0.06	23.05 ± 0.06	22.91 ± 0.07
LESS 117	26.42 ± 0.24	> 25.40	...	> 26.81	> 26.68	> 25.79	24.09 ± 0.15	...
LESS 118
LESS 120	> 26.85	> 25.40	...	26.77 ± 0.30	25.99 ± 0.18	> 25.79	24.60 ± 0.23	23.79 ± 0.16
LESS 122	24.83 ± 0.06	24.70 ± 0.19	24.42 ± 0.10	23.77 ± 0.02	23.44 ± 0.02	23.28 ± 0.03	22.94 ± 0.05	22.86 ± 0.07
LESS 126	> 26.85	> 25.40	26.87 ± 0.12	26.32 ± 0.21	26.61 ± 0.30	25.87 ± 0.32	> 24.94	...

^aSource names correspond to those in Table 4.5

4.3 Analysis and results

As we showed in Chapter 3 reliable photometric redshifts can be derived for SMGs using HYPERZ with the included Bruzual & Charlot (1993) E, Sb, Burst and Im spectral templates and reddening in the range of $A_V = 0-5$. Therefore, we begin our analysis of the photometric redshifts of LESS SMGs by using the E, Sb, Burst and Im spectral templates, and reddening (Calzetti et al. 2000) of $A_V = 0-5$ in steps of 0.2. Redshifts between 0 and 7 are considered and galaxy ages are required to be less than the age of the Universe at the appropriate redshift. In §4.3.5 we show that the HYPERZ-derived galaxy ages cannot be reliably determined, but we note here that the requirement for SMGs to be younger than the Universe does not significantly affect the derived redshifts.

4.3.1 Calibrating the photometry and templates

Although, as discussed in § 4.2.1, we have taken care to extract accurate and reliable photometry for LESS SMGs, some systematic errors may remain. It is also possible that there may be systematic differences between the model SEDs and observed SEDs. Therefore, prior to calculating photometric redshifts of the SMGs, we utilise the extensive spectroscopy of numerous galaxies and AGN in the ECDFS to calibrate the model SEDs with the observed photometry.

We test for any small systematic discrepancies between the photometry and model SEDs by running HYPERZ on 1796 galaxies and AGN with spectroscopic redshifts in

Table 4.4: Observed near-infrared photometry for robust counterparts to LESS SMGs. 3σ limiting magnitudes are presented where sources are observed but not detected; SMGs which are not observed in a given filter have no photometry listed in that band. The J -band, 3.6- and 8- μm magnitudes have been corrected according to §4.3.1.

Source ^a	MUSYC J	HAWKI J	MUSYC H	MUSYC K	HAWKI K	3.6 μm	4.5 μm	5.8 μm	8 μm
LESS 2a	22.81 ± 0.16	22.88 ± 0.04	> 23.02	21.65 ± 0.13	22.18 ± 0.03	21.37 ± 0.07	21.18 ± 0.07	21.13 ± 0.14	21.49 ± 0.09
LESS 2b	> 23.64	24.44 ± 0.09	22.94 ± 0.29	> 22.72	23.26 ± 0.05	22.38 ± 0.11	22.08 ± 0.10	21.86 ± 0.20	22.23 ± 0.14
LESS 3	> 23.64	...	> 23.02	> 22.72	23.30 ± 0.05	22.72 ± 0.12	22.09 ± 0.10	21.74 ± 0.19	21.42 ± 0.09
LESS 6	21.83 ± 0.07	22.09 ± 0.03	21.73 ± 0.10	21.10 ± 0.08	21.15 ± 0.02	21.14 ± 0.06	21.52 ± 0.08	21.92 ± 0.21	22.36 ± 0.17
LESS 7	21.69 ± 0.06	21.44 ± 0.02	21.07 ± 0.06	20.47 ± 0.04	20.46 ± 0.01	20.02 ± 0.04	19.91 ± 0.04	19.86 ± 0.08	20.15 ± 0.05
LESS 9	> 23.64	24.19 ± 0.08	> 23.02	> 22.72	22.47 ± 0.04	21.85 ± 0.08	21.43 ± 0.08	21.29 ± 0.15	21.13 ± 0.08
LESS 10a	> 23.64	24.56 ± 0.10	> 23.02	> 22.72	23.33 ± 0.05	22.21 ± 0.10	21.78 ± 0.09	21.72 ± 0.19	21.46 ± 0.09
LESS 10b	21.41 ± 0.05	21.18 ± 0.02	20.81 ± 0.05	20.51 ± 0.05	20.29 ± 0.01	19.87 ± 0.03	20.14 ± 0.04	20.75 ± 0.12	21.32 ± 0.09
LESS 11	> 23.64	25.04 ± 0.12	> 23.02	> 22.72	23.58 ± 0.06	22.16 ± 0.10	21.63 ± 0.09	21.29 ± 0.15	21.15 ± 0.08
LESS 12	> 23.64	25.71 ± 0.18	> 23.02	> 22.72	23.83 ± 0.06	22.72 ± 0.12	22.35 ± 0.12	22.17 ± 0.23	21.98 ± 0.12
LESS 14	> 23.64	25.56 ± 0.19	...	> 22.72	23.53 ± 0.06	22.55 ± 0.11	21.87 ± 0.09	21.56 ± 0.17	21.14 ± 0.08
LESS 15	> 23.64	> 22.72	...	21.91 ± 0.09	21.30 ± 0.07	21.11 ± 0.14	21.05 ± 0.08
LESS 16	20.95 ± 0.03	20.93 ± 0.02	20.44 ± 0.05	20.16 ± 0.03	20.15 ± 0.01	19.51 ± 0.03	19.71 ± 0.04	20.03 ± 0.08	20.08 ± 0.05
LESS 17	22.05 ± 0.08	22.16 ± 0.03	21.64 ± 0.10	21.25 ± 0.09	21.07 ± 0.02	20.36 ± 0.04	20.16 ± 0.04	20.38 ± 0.10	20.76 ± 0.07
LESS 18	23.21 ± 0.22	22.81 ± 0.04	22.05 ± 0.14	21.35 ± 0.10	21.45 ± 0.02	20.38 ± 0.04	20.06 ± 0.04	20.01 ± 0.08	20.67 ± 0.06
LESS 19	> 23.64	23.82 ± 0.07	...	> 22.72	24.22 ± 0.08	22.74 ± 0.12	22.23 ± 0.11	21.83 ± 0.19	21.98 ± 0.12
LESS 20	> 23.64	24.56 ± 0.09	> 23.02	> 22.72	22.57 ± 0.03	21.83 ± 0.08	21.48 ± 0.08	21.16 ± 0.14	21.46 ± 0.09
LESS 22	20.47 ± 0.04	20.16 ± 0.04	20.04 ± 0.08	20.55 ± 0.06
LESS 24	22.71 ± 0.14	21.39 ± 0.10	...	20.67 ± 0.05	20.41 ± 0.05	20.73 ± 0.12	20.97 ± 0.08
LESS 25	> 23.64	23.23 ± 0.05	...	21.82 ± 0.15	21.67 ± 0.02	21.03 ± 0.06	20.73 ± 0.05	20.58 ± 0.11	20.83 ± 0.07
LESS 27a	> 23.64	> 25.70	> 23.02	> 22.72	...	22.68 ± 0.12	22.30 ± 0.12	21.93 ± 0.22	22.31 ± 0.17
LESS 27b	> 23.64	> 22.72	...	22.01 ± 0.09	21.68 ± 0.09	21.45 ± 0.16	21.95 ± 0.12
LESS 29	> 23.64	> 22.72	...	22.22 ± 0.10	21.70 ± 0.09	21.27 ± 0.15	21.19 ± 0.09
LESS 31	> 23.64	26.49 ± 0.26	...	> 22.72	23.46 ± 0.05	22.70 ± 0.12	22.19 ± 0.11	21.68 ± 0.18	21.65 ± 0.10
LESS 34	20.94 ± 0.03	20.78 ± 0.02	20.29 ± 0.05	20.04 ± 0.03	19.90 ± 0.01	19.51 ± 0.03	19.71 ± 0.04	20.37 ± 0.10	20.73 ± 0.06
LESS 36	> 23.64	25.70 ± 0.16	...	22.67 ± 0.30	22.76 ± 0.04	21.53 ± 0.07	21.06 ± 0.06	20.65 ± 0.11	20.98 ± 0.07
LESS 37	22.86 ± 0.16	...	22.38 ± 0.18	21.16 ± 0.08	...	20.55 ± 0.05	20.41 ± 0.05	20.82 ± 0.13	20.94 ± 0.08
LESS 39	23.59 ± 0.30	24.32 ± 0.10	...	22.01 ± 0.17	...	21.62 ± 0.07	21.28 ± 0.07	21.06 ± 0.14	21.07 ± 0.08
LESS 40	23.04 ± 0.19	23.05 ± 0.05	22.52 ± 0.21	22.20 ± 0.20	22.09 ± 0.03	21.45 ± 0.07	21.12 ± 0.07	21.04 ± 0.13	20.99 ± 0.07
LESS 41	20.50 ± 0.04	20.19 ± 0.04	19.91 ± 0.08	19.93 ± 0.05
LESS 43	> 23.64	23.93 ± 0.07	23.11 ± 0.33	> 22.72	22.58 ± 0.03	21.46 ± 0.07	21.04 ± 0.06	21.09 ± 0.14	21.73 ± 0.11
LESS 44	20.94 ± 0.05	20.59 ± 0.05	20.37 ± 0.10	20.82 ± 0.07
LESS 47	> 23.64	> 22.72	...	22.37 ± 0.10	22.00 ± 0.10	21.80 ± 0.19	21.83 ± 0.12
LESS 48	20.27 ± 0.04	20.15 ± 0.04	20.14 ± 0.09	20.80 ± 0.07
LESS 49a	...	23.85 ± 0.07	22.20 ± 0.03	21.26 ± 0.06	20.97 ± 0.06	21.41 ± 0.16	21.67 ± 0.11
LESS 49b	...	23.85 ± 0.07	22.49 ± 0.03	22.16 ± 0.10	21.88 ± 0.09	21.65 ± 0.18	21.67 ± 0.11
LESS 50a	21.75 ± 0.06	21.62 ± 0.02	21.55 ± 0.09	21.32 ± 0.09	21.17 ± 0.02	21.20 ± 0.06	21.67 ± 0.09	22.17 ± 0.25	23.24 ± 0.32
LESS 50b	> 23.64	24.22 ± 0.08	> 23.02	22.63 ± 0.29	22.65 ± 0.03	21.70 ± 0.08	21.17 ± 0.07	20.76 ± 0.12	20.57 ± 0.06
LESS 54	> 23.64	> 22.72	...	21.66 ± 0.08	21.26 ± 0.07	21.31 ± 0.15	21.97 ± 0.12
LESS 56	23.77 ± 0.35	24.46 ± 0.09	22.57 ± 0.22	22.15 ± 0.20	22.00 ± 0.03	21.27 ± 0.06	20.95 ± 0.06	20.81 ± 0.12	21.26 ± 0.09
LESS 57	> 23.64	24.25 ± 0.08	23.05 ± 0.32	> 22.72	22.55 ± 0.03	22.02 ± 0.09	21.63 ± 0.08	21.35 ± 0.16	20.54 ± 0.06
LESS 59	23.14 ± 0.21	23.03 ± 0.04	22.53 ± 0.21	21.62 ± 0.12	21.71 ± 0.02	20.71 ± 0.05	20.51 ± 0.05	20.83 ± 0.12	21.27 ± 0.09
LESS 60	22.54 ± 0.12	22.23 ± 0.03	22.01 ± 0.13	21.49 ± 0.11	21.31 ± 0.02	20.59 ± 0.05	20.39 ± 0.05	20.54 ± 0.11	20.65 ± 0.06
LESS 62	22.17 ± 0.09	22.11 ± 0.03	21.50 ± 0.09	20.81 ± 0.06	20.85 ± 0.01	19.93 ± 0.03	19.75 ± 0.04	20.08 ± 0.09	20.28 ± 0.05
LESS 63	22.02 ± 0.08	21.83 ± 0.03	21.80 ± 0.11	21.21 ± 0.09	21.12 ± 0.02	20.69 ± 0.05	20.53 ± 0.05	20.76 ± 0.12	21.09 ± 0.08
LESS 64	> 23.64	24.28 ± 0.09	...	> 22.72	23.06 ± 0.04	22.51 ± 0.11	22.41 ± 0.12	22.27 ± 0.25	21.87 ± 0.12
LESS 66	21.21 ± 0.04	...	20.33 ± 0.05	20.30 ± 0.04	...	19.61 ± 0.03	19.44 ± 0.03	19.36 ± 0.06	19.32 ± 0.03
LESS 67	23.07 ± 0.20	22.79 ± 0.04	22.23 ± 0.16	21.16 ± 0.08	21.40 ± 0.02	20.63 ± 0.05	20.32 ± 0.05	20.20 ± 0.09	20.75 ± 0.06
LESS 70	22.56 ± 0.13	22.56 ± 0.04	22.51 ± 0.20	21.70 ± 0.13	21.60 ± 0.02	20.96 ± 0.06	20.78 ± 0.06	20.58 ± 0.11	20.89 ± 0.07
LESS 73	> 23.64	24.35 ± 0.09	> 23.02	> 22.72	23.53 ± 0.07	22.92 ± 0.13	22.79 ± 0.14	22.33 ± 0.25	21.99 ± 0.12
LESS 74a	23.23 ± 0.22	23.48 ± 0.05	23.08 ± 0.33	22.41 ± 0.24	22.08 ± 0.03	21.45 ± 0.07	21.17 ± 0.07	21.15 ± 0.14	21.81 ± 0.12
LESS 74b	23.36 ± 0.25	23.60 ± 0.06	> 23.02	22.08 ± 0.18	22.47 ± 0.03	21.58 ± 0.07	21.18 ± 0.07	21.04 ± 0.14	21.57 ± 0.10
LESS 75	22.81 ± 0.16	22.95 ± 0.04	...	22.10 ± 0.19	22.17 ± 0.03	21.07 ± 0.06	20.43 ± 0.05	19.79 ± 0.08	19.07 ± 0.03
LESS 79	22.63 ± 0.13	22.41 ± 0.03	22.09 ± 0.14	21.24 ± 0.09	21.20 ± 0.02	20.32 ± 0.04	20.16 ± 0.04	20.32 ± 0.10	20.87 ± 0.07
LESS 81	21.38 ± 0.04	22.45 ± 0.03	21.49 ± 0.08	20.90 ± 0.07	21.70 ± 0.02	20.18 ± 0.04	19.91 ± 0.04	20.11 ± 0.09	20.61 ± 0.07
LESS 84	> 23.64	23.36 ± 0.05	22.81 ± 0.26	21.71 ± 0.13	22.10 ± 0.03	21.43 ± 0.07	21.08 ± 0.06	20.92 ± 0.13	21.10 ± 0.08

Table 4.4: – *continued*

Source ^a	MUSYC <i>J</i>	HAWKI <i>J</i>	MUSYC <i>H</i>	MUSYC <i>K</i>	HAWKI <i>K</i>	3.6 μ m	4.5 μ m	5.8 μ m	8 μ m
LESS 87	21.32 \pm 0.06	21.07 \pm 0.06	21.03 \pm 0.14	20.90 \pm 0.07
LESS 88	23.25 \pm 0.23	23.51 \pm 0.06	23.05 \pm 0.32	22.00 \pm 0.17	22.05 \pm 0.04	21.15 \pm 0.06	20.85 \pm 0.06	20.73 \pm 0.12	21.09 \pm 0.08
LESS 96	19.74 \pm 0.01	19.50 \pm 0.01	19.77 \pm 0.04	19.76 \pm 0.02	19.59 \pm 0.01	19.63 \pm 0.03	19.43 \pm 0.03	19.07 \pm 0.05	18.59 \pm 0.02
LESS 98	23.41 \pm 0.26	22.98 \pm 0.04	...	21.49 \pm 0.11	21.40 \pm 0.02	20.22 \pm 0.04	19.84 \pm 0.04	19.99 \pm 0.08	20.31 \pm 0.05
LESS 101	> 23.64	24.33 \pm 0.10	> 23.02	> 22.72	23.16 \pm 0.05	22.44 \pm 0.11	21.93 \pm 0.10	21.62 \pm 0.18	21.55 \pm 0.10
LESS 102	22.91 \pm 0.17	21.29 \pm 0.09	...	20.43 \pm 0.04	20.13 \pm 0.04	20.17 \pm 0.09	20.92 \pm 0.08
LESS 103	> 23.64	22.78 \pm 0.33	...	21.51 \pm 0.07	21.25 \pm 0.07	21.12 \pm 0.14	21.77 \pm 0.12
LESS 106	23.07 \pm 0.20	22.71 \pm 0.04	21.76 \pm 0.11	21.33 \pm 0.10	21.22 \pm 0.02	20.22 \pm 0.04	19.83 \pm 0.04	19.91 \pm 0.08	20.06 \pm 0.05
LESS 108	17.41 \pm 0.00	17.35 \pm 0.00	17.15 \pm 0.04	17.00 \pm 0.00	16.99 \pm 0.00	...	17.79 \pm 0.01	17.84 \pm 0.03	...
LESS 110	23.13 \pm 0.16	22.44 \pm 0.12	21.82 \pm 0.20	21.72 \pm 0.12
LESS 111	22.75 \pm 0.15	21.57 \pm 0.12	...	21.04 \pm 0.06	20.98 \pm 0.06	20.81 \pm 0.12	20.23 \pm 0.05
LESS 112	20.93 \pm 0.05	20.59 \pm 0.05	20.43 \pm 0.10	21.06 \pm 0.08
LESS 114	21.63 \pm 0.06	21.62 \pm 0.02	20.97 \pm 0.05	20.68 \pm 0.05	20.67 \pm 0.01	19.93 \pm 0.03	19.66 \pm 0.03	19.86 \pm 0.08	20.10 \pm 0.05
LESS 117	22.58 \pm 0.13	...	21.60 \pm 0.09	21.47 \pm 0.11	...	20.56 \pm 0.05	20.31 \pm 0.05	20.53 \pm 0.11	20.93 \pm 0.08
LESS 118	...	24.30 \pm 0.08	23.98 \pm 0.08	23.39 \pm 0.17	23.81 \pm 0.25	22.77 \pm 0.34	> 23.50
LESS 120	23.34 \pm 0.25	23.23 \pm 0.05	22.79 \pm 0.26	21.77 \pm 0.14	21.87 \pm 0.03	20.99 \pm 0.05	20.70 \pm 0.05	20.74 \pm 0.12	21.33 \pm 0.09
LESS 122	21.96 \pm 0.07	21.96 \pm 0.03	21.43 \pm 0.08	21.20 \pm 0.09	21.00 \pm 0.02	20.24 \pm 0.04	19.88 \pm 0.04	19.59 \pm 0.07	19.67 \pm 0.04
LESS 126	> 23.64	23.84 \pm 0.07	22.72 \pm 0.24	22.99 \pm 0.38	22.24 \pm 0.03	21.29 \pm 0.06	21.04 \pm 0.06	21.21 \pm 0.14	21.68 \pm 0.10

^aSource names correspond to those in Table 4.5

the ECDFS and requiring the best-fit SED the observed redshift. We then compare the model and measured magnitudes in each filter for each galaxy, and iteratively adjust the zeropoints of the filters with the largest systematic offsets. This yields significant offsets for the following filters: VIMOS *U* (0.083 mag), MUSYC *U* (−0.091 mag), *U*38 (−0.074 mag), *R* (0.049 mag), *I* (0.048 mag), *z* (0.095 mag), HAWK-I *J* (0.043 mag), IRAC 3.6 (0.043 mag) and IRAC 8.0 μ m (0.110 mag). The typical uncertainties in these corrections are ± 0.02 mag and the remaining eight filters have no significant corrections. These corrections are applied to the extracted photometry of all SMGs and field sources and the resulting photometry is used throughout this Chapter and in Chapters 5 and 6.

4.3.2 Improving photometric redshifts for galaxies at $z = 2-3$

We initially calculate the photometric redshifts of the LESS SMGs using the HYPERZ parameters shown in Chapter 3 to be optimum for SMGs – four spectral types (E, Sb, Burst and Im), $A_V = 0-5$, and $z = 0-7$. We show in Fig. 4.2 a comparison of the photometric redshifts (z_{phot}) calculated with these parameters with the spectroscopic redshifts (z_{spec}). The inset figure is the histogram of $\Delta z = z_{\text{spec}} - z_{\text{phot}}$ for 1796 galaxies and AGN in the ECDFS, and shows that in general our photometric redshifts are a good proxy for spectroscopic redshift for these sources (median $\Delta z / (1+z) = 0.02 \pm 0.002$ and 1σ dispersion of 0.13). However, the median redshift, $z = 0.84$, is lower than that expected for SMGs and the targets are typically brighter at optical wavelengths, limiting the usefulness of these comparisons for the SMGs. Therefore, we also test our photometric redshift calculation on the 30 robust SMG counterparts with available spectroscopic redshifts.

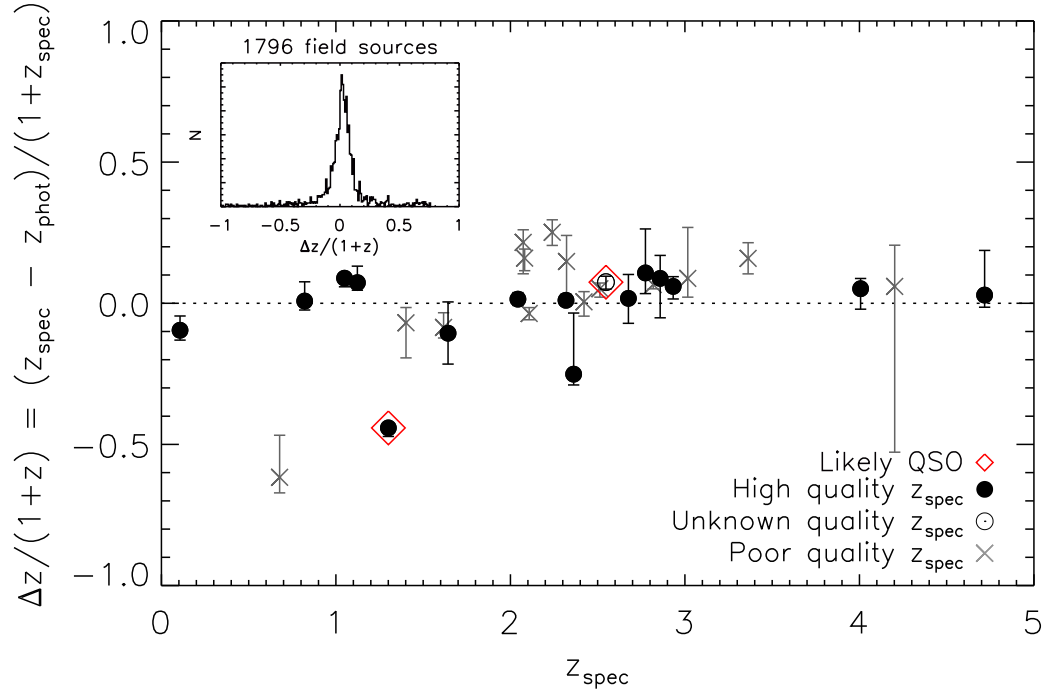


Figure 4.2: Spectroscopic redshift against $\Delta z / (1+z)$ for SMGs in the ECDFS with our initial photometric redshift estimates. We distinguish between high and low quality spectroscopic redshifts as determined by the flags provided in most archival catalogues, and highlight the two likely QSOs (LESS 66 and LESS 96; § 4.3.4). The inset plot shows the histogram of $\Delta z / (1+z)$ for 1796 galaxies and AGN in the ECDFS with spectroscopic redshifts. Qualitatively the photometric redshifts of the 1796 field sources appear to be good representations of their spectroscopic redshifts. However, photometric redshifts of SMGs with $z_{\text{spec}} \gtrsim 2$ appear to be systematically underestimated.

Fig. 4.2 shows spectroscopic redshift against $\Delta z/(1+z)$ for the 30 robust LESS SMG counterparts with spectroscopic redshifts from archival surveys of the ECDFS (10 counterparts) and our spectroscopic survey of SMGs in the ECDFS (20 counterparts). Quality flags are published in many catalogues and where possible we distinguish between high- and low-quality spectroscopic redshifts. Error bars are the HYPERZ 99% confidence intervals, which similarly to Chapter 3 more reasonably represent the 1σ errors; we return to this issue in § 4.3.3.2. The mean (median) $\Delta z/(1+z) = 0.004 \pm 0.18$ (0.05 ± 0.02) for the 30 SMGs (where here and throughout this chapter errors on the median are calculated from bootstrapping), suggesting that on average the photometric redshifts are a good proxy for spectroscopic redshift. However, qualitatively, the photometric redshifts of SMGs with $z_{\text{spec}} \gtrsim 2$ appear to be systematically underestimated. Indeed, the 21 SMGs with $z_{\text{spec}} \geq 2$ have mean (median) $\Delta z/(1+z) = 0.065 \pm 0.10$ (0.06 ± 0.02).

The statistics suggest that for the 17-band photometry and the HYPERZ set-up described above the photometric redshifts are underestimated for SMGs with $z > 2$. In fact, an equivalent analysis of the field galaxies also shows this behaviour, whereby the median $\Delta z/(1+z) = 0.09 \pm 0.007$ for galaxies at $z \geq 2$, compared to 0.01 ± 0.002 for galaxies at $z < 2$, indicating that the cause of this systematic error is not specific to SMGs. A significant fraction of SMGs are expected to have $z > 2$ (Chapman et al. 2005) and thus to be able to thoroughly and unbiasedly investigate SMG properties (as we do in Chapters 5 and 6) photometric redshifts which are not systematically underestimated are required.

At $z \gtrsim 3$ galaxies will “dropout” of U -band imaging due to Lyman- α absorption (similarly at $z \gtrsim 4$ they dropout of the B -band, and at $z \gtrsim 5$ the V -band is also affected). That photometric redshifts are systematically underestimated only in high redshift galaxies suggests that there is a mismatch between the observed and the template SEDs at the shortest wavelengths. In particular, it suggests that there may be a mismatch between the observed U -band photometry and the model SEDs at this wavelength, with the models underpredicting the detectable flux and/or the observations over-stating the received flux. We now investigate the possible causes and potential fixes of this bias.

U -band zeropoint offset:

In order to estimate the size of the mismatch between the models and the measured photometry we incrementally change the zeropoint of the VIMOS U -band photometry. We use the VIMOS U -band because it is > 1 mag deeper than the two MUSYC U -bands and many of the $z = 2$ – 3 SMGs observed are only detected in this filter, providing

significant constraints on the photometric redshift. In the left-hand panel of Fig. 4.3 we plot the median Δz for the LESS SMGs at each offset in U -band zeropoint applied. It is clear that to derive accurate photometric redshifts for $z = 2-3$ SMGs by simply modifying the photometry the U -band zeropoint is required to be $\gtrsim 1$ mag fainter than its original calibration, which, given the precision of the U -band zeropoint, is hard to justify. Moreover, as we show in the left-hand panel of Fig. 4.3 a +1 mag offset to the VIMOS U -band zeropoint also causes a significant increase in the scatter in the photometric redshifts of the $z \lesssim 2$ SMGs. We conclude that it is inappropriate to simply increase the U -band magnitudes, since any change to the photometric redshift calculations with the purpose of removing the systematic error in $z \gtrsim 2$ SMGs must affect only the high-redshift SMGs. Therefore, we next consider alternative methods of correcting the $z \gtrsim 2$ offset.

Additional templates:

Since we require a change to the fitting routine that does not necessarily affect the low redshift SMGs we consider the affect of including additional model templates. As expected from our tests of photometric redshifts in Chapter 3, we find that including S0, Sa, Sc, Sd SED templates in addition to the Burst, E, Sb and Im templates that were originally included does not significantly affect the photometric redshifts and the systematic error for $z = 2-3$ galaxies remains.

Limiting magnitudes:

We next investigate the effect of changing the handling of undetected SMGs on the photometric redshifts. HYPERZ has four options for handling undetected sources:

1. Ignore the filter in the calculation
2. Set the flux in the filter to zero and the photometric error to the equivalent of the limiting magnitude
3. The flux and its error are each set to half the limiting magnitude
4. The flux and its error are each set to the limiting magnitude

We had been using the second option using the 3σ limiting magnitudes listed in Table 4.2. However, we note that HYPERZ performs a χ^2 fitting to determine the photometric redshift. Therefore, using the 3σ limiting magnitudes as the error provides weaker constraints on the fluxes of undetected sources than we actually have, and will lead to artificially small χ^2 values. In addition, it means that galaxies can be fitted at lower redshifts than if 1σ limiting magnitudes are employed without the χ^2 being prohibitively high. Therefore,

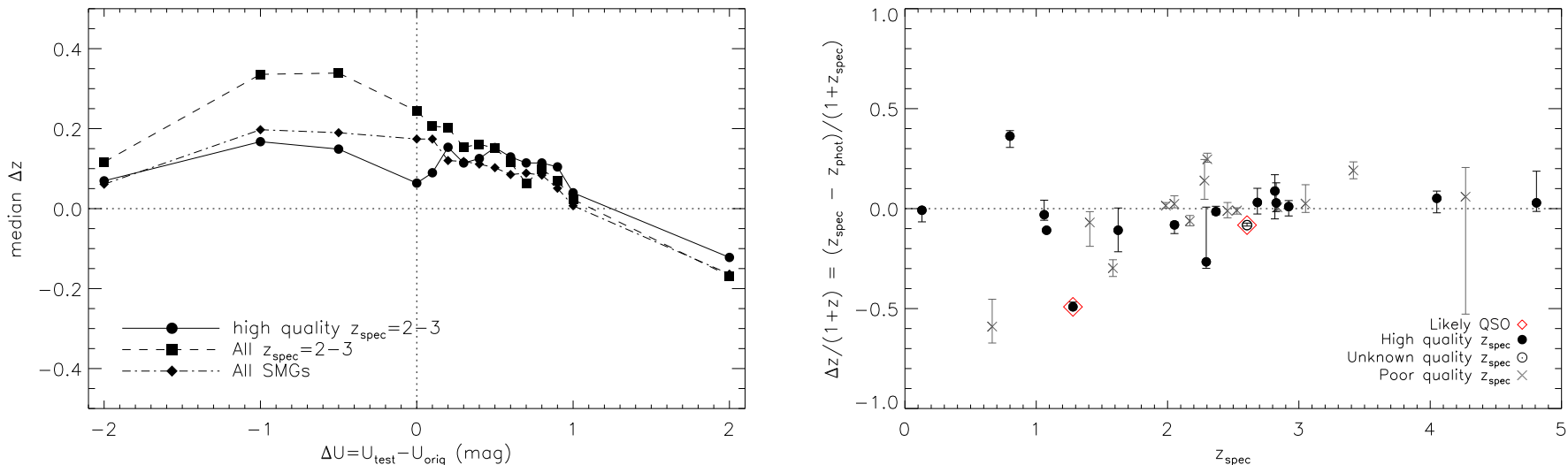


Figure 4.3: [left] Plot of median Δz against the change in the VIMOS U -band magnitude, where ΔU is the amount added to the extracted VIMOS U -band magnitude. This graph shows that to derive accurate photometric redshifts for LESS SMGs with $z = 2-3$ by simply modifying the VIMOS U -band zeropoint the U -band photometry needs to be $\gtrsim 1$ magnitude fainter than originally measured. [right] $\Delta z / (1+z)$ for SMGs when a zeropoint offset of +1 mag is applied to the VIMOS U -band photometry. The $z = 2-3$ SMGs no longer have systematically underestimated photometric redshifts. However, the scatter in Δz of the $z \lesssim 2$ SMGs has increased significantly. This suggests that a photometric offset in the U -band magnitudes is not the origin of the biased photometric redshifts at $z \gtrsim 2$ and we conclude that it is more likely to be due to the details of Lyman- α absorption modelling in HYPERZ.

we recalculate the photometric redshifts using the 1σ limiting magnitudes as the photometric error and find that this does marginally improve the accuracy of the photometric redshifts, although a significant bias at $z \gtrsim 2$ remains.

Lyman- α forest:

By default HYPERZ considers only one value for the Lyman- α forest absorption at each redshift, calculated according to Madau (1995). Given the systematic underestimation of photometric redshifts at $z \gtrsim 2$ we hypothesise that the Lyman- α absorption in HYPERZ is too strong – such that high-redshift galaxies are estimated to be at lower redshifts than they really are because the expected flux in the short wavelength filters is less than that observed. In HYPERZ v10.0 the “LY_FOREST” parameter allows three different values of the optical depth to be considered in calculating the strength of absorption in the Lyman- α forest. The three values of optical depth are τ_{eff} , $\tau_{\text{eff}} \times \text{LY_FOREST}$ and $\tau_{\text{eff}}/\text{LY_FOREST}$, where τ_{eff} is fixed and set in the HYPERZ source code.

We experimented with different values of LY_FOREST, for both the SMGs and the larger field sample, and found a small improvement in the accuracy of the photometric redshifts when three values were allowed, but that the systematic offset was not entirely removed. We believe that although in some cases the photometric redshift is improved, in many cases the χ^2 analysis favours the fit with the original optical depth. To force HYPERZ to consider models with less Lyman- α absorption we edit the source code to decrease the intragalactic absorption in the models. In the Oke & Korycansky (1982) prescription Lyman- α absorption is characterised by the depressing factors D_A and D_B , which quantify the absorption between Lyman- α and Lyman- β , and between Lyman- β and the Lyman limit, respectively. HYPERZ uses $\langle D_A \rangle$ and $\langle D_B \rangle$ – corresponding to D_A and D_B averaged over all lines of sight – as calculated by (Madau 1995) – to incorporate Lyman- α absorption in the photometric redshift estimates. We reduce the Lyman- α absorption by setting $\text{da}_{\text{new}} = 3\text{da}_{\text{orig}}$ and $\text{db}_{\text{new}} = 3\text{db}_{\text{orig}}$, where $\text{da} = 1 - \langle D_A \rangle$ and $\text{db} = 1 - \langle D_B \rangle$. In addition we simultaneously force the code to consider three values of optical depth: $0.5\tau_{\text{eff}}$, τ_{eff} and $2\tau_{\text{eff}}$. We find that with the slightly less intragalactic absorption than default the systematic offset in photometric redshifts for SMGs at $z \gtrsim 2$ is minimised, and the lower-redshift SMGs are not affected. This is also true of the larger sample of field galaxies, and in § 4.3.3 we next perform a detailed analysis of the accuracy of the resulting photometric redshifts.

4.3.3 Reliability of photometric redshifts

To test the reliability of the photometric redshifts calculated with 1σ limiting magnitudes and weaker Lyman- α absorption (z_{phot}) we again initially compare them to the spectroscopic redshifts (z_{spec}) for 1796 galaxies and AGN in the ECDFS and calculate $\Delta z = z_{\text{spec}} - z_{\text{phot}}$ for each source. The histogram of $\Delta z/(1+z)$ for these 1796 sources is shown as an inset in Fig. 4.4; the sample is centered on $\Delta z/(1+z) = 0.016 \pm 0.002$ and has a 1σ dispersion of 0.05. For sources at $z > 2$ the median $\Delta z/(1+z) = 0.067 \pm 0.01$, which is a modest improvement on the initial case. We define outliers as sources with $|\Delta z|/(1+z) > 0.3$; the outlier fraction for these 1796 field galaxies and AGN is 0.15. We also calculate the outlier resistant normalised median absolute deviation (NMAD) of Δz , $\sigma_{\text{NMAD}} = 1.48 \times \text{median}(|\Delta z - \text{median}(\Delta z)|/(1+z)) = 0.097$. These statistics show that our photometric redshifts are a good proxy for spectroscopic redshift for these sources.

Fig. 4.4 also shows spectroscopic redshift against $\Delta z/(1+z)$ for the 30 robust LESS SMG counterparts with spectroscopic redshifts. The median $\Delta z/(1+z)$ for SMGs is 0.023 ± 0.021 the mean $\Delta z/(1+z) = -0.013 \pm 0.178$, and $\sigma_{\text{NMAD}} = 0.037$, suggesting that for SMGs our photometric redshifts are reliable. We caution that the SMGs without spectroscopic redshifts are fainter on average than the SMGs with spectroscopic redshifts, which could affect the quality of their photometric redshifts.

4.3.3.1 Comparison to other photometric redshift codes

Dunlop et al. (2009) have independently calculated photometric redshifts for the six LESS SMGs (five with robust counterparts) in GOODS-South that were also detected by BLAST at $250\ \mu\text{m}$ (Devlin et al. 2009). Their photometry uses imaging from *HST* (B_{435} , V_{606} , i_{775} , z_{850}), the VLT (J , H , K) and *Spitzer* (3.6, 4.5, 5.8 and $8\ \mu\text{m}$) and they use HYPERZ with the stellar population models of Charlot & Bruzual (e.g. Bruzual 2007) which have a Salpeter IMF. The five SMGs with photometric redshifts from Dunlop et al. (2009, D09) are: LESS 10a ($z_{\text{D09}} = 2.29_{-0.24}^{+0.06}$), LESS 12 ($z_{\text{D09}} > 2.50$), LESS 18 ($z_{\text{D09}} = 1.94_{-0.09}^{+0.16}$), LESS 67 ($z_{\text{D09}} = 2.09_{-0.44}^{+0.31}$) and LESS 79 ($z_{\text{D09}} = 1.85_{-0.15}^{+0.10}$). In all cases the Dunlop et al. (2009) photometric redshifts agree with those calculated here (see Table 4.5), providing further confidence that our photometric redshifts are reasonable for SMGs.

To assess the level of systematic uncertainties for the derived photometric redshifts due to the adopted methodology, SED templates, and/or photometric data, we also use

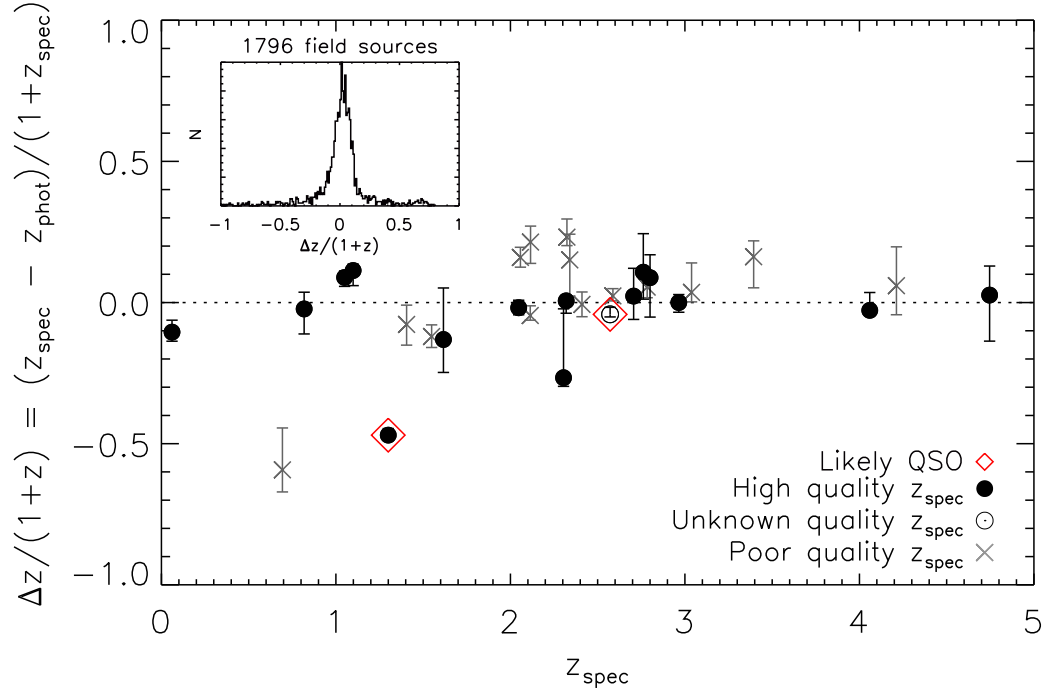


Figure 4.4: Spectroscopic redshift against $\Delta z / (1+z)$ for our most reliable photometric redshifts of LESS SMGs. We distinguish between high and low quality spectroscopic redshifts as determined by the flags provided in most archival catalogues, and highlight the two likely QSOs (LESS 66 and LESS 96; § 4.3.4). The median (mean) $\Delta z / (1+z)$ for all the SMGs is 0.023 ± 0.021 (-0.013 ± 0.178). The inset plot shows the histogram of $\Delta z / (1+z)$ for 1796 galaxies and AGN in the ECDFS with spectroscopic redshifts. The distribution is centered on 0.016 ± 0.002 and has a 1σ dispersion of 0.05. We conclude that our photometric redshifts are a good proxy for spectroscopic redshifts for both samples.

ZEBRA (Feldmann et al. 2006) to calculate photometric redshifts. Our adopted procedure is similar to that discussed in §3.2 of Luo et al. (2010). Briefly, we use ZEBRA to obtain a maximum-likelihood estimate for the photometric redshifts of individual galaxies or AGNs using an initial set of 265 galaxy, AGN, and galaxy/AGN hybrid SED templates. These SED templates were then expanded to 463 templates during the template-training mode of ZEBRA to best represent the SEDs of the ≈ 2 Ms CDFS X-ray sources (Luo et al. 2010), including AGN. Besides the different SED templates used, this method differs from the HYPERZ approach described in § 4.3.2 in some additional details such as how the redshift intervals and minimum photometric errors are determined; see §3.2 of Luo et al. (2010) for details.

The ZEBRA-derived photometric redshifts ($z_{\text{phot,check}}$) were compared to those listed in Table 4.5 (z_{phot}); the difference was measured by $\delta z_{\text{phot}} = (z_{\text{phot,check}} - z_{\text{phot}})/(1 + z_{\text{phot}})$. For sources with secure spectroscopic redshifts, individual $|\delta z_{\text{phot}}|$ values range from ≈ 0.01 to 0.10, indicating that both methods are able to deliver photometric redshifts to a similar accuracy. For the full sample, the mean (median) value of δz_{phot} is -0.006 (0.011), with an rms scatter of 0.028, suggesting that the photometric redshifts in Table 4.5 are fairly robust. After accounting for the effective 1σ errors of the photometric redshifts, only three (sources LESS 7, LESS 37 and LESS 111) of the 74 sources have inconsistent z_{phot} and $z_{\text{phot,check}}$. As some sources have photometry data in addition to those presented in Tables 4.3 and 4.4, we also tested the effect of including more data points. The photometric redshifts differ by a mean value of $|\delta z_{\text{phot}}|$ of 0.024 with an rms error of 0.030, after including the WFI *R*-band data (Giacconi et al. 2002; Giavalisco et al. 2004) for 25 sources and the *GALEX* near-UV and far-UV data (Morrissey et al. 2007) for 3 sources. Given the small difference caused by the additional data, we consider the consistent aperture photometry in Table 2 suitable for the purpose of deriving reliable photometric redshifts.

4.3.3.2 Photometric redshifts of LESS SMGs

We conclude that the most accurate photometric redshifts, for galaxies (including SMGs) in the ECDFS, including those at $z \gtrsim 2$ are determined using the following parameters in HYPERZ:

- Bruzual & Charlot (1993) Burst, E, Sb and Im SED templates.
- Redshifts $z = 0-7$ in steps of 0.05 are considered, and the step size is automatically

reduced to 0.005 when the most probable region of redshift space is located.

- The Calzetti et al. (2000) reddening law is used, with $A_V = 0\text{--}5$ mag in steps of 0.1 mag.
- Galaxies are assigned zero flux in any filter in which they are not detected, with an error equal to the 1σ detection limit of that filter.
- The handling of the Lyman- α forest in HYPERZ is modified, such that intragalactic absorption in the models is decreased and three different levels of absorption are considered in the fitting process.
- 1σ errors in the redshift are represented by the HYPERZ 99% confidence intervals.

The final photometric redshifts of all LESS SMGs, calculated using these parameters, are presented in Table 4.5. In Fig. 4.6 we show the photometry and best-fit SEDs for all 74 robust LESS SMG counterparts.

In Table 4.5 we also provide the reduced χ^2 of the best fit SED at the derived photometric redshift and the number of filters in which the SMG was detected and undetected (but observed). We caution that the reduced χ^2 for galaxies with only a few photometric detections is typically low ($\lesssim 0.5$) but the error on the photometric redshift is typically large, since there are only weak limits on the SED from the photometry. Therefore, the values of the reduced χ^2 should be considered in conjunction with the number of photometric detections when considering the reliability of the photometric redshifts.

The median reduced χ^2 of the SMG counterparts is 2.3 (2.1 if only the galaxies with reduced $\chi^2 \leq 10$ are considered); this slightly inflated average χ^2 is related to the apparently over-precise 68% photometric redshift limits. Therefore, we investigate possible causes of the slightly inflated median χ^2 . We begin by repeating the photometric redshift calculations with the flux limits ignored in the fitting, such that the χ^2 values do not have a contribution from limiting magnitudes, and find that the median reduced χ^2 is still ~ 2 and higher than expected, suggesting that the photometric limits are not driving the large values. An alternative explanation is that our photometric errors are slightly underestimated. Therefore, we next investigate whether and a small number of photometric bands are the cause of the majority of the contribution to this inflated reduced χ^2 . We consider the average contribution of each band to the χ^2 of the best-fit SED at the spectroscopic redshift by calculating $\chi_{\text{filt}}^2 = (\text{observed mag} - \text{model mag})^2 / \text{error}^2$. In all cases $> 50\%$ of sources have $\chi_{\text{filt}}^2 \leq 1$, and none of the filters have a significant offset or

broader distribution than the others. This suggests that the inflated reduced χ^2 for the best-fit SEDs is not a result of underestimated photometric errors in a small number of filters, but is more likely to be the result of a general mis-match between the models and the photometry. Since we have empirically determined that the HYPERZ 99% confidence intervals more reliably represent the 1σ errors and we have been unable to isolate and remove the cause, we use the HYPERZ 99% confidence intervals on the photometric redshift estimates to represent the $1-\sigma$ uncertainty throughout this Chapter and Chapters 5 and 6.

Of the 74 robust SMG counterparts examined there are eight with poor fits of the SED to the photometry (indicated with reduced $\chi^2 > 10$). Of these, one (LESS 39) is blended in the optical imaging and two others (LESS 66 and LESS 81) lie in stellar halos. LESS 66 is also likely to be a QSO, as is LESS 96 (§ 4.3.4), and another four SMGs with reduced $\chi^2 > 10$ (LESS 19, LESS 57, LESS 75 and LESS 111) have excess $8\ \mu\text{m}$ flux compared to the best-fit SED, which is indicative of a hot-dust component, possibly caused by an AGN (see §4.3.4 for a full discussion). Since we did not include any QSO or AGN templates in the fitting procedure it is unsurprising that these sources are not well represented by the employed SEDs. However, we note here that, as we show in §4.3.4, the exclusion of AGN templates does not bias our photometric redshift estimates.

4.3.4 The effect of AGN on photometric redshifts

As briefly discussed in Chapter 3 our photometric redshift calculations are based on fitting stellar templates to the SMG photometry, yet studies have shown that the $8\ \mu\text{m}$ flux in SMGs with a significant AGN component can be dominated by the AGN (Hainline et al. 2009, 2010; Coppin et al. 2010b) and therefore fitting stellar templates may yield misleading results. With the larger sample of SMGs with spectroscopic redshifts in the ECDFS we now further investigate the effect of AGN on the photometric redshift estimates.

We employ two methods to identify potential AGN in the LESS SMGs. Firstly, we cross-correlate the LESS SMG counterparts with the *Chandra* X-ray catalogues of the CDFS (Luo et al. 2008) and ECDFS (Lehmer et al. 2005). The Lehmer et al. (2005) catalogue contains ~ 800 sources detected in a *Chandra* 250 ks exposure of the ECDFS, and the Luo et al. (2008) catalogue details ~ 500 sources detected in 2 Ms of *Chandra* data in the smaller CDFS. We use a radius of $1''$ to match the *Chandra* and LESS counterparts, and find 12 X-ray luminous SMGs – five in the ECDFS, three in the CDFS and four are detected both fields, due to overlap between the observations. Secondly, we identify nine

Table 4.5: The catalogue of 74 robust counterparts to LESS SMGs that are detected at optical or near-infrared wavelengths, and their photometric redshifts. We also provide the reduced χ^2 of the best-fit SED and the number of photometric filters in which each galaxy is observed.

SMG ^a	Short name	RA ^b	Dec ^b	z_{phot}^c	$\chi_{\text{red}}^2{}^d$	Filters ^e	ID type ^f
LESSJ033302.5-275643	LESS 2a	03 ^h 33 ^m 02 ^s :55	-27°56′44″.7	1.80 ^{+0.35} _{-0.14}	2.8	16 [1]	M
LESSJ033302.5-275643	LESS 2b	03 ^h 33 ^m 02 ^s :68	-27°56′42″.6	2.27 ^{+0.16} _{-0.55}	1.1	8 [9]	R
LESSJ033321.5-275520	LESS 3	03 ^h 33 ^m 21 ^s :50	-27°55′20″.1	3.92 ^{+0.54} _{-0.72}	0.5	5 [10]	M
LESSJ033257.1-280102	LESS 6	03 ^h 32 ^m 57 ^s :15	-28°01′01″.5	0.40 ^{+0.09} _{-0.03}	4.3	16 [1]	RM
LESSJ033315.6-274523	LESS 7	03 ^h 33 ^m 15 ^s :41	-27°45′24″.0	2.81 ^{+0.18} _{-0.07}	6.9	16 [1]	RM
LESSJ033211.3-275210	LESS 9	03 ^h 32 ^m 11 ^s :35	-27°52′12″.9	4.63 ^{+0.10} _{-1.10}	2.4	6 [9]	RM
LESSJ033219.0-275219	LESS 10a	03 ^h 32 ^m 19 ^s :04	-27°52′14″.3	2.46 ^{+0.15} _{-0.15}	6.0	12 [5]	R
LESSJ033219.0-275219	LESS 10b	03 ^h 32 ^m 19 ^s :30	-27°52′19″.1	0.91 ^{+0.07} _{-0.05}	4.5	15 [2]	R
LESSJ033213.6-275602	LESS 11	03 ^h 32 ^m 13 ^s :84	-27°55′59″.8	2.60 ^{+0.30} _{-0.36}	3.2	7 [9]	R
LESSJ033248.1-275414	LESS 12	03 ^h 32 ^m 47 ^s :96	-27°54′16″.1	3.92 ^{+1.02} _{-2.11}	0.1	6 [11]	RM
LESSJ033152.6-280320	LESS 14	03 ^h 31 ^m 52 ^s :47	-28°03′18″.6	3.56 ^{+0.92} _{-0.56}	0.8	7 [9]	RM
LESSJ033333.4-275930	LESS 15	03 ^h 33 ^m 33 ^s :35	-27°59′29″.4	1.95 ^{+3.05} _{-0.39}	0.2	4 [8]	M
LESSJ033218.9-273738	LESS 16	03 ^h 32 ^m 18 ^s :70	-27°37′43″.5	1.09 ^{+0.08} _{-0.09}	4.1	17 [0]	R
LESSJ033207.6-275123	LESS 17	03 ^h 32 ^m 07 ^s :26	-27°51′20″.1	1.55 ^{+0.11} _{-0.11}	1.0	17 [0]	RM
LESSJ033205.1-274652	LESS 18	03 ^h 32 ^m 04 ^s :87	-27°46′47″.4	2.07 ^{+0.08} _{-0.09}	2.4	16 [1]	RM
LESSJ033208.1-275818	LESS 19	03 ^h 32 ^m 08 ^s :23	-27°58′13″.7	2.11 ^{+0.11} _{-0.10}	10.3	10 [6]	RI
LESSJ033316.6-280018	LESS 20	03 ^h 33 ^m 16 ^s :77	-28°00′15″.8	2.80 ^{+0.17} _{-0.27}	2.2	9 [7]	RM
LESSJ033147.0-273243	LESS 22	03 ^h 31 ^m 46 ^s :90	-27°32′38″.8	1.95 ^{+0.34} _{-0.38}	2.4	6 [4]	RM
LESSJ033336.8-274401	LESS 24	03 ^h 33 ^m 36 ^s :97	-27°43′58″.1	1.72 ^{+0.29} _{-0.36}	2.6	11 [2]	RM
LESSJ033157.1-275940	LESS 25	03 ^h 31 ^m 56 ^s :85	-27°59′38″.9	2.28 ^{+0.09} _{-0.15}	3.0	13 [2]	RM
LESSJ033149.7-273432	LESS 27a	03 ^h 31 ^m 49 ^s :88	-27°34′30″.4	2.10 ^{+1.00} _{-0.88}	0.1	4 [11]	I
LESSJ033149.7-273432	LESS 27b	03 ^h 31 ^m 49 ^s :92	-27°34′36″.7	2.46 ^{+0.42} _{-0.72}	1.9	7 [6]	MI
LESSJ033336.9-275813	LESS 29	03 ^h 33 ^m 36 ^s :88	-27°58′08″.8	2.64 ^{+4.36} _{-0.87}	0.1	4 [8]	R
LESSJ033150.0-275743	LESS 31	03 ^h 31 ^m 49 ^s :77	-27°57′40″.4	3.63 ^{+0.84} _{-0.70}	0.3	6 [9]	I
LESSJ033217.6-275230	LESS 34	03 ^h 32 ^m 17 ^s :60	-27°52′28″.1	0.86 ^{+0.11} _{-0.05}	3.8	17 [0]	M
LESSJ033149.2-280208	LESS 36	03 ^h 31 ^m 48 ^s :94	-28°02′13″.6	2.49 ^{+0.53} _{-0.31}	0.3	7 [7]	RM
LESSJ033336.0-275347	LESS 37	03 ^h 33 ^m 36 ^s :01	-27°53′49″.4	3.52 ^{+0.26} _{-0.36}	4.0	11 [1]	M
LESSJ033144.9-273435	LESS 39	03 ^h 31 ^m 45 ^s :00	-27°34′36″.3	2.59 ^{+0.16} _{-0.06}	12.6	13 [1]	RM
LESSJ033246.7-275120	LESS 40	03 ^h 32 ^m 46 ^s :77	-27°51′20″.7	1.90 ^{+0.10} _{-0.11}	3.1	17 [0]	RM
LESSJ033110.5-275233	LESS 41	03 ^h 31 ^m 10 ^s :09	-27°52′36″.3	2.74 ^{+4.26} _{-0.91}	0.0	4 [0]	I
LESSJ033307.0-274801	LESS 43	03 ^h 33 ^m 06 ^s :63	-27°48′01″.9	1.67 ^{+0.23} _{-0.14}	2.0	8 [9]	MI
LESSJ033131.0-273238	LESS 44	03 ^h 31 ^m 31 ^s :19	-27°32′38″.6	2.49 ^{+0.00} _{-0.08}	2.8	11 [0]	RM
LESSJ033256.0-273317	LESS 47	03 ^h 32 ^m 55 ^s :99	-27°33′18″.9	2.90 ^{+0.14} _{-0.42}	1.5	8 [6]	MI
LESSJ033237.8-273202	LESS 48	03 ^h 32 ^m 38 ^s :00	-27°31′59″.4	1.91 ^{+0.36} _{-0.43}	0.2	4 [1]	RM
LESSJ033124.5-275040	LESS 49a	03 ^h 31 ^m 24 ^s :45	-27°50′37″.5	1.50 ^{+0.15} _{-0.10}	5.0	12 [1]	RM
LESSJ033124.5-275040	LESS 49b	03 ^h 31 ^m 24 ^s :69	-27°50′46″.4	3.31 ^{+0.22} _{-0.38}	0.7	11 [2]	R
LESSJ033141.2-274441	LESS 50a	03 ^h 31 ^m 41 ^s :11	-27°44′42″.4	0.85 ^{+0.16} _{-0.11}	2.3	17 [0]	M
LESSJ033141.2-274441	LESS 50b	03 ^h 31 ^m 40 ^s :97	-27°44′34″.8	2.69 ^{+0.49} _{-0.25}	7.6	11 [5]	RM
LESSJ033243.6-273353	LESS 54	03 ^h 32 ^m 43 ^s :62	-27°33′56″.6	1.84 ^{+0.62} _{-0.25}	3.7	7 [6]	M
LESSJ033153.2-273936	LESS 56	03 ^h 31 ^m 53 ^s :11	-27°39′37″.3	2.46 ^{+0.41} _{-0.24}	0.6	9 [8]	RM
LESSJ033152.0-275329	LESS 57	03 ^h 31 ^m 51 ^s :93	-27°53′26″.8	2.94 ^{+0.14} _{-0.11}	10.8	11 [6]	RM

Table 4.5: – *continued*

SMG ^a	Short name	RA ^b	Dec ^b	z_{phot}^c	$\chi_{\text{red}}^2{}^d$	Filters ^e	ID type ^f
LESSJ033303.9-274412	LESS 59	03 ^h 33 ^m 03 ^s .62	−27° 44′ 12″.6	1.40 ^{+0.29} _{−0.13}	1.9	13 [4]	RM
LESSJ033317.5-275121	LESS 60	03 ^h 33 ^m 17 ^s .53	−27° 51′ 27″.5	1.64 ^{+0.10} _{−0.24}	5.1	17 [0]	RM
LESSJ033236.4-273452	LESS 62	03 ^h 32 ^m 36 ^s .52	−27° 34′ 53″.0	1.52 ^{+0.10} _{−0.21}	0.8	16 [1]	RM
LESSJ033308.5-280044	LESS 63	03 ^h 33 ^m 08 ^s .49	−28° 00′ 42″.8	1.39 ^{+0.07} _{−0.05}	2.5	15 [1]	RM
LESSJ033201.0-280025	LESS 64	03 ^h 32 ^m 00 ^s .98	−28° 00′ 25″.3	4.19 ^{+0.04} _{−0.32}	1.9	11 [4]	RM
LESSJ033331.7-275406	LESS 66	03 ^h 33 ^m 31 ^s .92	−27° 54′ 10″.3	2.39 ^{+0.04} _{−0.05}	37.2	14 [0]	RM
LESSJ033243.3-275517	LESS 67	03 ^h 32 ^m 43 ^s .18	−27° 55′ 14″.2	2.27 ^{+0.05} _{−0.11}	3.2	16 [1]	RM
LESSJ033144.0-273832	LESS 70	03 ^h 31 ^m 43 ^s .92	−27° 38′ 35″.2	2.31 ^{+0.15} _{−0.06}	3.8	17 [0]	RM
LESSJ033229.3-275619	LESS 73	03 ^h 32 ^m 29 ^s .28	−27° 56′ 18″.9	4.61 ^{+0.94} _{−0.59}	1.1	8 [9]	R
LESSJ033309.3-274809	LESS 74a	03 ^h 33 ^m 09 ^s .34	−27° 48′ 15″.9	1.84 ^{+0.32} _{−0.49}	0.9	10 [6]	RI
LESSJ033309.3-274809	LESS 74b	03 ^h 33 ^m 09 ^s .14	−27° 48′ 16″.6	1.71 ^{+0.20} _{−0.17}	2.5	10 [6]	RI
LESSJ033126.8-275554	LESS 75	03 ^h 31 ^m 27 ^s .17	−27° 55′ 50″.9	2.46 ^{+0.06} _{−0.09}	33.2	15 [0]	RM
LESSJ033221.3-275623	LESS 79	03 ^h 32 ^m 21 ^s .61	−27° 56′ 23″.1	1.41 ^{+0.23} _{−0.17}	2.2	16 [1]	RM
LESSJ033127.5-274440	LESS 81	03 ^h 31 ^m 27 ^s .54	−27° 44′ 39″.5	2.23 ^{+0.13} _{−0.15}	27.9	14 [1]	RM
LESSJ033154.2-275109	LESS 84	03 ^h 31 ^m 54 ^s .49	−27° 51′ 05″.3	2.29 ^{+0.15} _{−0.07}	3.6	14 [3]	I
LESSJ033251.1-273143	LESS 87	03 ^h 32 ^m 50 ^s .83	−27° 31′ 41″.2	3.20 ^{+0.10} _{−0.81}	0.1	5 [0]	RM
LESSJ033155.2-275345	LESS 88	03 ^h 31 ^m 54 ^s .81	−27° 53′ 40″.9	2.35 ^{+0.11} _{−0.10}	1.1	16 [1]	R
LESSJ033313.0-275556	LESS 96	03 ^h 33 ^m 12 ^s .62	−27° 55′ 51″.6	2.71 ^{+0.03} _{−0.09}	22.0	17 [0]	RM
LESSJ033130.2-275726	LESS 98	03 ^h 31 ^m 29 ^s .89	−27° 57′ 22″.4	1.55 ^{+0.17} _{−0.16}	1.0	10 [4]	RM
LESSJ033151.5-274552	LESS 101	03 ^h 31 ^m 51 ^s .53	−27° 45′ 53″.1	2.39 ^{+0.36} _{−0.52}	2.5	10 [7]	R
LESSJ033335.6-274020	LESS 102	03 ^h 33 ^m 35 ^s .56	−27° 40′ 23″.2	1.68 ^{+0.13} _{−0.25}	1.1	11 [2]	M
LESSJ033325.4-273400	LESS 103	03 ^h 33 ^m 25 ^s .37	−27° 33′ 58″.5	1.84 ^{+0.59} _{−0.87}	0.3	5 [7]	M
LESSJ033140.1-275631	LESS 106	03 ^h 31 ^m 40 ^s .17	−27° 56′ 22″.4	1.96 ^{+0.31} _{−0.48}	2.1	11 [5]	RI
LESSJ033316.4-275033	LESS 108	03 ^h 33 ^m 16 ^s .51	−27° 50′ 39″.3	0.20 ^{+0.03} _{−0.05}	6.3	15 [0]	RM
LESSJ033122.6-275417	LESS 110	03 ^h 31 ^m 22 ^s .63	−27° 54′ 17″.0	2.35 ^{+4.65} _{−0.44}	0.0	4 [0]	MI
LESSJ033325.6-273423	LESS 111	03 ^h 33 ^m 25 ^s .21	−27° 34′ 25″.9	2.61 ^{+0.14} _{−0.06}	14.4	13 [0]	RM
LESSJ033249.3-273112	LESS 112	03 ^h 32 ^m 48 ^s .85	−27° 31′ 12″.8	1.81 ^{+0.42} _{−0.30}	0.7	5 [0]	RI
LESSJ033150.8-274438	LESS 114	03 ^h 31 ^m 51 ^s .08	−27° 44′ 37″.0	1.57 ^{+0.08} _{−0.07}	1.6	17 [0]	RM
LESSJ033128.0-273925	LESS 117	03 ^h 31 ^m 27 ^s .62	−27° 39′ 27″.3	1.73 ^{+0.29} _{−0.34}	3.3	9 [4]	R
LESSJ033121.8-274936	LESS 118	03 ^h 31 ^m 21 ^s .91	−27° 49′ 34″.0	2.17 ^{+4.83} _{−1.49}	1.7	5 [1]	R
LESSJ033328.5-275655	LESS 120	03 ^h 33 ^m 28 ^s .55	−27° 56′ 54″.1	1.43 ^{+0.30} _{−0.21}	2.2	13 [3]	RM
LESSJ033139.6-274120	LESS 122	03 ^h 31 ^m 39 ^s .52	−27° 41′ 19″.4	2.08 ^{+0.08} _{−0.08}	5.2	17 [0]	RM
LESSJ033209.8-274102	LESS 126	03 ^h 32 ^m 09 ^s .60	−27° 41′ 06″.9	2.02 ^{+0.17} _{−0.13}	2.4	12 [4]	MI

^aThe SMG names correspond to those in Weiß et al. (2009) and Biggs et al. (2010).

^bCoordinates are the J2000 position of the optical/near-infrared counterpart.

^cSince HYPERZ was restricted to $0 < z < 7$ the six galaxies whose upper redshift limits yield a formal maximum redshift of $z_{\text{max}} = 7$ are actually only constrained in the lower redshift limit. Therefore, throughout this thesis the redshifts of these galaxies are plotted as lower limits.

^dThe reduced χ^2 of the best-fit SED at the derived photometric redshift.

^eThe number of photometric filters in which each SMG counterpart was detected [and the number of filters in which the SMG was observed but not detected, providing a limiting flux].

^fID types R, M and I indicate radio, 24 μm and IRAC identified counterparts respectively (see § 4.2 and Biggs et al. 2010 for details).

SMG counterparts with a large excess of $8\ \mu\text{m}$ flux compared to the best-fit SED template (see Fig. 4.6), which potentially indicates obscured power-law emission from an AGN. This yields 15 SMG counterparts which may contain AGN (six are both X-ray detected and have an $8\ \mu\text{m}$ excess). We also note that LESS 66 and LESS 96 are both X-ray detected, optically bright point sources and are most likely QSOs. Indeed, our VIMOS spectrum of LESS 66 exhibits broad emission lines and the spectroscopic classification (unobscured AGN) of LESS 96 by Treister et al. (2009) also indicates the presence of broad emission lines. In this Section we examine whether the presence of AGN can affect the accuracy of the photometric redshifts and in Chapter 6 we study the LESS AGN in detail.

The photometric redshifts of the 12 LESS AGN that have available spectroscopic redshifts are not systematically offset from the spectroscopic values; the median $\Delta z/(1+z) = -0.018 \pm 0.024$, which is consistent with the whole sample (§ 4.3.3). We determine whether AGN contamination in the $8\text{-}\mu\text{m}$ filter reduces the accuracy of our photometric redshift estimates by re-fitting the photometry of the counterparts that display an $8\text{-}\mu\text{m}$ excess whilst excluding the $8\ \mu\text{m}$ photometry. Spectroscopic redshifts are available for eight of the affected galaxies and we find that the average $|\Delta z|$ of these eight galaxies is not significantly decreased when the $8\ \mu\text{m}$ photometry is excluded from the fitting (median $\Delta z/(1+z) = 0.034 \pm 0.044$). The X-ray detected SMGs may also have some AGN contribution to the $8\text{-}\mu\text{m}$ flux, which is undetected from the best-fit SED. Therefore, we repeat this experiment whilst also excluding the $8\ \mu\text{m}$ photometry of the SMGs which are X-ray detected and find no change in the results.

It is also possible that our sample of SMG counterparts contains some AGN which enhance the $8\ \mu\text{m}$ flux but do not cause a detectable excess. Therefore, we also exclude the $8\ \mu\text{m}$ photometry of *all* the SMG counterparts during the fitting procedure. Once again the average $|\Delta z|$ for the spectroscopic sample does not change significantly (median $\Delta z/(1+z) = 0.032 \pm 0.021$, compared to median $\Delta z/(1+z) = 0.023 \pm 0.021$ originally). These results indicate that when calculating photometric redshifts the benefit of including the longer-wavelength data is greater than the bias which is removed by excluding $8\ \mu\text{m}$ photometry.

4.3.5 Reliability of SED parameters

In addition to calculating photometric redshifts, HYPERZ also returns the spectral type, age and reddening of the best-fit SED template. To test the sensitivity of the choice of template we refit the photometry of the SMGs allowing only the Burst template, and then

only a constant star-formation rate history. These two templates represent the extremes of the star-formation histories and so they enable us gauge the sensitivity of the derived parameters to the choice of the best-fit template.

We compare the quality of the Burst and Im fits of each galaxy with $\Delta\chi_{\text{red}}^2$ – the difference in the reduced χ^2 of the Burst and Im fits. We find that 63% of the SMGs have $|\Delta\chi_{\text{red}}^2| \leq 1$ and as such the Burst and Im templates are indistinguishable at the 99% level for these SMGs. 61% (17) of the SMGs with $|\Delta\chi_{\text{red}}^2| > 1$ between the two template fits are best-fit by Bursts and 39% (11) by Im templates. If three templates – Burst, Sb and Im – are considered the star-formation histories of only 23% (17) of all the SMG counterparts can be distinguished. Therefore, although it may be possible to crudely distinguish the star-formation histories of a fraction ($\sim 20\text{--}40\%$) of SMG counterparts with HYPERZ, the star-formation histories of most SMGs counterparts cannot be reliably established. In Fig. 4.5 we show the best-fit Burst and Im star-formation histories for two SMGs – LESS 2a which has $|\Delta\chi_{\text{red}}^2| = 0.1$, and LESS 49 which has $|\Delta\chi_{\text{red}}^2| = 2.6$. Qualitatively, Fig. 4.5 highlights that the differences between the SEDs of the best-fit Im and Burst models are minor, even when $\Delta\chi_{\text{red}}^2 > 1$, as is the case for LESS 49.

We find that the SMGs that have SED fits with $|\Delta\chi_{\text{red}}^2| \leq 1$ and can be equally well fit by either Burst or Im templates have vastly different age estimates depending on the template. The age and star-formation history of a stellar population significantly affects the light-to-mass ratio; thus our inability to distinguish between star-formation histories leads to uncertainties in the light-to-mass ratios and stellar mass estimates. Using the H -band light-to-mass ratios for Burst and Im models from the STARBURST99 stellar population model (Leitherer et al. 1999) we calculate that the uncertainties in SED fitting parameters result in a 1σ dispersion of a factor of 4.6 in the light-to-mass ratios and consequently in the resulting stellar mass estimates.

We also compare reddening measurements for those galaxies with SED fits with $|\Delta\chi^2| \leq 1$ and find that on average the difference between A_V for the best-fit Im and Burst templates, ΔA_V , is equal to 0.32 ± 0.16 . Since average estimates based on either template return the same value of A_V (to $\sim 2\sigma$) we conclude that average reddening measurements for the SMG population are not strongly sensitive to the adopted star-formation history and are likely to be statistically meaningful (although we caution against trusting values for individual SMGs). When fitting E, Sb, Burst, or Im templates and allowing $A_V = 0\text{--}5$, as in our photometric redshift calculations we determine a median $A_V = 1.5 \pm 0.1$ and 96% of SMGs have $A_V \leq 3$. We conclude that in most instances restricting to $A_V \leq 3$

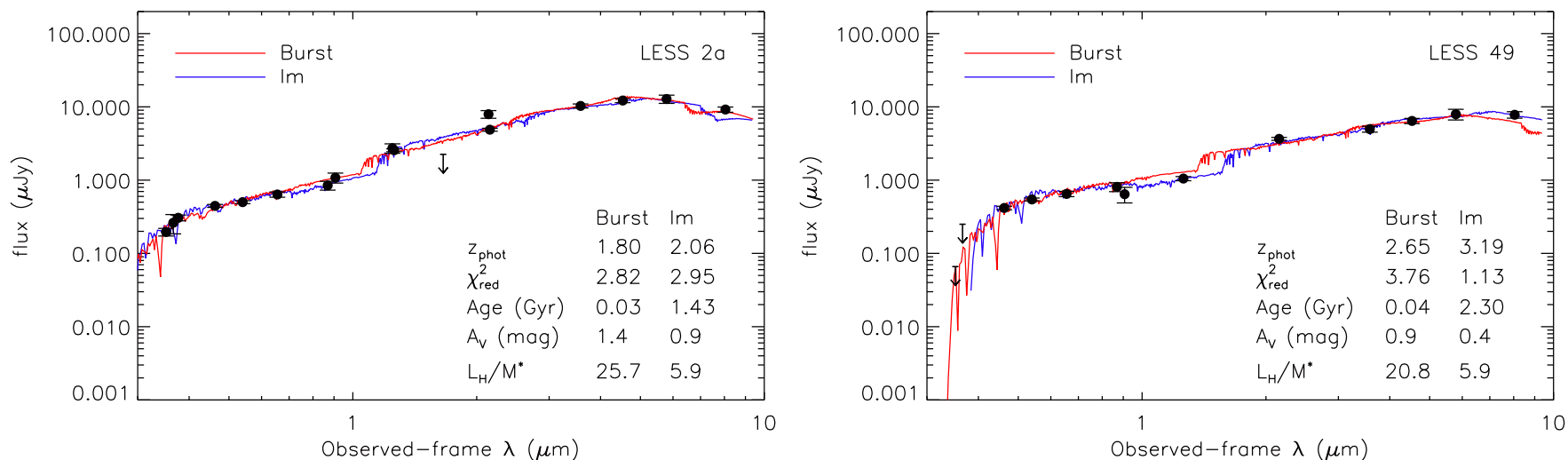


Figure 4.5: Comparison of the best-fit Burst and Im templates for two LESS SMGs. LESS 2a has $|\Delta\chi_{\text{red}}^2| = 0.1$ so the two fits are considered statistically indistinguishable; LESS 49 has $|\Delta\chi_{\text{red}}^2| = 2.6$ and statistically the constant star-formation history (Im) is preferred. It is clear from these examples that the differences between the SEDs of the best-fit Im and Burst models is often minor, yet the different light-to-mass ratios resulting from their star-formation histories is significant.

is sufficient for calculating photometric redshifts of SMGs. We note that these values of A_V are integrated across the whole galaxy and that obscuration in the regions responsible for the majority of the far-infrared/submillimetre emission is considerably larger (e.g. Chapman et al. 2004b; Takata et al. 2006; Ivison et al. 2010b).

4.4 Conclusions

We have extracted 17-band photometry of IRAC-selected sources, including 74 robust counterparts to SMGs from the LESS survey. 30 of these SMG counterparts currently have spectroscopic redshifts from archival surveys and on-going observations of SMGs in the ECDFS.

We have expanded on our analysis of the reliability of photometric redshifts of SMGs from the small sample of 12 galaxies in the CDFN that were analysed in Chapter 3 to investigate, improve and calculate the photometric redshifts of these LESS SMGs. We used the HYPERZ SED fitting code (Bolzonella et al. 2000a) and determined the optimum parameters for reliable photometric redshifts and tested the accuracy of the derived photometric redshifts using spectroscopy.

We found that for reliable photometric redshifts of galaxies at $z \gtrsim 2$ we need to decrease the strength of the intragalactic absorption from the Lyman- α forest compared to the Madau (1995) model. Undetected galaxies in each filter are assigned zero flux with an error equal to the 1σ detection limit in that filter for the photometric redshift calculations. With the reduced Lyman- α absorption the median $\Delta z/(1+z) = 0.023 \pm 0.021$ for the LESS SMGs and we conclude that the photometric redshifts are a reliable proxy for spectroscopic redshift. In Chapters 5 and 6 we use the photometric redshifts derived here to study the properties of the LESS SMGs.

We have also shown that even with extensive 17-band photometry for most SMGs it is not possible to statistically distinguish between different star-formation histories. The mass-to-light ratio is heavily dependent on the star-formation history and age of the galaxy, and therefore, we estimate that there is a factor of ~ 5 uncertainty in the mass-to-light ratios derived from this SED fitting. This factor ~ 5 uncertainty also impacts on accuracy of the stellar masses that can be computed from this analysis (Chapter 5).

4.5 Appendix: LESS SED fits

In Fig. 4.6, for each SMG counterpart, we show the measured photometry and best-fit SED in the observed frame. The calculated photometric redshifts and errors are shown, and the probability distribution functions presented for each galaxy. Most SMGs are well-fit by our template SEDs, although nine have excess $8\ \mu\text{m}$ flux above the best-fit SED, which is likely caused by power-law emission from an AGN. In Chapter 6 we examine these galaxies and other likely LESS AGN in detail.

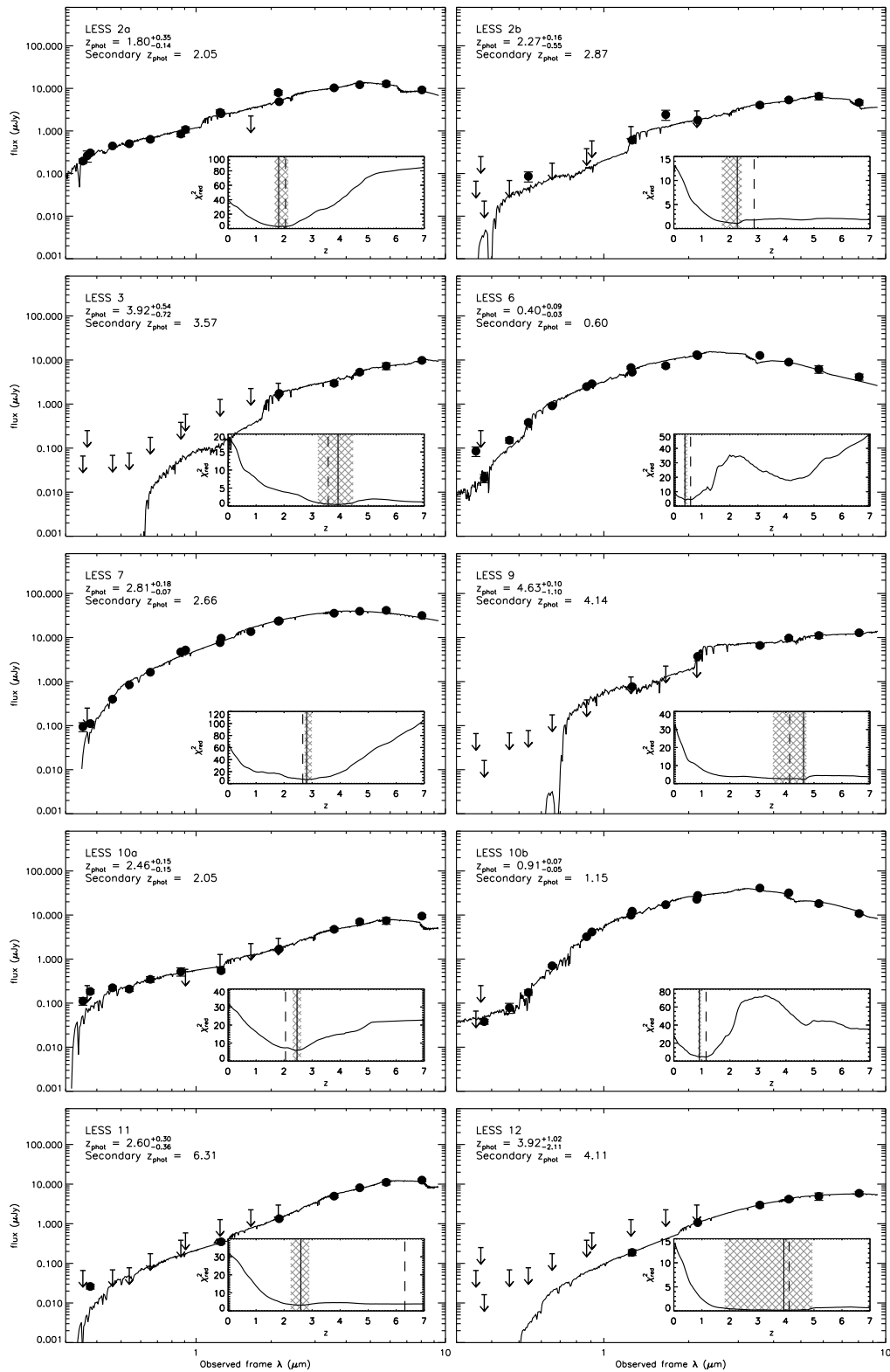
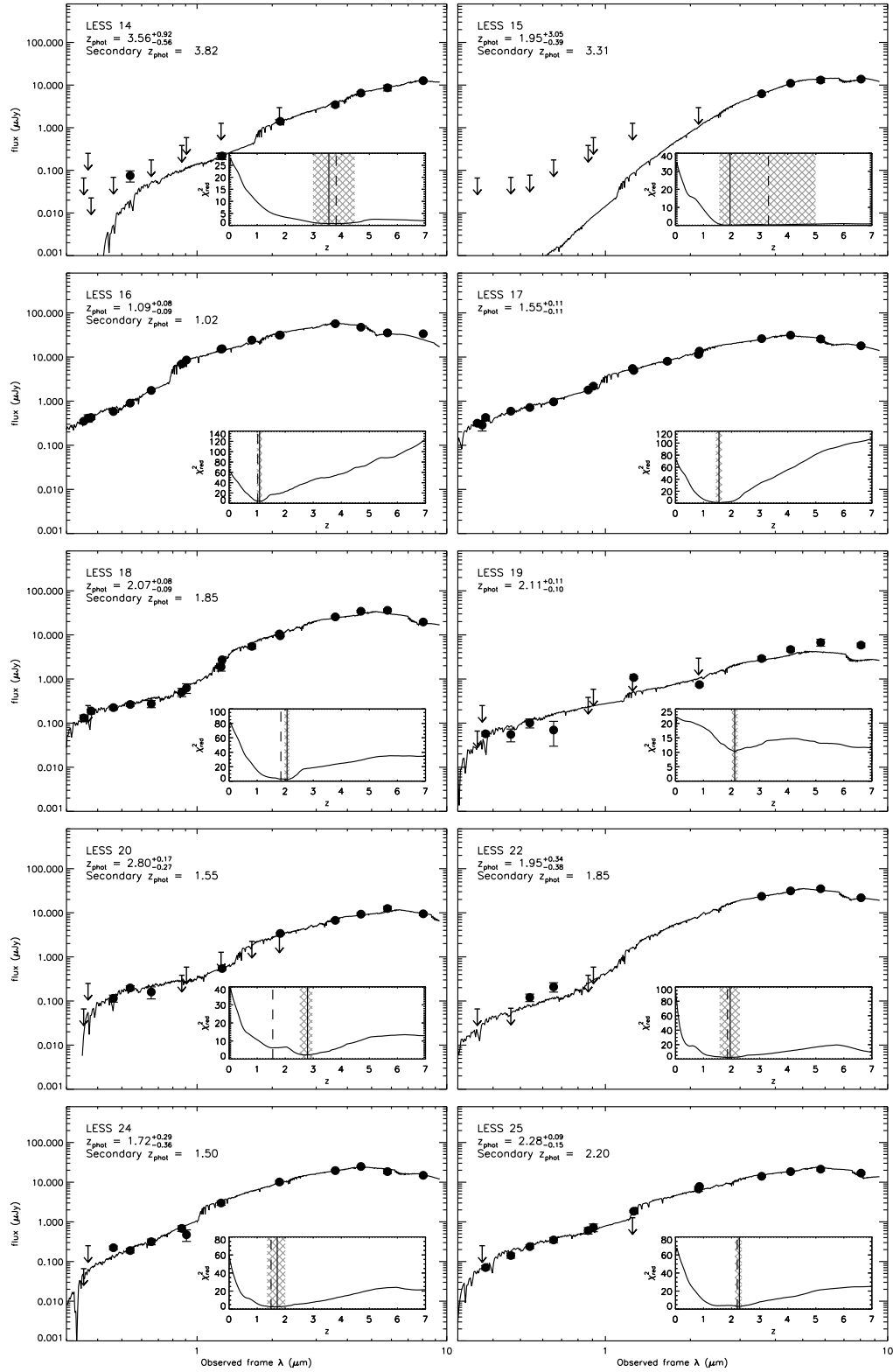
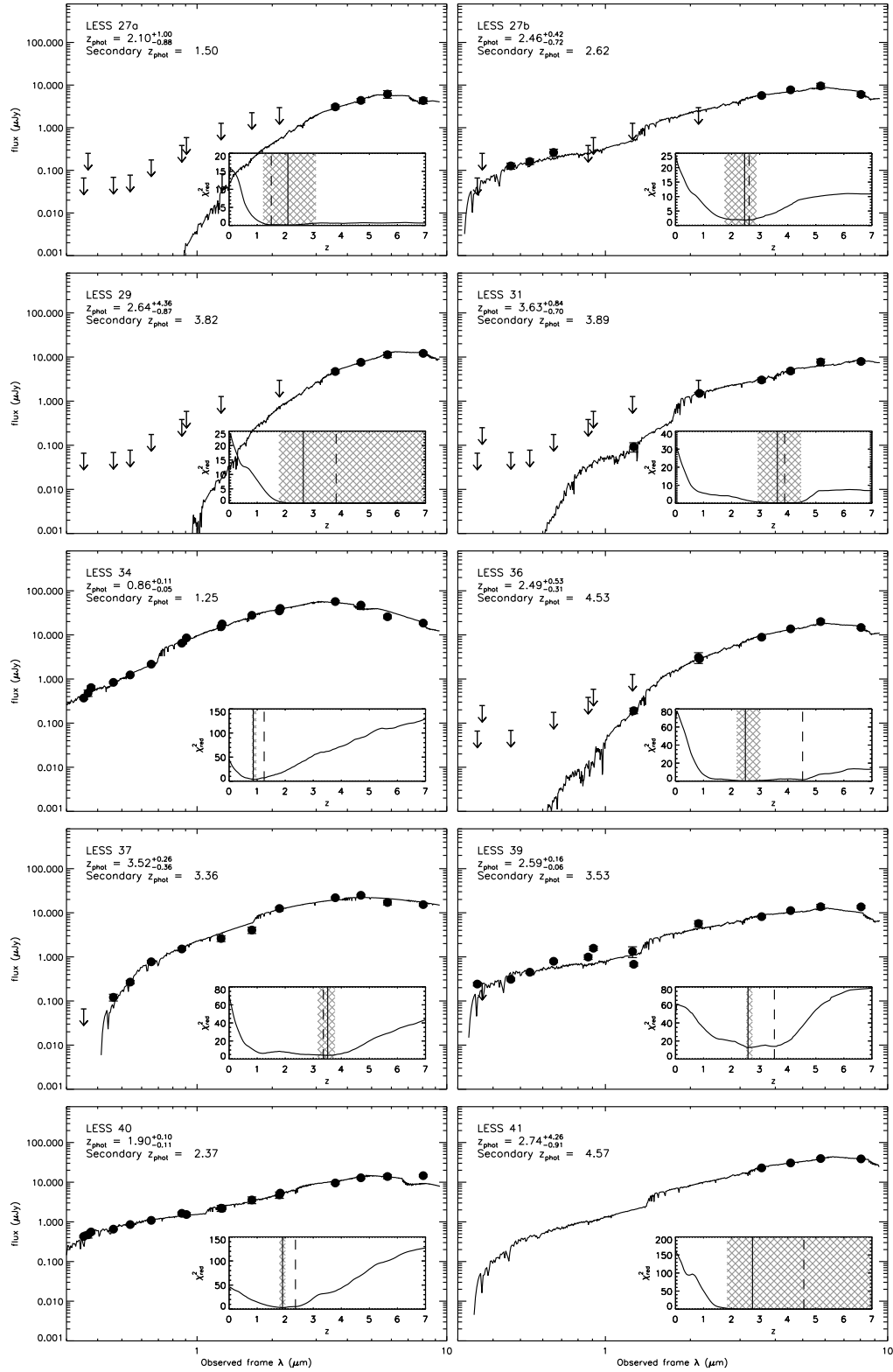
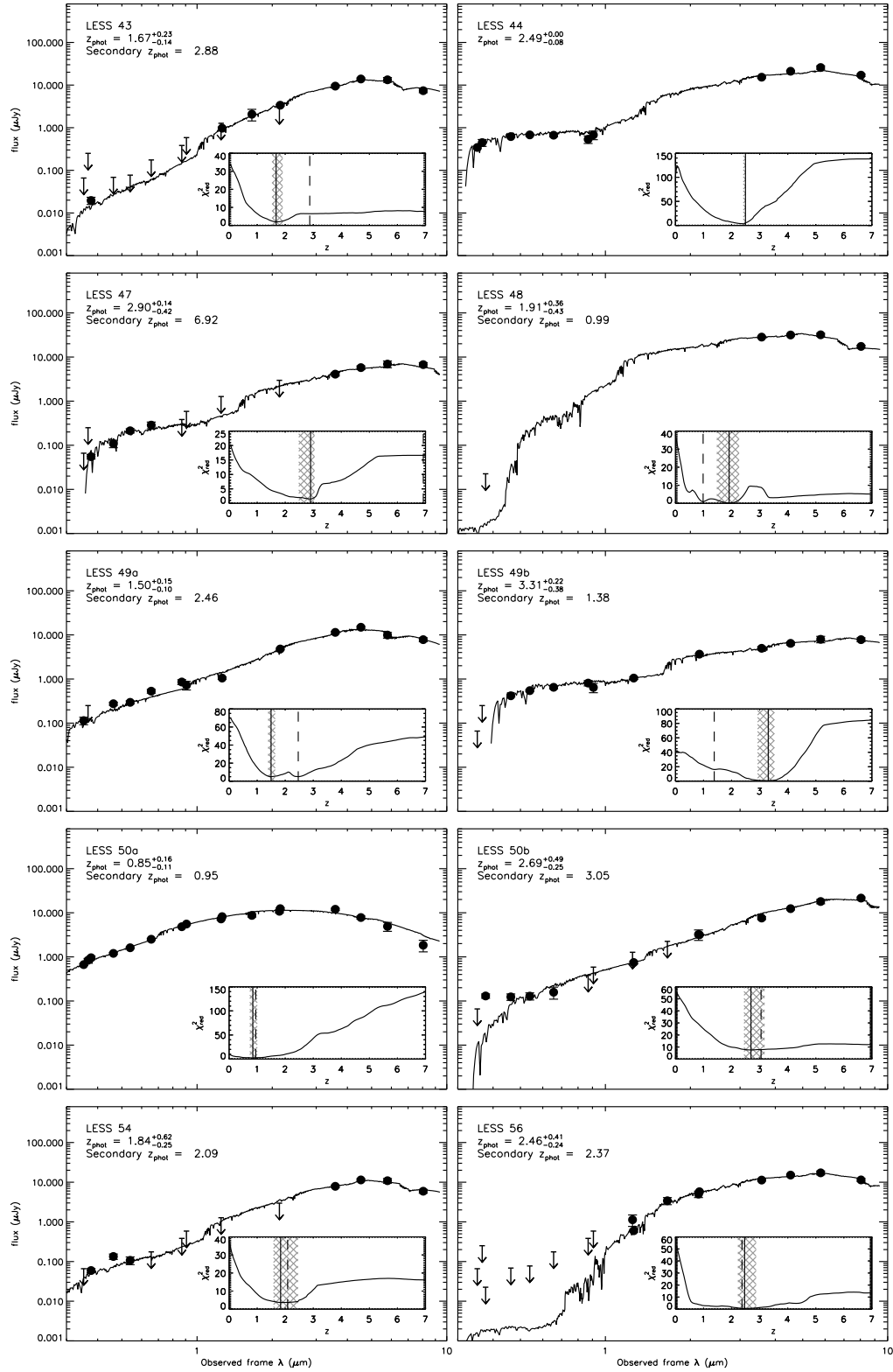
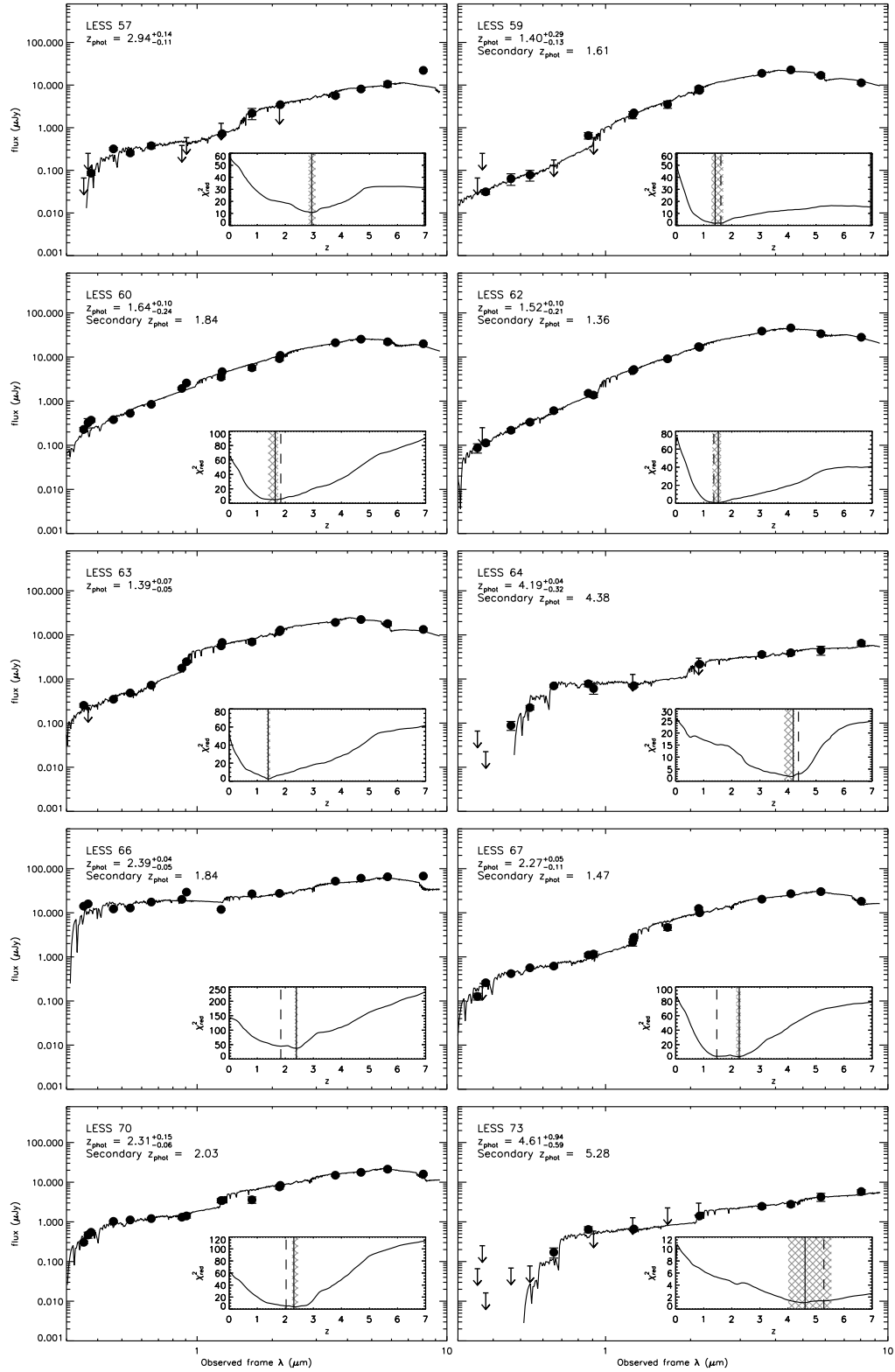


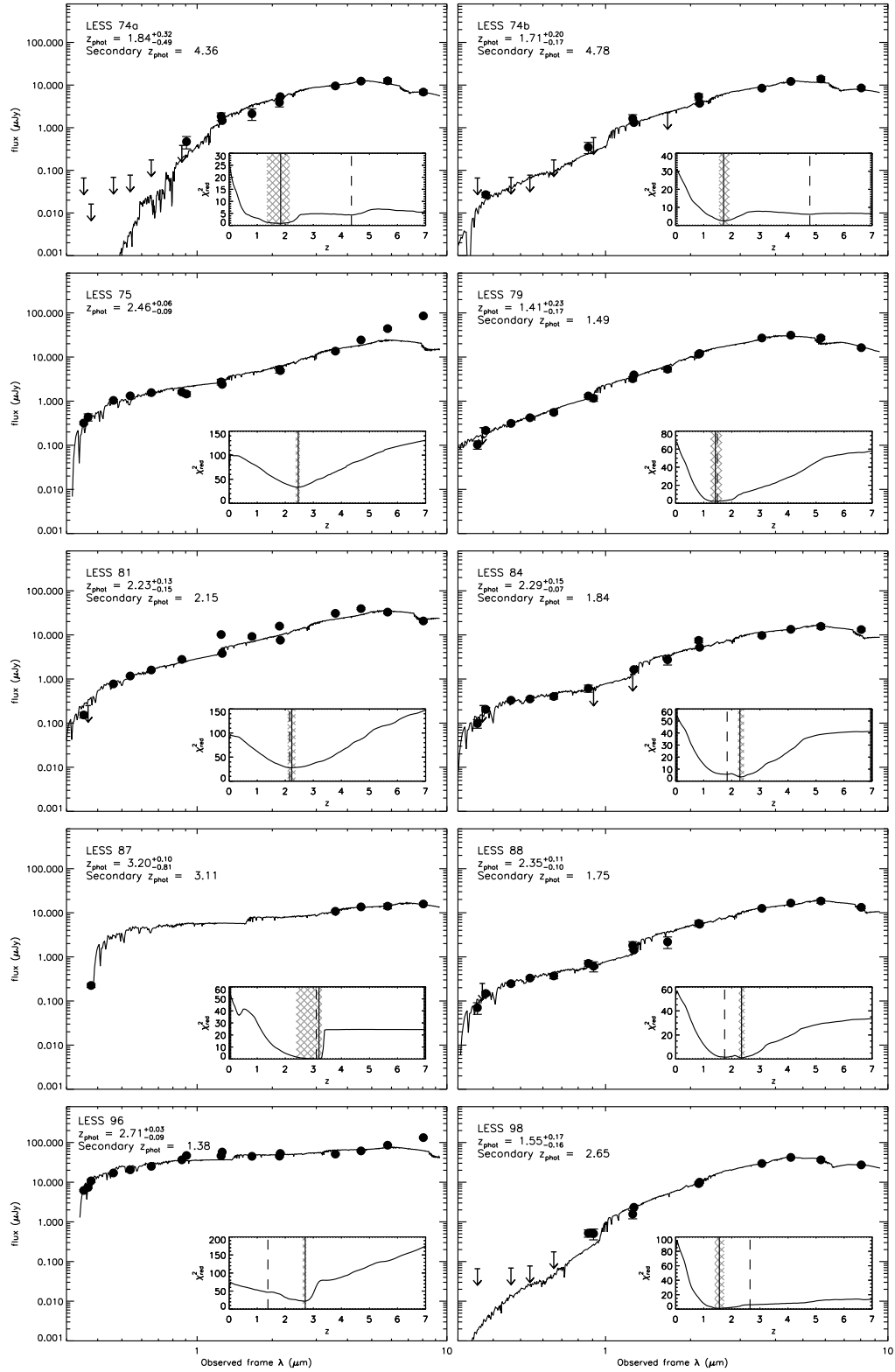
Figure 4.6: Photometry and best-fit SEDs for robust SMG counterparts; points and error-bars show measured photometry and arrows represent 3σ detection limits. Error bars on the primary photometric redshift are 99% confidence limits, which empirically correspond to 1σ . Inset panels show the minimum reduced χ^2 at each redshift step with the photometric redshift primary and secondary solutions (where they exist) marked by solid and dashed lines respectively; the photometric redshift error is represented by the shaded region.

Figure 4.6: – *continued*

Figure 4.6: – *continued*

Figure 4.6: – *continued*

Figure 4.6: – *continued*

Figure 4.6: – *continued*

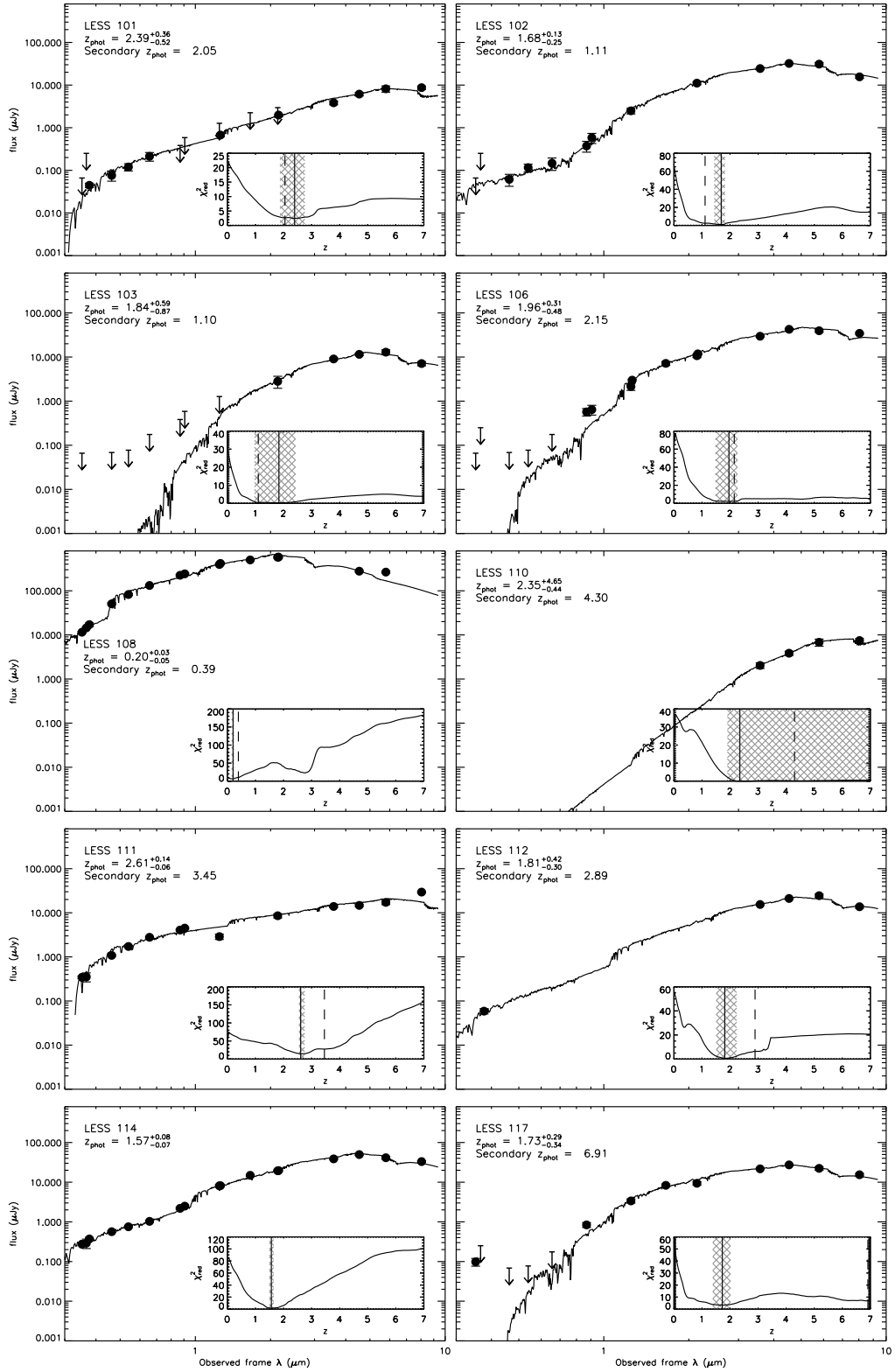
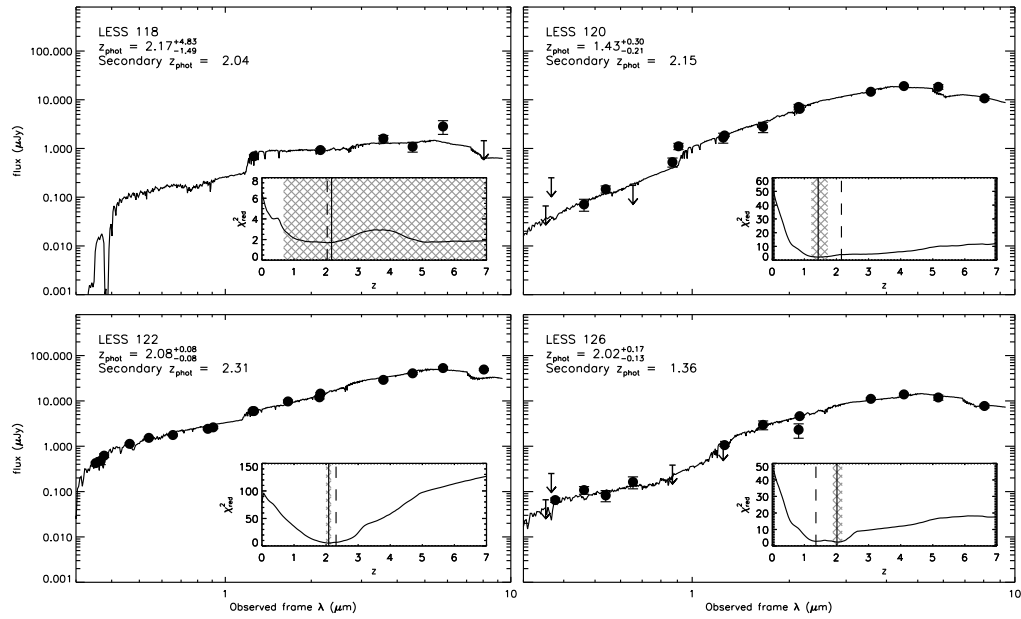


Figure 4.6: – continued

Figure 4.6: – *continued*

Chapter 5

A photometric redshift survey of SMGs

5.1 Introduction

Observations in the millimetre and submillimetre wavebands provide a uniquely powerful route to survey the distant Universe for intense dust-obscured starbursts (Blain & Longair 1993). This is due to the negative K-correction arising from the shape of the spectral energy distribution (SED) of the dust emission in the rest-frame far-infrared, which results in an almost constant apparent flux for sources with a fixed luminosity at $z \sim 1-8$.

Over the past decade, a series of ever larger surveys in the submillimetre and millimetre wavebands have mapped out a population of sources at mJy-flux limits with a surprisingly high surface density (e.g. Smail et al. 1997; Barger et al. 1998; Hughes et al. 1998; Blain et al. 1999; Eales et al. 1999; Bertoldi et al. 2000, 2007; Coppin et al. 2006; Knudsen et al. 2008; Weiß et al. 2009; Austermann et al. 2010). The mJy fluxes of these sources imply far-infrared luminosities of $\gtrsim 10^{12} L_{\odot}$, if the sources are at cosmological distances ($z \gtrsim 1$) classing them as ultraluminous infrared galaxies (ULIRGs; Sanders & Mirabel 1996); although as Chapter 3 showed, if they are at lower redshifts, $z \sim 0.5$, they may more typically be cool LIRGs. Their high surface density is far in excess of that expected from a “no evolution” model, suggesting very strong evolution of the population: $\propto (1+z)^4$ (Smail et al. 1997; Blain et al. 1999). If this results from strong luminosity evolution of starburst galaxies (as opposed to obscured AGN; Alexander et al. 2005; Hill & Shanks 2010) then a significant fraction of the massive star formation (and metal production) at high redshift may be occurring in this population.

To confirm this evolution and understand the physical processes driving it requires redshifts for the submillimetre galaxies (SMGs). Due to the coarse spatial resolution of the submillimetre and millimetre maps from which the SMGs can be identified, combined with their optical faintness (in part due to their high dust obscuration), it has proved challenging to measure their spectroscopic redshift distribution (e.g. Barger et al. 1999; Chapman et al. 2003a, 2005).

In fact, spectroscopic redshifts are not necessary to map the broad evolution of the SMG population and cruder photometric redshifts can be sufficient, if they are shown to be reliable (e.g. Chapter 4). Various photometric redshift techniques have therefore been applied in an attempt to trace the evolution of SMGs, using their optical/near-/mid-infrared or far-infrared/radio SEDs (e.g. Carilli & Yun 1999; Smail et al. 2000; Ivison et al. 2004; Pope et al. 2005, 2006; Ivison et al. 2007; Aretxaga et al. 2007; Clements et al. 2008; Dye et al. 2008; Biggs et al. 2010).

Both spectroscopic and photometric analyses suggest that the bulk of the SMG population lies at $z \gtrsim 1$, with an apparent peak at $z \sim 2.2$ for the subset of SMGs which can be located through their μJy radio emission (Chapman et al. 2005). Nevertheless, there are significant disagreements between the different studies (see e.g. Chapman et al. 2005; Clements et al. 2008; Dye et al. 2008), which may arise in part due to differing levels and types of incompleteness in the identifications and biases in the redshift measurements. The most serious of these is the incompleteness due to challenges in reliably locating the correct SMG counterpart. They are typically identified through statistical arguments and physical correlations based on radio, mid- or near-infrared emission (e.g. Chapters 3 and 4; Ivison et al. 1998, 2000, 2005; Smail et al. 1999; Pope et al. 2005; Bertoldi et al. 2007; Hainline et al. 2009; Biggs et al. 2010), but these locate only $\sim 60\text{--}80\%$ of SMGs. The expectation is that the SMGs whose counterparts are missed could potentially include the highest redshift (and thus the faintest in the radio and mid-infrared) examples, biasing the derived evolution (Chapman et al. 2005; Ivison et al. 2005). Attempts to address this incompleteness through time-intensive submillimetre interferometry have located a small fraction of previously unidentified SMGs (e.g. Chapter 3; Dannerbauer et al. 2002, 2008; Younger et al. 2007, 2009; Wang et al. 2007) but the nature and redshifts of this unidentified subset of SMGs remains a critical issue for studies of the population as a whole.

In this Chapter we use optical, near- and mid-infrared photometric redshifts to study SMGs detected in the Extended *Chandra* Deep Field South (ECDFS) by the Large APEX

BOLometer CAMERA (LABOCA; Siringo et al. 2009) on the Atacama Pathfinder EXperiment (APEX; Güsten et al. 2006) 12-m telescope in the LABOCA ECDFS Submillimetre Survey (LESS; Weiß et al. 2009). LESS mapped the full $30' \times 30'$ ECDFS at $870\text{-}\mu\text{m}$ to a noise level of $\sigma_{870\mu\text{m}} \approx 1.2 \text{ mJy beam}^{-1}$, for a beam with angular resolution of $19''.2$. 126 SMGs were detected at $> 3.7\sigma$ significance (equivalent to a false-detection rate of $\sim 4\%$, Weiß et al. 2009) and robust or tentative radio, $24\text{-}\mu\text{m}$ or IRAC mid-infrared counterparts are identified to 93 (71 robust and 22 tentative) SMGs (Chapter 4; Biggs et al. 2010). In Chapter 4 we determined the photometric redshifts for the 91 (68 robust and 22 tentative) of these SMGs with detectable optical and near-infrared counterparts in new and archival multiband photometry of the ECDFS and here we analyse the properties of the LESS SMGs using those photometric redshifts. LESS is an ideal survey for this purpose because of its panoramic, deep and uniform submillimetre coverage and extensive auxiliary data. In addition, the large size of the survey allows us to statistically measure the redshift distribution of the SMGs that we are unable to locate directly, and test whether their redshift distribution differs significantly from the identified population.

The plan of the Chapter is as follows: in §5.2 we recount the sample selections and discuss possible sources of bias in § 5.3.2. The photometric redshift distributions, infrared luminosities, dust temperatures and star-formation rates of SMGs are presented and discussed in §5.3 and we present our conclusions in §5.4. Throughout this Chapter we use deboosted submillimetre fluxes from Weiß et al. (2009), J2000 coordinates and Λ CDM cosmology with $\Omega_M = 0.3$, $\Omega_\Lambda = 0.7$ and $H_0 = 70 \text{ km s}^{-1} \text{ Mpc}^{-1}$. Unless otherwise stated all photometry is on the AB magnitude system, in which $23.9 \text{ m}_{\text{AB}} = 1 \mu\text{Jy}$.

5.2 Sample selection

We consider the optical and infrared counterparts SMGs detected in the LESS survey (Weiß et al. 2009) and identified by VLA radio, MIPS (Rieke et al. 2004) $24\text{-}\mu\text{m}$ and IRAC (Fazio et al. 2004) emission (Chapter 4; Biggs et al. 2010). The photometry and photometric redshifts of the robust SMG counterparts are derived in Chapter 4 and presented in Table 4.5.

Six of the SMGs have multiple robust counterparts; of these four SMGs (LESS 2, LESS 27, LESS 49 and LESS 74) have two robust counterparts with photometric redshifts consistent with them being at the same distance and are possibly physically associated. Two SMGs (LESS 10 and LESS 49) each have two robust counterparts with photometric

redshifts and SEDs that suggest they are not physically associated. In these cases, from the information currently available, it is not possible to determine which of the two counterparts is the source of the submillimetre flux, or whether the LABOCA detection is a blend of submillimetre emission from two galaxies. To avoid bias we have included all of the multiple counterparts in our analysis, but we note that their small number means that their inclusion does not significantly affect our results.

5.3 Results and Discussion

5.3.1 Redshift distribution of identified SMGs

In Fig. 5.1 we show our photometric redshift distribution for the 74 robust SMG counterparts; it peaks at $z = 2.2 \pm 0.1$ and has an interquartile range of 1.8–2.7. We compare to the photometric redshift distribution of SMG counterparts in the SCUBA Half-Degree Extragalactic Survey (SHADES) (Clements et al. 2008; Dye et al. 2008), median $z = 1.5 \pm 0.1$, and the spectroscopic sample from Chapman et al. (2005), median $z = 2.2 \pm 0.1$, both of which have similar submillimetre flux limits as our survey. The LESS SMGs have a similar redshift distribution to Chapman et al. (2005), although in our photometric redshift analysis of LESS the spectroscopic ‘redshift desert’ at $z \sim 1.2$ – 1.8 is filled and there is a larger high-redshift tail. The redshift distributions of both LESS and Chapman et al. (2005) SMGs are peaked at higher redshifts than the SHADES SMGs. A KS-test between Chapman et al. (2005) and LESS SMGs yields $P_{KS} = 0.44$, suggesting the two samples are consistent with being drawn from the same parent population. However, a KS-test between the LESS and SHADES SMGs gives $P_{KS} = 1.3 \times 10^{-5}$ indicating that these samples appear to be drawn from intrinsically different populations. We also note that (excluding the potential cluster members) our photometric analysis of SMGs in the field of MS 0451–03 (Chapter 3) suggests they are peaked at $z = 1.6$ – significantly lower than the LESS SMGs and those from Chapman et al. (2005). As discussed in Chapter 3 this is likely to be due to biases in the photometric redshifts of galaxies at $z \gtrsim 2$ in our analysis of SMGs in the field of MS 0451–03 (see Chapter 4).

We conclude that the global properties of our photometric redshifts are consistent with the largest previous spectroscopic survey, albeit with a higher-redshift tail – we find 10 (14%) SMGs with $z \geq 3$ and eight (11%) with $z \geq 3.5$, of which three are spectroscopically confirmed, including LESS 73 at $z = 4.76$ (see Coppin et al. 2009, 2010a). The comparable fractions for Chapman et al. (2005) are 10% at $z \geq 3$ and just 1% at

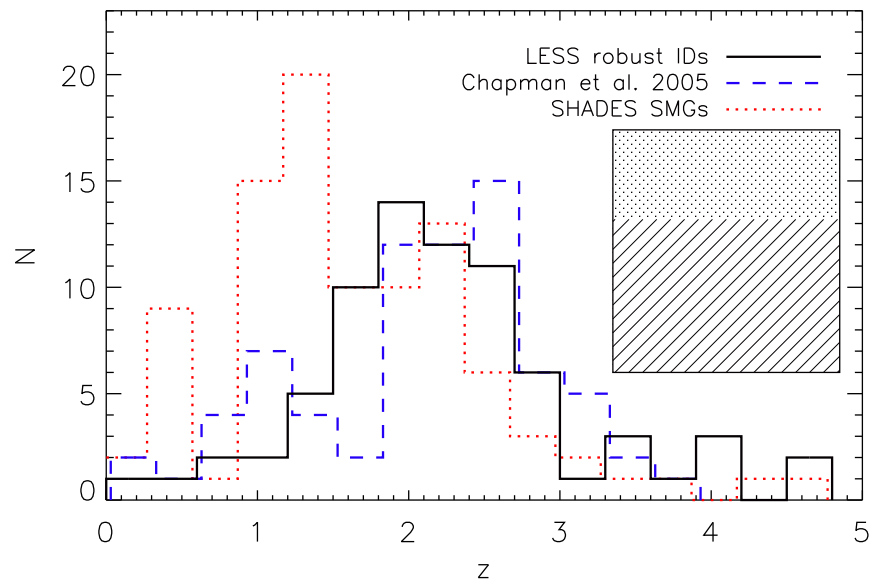


Figure 5.1: The photometric redshift distribution of robust LESS SMG counterparts. We compare this to the photometric redshift distribution of SHADES SMG counterparts (Clements et al. 2008; Dye et al. 2008), and the spectroscopic redshift distribution of SMGs from Chapman et al. (2005); for clarity the SHADES and Chapman et al. (2005) samples are offset slightly in redshift. The median redshift of identified SMGs in LESS is $z = 2.2 \pm 0.1$, which is the same as that from the Chapman et al. (2005) spectroscopic survey; SHADES has a lower median redshift of $z = 1.5 \pm 0.1$. There is a slightly larger high-redshift tail in the LESS SMG population than the Chapman et al. (2005) SMG population. Additionally, the so-called ‘redshift desert’ at $z \sim 1.5$, which is evident in the Chapman et al. (2005) study does not affect our photometric redshifts and as such, in contrast with Chapman et al. (2005), the increase in the number of galaxies from $z \sim 1$ to $z \sim 2$ is smooth. Statistical comparisons show that the Chapman et al. (2005) and LESS SMGs are drawn from populations with similar redshift distributions, but that the SHADES SMGs are biased to low redshifts either from systematic errors in the photometric redshift calculations, sample selection, or cosmic variance. The shaded region represents the area that would be added to the histogram were the redshifts of the 57 statistically identified or completely unidentified SMGs known and is designed to give an impression of the potential contribution of the unidentified SMGs to this figure. The lower region corresponds to the unidentified SMGs that we statistically identify in §5.3.3, and which have redshifts similar to the identified SMGs. The upper shaded region represents the SMGs which remain unaccounted for after the statistical analysis and likely have $z \gtrsim 3$.

$z \gtrsim 3.5$. This difference between LESS and Chapman et al. (2005) is likely to be due to deeper radio data (on average), the inclusion of 24- μm counterparts in LESS (Biggs et al. 2010) and most critically the use of photometric redshifts covering the UV to mid-infrared which are less reliant on the detection of spectral features in the optical. Conversely, the SHADES SMGs appear to typically lie at lower redshifts. We stress that compared to the SHADES analyses we have used about twice as many photometric bands, tested against a larger spectroscopic sample of SMGs, and obtained qualitatively better fits to the SEDs. We suggest that either there is a systematic error in the original SHADES photometric redshifts or their counterpart identifications, or that cosmic variance is the cause of the different redshift distributions. However, we note that a re-analysis of the optical-to-infrared photometry of the SHADES SMGs yields a median photometric redshift of $z = 2.05$ (Schael et al. in prep.) – more similar to our sample of LESS SMGs and Chapman et al. (2005) than the original SHADES analyses.

Studies have suggested that the brightest SMGs may have higher redshifts than those with lower submillimetre fluxes (e.g. Ivison et al. 2002; Pope et al. 2005; Biggs et al. 2010). In Fig. 5.2 we plot the photometric redshift against 870 μm flux ($S_{870\mu\text{m}}$) for robust LESS SMG counterparts. We split the galaxies into those brighter and fainter than the median deboosted submillimetre flux of the sample, $S_{870\mu\text{m}} = 5.6$ mJy. SMGs with $S_{870\mu\text{m}} \leq 5.6$ mJy have a median redshift of $z = 2.1 \pm 0.2$ and SMGs with $S_{870\mu\text{m}} > 5.6$ mJy have a median redshift of $z = 2.3 \pm 0.2$, where the errors are bootstrap uncertainties on the medians. Spearman’s rank correlation coefficient between $S_{870\mu\text{m}}$ and z_{phot} is 0.20, which corresponds to a probability of zero correlation of 0.08 and indicates that there is no significant correlation between submillimetre flux and redshift for SMGs in our sample. We have verified that the result is not dependent on the choice of the flux limit between the two bins. Additionally, if all the unidentified SMGs lie at $z = 5$ or $z = 1$ (in §5.3.3 both of these scenarios are shown to be unlikely) we still find no statistically significant difference between the redshifts of SMGs in the two flux bins. The sample of SMGs with optical-infrared photometric redshifts in this work is larger than previous studies of this claimed trend and our analysis finds no significant correlation between $S_{870\mu\text{m}}$ and redshift for robustly identified sources, also implying that $S_{870\mu\text{m}}$ is not a good proxy for redshift. This result agrees with Knudsen et al. (2010), who find no difference in the redshift distributions of faint lensed SMGs ($S_{850\mu\text{m}} < 2$ mJy) and the brighter ($S_{850\mu\text{m}} \gtrsim 3$ mJy) SMGs from Chapman et al. (2005). We note that SMGs in the semi-analytic ΛCDM GALFORM model (Baugh et al. 2005; Lacey et al. 2008; Swinbank et al. 2008) also show

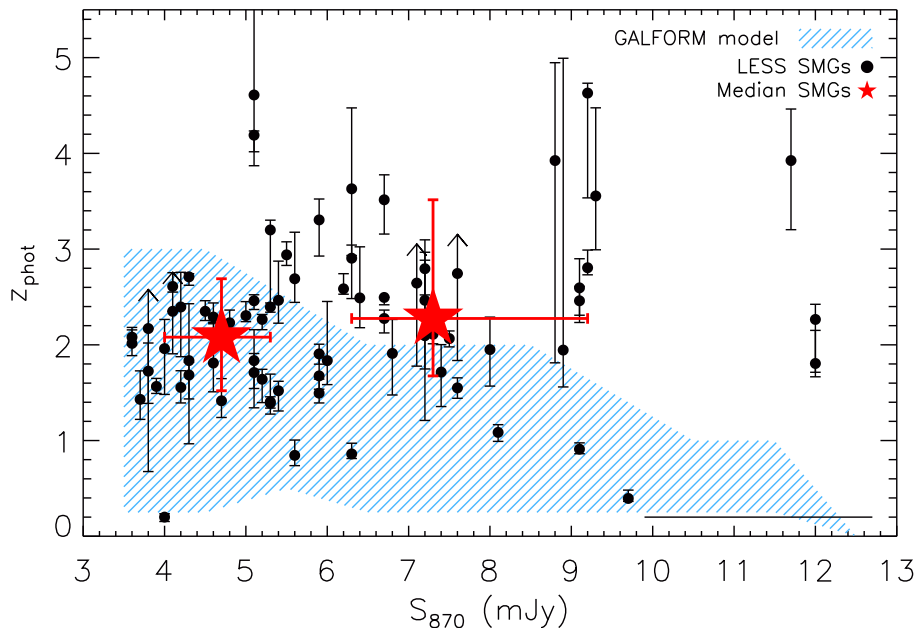


Figure 5.2: Photometric redshift versus submillimetre flux for LESS SMGs; the median $S_{870\mu m}$ error bar is shown in the bottom right. The median $S_{870\mu m}$ and redshift, with 1σ error bars, are presented for SMGs with $S_{870\mu m} \leq 5.6$ mJy and $S_{870\mu m} > 5.6$ mJy. Previous studies have suggested that the brightest SMGs may lie at the highest redshifts. This work contains optical-infrared photometric redshifts for a larger sample of SMGs than previous studies of the phenomenon and finds no evidence for a trend. For comparison we also highlight the $1\text{-}\sigma$ distribution of SMGs in flux bins of 1 mJy in the Λ CDM GALFORM model (Baugh et al. 2005; Lacey et al. 2008; Swinbank et al. 2008), which also shows no correlation between redshift and submillimetre flux.

no correlation between $S_{870\mu m}$ and redshift (although the error range decreases at high fluxes where there are few galaxies in the model).

5.3.2 Potential sample biases

As discussed in Chapter 4, Biggs et al. (2010) identified robust counterparts to 71 SMGs (of which 68 have detectable optical counterparts) and tentative counterparts to 22 LESS SMGs, respectively. In Fig. 5.3 we show the redshift distribution of robust counterparts and compare this to the redshift distribution of the tentative counterparts to determine whether our results may be biased by the exclusion of tentative counterparts in our main analysis. The median redshifts of robust and tentative counterparts are 2.2 ± 0.1 and

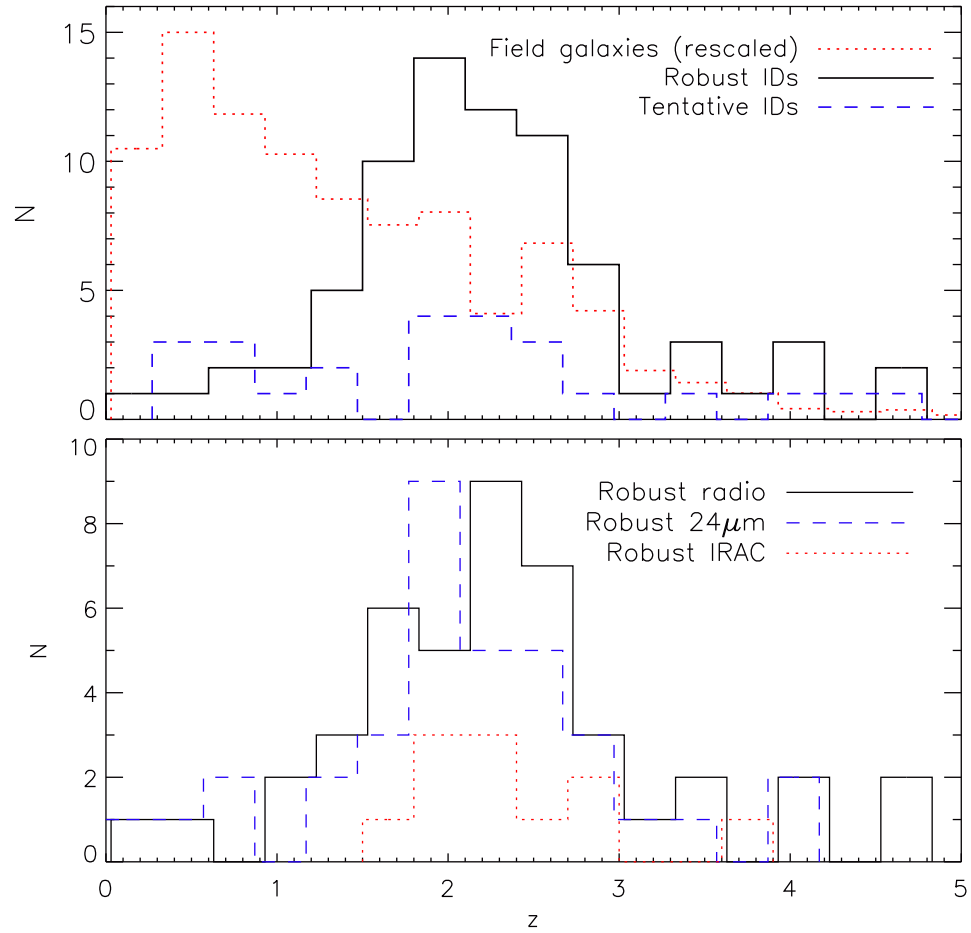


Figure 5.3: In the top panel we present a comparison between robustly and tentatively identified SMG counterparts and the field population of the ECDFS; tentative counterparts and field galaxies are offset slightly in redshift for clarity. The robust counterparts have a median redshift of $z = 2.2 \pm 0.1$, compared to $z = 2.0 \pm 0.2$ for the tentative counterparts. Tentative counterparts have a larger interquartile range – 1.2–2.8 compared to 1.8–2.7 for the robust SMG counterparts. We interpret these distributions as evidence that tentative counterparts are mainly drawn from the same parent population as the robust counterparts, but with the addition of some contamination, particularly at low redshifts. In the lower panel we compare the redshift distributions of robust counterparts (with $p \leq 0.05$) in radio, $24\mu\text{m}$ and IRAC data; for clarity radio and $24\mu\text{m}$ counterparts are plotted offset slightly in redshift. The radio, $24\mu\text{m}$ and IRAC samples have median redshifts of 2.3 ± 0.1 , 2.1 ± 0.2 and 2.3 ± 0.2 and interquartile ranges of 1.8–2.8, 1.6–2.5 and 1.9–2.7 respectively. Therefore, we find no significant differences in the redshift distributions of the three identification methods used by Biggs et al. (2010, see also Chapter 4).

2.0 ± 0.2 (here and throughout this Chapter errors on the median are from bootstrapping) and the interquartile ranges are $z = 1.8\text{--}2.7$ and $z = 1.2\text{--}2.8$, respectively. We also use a Kolmogorov-Smirnov test (KS-test), which calculates the probability that two samples are drawn from the same parent population (P_{KS}), to compare the redshift distributions of robust and tentative counterparts statistically. We find $P_{KS} = 0.09$ and conclude that it is likely that there is some contamination from physically unassociated foreground ($z \lesssim 1$) galaxies in the tentative identifications. Therefore, throughout the remainder of this Chapter we restrict our analysis to robust counterparts only.

We note that our identified sample contains two potential gravitational lenses (LESS 6 and LESS 11; see Appendix 5.5). These are typically low-redshift counterparts where the radio or mid-infrared emission is offset from the optical source. These are discussed individually in Appendix 5.5 and we have confirmed that their inclusion does not affect our results.

In Fig. 5.3 we also compare the redshift distributions of counterparts with $p \leq 0.05$ in the radio, $24\mu\text{m}$ and IRAC data. The median redshifts are $z = 2.3 \pm 0.1$, 2.1 ± 0.2 and 2.3 ± 0.2 , and the interquartile ranges are $z = 1.8\text{--}2.8$, $1.6\text{--}2.5$ and $1.9\text{--}2.7$ for the radio, $24\mu\text{m}$ and IRAC samples respectively. A comparison of the three redshift samples shows that they are statistically indistinguishable. We conclude that the three counterpart identification methods select galaxies with similar redshift distributions, and are not significantly biased with respect to each other.

5.3.3 Redshift distribution of unidentified SMGs

To date, redshift surveys of SMGs have focused on the $\sim 60\text{--}80\%$ of the population with counterparts identified from radio and $24\mu\text{m}$ imaging, and a few located using high-resolution (sub-)millimetre interferometry (e.g. Chapter 3). The requirement for radio or infrared counterparts to SMGs can bias the redshift or the dust temperature distributions of identified SMGs (Chapman et al. 2005) and it is currently unknown if the identified population is representative of the $\sim 20\text{--}40\%$ of SMGs without identified counterparts. In particular, it is unclear whether they have the same redshift distribution. In order to investigate the redshift distribution of the unidentified SMGs we utilise our extensive 17-band photometric redshifts in the ECDFS to investigate the photometric redshifts of sources around SMGs without robustly identified counterparts to the field population.

In Fig. 5.4 we show the redshift histogram of galaxies within the error circles of the 55 unidentified SMGs in the ECDFS, where the region considered is that used by Biggs et al.

(2010) to identify SMG counterparts (both the completely unidentified and those with only tentative identifications). For comparison, we show the redshift histogram of all the galaxies in the submillimetre error circles of SMGs with robustly identified counterparts, scaled such that the number of error circles examined is the same as the unidentified SMG sample. We also consider the photometric redshifts of galaxies in the same area around random positions in the field, which are required to be $> 15''$ from any LESS SMGs. We consider 50 Monte Carlo simulations of 55 random field positions (equal to the number of unidentified SMGs), and employ the mean and standard deviation of the 50 simulations in each redshift bin for our statistical analyses. As discussed in Chapter 4 our photometric source extraction procedure included manually examining the regions around the SMGs and adding to the catalogue potential sources which may have been missed by the automated procedure. To remove any bias and ensure a fair comparison between the SMGs and random positions, we exclude these additional sources from this analysis.

In the lower panel of Fig. 5.4 we show the difference between the redshift distributions of the field and SMGs without robustly identified counterparts. Compared to the field there is an excess of 26 ± 12 (2.2σ) at $z > 1$ around unidentified SMGs. There are positive excesses of galaxies in the $z = 2-3$ (14 ± 8 ; 1.8σ) and $z = 4-5$ (4 ± 2 ; 1.6σ) bins around unidentified SMGs. We also note that the number of galaxies with $z = 2-3$ or $z = 4-5$ around the SMGs is not exceeded by any of the 50 Monte Carlo simulations, and therefore the probability of observing excesses of the magnitude of either of these by chance is $< 2\%$.

To crudely compare the redshift distributions of the identified and unidentified SMGs we also plot the difference between redshifts of sources in the submillimetre error circles of the identified SMGs and the field (scaled to the value in the $z = 2-3$ bin of the unidentified SMGs). We conclude that the redshift distribution of unidentified SMGs is broadly similar to that of robustly identified SMGs.

To provide a more reliable estimate of the average redshift of the unidentified SMGs we evenly distribute the excess galaxies in the SMG error circles in each redshift bin. We verify that this method is valid by using it to calculate the average redshift for identified SMGs, which yields $z = 2.2 \pm 0.1$, in agreement with that derived by simply calculating the median of the redshifts (§5.3.1). For unidentified SMGs we derive an average redshift of $z = 2.5 \pm 0.3$. This suggests that unidentified SMGs may lie at marginally higher redshifts than the identified sample, although we stress that the difference is not statistically

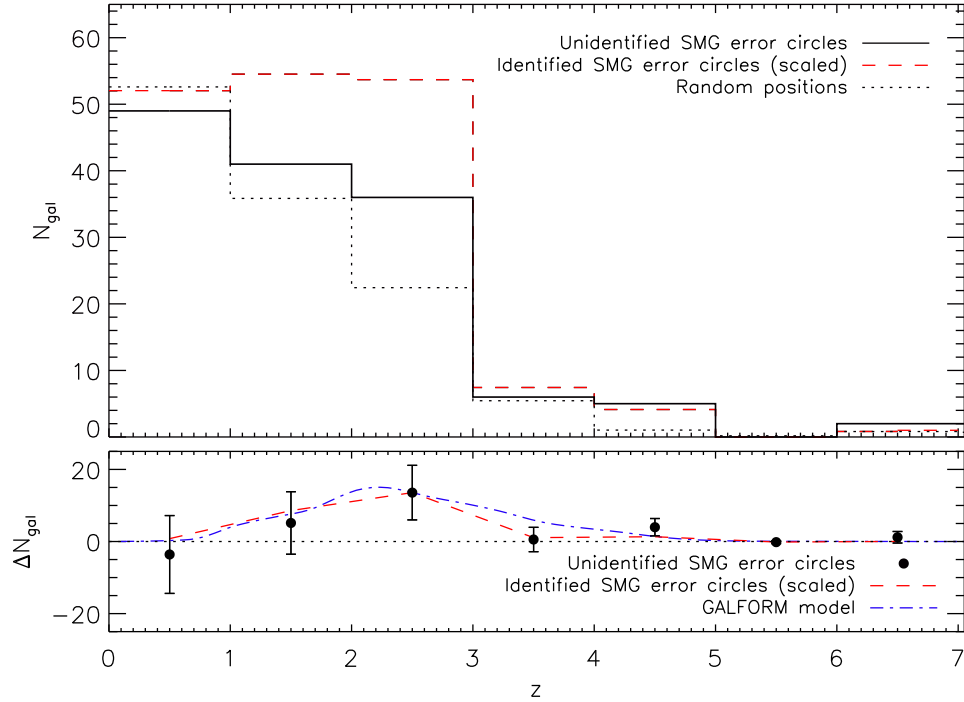


Figure 5.4: The top panel shows the redshift histogram of sources within the submillimetre positional error circles of SMGs without robust radio, $24\ \mu\text{m}$ or IRAC counterparts compared to the same number of random positions in the field. For comparison we also plot the redshift histogram for sources in the submillimetre positional error circles of SMGs *with* robust counterparts, also scaled to the same number of error circles. In the bottom panel we show the difference between the redshift histogram of galaxies around unidentified SMGs and the field population (from random positions). We also plot both the difference in redshift of galaxies around identified SMGs and the field population, and the redshift distribution of radio-undetected SMGs in the ΛCDM GALFORM model (Swinbank et al. 2008). In order to highlight potential differences in the redshift distributions of the populations the latter two datasets are scaled to match the value of ΔN_{gal} of unidentified SMGs in the $z = 2\text{--}3$ bin. By using ΔN_{gal} and assuming a uniform distribution of galaxies within the bins we calculate that the average redshift of unidentified SMGs is $z = 2.5 \pm 0.3$.

significant. This conclusion is consistent with the predicted redshift distribution of radio undetected SMGs from the semi-analytic Λ CDM GALFORM model, which predicts they should lie at $z \sim 2.2$, similar to the observed SMGs (Swinbank et al. 2008).

There are 14 ± 8 more galaxies at $z = 2-3$ in the error circles of unidentified SMGs than expected from comparing to the field population. We showed in §5.3.2 that there are nine tentative SMG counterparts with $z = 2-3$ and two with $z = 4-5$. Thus potentially half of the excess seen around the unidentified SMGs could be attributed to tentative counterparts. Indeed, if tentative SMGs are removed from this analysis just a 0.6σ (3 ± 5) excess of $z = 2-3$ galaxies and a 1.3σ (2.4 ± 1.9) excess of $z = 4-5$ galaxies around SMGs remains.

Finally, we use statistical arguments to estimate how many SMGs are still unaccounted for in our redshift analysis. There are 55 out of the sample of 126 LESS SMGs without robust radio, $24 \mu\text{m}$ or IRAC counterparts (Biggs et al. 2010). Due to the signal-to-noise ratio limit on the submillimetre catalogue ($S/N \geq 3.7\sigma$) only five of the 126 SMGs are expected to be false detections (Weiß et al. 2009); an additional 1–2 are expected to have counterparts outside of the search radii used (Biggs et al. 2010). This leaves 48–49 SMGs with currently unidentified counterparts that are expected to lie within our search area. We then calculate the total excess of galaxies in unidentified error circles over the field. Due to clustering, an error circle can contain more than one galaxy associated with the SMG (see also Chapter 6). We then compare the sources around identified SMGs with the number of identified counterparts to determine this “overcounting factor”: $\sim 1.2\times$. We scale the difference between the field and unidentified SMG regions by this factor to estimate that there are 21 ± 19 LESS SMGs ($17 \pm 15\%$ of the total) that have no robust radio, $24 \mu\text{m}$ or IRAC counterparts and have mid-infrared fluxes below the limits of our imaging (or they lie at sufficiently high redshifts that any excess is overwhelmed by the unrelated field population).

As we show in Chapter 6 these unidentified SMGs could lie at $z \sim 1-3$ and be fainter than $M_H \lesssim -23.5$ (Fig. 6.5). However, the specific star-formation rates of such sources would be $\gtrsim 10^{-7} \text{yr}^{-1}$, corresponding to formation times of $\lesssim 10 \text{Myr}$. The duty cycle for such short-lived sources means that to detect ~ 20 sources in our 0.5deg^2 survey, we require a parent population with a space density of $\gtrsim 0.02 \text{Mpc}^{-3}$, which we consider unlikely. Alternatively, if they have rest-frame near-infrared luminosities similar to the identified SMG population, then Fig. 6.5 suggests that they must lie at $z \gtrsim 3$. If correct we should add these sources to the SMGs identified at $z \gtrsim 3$. We have identified 10 SMGs

at $z > 3$, as well as 4 ± 2 which have been statistically identified in our IRAC sample. To these we add the 21 ± 19 SMGs which are unaccounted for in our statistical analysis, to derive a total of 35 ± 19 SMGs ($28 \pm 15\%$ of the whole population) at $z \geq 3$ in our survey. We conclude that $\sim 30\%$, and at most $\sim 45\%$ of the SMG population could reside at $z \gtrsim 3$. This corresponds to a volume density of $2.8 \times 10^{-6} \text{ Mpc}^{-3}$ (assuming they span the range $z = 3-7$, or 80% higher if they only span $z = 3-5$). For comparison, the equivalent volume density of $z = 2-3$ SMGs, including identified counterparts and the 14 that are statistically identified in this redshift range, is $1.2 \times 10^{-5} \text{ Mpc}^{-3}$, signifying an order of magnitude decline in the abundance of SMGs from $z \sim 2.5$ to $z > 3$. We note that for there to be no decline in the space density of SMGs at $z > 3$ then all the SMGs are required to be at $z \lesssim 3.8$. However, five of the identified SMGs have higher photometric redshifts than this, and three of those are spectroscopically confirmed – verifying that there is a decline in the space density of SMGs at $z > 3$.

We have statistically determined the redshift distribution of $\sim 60\%$ of the unidentified SMGs, and shown that the remainder likely lie at $z \gtrsim 3$. In Fig. 5.5 we combine the redshift distributions of the identified and unidentified SMGs to provide the probable redshift distribution of the *entire* $S_{870\mu\text{m}} \gtrsim 4 \text{ mJy}$ SMG population. We conclude that the most likely median redshift for the $S_{870\mu\text{m}} \gtrsim 4 \text{ mJy}$ SMG population is $z = 2.5 \pm 0.6$.

5.3.4 Simple redshift estimators for SMGs

We next consider whether the SMG population has a characteristic SED shape that can be used to predict its redshift. Previous studies have investigated and used optical (BzK ; Chapter 3; Daddi et al. 2004), ultraviolet (BX/BM; Steidel et al. 2004; Chapman et al. 2005) and IRAC colours (Yun et al. 2008; Hainline et al. 2009) and radio-to-submillimetre flux ratios (e.g. Chapter 3; Carilli & Yun 1999; Ivison et al. 2007; Biggs et al. 2010) as simple estimators of the redshifts of SMGs. Here we use our 17-band photometric redshifts and large sample of SMG counterparts to investigate the reliability of the BzK colours and radio-to-submillimetre fluxes as redshift estimators and derive a simple IRAC colour indicator of redshift.

In Fig. 5.6 we show the BzK colour-colour plot (Daddi et al. 2004), which is designed to identify galaxies at $1.4 < z \lesssim 2.5$, for LESS SMG counterparts. We have distinguished between counterparts with photometric redshifts above and below $z = 1.4$ and find that all the SMGs with $z_{\text{phot}} < 1.4$ lie in the expected region of colour-colour space. However, whilst SMG counterparts with $z_{\text{phot}} \geq 1.4$ typically have the colours of high-redshift

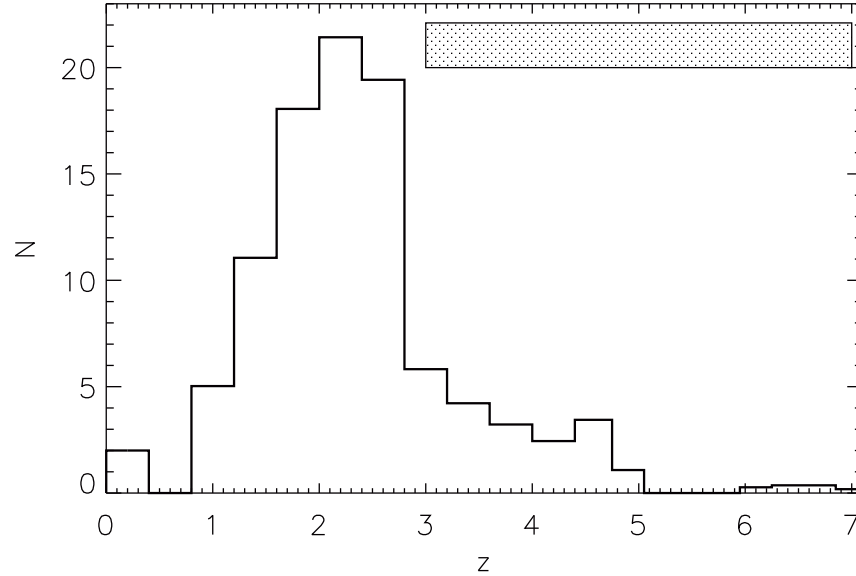


Figure 5.5: The redshift distribution of LESS SMGs, including robustly identified counterparts (Fig. 5.1) and the statistically identified SMG population from §5.3.3. These are distributed uniformly within the relevant $\Delta z = 1$ ranges. The shaded area represents the remaining unidentified SMGs, which are likely to lie at $z \gtrsim 3$. We conclude that the median redshift of the $S_{870\mu\text{m}} \gtrsim 4$ mJy SMG population is likely to be $z = 2.5 \pm 0.6$.

star-forming galaxies, this population does scatter into the low-redshift region. Two galaxies with $z_{\text{phot}} > 1.4$, $B - z \sim 1$ and $z - K \sim -0.1$ lie near the separation between $z < 1.4$ galaxies and stars and are both likely to be submillimetre-bright QSOs (LESS 66 and LESS 96 see Appendix 5.5). We note that for the smaller sample of MS 0451–03 SMGs (Chapter 3; Fig. 3.6) three of the galaxies with $z_{\text{phot}} < 1.4$ were scattered into the $z > 1.4$ region. We conclude that the BzK analysis of SMG counterparts can, on average, differentiate between SMGs at $z > 1.4$ and those at $z < 1.4$ but there is some scatter between the populations. We compare the observed BzK colours with a redshift track of the average SMG SED (Chapter 6) and note that the median SED of SMGs has a redder rest-frame ($U - z$) colour (corresponding to observed $(z - K)$ at $z \sim 1.4$) than used to define the selection areas for $z > 1.4$ galaxies and thus the SMGs at the highest redshifts may fall in the passive BzK or $z < 1.4$ region.

In Fig. 5.7 we plot the photometric redshift against $S_{870\mu\text{m}}/S_{1.4\text{GHz}}$ for the LESS SMGs (Weiß et al. 2009; Biggs et al. 2010), the tracks of Arp 220 and M82 (based on the

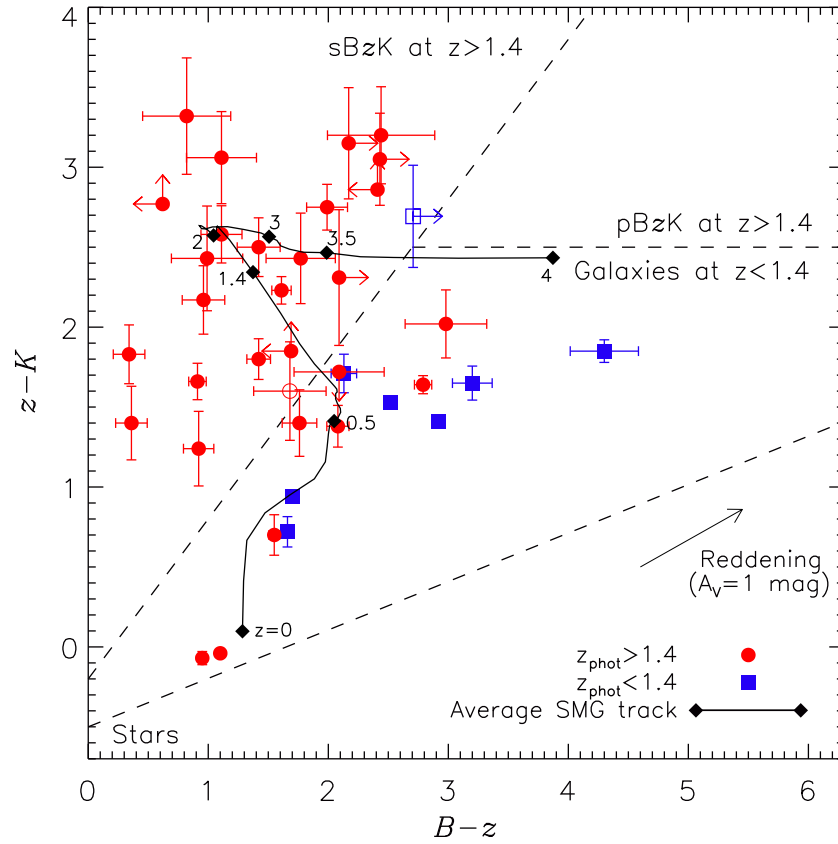


Figure 5.6: $(B - z)$ versus $(z - K)$ colour-colour plot of LESS SMG counterparts. The selection regions for star-forming and passive $z > 1.4$ BzK galaxies (sBzK and pBzK respectively), $z < 1.4$ galaxies, and stars (Daddi et al. 2004) are shown, and we distinguish between SMG counterparts with $z_{\text{phot}} \geq 1.4$ and $z_{\text{phot}} < 1.4$. The photometric redshifts typically agree with the BzK colours and most of the SMG counterparts have BzK colours of $z > 1.4$ star-forming galaxies and none have colours of stars or $z > 1.4$ passive galaxies (similar to the result of Bertoldi et al. 2007). We also show the redshift track of the average SMG SED (Chapter 6) from $z = 0-4$ and the reddening vector for $A_V = 1$ magnitude. The scatter in the photometry of individual SMGs compared to the redshift track of the average SMG SED suggests that the SMGs have a range in optical SEDs. Open symbols show galaxies which lie in halos of bright stars in the z -band, in these cases, for the purpose of this plot only, the z -band magnitude is extrapolated from the SED fit and the measured I -band magnitude.

SEDs of Silva et al. 1998). We also show the Λ CDM GALFORM predictions (Baugh et al. 2005) and the Carilli & Yun (2000) relationship. The wide range in $S_{870\mu\text{m}}/S_{1.4\text{GHz}}$ at a fixed redshift limits the usefulness of $S_{870\mu\text{m}}/S_{1.4\text{GHz}}$ as a redshift indicator for SMGs and indicates that SMGs have a variety of submillimetre-to-radio flux ratios, suggesting a range in dust temperatures (Chapman et al. 2005; Clements et al. 2008). We also note that the majority of SMGs lie above the redshift track of M82, suggesting higher submillimetre-to-radio flux ratios (potentially due to the presence of more cold dust). In addition, LESS 20 has $z_{\text{phot}} \sim 2.8$ and $S_{870\mu\text{m}}/S_{1.4\text{GHz}} \sim 1.7$, which is lower than expected from its redshift, indicating that it is most likely a radio-bright AGN (Chapter 6), so we remove it from our subsequent analyses of far-infrared luminosities, star-formation rates, and characteristic dust temperature (§5.3.5).

Studies of mid-infrared spectra of SMGs have shown that they are similar to M82 with an additional power-law contribution from AGN emission (Menéndez-Delmestre et al. 2007, 2009; Pope et al. 2008). In Fig. 5.7 we plot photometric redshift against $S_{870\mu\text{m}}/S_{24\mu\text{m}}$, which shows that the mid-infrared to submillimetre flux ratios of SMGs are similar to Arp 220 and those derived in the Λ CDM GALFORM model, but are poorly represented by M82. This suggests that although SMGs have mid-infrared spectra similar to M82, the mid-infrared continuum emission is fainter compared to the far-infrared emission and is more comparable to that of Arp 220. We note that although $S_{870\mu\text{m}}/S_{24\mu\text{m}}$ for SMGs varies with redshift in a manner comparable to Arp 220, the scatter and the effect of PAH and silicate features passing through the 24 μm filter makes this measurement unsuitable for redshift derivation (Pope et al. 2006).

We expand on the work of Yun et al. (2008) and Hainline et al. (2009) and propose a new redshift estimator for SMGs, which is based on the IRAC 8 and 3.6 μm fluxes and for LESS SMGs exhibits less scatter than the commonly-employed radio-to-submillimetre flux ratio. In Fig. 5.8 we plot this ratio against redshift for the LESS SMGs and using the ROBUST_LINEFIT procedure from the IDL Astronomy Library (Landsman 1993) we fit an outlier-resistant linear relationship to SMGs with $z_{\text{phot}} < 4$, which yields:

$$z = (2.1 \pm 0.1) + (1.9 \pm 0.2)\log_{10}(S_8/S_{3.6}) \quad (5.1)$$

We exclude SMGs with $z_{\text{phot}} \geq 4$ from the fit because at high redshifts the 1.6 μm stellar peak passes through the 8 μm filter making this redshift estimator unreliable. For LESS SMGs with $z < 4$ the 1σ dispersion in redshift estimated using Eqn. 5.1 is $\sigma_z = 0.44$ and we find that $\sim 90\%$ of LESS SMGs at $z > 2$ have $S_8/S_{3.6} > 1$. However, we find that

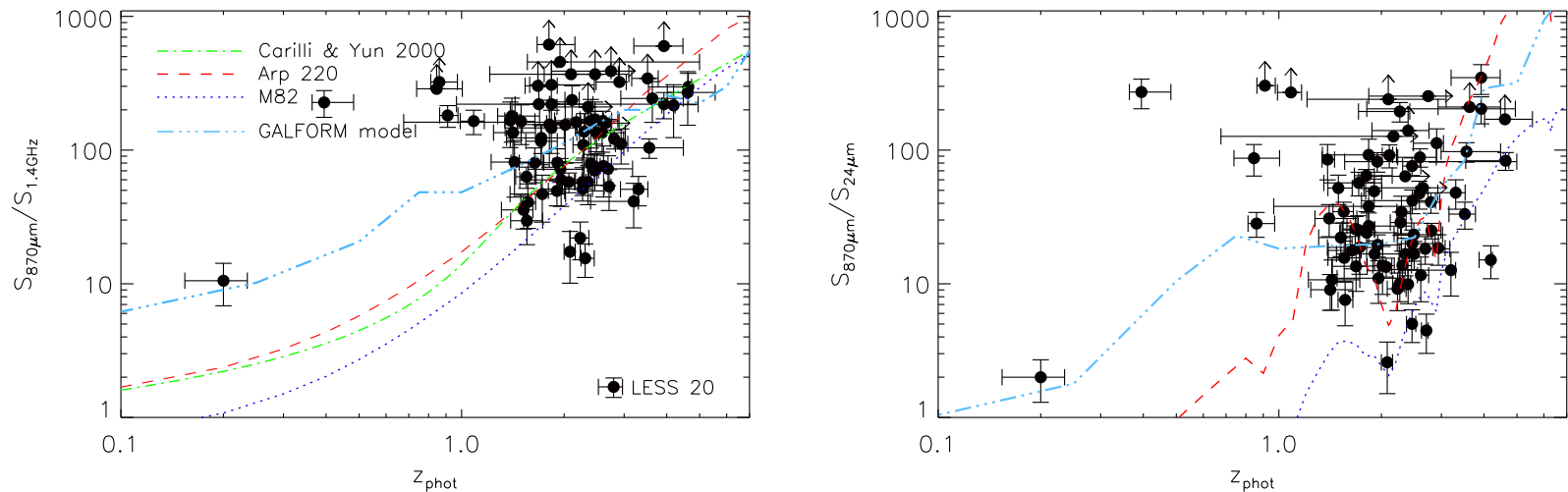


Figure 5.7: The variation of submillimetre to radio (left) and submillimetre to mid-infrared (right) flux ratios with redshift, compared with Arp 220 and M82 (based on the SEDs of Silva et al. 1998) and SMGs in the Λ CDM GALFORM model (Baugh et al. 2005) with $S_{850\mu m} \geq 3$ mJy; we also show the relationship between redshift and radio-to-submillimetre spectral index derived by Carilli & Yun (2000) in the left-hand panel. The SMGs show two orders of magnitude dispersion in both $S_{870\mu m}/S_{1.4\text{GHz}}$ and $S_{870\mu m}/S_{24\mu m}$. The model track of $S_{870\mu m}/S_{1.4\text{GHz}}$ for M82 lies below the majority of the SMGs, while that of Arp 220 more closely follows the SMGs, suggesting that they typically contain more colder dust than M82. Similarly, although studies have found that mid-infrared spectral properties of SMGs are similar to M82 (Menéndez-Delmestre et al. 2009) we find that M82 does not describe the submillimetre to mid-infrared continuum flux ratios well, and that Arp 220 fits better to this data. LESS 20 (labelled) is significantly brighter at 1.4GHz than expected from its submillimetre flux and redshift and is most likely a radio-bright AGN (Chapter 6).

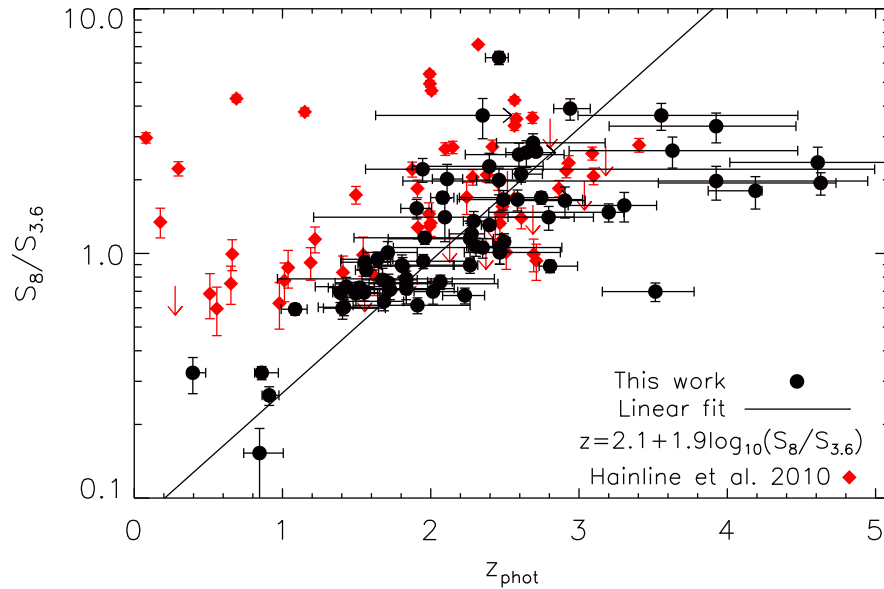


Figure 5.8: The correlation between redshift and the ratio of $8\ \mu\text{m}$ to $3.6\ \mu\text{m}$ flux for the LESS SMGs with photometric redshifts and those with spectroscopic redshifts (Chapman et al. 2005) and photometry from Hainline et al. (2010). The LESS SMGs show a trend and so we plot a linear fit to the SMGs with $z < 4$, which yields $z = 2.1 + 1.9 \log_{10}(S_8/S_{3.6})$, with a 1σ dispersion in redshift of $\sigma_z = 0.44$. This relation may be useful as a crude redshift indicator for SMGs as we note that $\sim 90\%$ of all LESS SMGs with $z > 2$ have $S_8/S_{3.6} > 1$, while similarly $\sim 90\%$ of all LESS SMGs with $z < 2$ have $S_8/S_{3.6} < 1$. However, the SMGs from Hainline et al. (2010), which contain a large fraction of AGN contamination do not conform to the trend, and therefore we caution against the use of $S_8/S_{3.6}$ as a redshift indicator for SMGs which are likely to contain strong AGN contamination.

for SMGs with strong AGN contamination (Hainline et al. 2009, 2010) Eqn. 5.1 is *not* a good redshift discriminator and should be used with caution.

5.3.5 Dust temperatures, far-infrared luminosities and star-formation history

In order to further investigate the intrinsic properties of the LESS SMGs we next use our photometric redshifts and the observed radio and submillimetre fluxes to derive the characteristic dust temperatures (T_D), far-infrared luminosities ($8\text{--}1000\ \mu\text{m}$; L_{FIR}) and

star-formation rates.

Blain et al. (2002) showed that the submillimetre-to-radio flux ratio in SMGs is mainly influenced by redshift and the characteristic dust temperature. Chapman et al. (2005) assumed a dust emissivity, $\beta = 1.5$, and the $z = 0$ far-infrared–radio correlation, to determine empirically that for their sample of SMGs:

$$T_D = \frac{6.25(1+z)}{(S_{850\mu\text{m}}/S_{1.4\text{GHz}})^{0.26}} \quad (5.2)$$

where $S_{850\mu\text{m}}$ is measured in mJy and $S_{1.4\text{GHz}}$ in μJy . We note that the most reliable method of calculating T_D is to fit template SEDs to multiple far-infrared and submillimetre photometric points, but for simplicity and due to the absence of published deep far-infrared photometry in the ECDFS we use Eqn. 5.2 to calculate T_D of LESS SMGs (although we next use shallow far-infrared observations to confirm the validity of this assumption).

We also use the infrared-radio correlation (Helou et al. 1985; Condon 1992),

$$q_{FIR} = \log_{10} \left(\frac{L_{FIR}}{3.75 \times 10^{12} \text{W}} \right) - \log_{10} \left(\frac{L_{1.4\text{GHz}}}{\text{WHz}^{-1}} \right) \quad (5.3)$$

with radio spectral index $\alpha = 0.8$ (where $S_\nu \propto \nu^{-\alpha}$) and $q_{FIR} = 2.64$ (Bell 2003, for star-forming galaxies), to calculate far-infrared luminosities of the LESS SMGs from their radio fluxes, as done by Chapman et al. (2005). Although this approach was recently verified by Magnelli et al. (2010) who used *Herschel* data to show that the local far-infrared radio correlation is consistent with SMGs, we caution that there may be a factor of ~ 2 uncertainty in the derived luminosities due to possible evolution in the far-infrared–radio correlation (Ivison et al. 2010a) and hence the appropriate value of q_{FIR} .

In Fig. 5.9 we plot the far-infrared luminosity against T_D for the LESS SMGs and optically faint radio galaxies (OFRGs; Chapman et al. 2004a; Casey et al. 2009; Magnelli et al. 2010). The LESS SMGs have a median $T_D = 35.9 \pm 1.4 \text{K}$, with an interquartile range of 28.5–43.3 K, and $L_{FIR} = (8.2 \pm 1.2) \times 10^{12} L_\odot$, with an interquartile range of $(3.0\text{--}13) \times 10^{12} L_\odot$, comparable to previous surveys (e.g. Chapman et al. 2005; Magnelli et al. 2010).

To check this result we also employ the 250, 350, and 500 μm Balloon-borne Large Aperture Submillimeter Telescope (BLAST) maps of the ECDFS (Devlin et al. 2009). We can stack the emission in these maps at the positions of the LESS SMG counterparts to obtain the average LESS SED from 250 to 870 μm . The stacked fluxes are fitted with a modified black body with $\beta = 1.5$ at $z = 2.2$ and correct the luminosity of the fitted

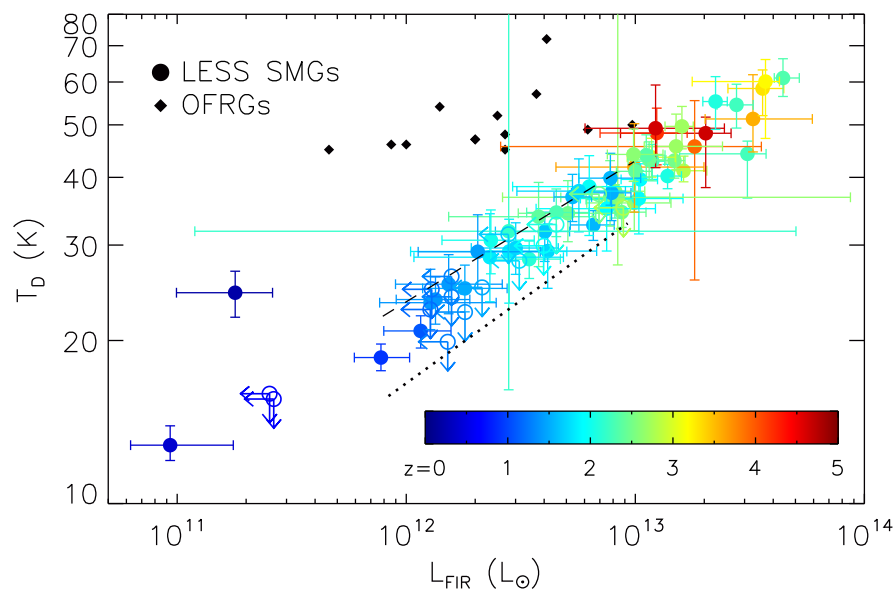


Figure 5.9: The characteristic dust temperature (T_D) versus far-infrared luminosity (L_{FIR}) for our SMGs. The SMGs are colour coded on the basis of their photometric redshifts and as expected the most luminous galaxies are the hottest, and are also tend to be those at the highest redshifts. This trend is driven in part by the radio luminosities of the SMGs (which lack the positive K correction of the submillimetre waveband) hence why there is a correlation between L_{FIR} and z , but not between $S_{870\mu m}$ and z (Fig. 5.2). The regions above the dashed line and below the dotted line are illustrative of the regions excluded by our submillimetre and radio detection limits respectively. The dashed line, which roughly demarcates the upper envelope of the data, represents the derived temperature of galaxies at $z = 2$ with various radio fluxes and $S_{870\mu m} = 4.2$ mJy. The dotted line, which similarly demarcates the lower envelope, is derived for submillimetre-luminous ($S_{870\mu m} = 16$ mJy) sources with radio flux equal to our detection limit ($3\sigma = 19.5\mu\text{Jy}$) at redshifts of $z = 1.4$ – 4 . This reflects both the strong cut-off in the submillimetre luminosity function at high luminosities and the fact that our radio data is only just deep enough to detect counterparts to the majority of SMGs. We conclude that the apparent correlation between T_D and L_{FIR} is in part caused by selection bias. We note that OFRGs (Chapman et al. 2004a; Casey et al. 2009; Magnelli et al. 2010), which are detected in the radio but not the submillimetre, lie above the upper dashed line.

black body to *total* far-infrared luminosity, 8–1000 μm , based on Ivison et al. (2010c). From this calculation of the stacked fluxes the typical characteristic dust temperature of the LESS SMGs is $T_D = 33.6 \pm 1.1$, and the typical far-infrared luminosity is $L_{FIR} = (7.6^{+1.7}_{-1.5}) \times 10^{12} L_{\odot}$. These values are in good agreement with those derived above from the local far-infrared–radio correlation.

We find that the highest redshift galaxies also have the highest luminosities due to a combination of the radio K-correction (preventing the detection of low-luminosity galaxies at high redshifts) and luminosity evolution (see Fig. 5.10). There is an apparent trend between the T_D and L_{FIR} but this is likely at least partially a selection effect, although we note that locally *IRAS* galaxies exhibit a tight correlation between T_D and L_{FIR} (Chapman et al. 2003b; Chapin et al. 2009). To illustrate the selection effects we also show OFRGs (Chapman et al. 2004a) in Fig. 5.9; OFRGs are detected at radio but not submillimetre wavelengths and have radio luminosities similar to SMGs, but contain warmer dust ($T_D \sim 45$ K; Casey et al. 2009; Magnelli et al. 2010). Our 870- μm detection limit misses warmer and lower luminosity galaxies from the sample and the radio detection limit excludes the colder luminous galaxies (e.g. Chapman et al. 2005).

In Fig. 5.10 and Table 5.1 we present the far-infrared luminosity functions of the radio-detected LESS SMGs with $z = 1\text{--}2$ and $z = 2\text{--}3$, compared to the $z = 2\text{--}3$ result from Chapman et al. (2005). We calculate the LESS SMG luminosity function with an accessible volume technique where:

$$\Phi(L)\Delta L = \sum_i \frac{1}{V_i} \quad (5.4)$$

which accounts for the flux limited nature of our survey. $\Phi(L)\Delta L$ is the number density of sources with luminosities between L and $L + \Delta L$, and V_i is the comoving volume within which the i th source can be detected in the luminosity bin under consideration. Since we derive the far-infrared luminosity from the radio flux, V_i is calculated using the radio luminosity. Error bars are calculated by bootstrapping and account for the redshift, luminosity and binning errors; we exclude the radio-bright AGN (LESS 20) from this analysis. We use the same method to calculate the luminosity function for Chapman et al. (2005) SMGs based on the redshifts and radio fluxes listed in that paper. By assuming that unidentified SMGs have radio fluxes equal to our detection limit and the redshift distribution that we measure in §5.3.3, we also calculate the maximum contribution of unidentified SMGs to the far-infrared luminosity functions.

If Fig. 5.10 we observe strong evolution in the far-infrared luminosity function: the

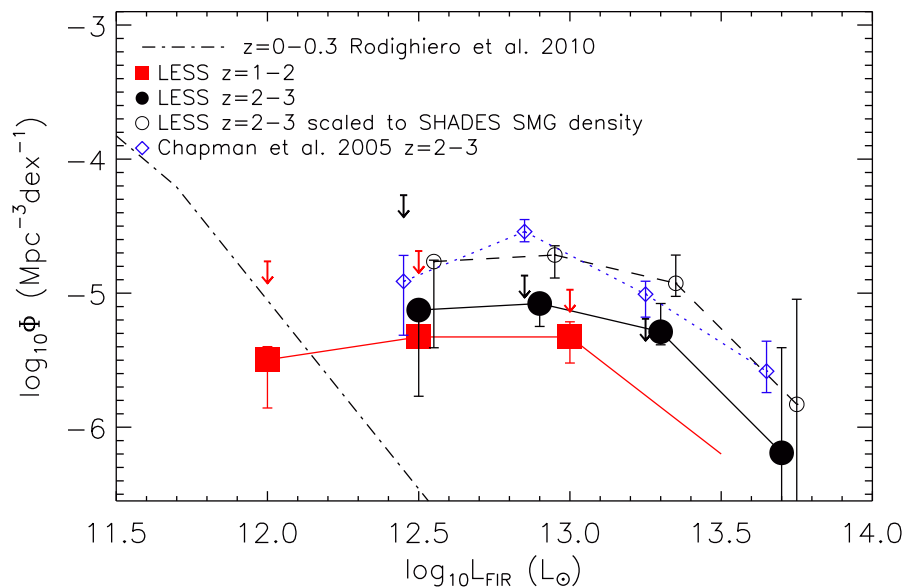


Figure 5.10: Far-infrared luminosity functions of the radio-detected LESS SMGs with $z = 1-2$ and $z = 2-3$. Evolution is evident in the luminosity function of the LESS SMGs between the two redshift bins, and from the 24- μm selected low redshift comparison sample (Rodighiero et al. 2010). The SMGs have higher luminosities than the $z < 0.3$ 24- μm galaxies, and the $z = 2-3$ SMGs having higher luminosities and Φ^* . We also show the $z = 2-3$ luminosity function of Chapman et al. (2005) SMGs (offset slightly in $\log_{10}L_{FIR}$ for clarity) for comparison. The LESS $z = 2-3$ sample has a systematically lower luminosity density than Chapman et al. (2005) SMGs in the same redshift range. Weiß et al. (2009) showed that the ECDFS is underdense at submillimetre wavelengths and by scaling the LESS luminosity function such that the SMG number density matches that of SHADES survey (Coppin et al. 2006) we show that the disparity in Φ^* between LESS and Chapman et al. (2005) is likely due to the relative density of SMGs in the two surveys (the scaled LESS luminosity function is offset slightly in $\log_{10}L_{FIR}$ SMGs for clarity). We calculate the maximum contribution from unidentified SMGs, by assigning them the redshift distribution that we measure in §5.3.3 and radio fluxes equal to our detection limit. Including the contribution from unidentified SMGs the total maximum Φ in each luminosity bin is represented by an arrow (offset slightly in $\log_{10}L_{FIR}$ for $z = 2-3$ SMGs for clarity).

Table 5.1: Far-infrared luminosity function for radio-detected LESS SMGs

$z = 1-2$ SMGs		$z = 2-3$ SMGs	
$\log_{10} L_{FIR}$	$\log_{10} \Phi$	$\log_{10} L_{FIR}$	$\log_{10} \Phi$
(L_{\odot})	$(\text{Mpc}^{-3} \text{dex}^{-1})$	(L_{\odot})	$(\text{Mpc}^{-3} \text{dex}^{-1})$
12.0	$-5.5^{+0.2}_{-0.3}$	12.5	$-5.1^{+0.1}_{-0.6}$
12.5	-5.3 ± 0.1	12.9	$-5.1^{+0.1}_{-0.2}$
13.0	$-5.3^{+0.1}_{-0.2}$	13.3	$-5.3^{+0.2}_{-0.1}$
13.5	< -6.2	13.7	$-6.2^{+0.7}_{-6.2}$

$z = 2-3$ SMGs are more luminous and have higher space densities than the $z = 1-2$ SMGs, which in turn are more luminous than the $z < 0.3$ $24 \mu\text{m}$ -selected galaxies from Rodighiero et al. (2010) (see also the *Herschel* sample of Vaccari et al. 2010). LESS SMGs at $z = 2-3$ have $\Phi^* \sim 1.6\times$ and $L^* \sim 2\times$ higher than those at $z = 1-2$.

The $z = 2-3$ LESS SMGs have systematically lower Φ^* than the Chapman et al. (2005) SMGs in the same redshift range. This may be due to cosmic variance since Weiß et al. (2009) showed that the ECDFS is a factor of ~ 2 underdense compared to other large submillimetre surveys at flux densities $\gtrsim 3 \text{ mJy}$. By rescaling the LESS luminosity function so that the $870 \mu\text{m}$ number counts agree with those of the SHADES survey (Coppin et al. 2006), which should be similar to that of Chapman et al. (2005) since both covered multiple fields, Fig. 5.10 shows that the low surface density of SMGs in the ECDFS is most likely the cause of the disparity in Φ^* .

In Fig. 5.11 we show the evolution of the star-formation rate density (SFRD) of the radio-detected LESS SMGs. We use the same accessible volume technique as in our luminosity function calculations to account for the flux limited nature of the survey. Error bars are calculated from bootstrapping and include the uncertainties in binning, redshifts and SFRs. Since the SFRs are based upon radio fluxes we exclude the suspected radio-bright AGN LESS 20 from this analysis.

We do not know the individual redshifts, infrared luminosities or SFRs for 45% of the LESS SMGs because they do not have robustly identified optical counterparts. In Fig. 5.11 we account for this population by assigning them the redshift distribution that we measure in §5.3.3 and assuming radio fluxes equal to our detection limit. The calculated SFRD of the unidentified SMGs from this analysis is an upper limit since the actual radio fluxes will typically be lower than the detection limit. In Fig. 5.11 we indicate the

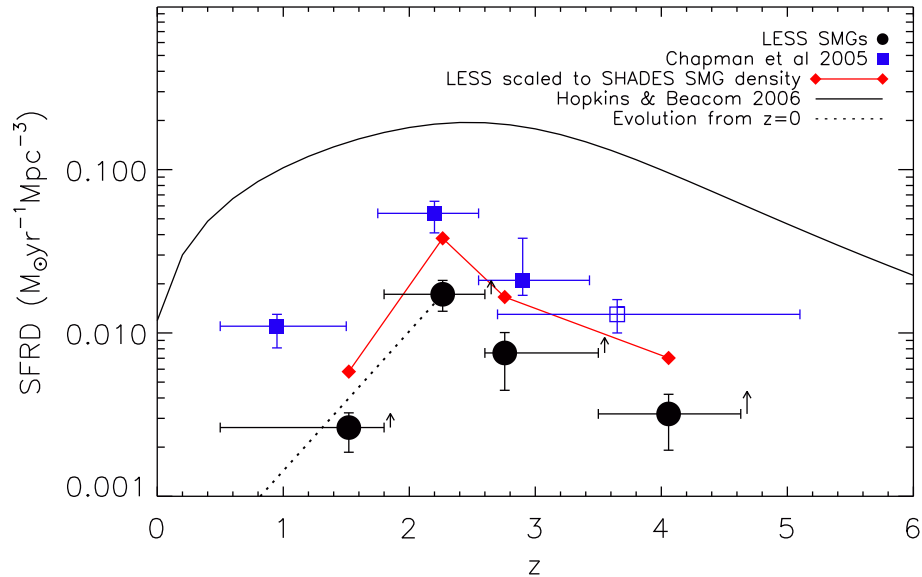


Figure 5.11: Evolution of the SFRD for the radio-detected LESS SMGs compared to Chapman et al. (2005). Arrows to the right of each LESS redshift bin indicate the maximum additional contribution from unidentified SMGs and the open symbol represents unidentified SMGs from Chapman et al. (2005). We also show the modified Salpeter A IMF fit to the SFRD compilation from Hopkins & Beacom (2006) and a line showing the evolution from *IRAS* ULIRGs at $z = 0$ (Elbaz & Cesarsky 2003) to LESS SMGs at $z = 2.3$. The LESS SMG activity peaks at $z \sim 2$ – similar to that found by previous studies of star-forming galaxies and the peak activity of QSOs (Hopkins et al. 2007). The contribution from SMGs to the total SFRD also peaks at $z \sim 2$ where they are responsible for $\sim 10\%$ of the Hopkins & Beacom (2006) SFRD. The ECDFS is underdense at submillimetre wavelengths (Weiß et al. 2009) so similarly to Fig. 5.10 we also scale the SFRD of the LESS SMGs such that the number counts match the SHADES survey allowing a closer comparison to Chapman et al. (2005).

maximum contribution to the SFRD of unidentified SMGs in each redshift bin.

The SFRD of the LESS SMGs appears to peak at $z \sim 2$, similar to Chapman et al. (2005). The LESS SMGs have a lower SFRD than the SMGs from Chapman et al. (2005) but we note that the lower number density of SMGs in the ECDFS is sufficient to account for this effect. This corresponds to the peak of QSO activity at $z = 2.15 \pm 0.05$ (Hopkins et al. 2007). The fractional contribution of LESS SMGs to the SFRD of the Universe also peaks at $z \sim 2$ where they are responsible for $\sim 10\%$ of the SFRD as estimated by Hopkins & Beacom (2006) from a compilation of surveys that does not include any submillimetre surveys. We stress that this only includes SMGs with $S_{870\mu m} \gtrsim 4$ mJy. Assuming that fainter sources have the same redshift distribution then the contribution of SMGs with $S_{870\mu m} \gtrsim 1$ mJy is $\sim 100\%$ of the (Hopkins et al. 2007) value. Thus, SMGs (high-redshift ULIRGs) may contribute $\sim 50\%$ of the *total* SFRD of the Universe at $z \sim 2$.

5.4 Summary and Conclusions

We use photometric redshifts derived from deep multicolour imaging of the ECDFS in 17-bands to investigate the photometric properties and evolution of the counterparts of SMGs in the LESS LABOCA survey of the ECDFS (Weiß et al. 2009; Biggs et al. 2010).

We find that LESS radio, 24 μ m and IRAC-identified SMGs have a median redshift of $z = 2.2 \pm 0.1$ and interquartile range of $z = 1.8$ – 2.7 . Thus the peak activity in SMGs corresponds to the epoch of maximal QSO and star-formation activity in the Universe. The redshift distribution of LESS SMGs is consistent with the spectroscopic survey of Chapman et al. (2005), but higher than the photometric studies of the SHADES survey (Clements et al. 2008; Dye et al. 2008). We find a higher-redshift tail to the distribution of LESS galaxies, with 10 (14%) identified SMGs at $z \gtrsim 3$. Counterparts identified through radio, 24 μ m and IRAC emission have statistically indistinguishable redshift distributions; similarly robust and tentative counterparts have comparable redshift distributions, albeit with some foreground contamination in the tentative sample. Previous studies provided tentative evidence that SMGs with the highest submillimetre fluxes may be the highest redshift sources (e.g. Ivison et al. 2002; Pope et al. 2005), but with our extensive photometric redshifts we find no such correlation.

A statistical study of the source population in the error circles of the 55 SMGs that lack robust radio, 24 μ m and IRAC counterparts suggests that there is an excess of 26 ± 12 (2.2σ) $z > 1$ galaxies in these regions. This excess population corresponds to the

counterparts or companions of the unidentified SMGs and our analysis then suggests that the redshift distribution of these unidentified SMGs peaks at $z = 2.5 \pm 0.3$. This is similar to, but potentially slightly higher than, that of the identified population, suggesting that many of the unidentified SMGs are at $z \sim 2-3$ and have radio or $24\mu\text{m}$ fluxes just below our detection limits.

In total we estimate that there are 21 ± 19 ($17 \pm 15\%$ of all the SMGs) LESS SMGs that are not robustly identified, and which are not accounted for in our statistical analysis of unidentified SMGs. These should be galaxies without any detectable mid-infrared emission and as a result are likely to lie at $z \gtrsim 3$. Including the identified SMGs at $z > 3$ we estimate that $28 \pm 15\%$ of all LESS SMGs lie at $z > 3$.

We combine the redshift distribution of identified SMGs with that statistically determined for unidentified SMGs, including the SMGs which are not detected in our survey and are likely to lie at $z \gtrsim 3$. We conclude that the likely median redshift of the *entire* population of $S_{870\mu\text{m}} \gtrsim 4$ mJy SMGs is $z = 2.5 \pm 0.6$.

The separation of SMGs into those with redshifts above and below $z = 1.4$ broadly agrees with the *BzK* colour-colour criteria (Daddi et al. 2004), making the *BzK* colours a coarse but reliable redshift indicator for SMGs. Similarly the submillimetre-to-radio flux ratios of LESS SMGs broadly agrees with the prediction of Carilli & Yun (2000), although there is significant scatter, indicative of temperature variations between SMGs. This means that redshifts derived from submillimetre-to-radio flux ratios also exhibit significant scatter.

Using our photometric redshifts, submillimetre and radio fluxes we calculate that the median characteristic dust temperature of the SMGs is $T_D = 35.9 \pm 1.4$ K, with an interquartile range of 28.5–43.3 K. The median far-infrared luminosity of the SMGs, derived from the radio luminosity, is $L_{FIR} = (8.2 \pm 1.2) \times 10^{12} L_\odot$ and the interquartile range of $L_{FIR} = (3-13) \times 10^{12} L_\odot$. For a Salpeter IMF this corresponds to median $\text{SFR} = 1100 M_\odot \text{yr}^{-1}$, with an interquartile range of 300–1900 $M_\odot \text{yr}^{-1}$. We show that, for LESS SMGs, the apparent correlation between the far-infrared luminosity and T_D is in part a selection effect.

The far-infrared luminosity function of the LESS SMGs exhibits a strong redshift evolution, such that SMGs at $z = 2-3$ are more numerous and have higher luminosities than those at $z = 1-2$. We find that the normalisation of the luminosity function is lower for LESS than for the Chapman et al. (2005) SMG sample, and by scaling the ECDFS submillimetre number counts we show that this is due to the underdensity of the ECDFS

at submillimetre wavelengths (Weiß et al. 2009).

The SFRD and fractional contribution to the global SFRD of the LESS SMGs with $S_{870\mu m} \gtrsim 4$ mJy evolves with redshift and both peak at $z \sim 2$, where the LESS population contributes a total SFR density of $0.02 M_{\odot} \text{yr}^{-1} \text{Mpc}^{-1}$. If fainter submillimetre sources have the same redshift distribution then SMGs with $S_{870\mu m} > 1$ mJy (i.e. ULIRGs) produce $\sim 50\%$ of the SFRD of the Universe at $z \sim 2$.

The large star-formation rates of SMGs implies that they could build-up significant stellar masses within relatively short periods of time. Similarly the large SFRDs suggests that they contribute a large fraction of the stellar mass created at $z \sim 2$. Previous work has suggested that SMGs are massive (e.g. Borys et al. 2005; Hainline et al. 2010), and strongly clustered (e.g. Blain et al. 2004; Weiß et al. 2009), and thus may be the progenitors of giant galaxies on the CMR in local clusters (e.g. Chapter 2). Therefore, in Chapter 6 we next use the uniquely large, homogeneous LESS SMG sample to further investigate the stellar masses, clustering and halo masses of SMGs.

5.5 Appendix: Discussion of individual sources

Most LESS SMGs have properties similar to previous SMG populations. However, several robust counterparts have unusual properties, X-ray emission, or $8\mu m$ excesses indicative of the presence of an AGN (see Chapter 6 for a thorough discussion of LESS AGN). We discuss these galaxies on a case-by-case basis below and in Fig. 5.12 we show images centered on each LESS SMG, highlighting the radio, $24\mu m$ and IRAC identifications.

LESS 2a & 2b: LESS 2 has both a robust $24\mu m$ (LESS 2a) and a robust radio counterpart (LESS 2b), separated by $2.7''$, with $z = 1.80_{-0.14}^{+0.35}$ and $2.27_{-0.55}^{+0.16}$ respectively. It is possible that the two counterparts are at the same redshift ($z \sim 2$), separated by ~ 20 kpc and may in the process of merging.

LESS 6: LESS 6 is $\sim 1''$ from the robust $24\mu m$ counterpart and $\sim 2.5''$ from the robust radio counterpart and has a photometric redshift of $z = 0.40_{-0.03}^{+0.09}$, therefore it is possible that the submillimetre source is a background galaxy which is being gravitationally lensed by the proposed counterpart to LESS 6.

LESS 9: This SMG is X-ray luminous and has $z_{\text{phot}} = 4.63_{-1.10}^{+0.10}$ making it the highest redshift X-ray source in our sample. Our best-fitting SED shows no $8\mu m$ excess and thus no suggestion of an AGN from the rest-frame near-infrared, optical and UV photometry.

LESS 10a: LESS 10a is one of two counterparts to LESS 10 identified from extended or

blended radio emission. It has a slight $8\ \mu\text{m}$ excess over the best-fit SED, suggesting the presence of an AGN, but no detectable X-ray emission.

LESS 11: Similarly to LESS 9 this galaxy shows no $8\ \mu\text{m}$ excess but is X-ray bright.

LESS 19: Based upon the SED fitting LESS 19 has excess 5.8 and $8\ \mu\text{m}$ emission. However, the source is faint and the fit has $\chi^2 = 10.0$ so it is unclear whether the apparent excess is due to errors in the fitting or the presence of an AGN.

LESS 20: This SMG is unusually radio bright with $S_{1.4\text{GHz}} = 4.25$ mJy. There is no evidence of X-ray emission or an $8\ \mu\text{m}$ excess, suggesting that LESS 20 is a radio-bright AGN. If this is the case then the AGN contribution to the radio flux means that T_D and L_{FIR} are likely to be significantly over-estimated. Therefore, we exclude LESS 20 from our analyses of the SFRs and luminosity function of SMGs.

LESS 40: LESS 40 has X-ray emission and an $8\ \mu\text{m}$ excess and is highly likely to contain an AGN.

LESS 50b: This galaxy is X-ray luminous but does not exhibit a compelling $8\ \mu\text{m}$ excess.

LESS 57: LESS 57 has a strong $8\ \mu\text{m}$ excess and is X-ray bright, compelling evidence for the presence of an AGN in this SMG.

LESS 66: LESS 66 lies near the diffraction spike of a bright star, so some of the photometry may be unreliable. However, it is an optically bright point source with an $8\ \mu\text{m}$ excess and X-ray emission. There are broad emission lines in the spectra suggesting that LESS 66 is a submillimetre-bright QSO.

LESS 67: This galaxy has coincident X-ray emission and may contain an AGN.

LESS 74a & b: The two counterparts to LESS 74 have $z = 1.84_{-0.49}^{+0.32}$ and $1.71_{-0.17}^{+0.20}$, are separated by $2.7''$ (~ 20 kpc), and have some faint extended emission between them in the optical images. Therefore, it is likely that LESS 74a and LESS 74b are undergoing an interaction at $z \sim 1.8$ which triggered the submillimetre emission.

LESS 75: Although LESS 75 is not X-ray detected there is strong 8 and $5.8\ \mu\text{m}$ excess above the best-fit SED, indicative of a highly obscured AGN.

LESS 84: LESS 84 is X-ray detected, and has a small $8\ \mu\text{m}$ excess suggesting it may contain an AGN.

LESS 96: LESS 96 is similar to LESS 66 – it is X-ray luminous and has a strong $8\ \mu\text{m}$ excess above the best-fit SED, and it is an bright optical point source. We interpret this as evidence that LESS 96 is a submillimetre-bright QSO.

LESS 106: This SMG is X-ray detected but no $8\ \mu\text{m}$ excess is observed.

LESS 108: LESS 108 is identified as a bright local ($z = 0.086$) late-type spiral galaxy

from its strong radio and $24\ \mu\text{m}$ emission. The similarity of the radio, mid- and near-infrared, and optical morphologies suggests that this is not a case of gravitational lensing.

LESS 111: LESS 111 is X-ray detected and has a $8\ \mu\text{m}$ excess, indicating it may contain an AGN. It lies $\lesssim 3''$ from an extended foreground galaxy and is likely to be gravitationally lensed.

LESS 114: This SMG is coincident with an X-ray source, but shows no evidence of an $8\ \mu\text{m}$ excess above the best-fit SED.

LESS 122: LESS 122 has excess flux at $8\ \mu\text{m}$ compared to the best-fit SED but is not X-ray detected.

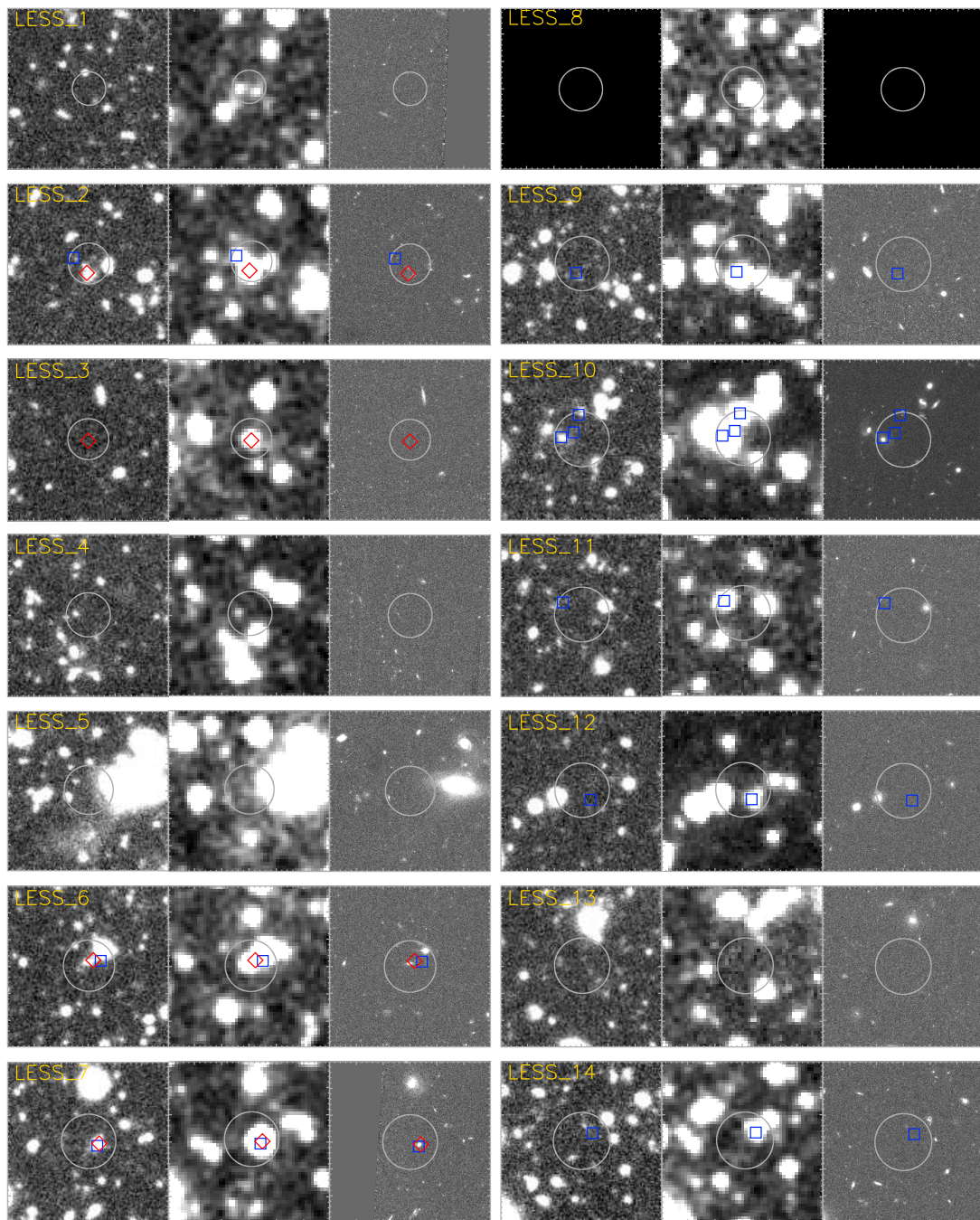
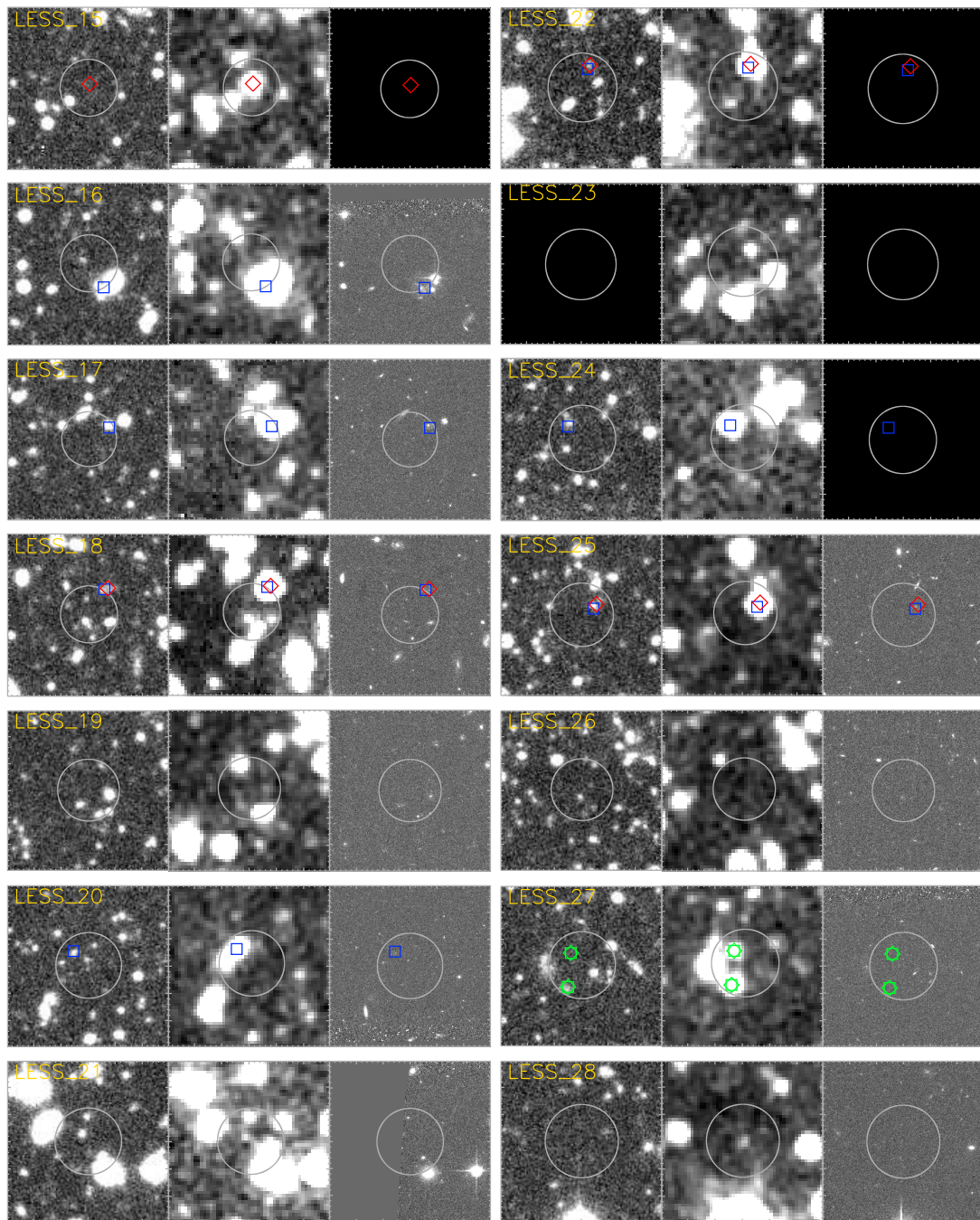
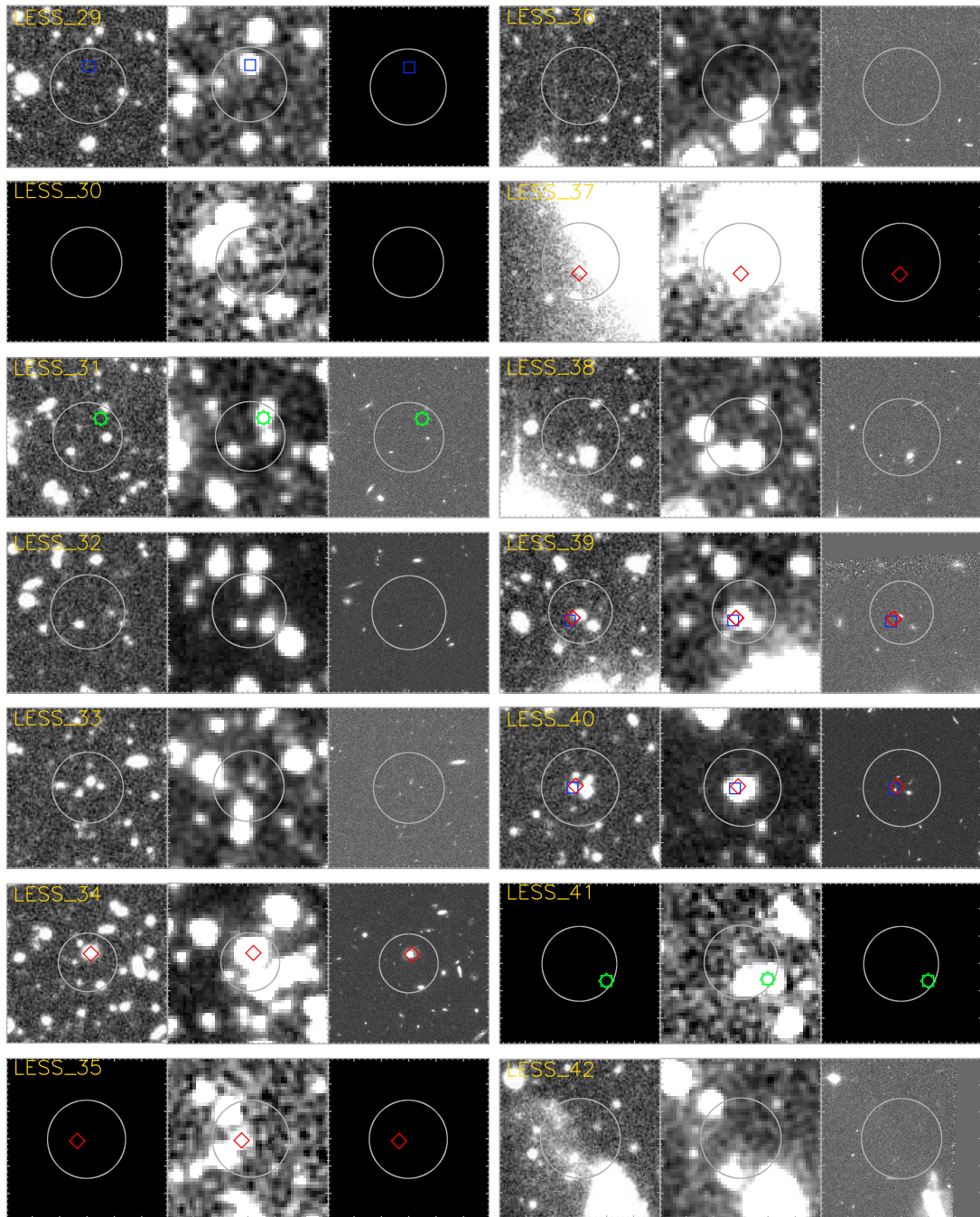
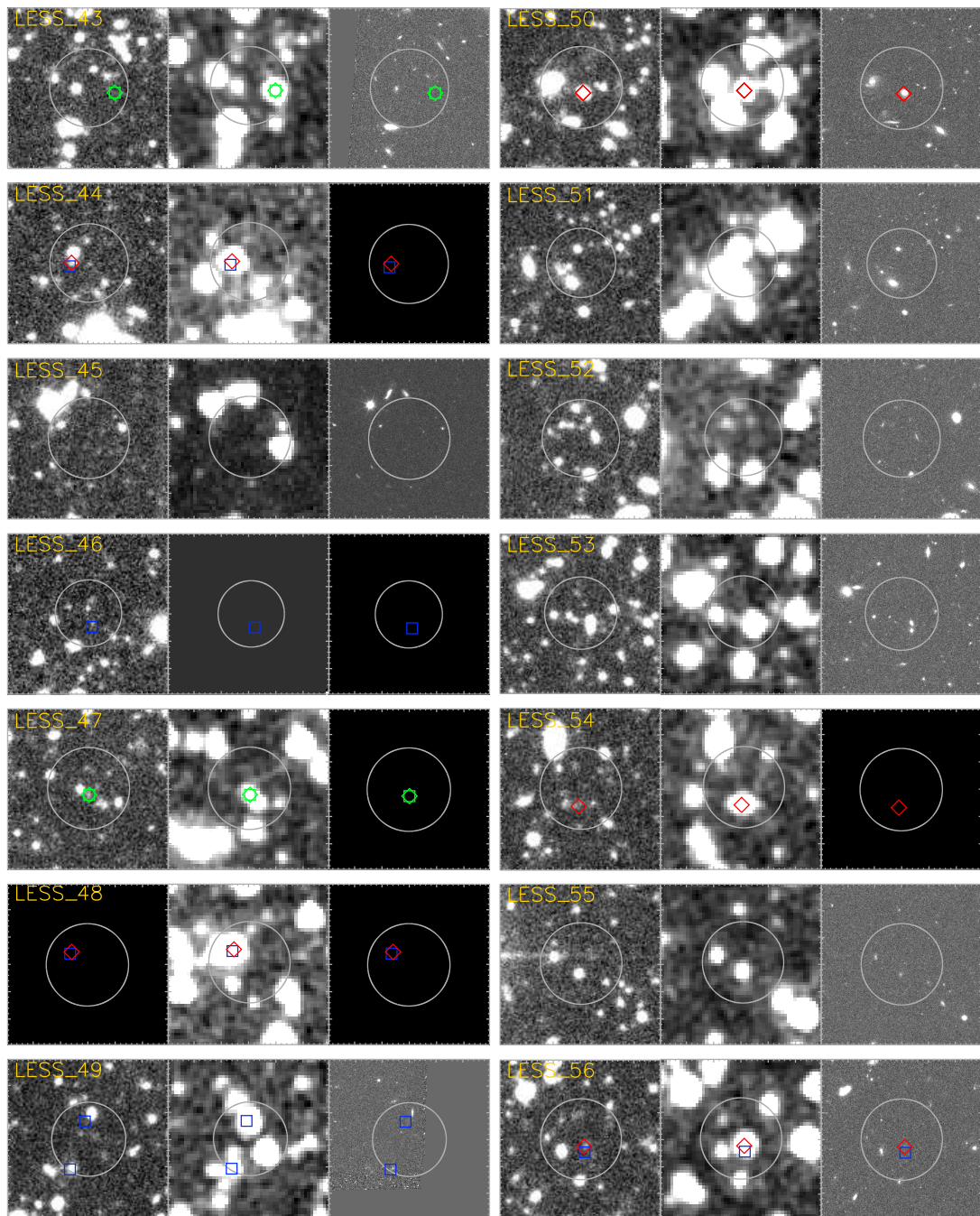
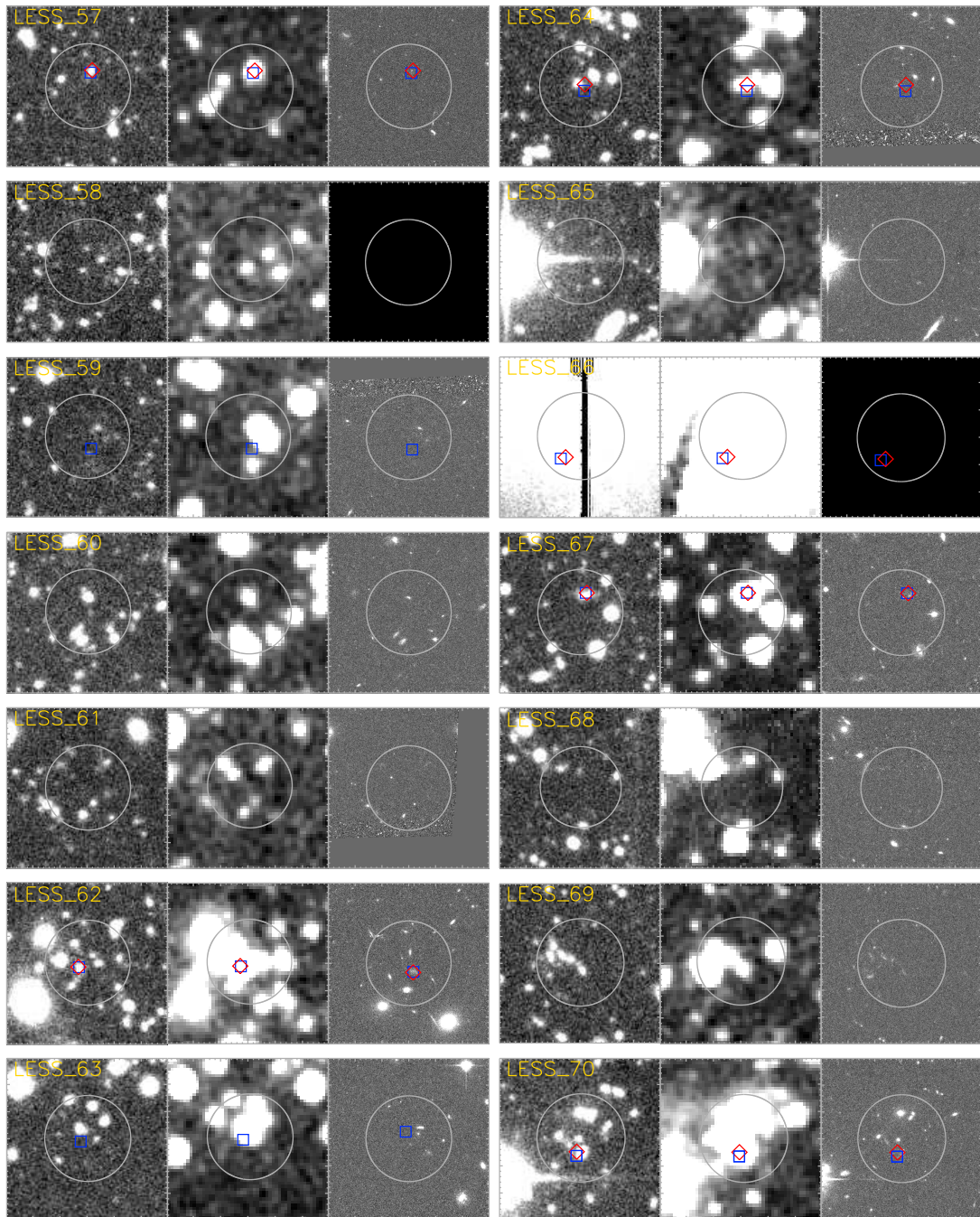


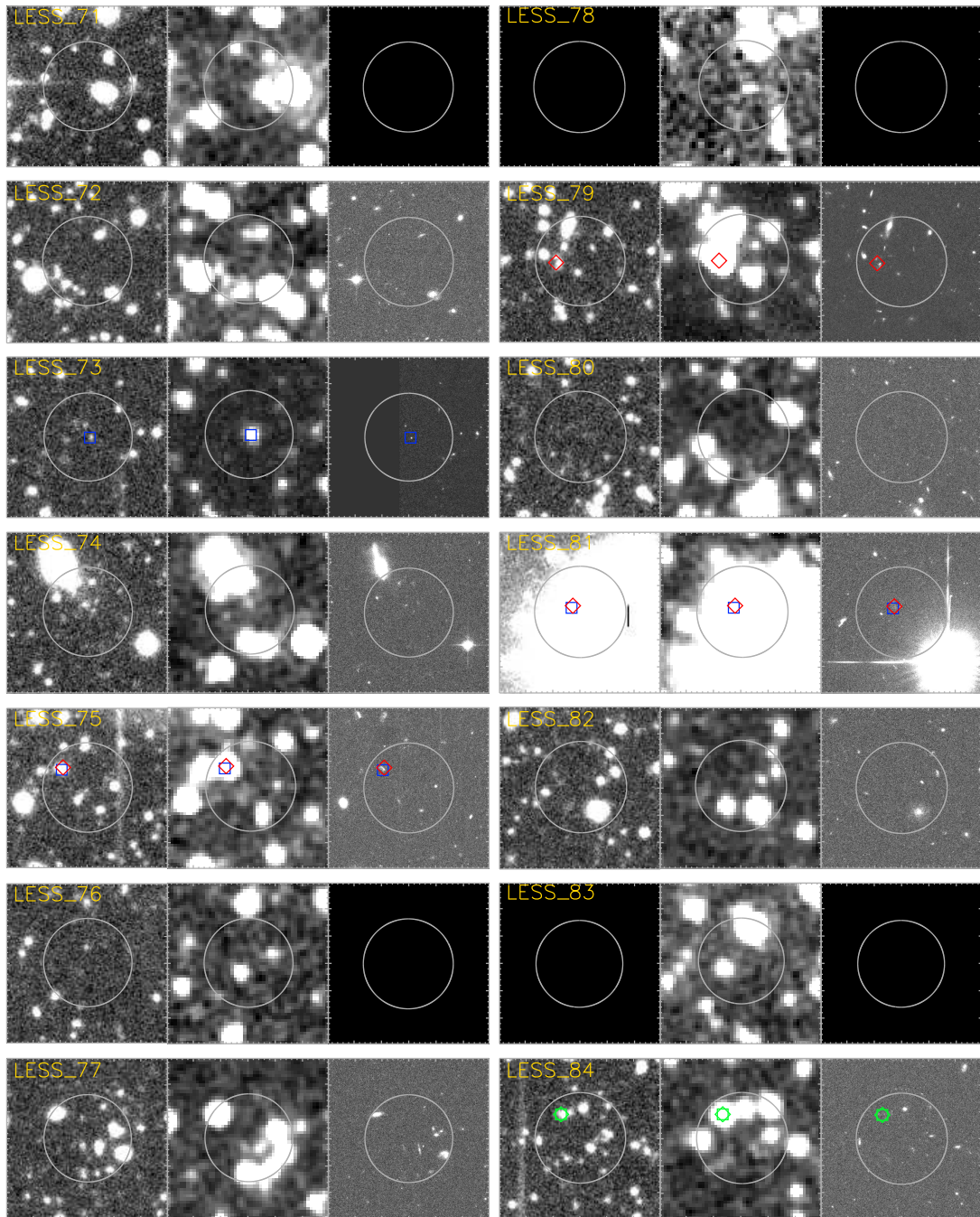
Figure 5.12: 30×30 arcsec images centred on each LESS SMG; north is up and east is to the left. In the left-hand panel we present the MUSYC BVR image, the central panel shows the IRAC $4.5\mu\text{m}$ image, and the HST ACS F850LP image is in the right-hand panel. Circles are centred on the AzTEC positions and have represent the size of the area used when searching for counterparts (Chapter 4; Biggs et al. 2010). We highlight robust radio, $24\text{-}\mu\text{m}$, and IRAC counterparts with blue squares, red diamonds, and green stars, respectively.

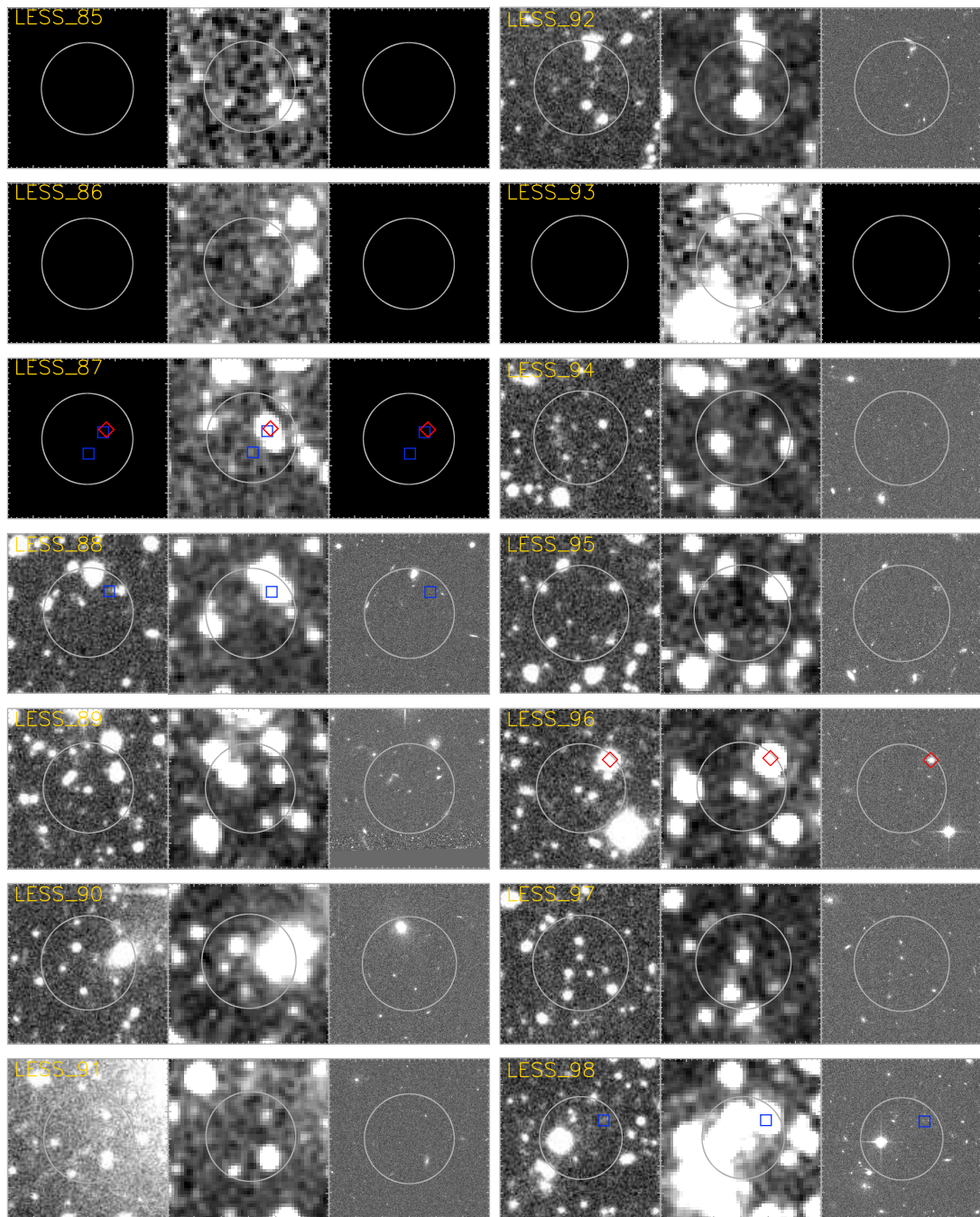
Figure 5.12: – *continued*

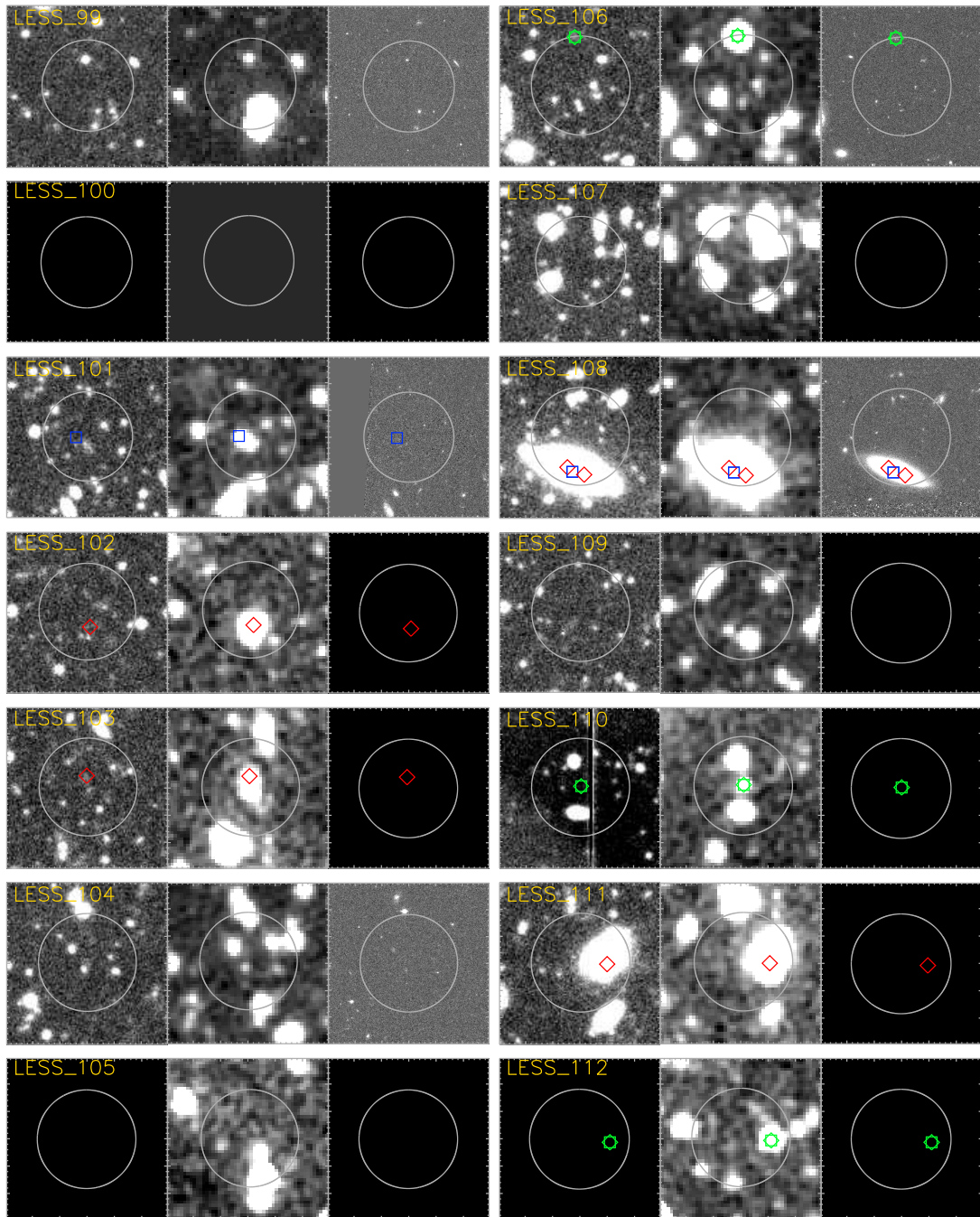
Figure 5.12: – *continued*

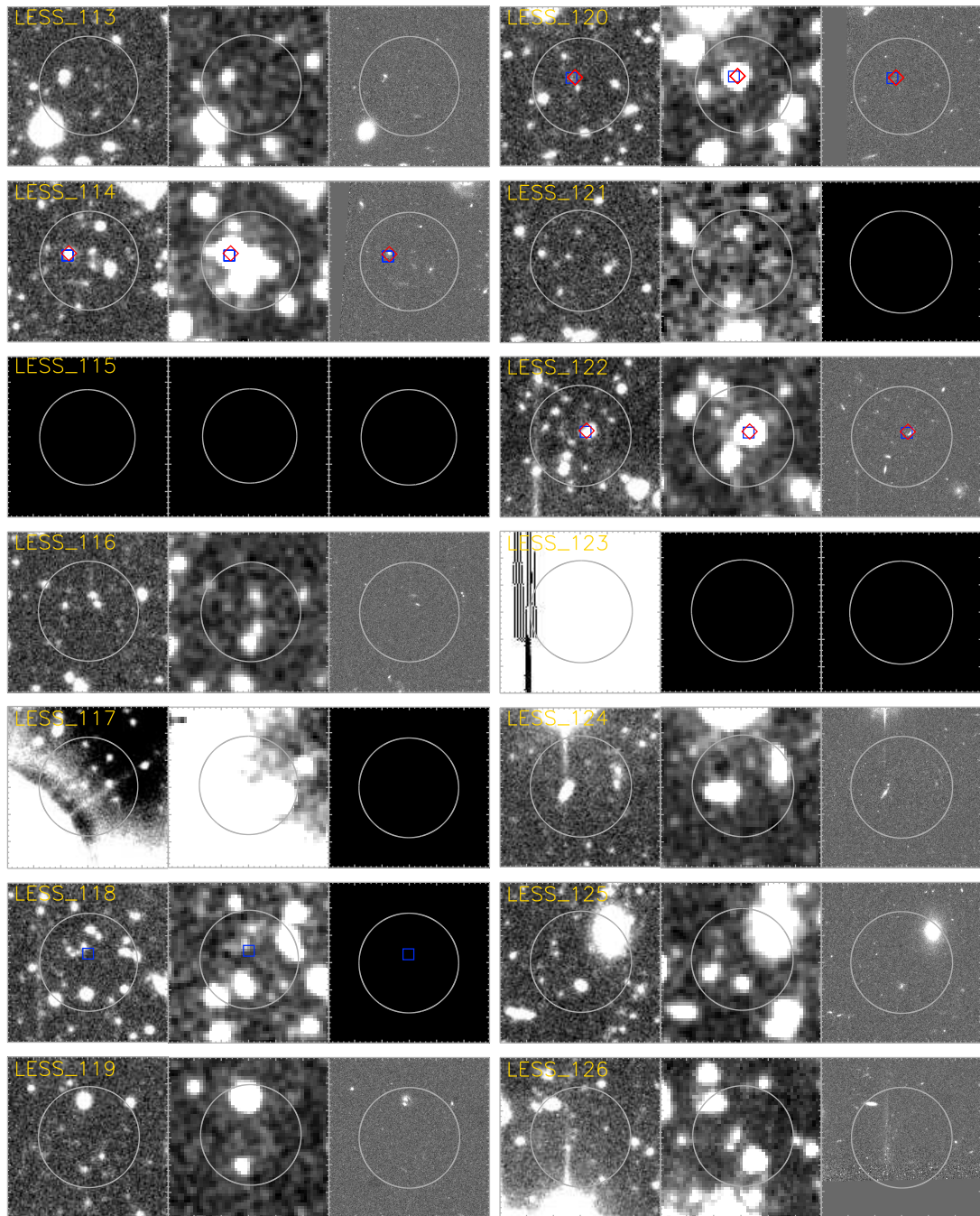
Figure 5.12: – *continued*

Figure 5.12: – *continued*

Figure 5.12: – *continued*

Figure 5.12: – *continued*

Figure 5.12: – *continued*

Figure 5.12: – *continued*

Chapter 6

The physical properties of SMGs

6.1 Introduction

SED fitting to the optical and near-infrared photometry of submillimetre galaxies (SMGs) suggests that they have stellar masses of $\gtrsim 7 \times 10^{10} M_{\odot}$ (e.g. Borys et al. 2005; Dye et al. 2008; Hainline et al. 2010). However, there is significant variation between different studies, which as we later discuss, is likely to be due to bias in some of the samples and systematic errors in others. Integral-field spectroscopy of SMGs suggests that they have dynamical masses of $\sim 5 \times 10^{11} M_{\odot}$ (Swinbank et al. 2006) and observations of CO emission lines indicates gas masses of $\sim 3 \times 10^{10} M_{\odot}$ and dynamical masses of $\sim 10^{11} M_{\odot}$ (e.g. Genzel et al. 2003; Greve et al. 2005). Thus, evidence from several different analyses suggests that SMGs are amongst the most massive galaxies in the Universe at $z \sim 2$.

If SMGs are the progenitor population of local massive early-type galaxies such massive galaxies are expected to be strongly clustered and typically located in high-density environments. Several authors have attempted to detect the clustering of SMGs (e.g. Webb et al. 2003; Blain et al. 2004; Scott et al. 2006; Serjeant et al. 2008; Weiß et al. 2009), and all find tentative evidence that SMGs are not randomly distributed and are likely to be strongly clustered. However, progress has been hampered by the typically small samples of SMGs, which often do not have sufficient redshift information to investigate the three-dimensional clustering of SMGs. However, we note that Blain et al. (2004) did manage to detect clustering using redshift information of a sample of SMGs and derived correlation length of $r_0 = 6.9 \pm 2.1 h^{-1} M_{\odot}$, corresponding to a dark-matter halo mass of $\sim 3 \times 10^{12} M_{\odot}$. Recently, Cooray et al. (2010) investigated the angular correlation function of sources selected at 250 μm from *Herschel* observations. They found that

sources selected by 350 μm -250 μm colour to have redshift distributions similar to “classic” $\sim 850\text{-}\mu\text{m}$ selected SMGs reside in dark matter halos of mass $> (5 \pm 4) \times 10^{12} M_{\odot}$.

Similarly, if SMGs are progenitors of local elliptical galaxies then as these are observed to follow a well-defined relationship between the mass of the bulge and that of the supermassive black hole (SMBH; e.g. Magorrian et al. 1998; Gebhardt et al. 2000), it could be expected that the build-up of stellar mass is associated with co-eval or subsequent growth of the SMBH. Therefore, it is important to understand the AGN fraction in SMGs to investigate the coevolution of the build-up of stellar mass and black-hole mass. Critically, the characteristic dust and gas in SMGs can obscure many of the usual AGN signatures in some systems, making it necessary to use a range of methods to identify AGN in SMGs. As many as $\sim 40\%$ of SMGs are found to contain signatures of both star-formation and AGN activity (e.g. Alexander et al. 2005; Takata et al. 2006; Pope et al. 2008; Coppin et al. 2009; Hainline et al. 2010), although the bolometric output and far-infrared luminosity is dominated by star-formation emission in a significant majority of cases (e.g. Alexander et al. 2005; Pope et al. 2008). However, complication arises because many surveys for AGN in SMGs are subject to selection biases due to requirements for radio or 24- μm counterparts, or secure spectroscopic redshifts. Therefore, it has proved difficult to accurately constrain the fraction of the SMG population that contain AGN, and thus investigate the evolution of the SMBHs in SMGs.

In Chapter 4 we derived photometric redshifts for 74 SMGs detected and identified in the LABOCA 870- μm submillimetre survey of the ECDFS (LESS; Weiß et al. 2009), and a sample of $\sim 50,000$ IRAC-selected field galaxies. In Chapter 5 we used this information to investigate the redshift distribution and star-formation activity of SMGs and showed that SMGs are undergoing intense bursts of star-formation at $z \sim 2$, as required if they evolve into the massive early-type galaxies found in clusters at lower redshifts (e.g. Chapters 2 and 3). In this Chapter we use this same sample of SMGs to investigate their stellar masses, clustering and dark matter halo masses to determine whether they have the required properties to be the progenitor population of local massive early-type galaxies. We also investigate to fraction of LESS SMGs that harbour AGN activity and have SMBHs that are undergoing a growth phase. Because of the large number of uniformly-selected SMGs in a single field with extensive auxiliary data LESS is uniquely suitable for this study.

We consider the AGN population, stellar masses, specific star-formation rates and clustering of SMGs in § 6.2 and in § 6.3 we present our conclusions. Throughout this

Chapter we use J2000 coordinates and Λ CDM cosmology with $\Omega_M = 0.3$, $\Omega_\Lambda = 0.7$ and $H_0 = 70 \text{ km s}^{-1} \text{ Mpc}^{-1}$. All photometry is on the AB magnitude system, in which $23.9 \text{ m}_{\text{AB}} = 1 \mu\text{Jy}$, unless otherwise stated.

6.2 Results and Discussion

6.2.1 AGN

In Chapter 4 we identified 16 LESS SMG counterparts which exhibit AGN signatures and are potential AGN and we summarise their properties in Table 6.1. There are 12 LESS SMGs coincident (within $1''$) with *Chandra* X-ray sources from the catalogues of Luo et al. (2008) and Lehmer et al. (2005) and nine with excess $8\text{-}\mu\text{m}$ flux compared to the best-fit SED template, of which six are also detected in the X-ray data. Hainline et al. (2010) showed that in addition to a stellar SED component these galaxies contain a power-law component of the form $f_\nu \propto \nu^{-\alpha}$ (for $\alpha = 2\text{--}3$), which represents hot-dust that may be powered by an AGN. We also find one radio-loud SMG, whose 1.4 GHz luminosity cannot be explained by star-formation alone (see Fig. 6.3), and two QSOs. All of these SMGs are likely to contain AGN; we next further investigate their properties and biases in the samples selected with each of these techniques.

In Fig. 6.1 we show the distribution of effective X-ray photon index (Γ) for the 11 X-ray detected LESS SMGs for which there are sufficient X-ray counts for Γ to be determined. Γ is taken from the catalogues from Lehmer et al. (2005) and Luo et al. (2008) and is calculated from the band ratio for a power-law model with Galactic column density. Obscured AGN are typically characterised by relatively flat spectral slopes ($\Gamma < 1$; e.g. Maiolino et al. 1998; Risaliti et al. 1999; Alexander et al. 2005), but unobscured AGN and star-forming galaxies have steeper X-ray slopes ($\Gamma > 1$; e.g. Nandra & Pounds 1994; Colbert et al. 2004; Alexander et al. 2005). Therefore, Γ can be used to distinguish between different sources of X-ray emission. Four of the 12 X-ray detected SMGs have $\Gamma < 1$ and are most likely have X-ray emission from an obscured AGN, although we note that the error bars of three of these have error bars that extend beyond $\Gamma = 1$. Therefore, based only on Γ the X-ray emission of 11 of the SMGs could be caused by AGN or starbursts, although as we show in Fig. 6.3 only LESS 67 shows no other AGN signatures and has an X-ray luminosity that could be caused by star-formation.

Therefore, excluding LESS 67, we identify just 11 SMGs with evidence of AGN activity from from X-ray emission, corresponding to 15% of the SMG counterparts in the field

Table 6.1: LESS SMGs with AGN signatures. We highlight SMGs that fulfil each of the selection criteria and provide the 0.5–8 keV flux or limit (Lehmer et al. 2005; Luo et al. 2008).

Source ^a	z_{phot}^b	X-ray detected?	8- μm excess?	Radio loud?	QSO?	0.5–8 keV flux ($10^{-15}\text{erg cm}^{-2}\text{s}^{-1}$)	Γ^c
LESS 9	$4.63^{+0.10}_{-1.10}$	✓				$6.34^{+0.27}_{-0.26}$	1.1 ± 0.2
LESS 10a	$2.46^{+0.15}_{-0.15}$		✓			< 0.14	...
LESS 11	$2.60^{+0.30}_{-0.36}$	✓				$1.17^{+0.22}_{-0.21}$	1.4 ± 0.2
LESS 20	$2.80^{+0.17}_{-0.27}$			✓		< 0.44	...
LESS 40	$1.90^{+0.10}_{-0.11}$	✓	✓			$0.44^{+0.11}_{-0.12}$	$0.8^{+0.6}_{-0.5}$
LESS 50b	$2.69^{+0.49}_{-0.25}$	✓				$9.03^{+0.97}_{-0.88}$	0.8 ± 0.2
LESS 57	$2.94^{+0.14}_{-0.11}$	✓	✓			$2.17^{+0.47}_{-0.45}$	$1.1^{+0.9}_{-0.8}$
LESS 66	$2.39^{+0.04}_{-0.05}$	✓	✓		✓	$31.6^{+1.4}_{-1.3}$	1.9 ± 0.1
LESS 67 ^d	$2.27^{+0.05}_{-0.11}$	✓				0.29 ± 0.14	...
LESS 75 ^e	$2.46^{+0.06}_{-0.09}$		✓			< 0.69	...
LESS 84	$2.29^{+0.15}_{-0.07}$	✓	✓			1.58 ± 0.25	0.7 ± 0.3
LESS 96	$2.71^{+0.03}_{-0.09}$	✓	✓		✓	20.3 ± 1.0	1.8 ± 0.1
LESS 106	$1.96^{+0.31}_{-0.48}$	✓				$3.35^{+0.53}_{-0.46}$	1.1 ± 0.3
LESS 111	$2.61^{+0.14}_{-0.06}$	✓	✓			$4.97^{+0.73}_{-0.66}$	1.2 ± 0.3
LESS 114	$1.57^{+0.08}_{-0.07}$	✓				$2.05^{+0.55}_{-0.51}$	0.7 ± 0.1
LESS 122	$2.08^{+0.08}_{-0.08}$		✓			< 0.76	...
Total: 16		12	9	1	2		

^a Source names correspond to those in Table 4.5

^b Photometric redshifts are from Chapter 4.

^c The effective X-ray photon index is taken from the catalogues of Lehmer et al. (2005) and Luo et al. (2008).

^d As we show in Fig. 6.3 although LESS 67 is X-ray detected its 0.5–8 keV luminosity suggests that the X-ray flux could be due to star-formation. LESS 67 is also too faint for Γ to be determined.

^e Compared to the best-fit SED LESS 75 has excess flux at 5.8 μm as well as at 8 μm .

of the X-ray observations. Previous X-ray studies of SMGs have significantly higher detection rates, although many of them have deeper observations than is available in the majority of the ECDFS. For example, Alexander et al. (2003) detected seven out of ten (70%) SMGs in the 2 Ms exposure of the *Chandra* Deep Field North (CDFN), which reached depths of $\approx 10^{-16}$ erg cm $^{-2}$ s $^{-1}$ in the 0.5–8 keV band. If the depth was instead more similar to the majority of the ECDFS at 10^{-15} erg cm $^{-2}$ s $^{-1}$ (see Fig. 6.2), Alexander et al. (2003) would have detected just three (30%) of their SMGs, all of which are classified as AGN by their X-ray properties. Alexander et al. (2005) expanded the sample from Alexander et al. (2003) to include 20 SMGs with spectroscopic redshifts from Chapman et al. (2005). They detected 17 (85%) of the SMGs in X-ray observations to $\approx 7 \times 10^{-17}$ erg cm $^{-2}$ s $^{-1}$, although only 11 (55%) are brighter than 10^{-15} erg cm $^{-2}$ s $^{-1}$ at 0.5–8 keV. Thus, under similar observing limitations as this work, only $\sim 50\%$ of the Alexander et al. (2005) SMGs would be classified as AGN from their X-ray emission. However, we caution that the SMG sample from Alexander et al. (2005) may be biased to include more AGN due to the requirement for optical spectroscopic redshifts, which selects for galaxies with emission lines in their spectra. Recently, Laird et al. (2010) examined the larger sample of 35 SMGs in the CDFN from the SCUBA Super-map (Borys et al. 2003), which are not required to have spectroscopic redshifts, and detected 16 (45%) in the deep *Chandra* imaging, of which only 20–30% have evidence that an AGN dominates the X-ray emission. Assuming a flux limit of 10^{-15} erg cm $^{-2}$ s $^{-1}$ at 0.5–8 keV only six (17%) of the parent sample would be detected as X-ray AGN – consistent with our result.

Nine (12%) of the LESS SMG counterparts have evidence for power-law emission in the near-infrared, which may be caused by AGN. Hainline et al. (2010) studied SMGs with spectroscopic redshifts from Chapman et al. (2005) and found that compared to stellar templates $\sim 30\%$ have a similar near-infrared excess. Similarly to the X-ray study by Alexander et al. (2005) this higher rate of AGN detected by Hainline et al. (2010) is likely to be due to a bias in the sample, introduced by the requirement for spectroscopic redshifts. However, for the SMGs in this work, it is possible that our current lack of spectroscopic redshifts at which to fix the SED fitting minimises the apparent 8- μ m excess such that in some cases it is no longer detectable.

Combining the numbers of AGN selected from X-ray emission, 8- μ m excess, QSO signatures and radio-loudness yields $\sim 20\%$ of LESS SMGs with evidence for AGN. Due to the relatively shallow X-ray observations in the outskirts of the ECDFS and the inherent bias in using the 8- μ m photometry when fitting the redshift and identifying AGN we

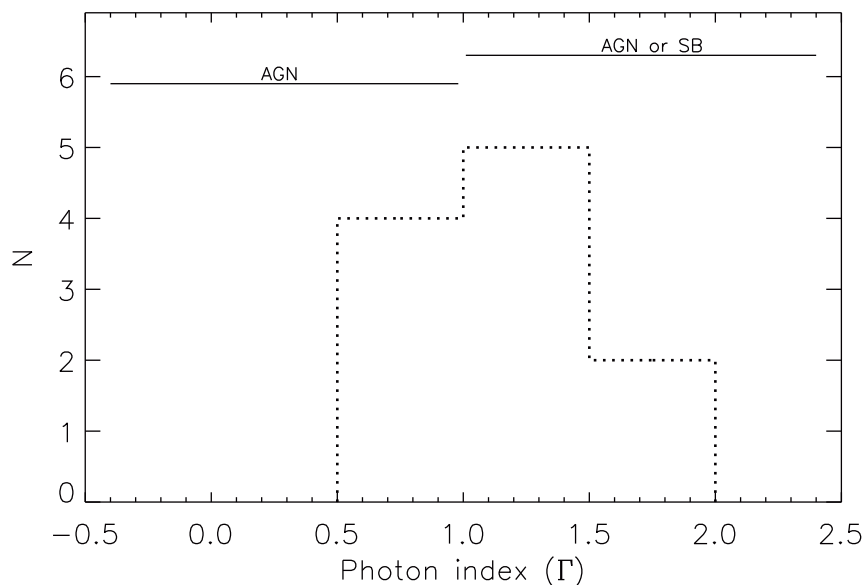


Figure 6.1: Distribution of the effective X-ray photon index (Γ) for X-ray detected LESS SMGs. X-ray emission from unobscured AGN and starburst typically have $\Gamma > 1$ and obscured AGN typically have $\Gamma < 1$. Γ suggests that the X-ray emission from up to four of the X-ray detected LESS SMGs are obscured AGN, although three have sufficiently large errors that they may have $\Gamma \geq 1$. LESS 67 is too faint for Γ to be reliably determined and therefore it is excluded from this figure.

consider that a minimum of 20% of LESS SMG counterparts contain AGN.

We show in Fig. 6.2 the 870 μm flux density against 0.5–8 keV flux for LESS SMGs. We highlight the SMGs with excess 8- μm emission compared to the best-fit SED, radio-loud AGN and QSOs. We also show the correlation expected for a QSO with the properties of 3C273, which is consistent with submillimetre observations of optical QSOs (e.g. Page et al. 2001; Vignali et al. 2001; Isaak et al. 2002, see also Alexander et al. 2005). The two SMGs that were identified as QSOs from their optical luminosity, morphology and spectra have X-ray and 870 μm fluxes consistent with those from optically selected QSOs, confirming that a QSO likely dominates the X-ray, optical and near-infrared emission of these SMGs, but not the far-infrared emission (e.g. Hao et al. 2008; Priddey et al. 2008). We note that the four LESS AGN that are identified from 8- μm excesses and the radio-loud SMG are undetected in the X-ray surveys and have 0.5–8 keV flux limits that are fainter than the majority (9/12) of the X-ray detected SMGs, suggesting that radio

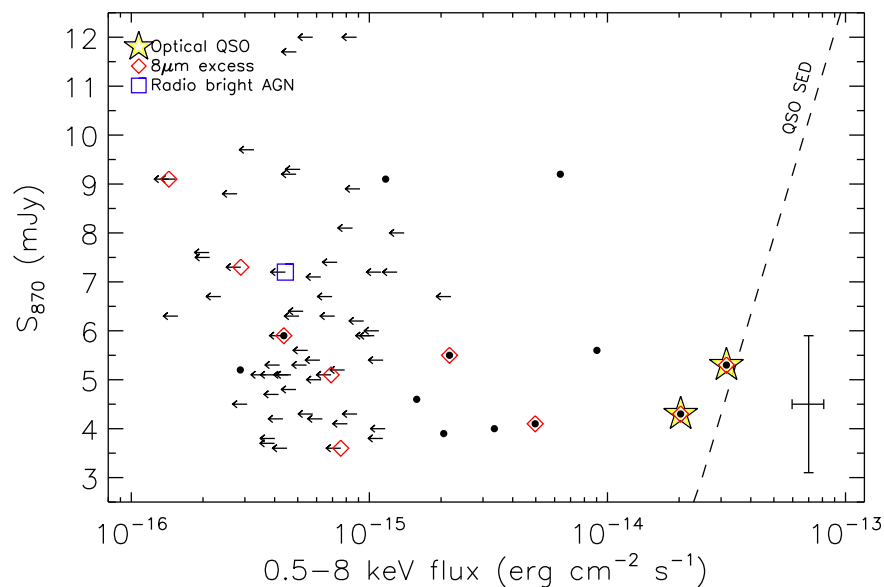


Figure 6.2: Submillimetre flux against 0.5–8 keV X-ray flux for robust SMG counterparts. We highlight SMGs identified as likely AGN based on excess 8- μm emission compared to the best-fit SED, those that have QSO signatures, and the radio-loud AGN. We also show the values expected for optically-selected QSOs, based on the properties of 3C273. The two SMGs with counterparts that are optically bright point sources with broad emission lines in their spectra have submillimetre and X-ray fluxes consistent with those of optically selected QSOs. The typical error bar is shown in the bottom-right-hand corner, but note that the X-ray error is a minimum because it does not include a contribution from modelling assumptions.

emission and excess 8- μm flux compared to the best-fit SED can identify fainter AGN than those selected from X-ray emission. It may be that these AGN may be more heavily obscured than the X-ray selected AGN.

To further investigate the potential differences in the LESS AGN populations selected with the different methods we next investigate their X-ray and radio luminosities (from Chapter 5). We assume $\Gamma = 2$ and calculate the 0.5–8 keV X-ray luminosity as:

$$L_X = 4\pi \left(\frac{d_L}{\text{cm}} \right)^2 \left(\frac{f_X}{\text{erg cm}^{-2}\text{s}^{-1}} \right) (1+z)^{(\Gamma-2)} \text{ erg s}^{-1} \quad (6.1)$$

Fig. 6.3 shows this X-ray luminosity against radio luminosity for all the LESS SMG counterparts. Similarly to Fig. 6.2 we highlight AGN with an 8- μm excess and the radio-loud AGN (LESS 20). The trend and observed scatter of starburst galaxies with X-ray

emission dominated by high-mass X-ray binaries (Persic et al. 2004) is also presented. LESS SMGs, including those with excess 8- μm emission compared to the best-fit SEDs, show several orders of magnitude scatter in X-ray luminosity, with the two QSOs amongst the brightest sources.

In addition to the two QSOs there are two LESS SMGs with $L_X \sim 10^{45}$ erg s $^{-1}$, which do not show evidence of an 8- μm excess. One of these, LESS 9, has $z_{\text{phot}} = 4.6_{-1.1}^{+0.1}$, so the observed 8- μm filter samples the rest-frame $\sim 1.4\mu\text{m}$ which is too short a wavelength for hot dust emission to be detected. However, the other, LESS 106, is at $z_{\text{phot}} = 2.0_{-0.5}^{+0.03}$ so any power-law emission in the near-infrared should be detectable. These findings suggest that identifying AGN from excess observed-frame 8- μm flux compared to the best-fit SED may miss some high-redshift AGN, and that in some cases the SED can be well-fit with pure-stellar templates.

Fig. 6.3 shows that the radio luminosity of LESS 20 is more than an order of magnitude higher than any of the other SMGs, and the simplest explanation is that it contains a radio-loud AGN. We validate this conclusion by using the observed 870- μm flux and the average SED from Dale & Helou (2002) to estimate that if the radio emission is due to the star-formation that drives the submillimetre emission then the expected radio luminosity of LESS 20 is $L_{\text{FIR}} = 4 \times 10^{25}$ WHz $^{-1}$. This is $\sim 5\times$ lower than observed, confirming that the radio emission in LESS 20 is mostly AGN driven.

Hainline et al. (2010) showed that for their sample of SMGs excess 8- μm flux compared to the best-fit stellar SED is associated with the presence of AGN. For LESS SMGs, as we show in Fig. 6.3, the galaxies with excess 8- μm flux have a range of X-ray luminosities, including some with 0.5–8 keV luminosities (or limits) that suggest the X-ray emission is powered by star-formation. However, the presence of the excess 8- μm flux compared to the best-fit SED suggests that these galaxies contain significant AGN activity. Therefore, we postulate that the AGN are obscured and that the intrinsic X-ray luminosities are brighter than observed, and next use the flux in the 8 μm excess to estimate the intrinsic X-ray luminosity of these SMGs.

We compare the 8- μm flux in the best-fit SED with the observed 8- μm flux for each SMG, to calculate the minimum luminosity in the power-law component of the observed-frame 8- μm emission. We consider it a minimum because the SED fitting included the 8- μm photometry so the difference between the observed and model flux at 8- μm was minimised by HYPERZ to improve the χ^2 of the fit. We next estimate the luminosity in the rest-frame K -band due to the AGN component ($L_{K(\text{PL})}$), adopting a power-law with a

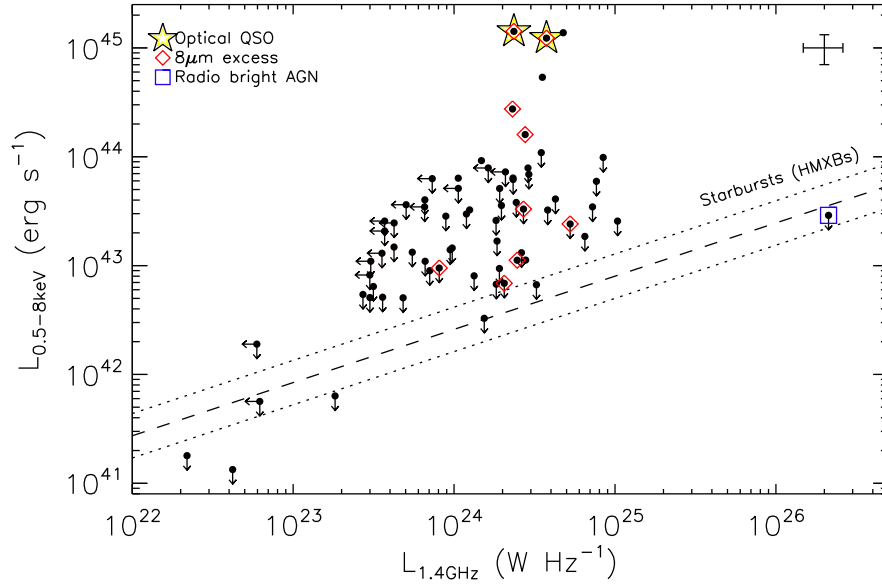


Figure 6.3: Plot of 0.5–8 keV X-ray luminosity against 1.4 GHz radio luminosity for LESS SMGs. We highlight SMGs with excess 8- μm emission compared to the best-fit SED, submillimetre-detected QSOs, and radio-loud AGN. There is a large range of X-ray luminosities for SMGs with excess 8- μm flux compared to the best-fit SED, and several of these SMGs have X-ray luminosities similar to that expected for star-forming galaxies. However, as described in the text, the AGN in these systems are typically obscured and corrections to the X-ray luminosity of $\sim 2.5\times$, corresponding to $N_H \sim 5 \times 10^{22} \text{ cm}^{-2}$ for $\Gamma = 2$, are required to recover the expected unobscured X-ray luminosity. The dashed line, (and corresponding dotted lines) represent the observed relationship (and scatter) for galaxies with X-ray emission dominated by high-mass X-ray binaries from star-formation (Persic et al. 2004, see also Alexander et al. 2005). We show the average error bar in the top-right-hand corner, but note that the error in the X-ray luminosity does not include a contribution from modelling assumptions. In addition, the luminosity errors are strongly dependent on the redshift error, so those galaxies with poorly constrained photometric redshifts have larger errors in both their X-ray and radio luminosities.

slope of $\alpha = 2$ (Hainline et al. 2010). $L_{K(\text{PL})}$ is then converted to 2–8 keV X-ray luminosity ($L_{2-8 \text{ keV}}$) using $L_K/L_{2-8 \text{ keV}} = 0.4$, which is the average of radio-quiet QSO SEDs (Elvis et al. 1994). Hainline et al. (2010) estimates the median $L_{K(\text{PL})}/L_{2-8 \text{ keV}} = 0.9 \pm 0.4$ for SMGs (RMS scatter = 1.9), but we use the results from Elvis et al. (1994) because the X-ray emission is likely to be less obscured in the Elvis et al. (1994) sample. Finally, to estimate the correction to the observed 0.5–8 keV luminosity due to obscuration, we convert $L_{2-8 \text{ keV}}$ to predict the expected 0.5–8 keV luminosity based on the 8- μm excess and assuming $\Gamma = 2$.

There are numerous assumptions and uncertainties in this calculation, so we consider the obscuration correction only statistically. The median minimum correction to the X-ray luminosity for SMGs with $L_{0.5-8 \text{ keV}} < 10^{44} \text{ erg s}^{-1}$ and an excess of 8- μm flux compared to the best-fit SED is $\sim 2.5\times$, corresponding to $N_H \sim 5 \times 10^{22} \text{ cm}^{-2}$ for $\Gamma = 2$; for all SMGs with an 8- μm excess the correction is $\sim 1.2\times$, corresponding to $N_H \sim 10^{21} \text{ cm}^{-2}$ for $\Gamma = 2$. We conclude that the observed X-ray emission in SMGs with evidence for power-law emission in their near-infrared SEDs can be significantly obscured and therefore the observed X-ray luminosity of these galaxies is not a reliable discriminator for AGN and star-forming powered X-ray emission. It also shows that an X-ray detection is not sufficient to select all AGN in SMG samples. We note that the majority of SMGs studied by Alexander et al. (2005) have $N_H \gtrsim 10^{23} \text{ cm}^{-2}$, suggesting that there may be additional absorption in the AGN studied here, which is not accounted for in our analysis.

6.2.2 Typical SMG SEDs

To investigate the typical stellar populations and extinction of SMGs we next consider the average rest-frame UV to near-infrared SED of LESS SMGs. We show in Fig. 6.4 the rest-frame photometry of the 74 robust LESS SMG counterparts, normalised in the H -band. Based on the average observed photometry we also calculate the fluxes expected in each of the 17 photometric filters used in our photometric redshift analysis (Chapter 4) as observed at $z = 2.2$ and determine the median flux in each.

We begin by noting that the data show evidence for a break at $\sim 3500\text{--}4000\text{\AA}$ suggestive of a Balmer or 4000 \AA break. Closer inspection hints at it being a Balmer break indicating that the blue rest-frame light is dominated by stars older than 20 Myr and younger than ~ 2 Gyr. Then, as in Chapter 4, we use HYPERZ to fit this photometry, with redshift fixed at $z = 2.2$, and show the best-fit templates for both the Burst and

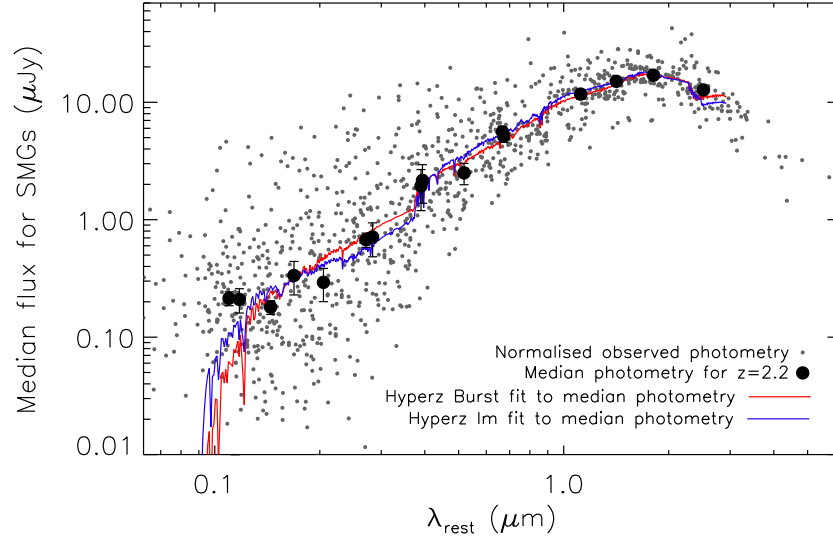


Figure 6.4: The photometry of SMG counterparts shifted to the rest frame and normalised to the H band ($1.6\mu\text{m}$). Redshifting this data to $z = 2.2$, the median redshift of the sample, we calculate the apparent fluxes in the 17 photometric filters considered throughout this paper and use HYPERZ to fit galaxy templates at this redshift. The median photometric points are shown and the resulting best HYPERZ Burst and constant star-formation template fits are displayed. The best fit HYPERZ templates have: Burst, $A_V = 1.7$, an age of 33 Myrs and a $L_H/M^* \sim 24$; constant star-formation, $A_V = 1.1$, an age of 3.5 Gyrs and an $L_H/M^* \sim 6$. It is clear from the figure that it is not possible to distinguish between these two very different star-formation histories and hence we conclude that we must assume a factor of ~ 5 uncertainty in the resulting masses. The MUSYC U38 filter has a $\geq 50\%$ contribution from limiting magnitudes and is excluded from the fit.

constant star-formation histories on Fig. 6.4. Comparing the χ^2 for these two models in the same manner as § 4.3.5, we find that we cannot accurately distinguish between different star-formation histories (and hence ages or light-to-mass ratios). The best-fit Burst model has an age of just 33 Myrs, an $A_V = 1.7$ and a resulting light-to-mass ratio of $L_H/M^* \sim 24$, in contrast the constant star-formation template yields an age of 3.5 Gyrs, $A_V = 1.1$ and an $L_H/M^* \sim 6$. The reddening derived from these two template fits are in agreement with the median of the individual SED fits ($A_V = 1.5 \pm 0.1$; Chapter 4), while the L_H/M^* span a range of $4\times$.

We also estimate the extinction in LESS SMGs by comparing the star-formation rate (SFR) derived from the rest-frame far-ultraviolet luminosity (median $\text{SFR}_{\text{UV}} = 2 M_{\odot} \text{yr}^{-1}$; Kennicutt 1998; Rosa-González et al. 2002) with the SFR derived from the far-infrared luminosity (median $\text{SFR}_{\text{FIR}} = 1400 M_{\odot} \text{yr}^{-1}$; Chapter 5). SFR_{UV} assumes that there is no dust reddening and is extremely sensitive to dust absorption because it is based on ultraviolet emission, in contrast SFR_{FIR} is calculated from dust reprocessed emission. For SFR_{UV} to match the observed SFR_{FIR} requires that intrinsic the far-ultraviolet emission is 7.0 ± 0.1 magnitudes brighter than observed. This corresponds to $A_V = 2.6 \pm 0.2$ and reddening ~ 4 times higher than the HYPERZ SED fit and indicating that the majority of the star formation within SMGs occurs in totally obscured regions. As discussed in Kennicutt (1998) the conversion from far-ultraviolet luminosity to SFR_{UV} assumes that the star-formation rate has been constant for $> 10^8$ years. SMGs are likely to be shorter bursts of activity and therefore for a fixed SFR they will be brighter at ultraviolet wavelengths and likely have higher A_V than estimated above.

6.2.3 Stellar masses

In order to investigate the evolution of SMGs once the burst is completed we first need to know the typical masses of SMGs. As discussed in Chapter 4 the uncertainties in the derived spectral types and ages result in an estimated factor of ~ 5 uncertainty in assumed mass-to-light ratios and thus stellar masses derived from the absolute H -band absolute magnitudes (M_H). Therefore, we only consider the stellar masses of the LESS SMGs statistically and we initially consider M_H of the LESS SMGs as a proxy for stellar mass, and investigate the scatter and any trends within the sample. M_H is used to as a proxy for stellar mass and to estimate the stellar mass of galaxies because it is less influenced by young stars than optical bands and is relatively unaffected by dust.

We use HYPERZ to estimate M_H from our SED fits and find a median $M_H = -24.1 \pm$

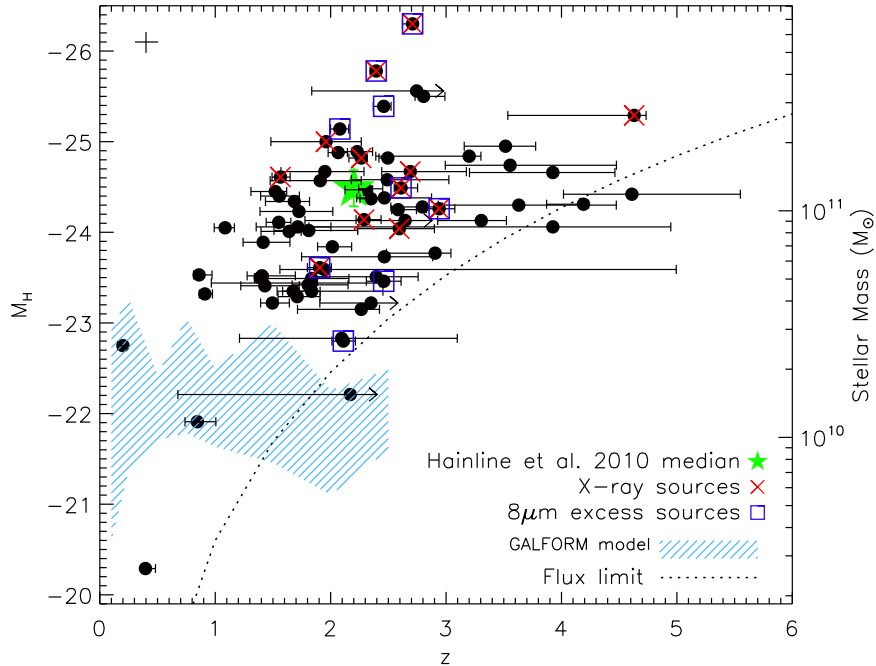


Figure 6.5: A plot of photometric redshift against rest-frame H -band absolute magnitude for LESS SMGs, and the approximate correspondence with stellar mass (as described in the text). The median M_H is -24.1 ± 0.1 with an interquartile range of -24.7 to -23.6 , in good agreement with the median M_H from Hainline et al. (2010). This corresponds to a median stellar mass of $\sim 9.2 \times 10^{10} M_\odot$ and interquartile range of $(4.7\text{--}14) \times 10^{10} M_\odot$, although we stress that there is a systematic error on these values of $\sim 5\times$. We also highlight SMGs with evidence for AGN activity (§ 6.2.1), which appear brighter than the average SMG. We also show the predicted $1\text{-}\sigma$ distribution of absolute H -band magnitudes of SMGs with $S_{850\mu\text{m}} \geq 3$ mJy that are brighter than our flux limit at $4.5\ \mu\text{m}$ (approximately the rest-frame H -band at $z = 2$) from the GALFORM semi-analytic model (Baugh et al. 2005; Lacey et al. 2008; Swinbank et al. 2008) and note that M_H is under-predicted in the model. Errors in M_H are dominated by the error in the photometric redshift; we calculate the error in M_H for SMGs with median redshift error by re-running the HYPERZ with the redshift forced to the extremes of the error range; the corresponding errors are shown in the top left-hand corner of the plot and can be scaled with the error in redshift. The dotted line illustrates the trend in M_H with redshift resulting from the flux limited nature of our survey.

0.1, with an interquartile range of -24.7 to -23.6 . In Fig. 6.5 we plot M_H against photometric redshift for the LESS SMG counterparts. There is the suggestion of a weak trend of M_H with redshift. However, as the plotted detection limit shows this is most likely a selection effect, with the higher redshift galaxies needing to be more luminous to be detected.

Hainline et al. (2010) estimated H -band mass-to-light ratios for SMGs with Burst and constant star-formation templates, assuming a Chabrier (2003) IMF. We use the average of their values converted to a Salpeter IMF (with a lower mass limit of $0.1 M_\odot$ and an upper mass cutoff of $100 M_\odot$) for our stellar mass calculation: $L_H/M^* = 3.8 L_\odot M_\odot^{-1}$. We adopt a Salpeter IMF as this has been shown to provide a better fit to the stellar masses of elliptical galaxies (Treu et al. 2010), while a Chabrier IMF leads to underestimated stellar masses. We estimate that the median stellar mass of the SMGs in our sample is $M^* = (9.2 \pm 0.9) \times 10^{10} M_\odot$ and the interquartile range is $(4.7\text{--}14) \times 10^{10} M_\odot$. The quoted errors do not include the systematic uncertainty from the star-formation histories and mass-to-light ratios, which adds a factor of ~ 5 uncertainty to the values (Chapter 4; Fig. 6.4). We also caution that the choice of IMF coupled with the assumption that all the light is from the current burst can affect the derived stellar masses by an additional factor of ~ 2 . Finally, we note that on average we observe the SMGs approximately halfway through the burst and typical SMG gas masses (Greve et al. 2005) suggest an additional $\sim 3 \times 10^{10} M_\odot$ of stellar mass could be added by the end of the burst.

We find that galaxies with evidence for AGN activity from an $8 \mu\text{m}$ excess or X-ray emission (§ 6.2.1) have median $M_H = -24.6 \pm 0.3$, compared to $M_H = -24.1 \pm 0.1$ for the remainder of the SMGs. The two SMGs with the brightest M_H are the two submillimetre bright QSOs (LESS 66 and LESS 96; § 6.2.1) in which the observed emission is expected to be dominated by the AGN rather than starlight. If these are excluded the median M_H of SMGs containing AGN is $M_H = -24.5 \pm 0.3$.

The median stellar mass for SMGs in SHADES Lockman Hole was claimed to be $M^* = (6.3_{-1.3}^{+1.6}) \times 10^{11} M_\odot$ by Dye et al. (2008). This is a factor of ~ 7 higher than our estimate for LESS SMGs. Dye et al. (2008) use nine-band photometry for their photometric redshift determination and claim to also be able to disentangle the star-formation histories of the SMGs with sufficient accuracy to identify a significant mass of old stars which underlies the current burst. This leads to a higher effective mass-to-light ratio and correspondingly higher stellar masses. In contrast, as discussed earlier (Chapter 4), we do not believe that with existing data it is possible to untangle the

influences of the potentially complex star-formation histories and dust distributions on the SEDs of SMGs. Hence, we do not believe that there is any observational evidence for significant old stellar populations in these galaxies, as required by the Dye et al. (2008) results. Hainline et al. (2010) have used optical and IRAC photometric data to calculate an average stellar mass for the Chapman et al. (2005) SMGs and they find $M^* = (1.4 \pm 0.3) \times 10^{11} M_{\odot}$ (converted to Salpeter IMF), comparable to our survey and a factor of ~ 5 lower than Dye et al. (2008).

In Fig. 6.5 we also show the absolute H -band magnitudes of SMGs in the Λ CDM GALFORM model (Baugh et al. 2005), which assumes a top-heavy IMF with slope $x = 0$. We consider only galaxies with $S_{850\mu m} \geq 3$ mJy and fluxes in the IRAC 4.5 μm filter brighter than our detection limit (4.5 μm corresponds to the rest-frame H -band at $z \sim 2$). Swinbank et al. (2008) showed that GALFORM predicts rest-frame absolute K -band luminosities of SMGs which are a factor of ten lower than observed. This arises primarily due to an order of magnitude lower stellar masses than implied by observations for SMGs (see also Lacey et al. 2010). As Fig. 6.5 shows the predicted rest-frame H -band magnitudes of the model SMGs are also a factor of ten lower than our observations. Indeed, if SMGs formed stars following the prescriptions used in the Baugh et al. (2005), then few of the SMGs above a redshift of $z \sim 2$ would have been detected in the IRAC observations of the ECDFS, which many actually are.

6.2.4 Specific star-formation rate

The SFR per unit stellar mass – the specific star-formation rate – can be used as a measure of the length of the current burst of star-formation and the formation timescale of the galaxy. We follow Kennicutt (1998), who assumes a Salpeter IMF with upper and lower mass limits of 0.1 and $100 M_{\odot}$ respectively, to calculate the SFRs of the LESS SMGs from their inferred far-infrared luminosities (Chapter 5). We derive a median SFR of $1100 \pm 200 M_{\odot} \text{yr}^{-1}$ and an interquartile range of 300–1900 $M_{\odot} \text{yr}^{-1}$. The median specific star-formation rate $\text{sSFR} = \text{SFR}/M^* = (1.2 \pm 0.1) \times 10^{-8} \text{yr}^{-1}$ and the interquartile range is $(0.6\text{--}1.8) \times 10^{-8} \text{yr}^{-1}$. Although again, we caution that due to the uncertainties in the stellar mass estimates there is an additional factor of ~ 5 uncertainty in these values (see Chapter 4 for a full discussion). The median formation timescale of the LESS SMGs is thus ~ 100 Myr and it is feasible that all of the stellar mass we see could be formed in the current burst. In Fig. 6.6 we plot the trend of sSFR against the redshift of the LESS SMGs. We note that the apparent lack of galaxies with low sSFR at high redshifts is

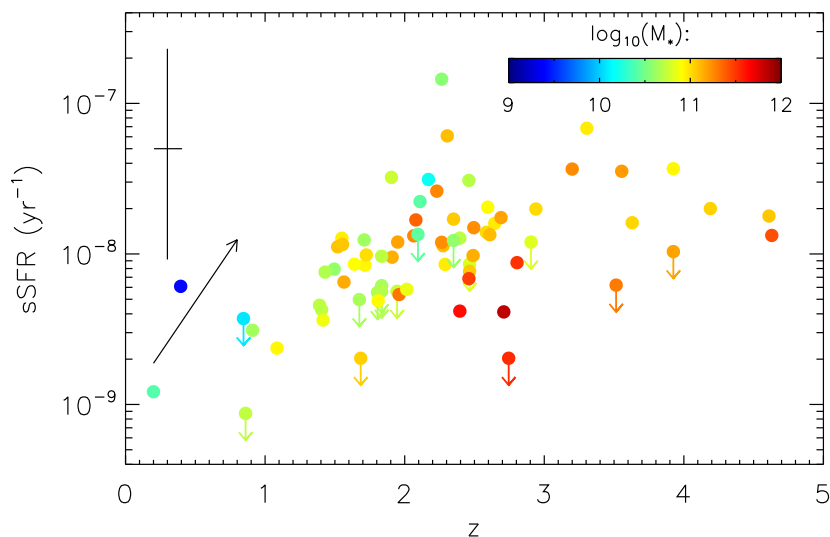


Figure 6.6: A plot of specific star-formation rate (sSFR) versus redshift for the LESS SMGs. Galaxies are colour-coded by mass and we show the median error bar in the top-left hand corner and note that similarly to Fig. 6.5 the error in sSFR is correlated with that in redshift. The arrow represents the gradient of the trend in sSFR with redshift for IRAC-selected galaxies with $\log_{10}(M_*) = 10.3\text{--}10.8 M_{\odot}$, offset in sSFR by two orders of magnitude for the purpose of display. We note that due to the requirement for radio counterparts no SMGs are detected in the high redshift and low sSFR region of this plot. Similarly, the short lifetime of SMGs with $\text{sSFR} \gtrsim 10^{-7}\text{yr}^{-1}$ and the limited volume of our survey means that few SMGs with very high sSFRs are detected. However, the dearth of SMGs at $z \lesssim 1.5$ with $\text{sSFR} \gtrsim 10^{-8}\text{yr}^{-1}$ may indicate an upper-limit to the sSFR of SMGs with a similar scaling to the trends seen in lower activity galaxies at lower redshifts (Damen et al. 2009).

a selection effect due to the requirement for a radio counterpart and that galaxies with $\text{sSFR} \gtrsim 10^{-7}\text{yr}^{-1}$ are rare due to the brevity of the burst phase. However, the dearth of SMGs at $z \lesssim 1.5$ with $\text{sSFR} \sim 10^{-8}\text{--}10^{-7}\text{yr}^{-1}$ is not a selection effect and this upper envelope may be following the same trend in sSFR with redshift seen in galaxies with similar masses but lower SFRs (e.g. Damen et al. 2009), indicating a decline in the SFR at low redshifts.

6.2.5 Volume density of SMGs

Finally, we relate our new estimate of the redshift distribution of SMGs (Chapter 5) to constraints on the evolution of their likely descendants: massive early-type galaxies (Swinbank et al. 2006). As we showed in Chapter 5, the bulk of the SMG population with observed 870- μm fluxes above $\sim 4\text{ mJy}$ lie at redshifts of $z \sim 1.5\text{--}3$ with a median redshift of $z \sim 2.5$. We estimate that the volume density of SMGs at $z = 2\text{--}3$ above our flux limit is $1.2 \times 10^{-5}\text{ Mpc}^{-3}$, where we include both the identified and statistically identified samples in this estimate (Chapter 5). Using a characteristic lifetime of the SMG phase of $\sim 100\text{ Myr}$ (§ 6.2.4), we can correct this density for the burst duty cycle to derive a volume density for the remnants of $2 \times 10^{-4}\text{ Mpc}^{-3}$. As we have shown, the estimated baryonic masses of these galaxies are $\sim 1.2 \times 10^{11}\text{ M}_{\odot}$ combining our best estimate of the stellar mass with the typical gas masses from Greve et al. (2005). If the burst of star formation we are seeing in the SMG phase is the last major star formation event in these galaxies then we expect their descendants to appear as passive, red galaxies at $z \sim 1.5$ ($> 1\text{ Gyr}$ after $z \sim 2$).

There have been various estimates of the volume density of massive, passive galaxies at $z \sim 1\text{--}2$ (McCarthy et al. 2004; Daddi et al. 2005; Taylor et al. 2009a). For passive galaxies with masses of $\gtrsim 10^{11}\text{ M}_{\odot}$, the estimated space densities are $1\text{--}2 \times 10^{-4}\text{ Mpc}^{-3}$ (at $z = 1.5\text{--}1.8$; Taylor et al. 2009a), $3 \times 10^{-4}\text{ Mpc}^{-3}$ (at $\langle z \rangle = 1.7$; Daddi et al. 2005) and $0.6 \times 10^{-4}\text{ Mpc}^{-3}$ (at $\langle z \rangle = 1.5$; McCarthy et al. 2004). These estimates, with their various uncertainties, are comparable to the predicted volume density of massive, passive galaxies if these all undergo an SMG-phase at an earlier epoch. Hence, the starbursts in SMGs may be responsible for the formation of a large fraction of the passive, massive galaxies seen at $z \sim 1.5$.

We can attempt a similar calculation comparing the SMG population at $z > 3$ with the constraints on massive galaxies at $z \gtrsim 2$. We estimate the volume density of $z > 3$ SMGs as $2.8 \times 10^{-6}\text{ Mpc}^{-3}$. This includes the 10 identified SMGs, 4 ± 2 statistically identified SMGs and the remaining 21 ± 19 unidentified sources and assumes that they are contained within a redshift range of $z = 3\text{--}7$ (see Chapter 5). Using a characteristic lifetime of the SMG phase of $\sim 100\text{ Myr}$, we can correct this density for the burst duty cycle to derive a volume density for the remnants of $3.8 \times 10^{-5}\text{ Mpc}^{-3}$. Again the estimated baryonic masses of these galaxies are $\sim 1.2 \times 10^{11}\text{ M}_{\odot}$. Unfortunately observable limits on the volume density of passive galaxies are increasingly uncertain at $z > 2$, but using the

estimates from Coppin et al. (2009) of the volume density of massive galaxies of $\sim 1\text{--}5 \times 10^{-5} \text{ Mpc}^{-3}$, we again conclude that it is possible that the SMG population we have identified is also responsible for the formation of a significant of the most massive galaxies at $z \sim 2.5$.

Thus we conclude that the presence of a sizable population of passive galaxies at high redshift may be intimately linked to the strong evolution in dust obscured starbursts in the distant Universe. Theoretical attempts to match the properties of high-redshift galaxies therefore need to focus on these observable constraints as aspects of the same problem (Swinbank et al. 2008).

We also estimate the fraction of local massive passive galaxies that underwent a SMG phase at $z = 1\text{--}3$, the peak epoch of SMG activity. The volume density of passive galaxies with stellar masses $> 10^{11} M_{\odot}$ at $z < 0.05$ ($z \sim 0.2$) is $\sim 6 \times 10^{-4} \text{ Mpc}^{-3}$ ($\sim 5 \times 10^{-4} \text{ Mpc}^{-3}$) Taylor et al. (2009a). The volume density of LESS SMGs with $z = 1\text{--}3$ is $1.1 \times 10^{-5} \text{ Mpc}^{-3}$ and accounting for a ~ 100 Myr SMG lifetime (§ 6.2.4) the volume density of the remnants is $\sim 4 \times 10^{-4} \text{ Mpc}^{-3}$. We conclude the $\sim 65\%$ of $z < 0.05$ ($\sim 80\%$ of $z \sim 0.5$) passive galaxies with $M^* > 10^{11} M_{\odot}$ likely underwent an SMG phase at $z = 1\text{--}3$.

6.2.6 Clustering of SMGs

We have established that SMGs are massive galaxies at $z \sim 2$ that are forming stars at considerable rates and which have volume densities that suggest to that a significant fraction of massive passive galaxies at lower redshifts may be the descendants of SMGs. Therefore, we next investigate the three-dimensional clustering of LESS SMGs to establish whether the environments of SMGs and the masses of the dark matter halos in which they reside are consistent with this hypothesis. Weiß et al. (2009) used a two-point correlation function to study the clustering of the 126 SMGs detected in LESS and found evidence at the $\sim 3.5\sigma$ level for clustering on scales of $< 1'$, corresponding to 500 kpc at the median redshift of $z = 2.2$. In this work we extend these results to investigate the projected real-space clustering of the 59 identified LESS SMGs at $z = 1\text{--}3$ (Chapter 4), with respect to $\sim 50,000$ IRAC-selected galaxies in the ECDFS. There are too few SMGs to obtain a statistically significant measure of their autocorrelation, but cross-correlating with the numerous IRAC galaxies enables a more reliable measure of the SMG clustering. We limit our analysis to the peak of the redshift distribution of SMGs, and only consider SMGs at $z = 1\text{--}3$, to maximise the signal.

Our method is described in detail in Hickox et al. (in prep.) and is similar to that of Hickox et al. (2009) but has been adapted, following the formulation of Myers et al. (2009), to derive the projected real-space cross-correlation function ($w_P(R)$) for galaxies that may only have photometric redshift information. We use spectroscopic redshifts where available, but for galaxies with only photometric redshifts we consider the probability density function (PDF). The PDFs are determined from the SED fitting (Chapter 4), and the PDFs of each galaxy are normalised such that the integral probability over all redshifts is unity, i.e. $\int P(z)dz = 1$.

We first calculate the two-point autocorrelation function of the dark matter (shown in Fig. 6.7) using the HALOFIT code from Smith et al. (2003), assuming Λ CDM cosmology with $\Omega_\Lambda = 0.3$, $\Omega_m = 0.3$, $H_o = 70 \text{ km s}^{-1}\text{Mpc}^{-1}$, $\sigma_8 = 0.9$ and the slope of initial fluctuation power spectrum, $\Gamma = \Omega_m h = 0.21$. We then calculate the angular autocorrelation function for IRAC-selected field galaxies (§ 6.2.6.1) to determine the bias of these galaxies relative to the dark matter, and next calculate the cross-correlation of SMGs with the IRAC galaxies (§ 6.2.6.2) to determine the relative bias between the SMGs and IRAC galaxies. Finally, we subtract the bias of the IRAC galaxies, as determined from the autocorrelation function of IRAC galaxies, to yield the bias of the SMGs relative to the dark matter, and thus determine the halo masses of SMGs.

In order to calculate the correlation functions we first create random catalogues of ‘galaxies’ at random positions within the actual spatial coverage of our survey. Like many fields, the ECDFS contains several bright stars with large halos, around which few galaxies are detected. Therefore, we use the background map produced by SExtractor from the combined IRAC image during the source extraction procedure (Chapter 4) to create a mask. This mask is applied to the random catalogues, the SMGs and the IRAC galaxies so that the positions of the random catalogue is unbiased with respect to the SMG and IRAC galaxy catalogues. As discussed in Chapter 4, during the source extraction procedure we manually examined the regions around SMGs, adding additional apertures to include potential SMG counterparts that may have been missed in the automated procedure. These additional apertures are excluded from the clustering analysis so as not to bias the results.

6.2.6.1 Angular autocorrelation of IRAC galaxies

We calculate the angular autocorrelation, $\omega(\theta)$, of IRAC galaxies using the formulation from Landy & Szalay (1993):

$$\omega(\theta) = \frac{1}{RR(\theta)}[DD(\theta) - 2DR(\theta) + RR(\theta)] \quad (6.2)$$

where $RR(\theta)$, $DD(\theta)$ and $DR(\theta)$ are the number of random-random, data-data and data-random galaxy pairs at a separation θ , respectively. Since the evolution of large scale structure in the Universe causes the galaxy autocorrelation function to vary with redshift it is important that the IRAC galaxies in this analysis have the same redshift distribution as the SMGs that are included in the cross-correlation (§ 6.2.6.2). The full sample of IRAC galaxies has a redshift distribution that peaks at lower redshifts than the SMGs and contains many galaxies whose PDFs do not overlap in redshift space with the SMGs. Therefore, in our analysis we only include IRAC galaxies with PDFs that overlap with SMGs at $z = 1-3$; these are the galaxies that dominate the cross-correlation analysis (§ 6.2.6.2).

We show in Fig. 6.7 the angular autocorrelation, for IRAC galaxies with PDFs that overlap with SMGs at $z = 1-3$, where uncertainties in $\omega(\theta)$ are from bootstrap resampling. We calculate the bias of the IRAC galaxies (b_{gal}) by scaling the autocorrelation function of the dark matter to fit that of the galaxies, taking into account the correlation of individual points and errors in the fitting procedure. The scaled dark-matter fit is shown in Fig. 6.7 and has $b_{\text{gal}} = 2.00 \pm 0.08$, and corresponding to halo mass ($M_{\text{halo,gal}}$), calculated according to Sheth et al. (2001), for the IRAC galaxies of $\log_{10}(M_{\text{halo,gal}}/M_{\odot}) = 12.17 \pm 0.09$.

6.2.6.2 Cross-correlation of SMGs and IRAC galaxies

The projected real-space correlation function ($w_p(R)$) is the integral of the real-space 3-D correlation function, $\xi(r)$, along the line of sight:

$$w_p(R) = 2 \int_0^{\pi_{\text{max}}} \xi(R, \pi) d\pi \quad (6.3)$$

where R is the projected comoving separation between galaxies perpendicular to the line of sight and π is the equivalent measure parallel to the line of sight. We consider $w_p(R)$, instead of $\xi(r)$ and integrate along the line-of-sight to remove the effect of redshift-space distortions that are caused by the peculiar motions of galaxies. In Fig. 6.8 we show the projected real-space cross-correlation of the 59 LESS SMGs at $z = 1-3$ with IRAC galaxies with PDFs that overlap with the SMGs, where $w_p(R)$ is calculated using the method of

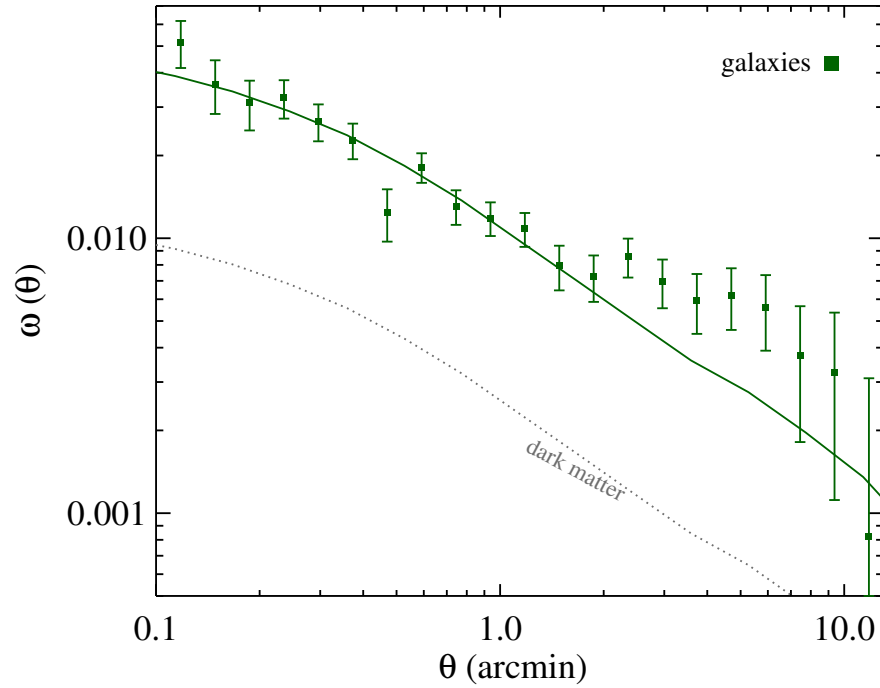


Figure 6.7: Autocorrelation function of IRAC-selected galaxies in the ECDFS with PDFs that overlap with SMGs at $z = 1-3$. The dotted line shows the autocorrelation of dark matter and the solid line shows the dark matter scaled to fit the data. We measure the galaxy bias as $b_{\text{gal}} = 2.00 \pm 0.08$, corresponding to halo mass of $\log_{10}(M_{\text{halo,gal}}/M_{\odot}) = 12.17 \pm 0.09$. Data points are not independent and errors are from bootstrap resampling.

Myers et al. (2009) (see also Hickox et al. in prep.). We have restricted the analysis to SMGs with $z = 1\text{--}3$, corresponding to the peak of the SMG redshift distribution (Chapter 5), to maximise the signal. Once again we calculate the dark-matter correlation function (Smith et al. 2003) and use a simple scaling to fit it to the data. From this analysis we calculate that the relative bias of the SMGs and IRAC galaxies is $b_{\text{SMG}}b_{\text{gal}} = 5.2 \pm 1.7$. We remove the contribution from the IRAC galaxies (§ 6.2.6.1) and hence derive SMG bias, $b_{\text{SMG}} = 2.6 \pm 0.9$. Using the formalism of Sheth et al. (2001) we calculate that the corresponding SMG halo mass at $z \sim 2$ is $\log_{10}(M_{\text{halo,SMG}}/h^{-1}M_{\odot}) = 12.6^{+0.5}_{-0.8}$, or $M_{\text{halo,SMG}} = (6^{+12}_{-5}) \times 10^{12} M_{\odot}$.

Traditionally, the correlation is used to describe the strength of clustering. This is derived from $\xi(r)$, which is observed to be a power-law, with the functional form $\xi(r) = (r_0/r)^{\gamma}$, where r_0 is the correlation length and γ is the power-law index. For our formalism, and in terms of the projected real-space correlation, the form is:

$$w_p(R) = R \left(\frac{r_0}{R} \right)^{\gamma} \frac{\Gamma(1/2)\Gamma[(\gamma-1)/2]}{\Gamma(\gamma/2)} \quad (6.4)$$

where Γ represents the Gamma Function, whereby $\Gamma(n) = (n-1)!$. We fit this form of the power-law to the projected real-space correlation function of SMGs and IRAC-galaxies in Fig. 6.8, and derive $r_0 = 4.4 \pm 0.6 h^{-1}\text{Mpc}$, and $\gamma = 1.9 \pm 0.2$.

Our correlation analysis is restricted by the requirement that included SMGs are identified and have photometric redshifts. However, we consider it unlikely that the results are biased by the exclusion of unidentified SMGs. As we showed in Chapter 5, $\sim 60\%$ of the unidentified SMGs have a redshift distribution similar to the identified SMGs, but contain more cold dust so they are not identified in the radio, 24- μm , or IRAC analyses. These galaxies are detected in our IRAC imaging and appear to have similar stellar masses and therefore likely also have similar clustering. We also show in Chapter 5 that the remaining $\sim 40\%$ of unidentified SMGs are not detected in our IRAC imaging and argue that they are typically high redshift galaxies with $z \gtrsim 3$. Thus these SMGs would not be included in our clustering analysis even if they had been identified.

We have calculated that on average SMGs at $z = 1\text{--}3$ occupy halos of mass $\sim 6 \times 10^{12} M_{\odot}$. Moster et al. (2010) recently showed that the expected stellar mass of galaxies in halos with $M_{\text{halo}} \sim 6 \times 10^{12} M_{\odot}$ at $z = 2$ is $\sim 7 \times 10^{10} M_{\odot}$, in reasonable agreement with our estimates of the stellar masses of SMGs (§ 6.2.3). At $z = 2$ the efficiency of mergers to trigger starburst and QSO activity peaks at $M_{\text{halo}} \sim 10^{12} M_{\odot}$ (Hopkins et al. 2008b), confirming that SMGs likely represent the peak of the star-formation activity of

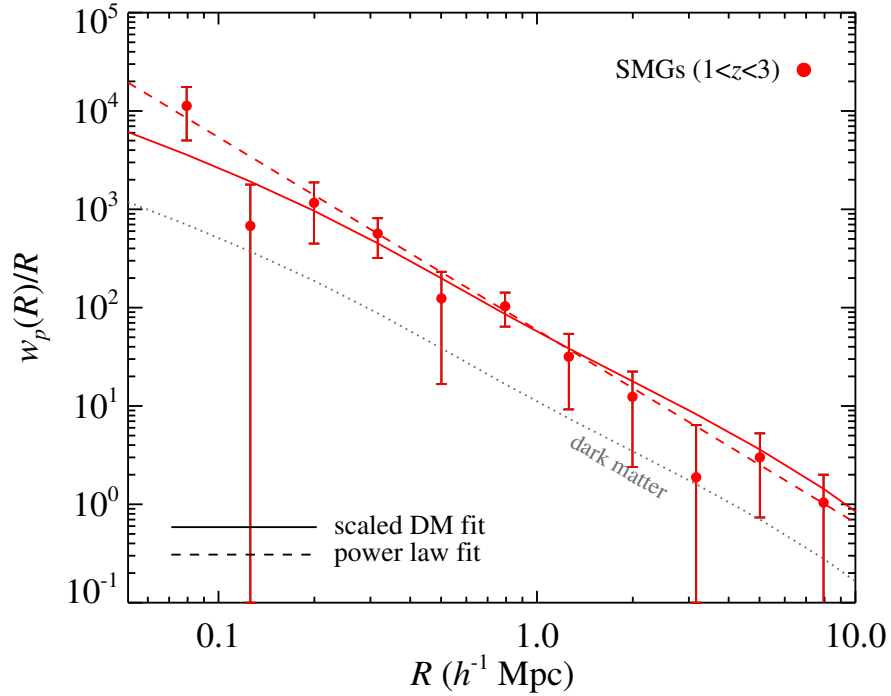


Figure 6.8: Projected real-space cross-correlation of LESS SMGs at $1 \leq z \leq 3$ and IRAC galaxies in the ECDFS that have overlapping PDFs. We show the correlation of the dark matter, and the fit of the dark matter to the data, corresponding to a combined bias for the SMGs and the IRAC galaxies of $b_{\text{SMG}}b_{\text{gal}} = 5.2 \pm 1.7$, and bias of the SMGs of $b_{\text{SMG}} = 2.6 \pm 0.9$. Thus we calculate the halo mass of SMGs as $\log_{10}(M_{\text{halo,SMG}}) = (6_{-5}^{+12}) \times 10^{12} M_{\odot}$. We also show the power-law fit to the projected real-space correlation-function (as described in the text), which has a correlation length, $r_0 = 4.4 \pm 0.6 h^{-1}\text{Mpc}$, and $\gamma = 1.9 \pm 0.2$.

major mergers. We also note that QSOs reside in halos of mass $M_{\text{halo}} \sim 3 \times 10^{12} M_{\odot}$ – comparable to SMGs (e.g. Croom et al. 2005; Ross et al. 2009). As we showed in Chapter 5 the peak epoch of QSO activity corresponds with the peak epoch in star-formation activity from SMGs. This, in combination with the similarity of the halo masses of these two populations provides further evidence that they are likely related, and may be part of the same evolutionary sequence of merging galaxies at high redshift (e.g. Hopkins et al. 2008b).

On average halos of mass $\sim 6 \times 10^{12} M_{\odot}$ at $z = 2$ evolve into $10^{14} M_{\odot}$ halos at $z = 0$ (Cole et al. 2008), although there is significant variation in the mass evolution. Locally, halos of this mass are predicted to be early-type galaxies $\gtrsim 90\%$ of the time (e.g. Hopkins et al. 2008a), and the richest galaxy clusters at $z = 0$ have halo masses up to $\sim 10^{15} M_{\odot}$. The errors and intrinsic scatter on all these calculations are significant, and therefore, the calculated halo masses of SMGs are consistent with typical SMGs evolving into massive early-type galaxies, in agreement with our calculations of the space density of SMGs and early-type galaxies (§ 6.2.5).

6.3 Conclusions

In this Chapter we have used the sample of 74 SMG counterparts from the LESS survey of the ECDFS to investigate the physical properties of SMGs.

We detect evidence for AGN activity in 15 (20%) LESS SMG counterparts. We find a lower fraction of SMGs with X-ray signatures of AGN than previous surveys (15%), however, this discrepancy is likely due to shallower data in the ECDFS and biases in some other samples. Nine of the LESS SMG counterparts (of which six are also X-ray detected) are identified as AGN due to an excess 8- μm flux compared to the best-fit SEDs. Two of these SMGs are also optically-identified QSOs (3%) and we detect one radio-loud AGN in the SMG sample (1%). There is evidence that many of the SMGs with excess 8- μm flux are obscured at X-ray energies. In addition, the variety of SMGs identified as AGN from each of the techniques discussed suggests that none of these methods can identify all the AGN and that they must be used in combination.

The median rest-frame H -band absolute magnitude of the LESS SMGs is $M_H = -24.1 \pm 0.1$ with an interquartile range of -24.7 to -23.6 . Using M_H and adopting the average mass-to-light ratio from Hainline et al. (2010) (converted to a Salpeter IMF) we calculate that the median stellar mass of the LESS SMGs is $(9.2 \pm 0.9) \times 10^{10} M_{\odot}$, with an

interquartile range of $(4.7\text{--}14) \times 10^{10} M_{\odot}$. However, uncertainties in the star-formation histories results in an additional factor of ~ 5 uncertainty in the mass-to-light ratios and hence the derived stellar masses. We use a real-space 3-D cross-correlation analysis to show that SMGs at $z = 1\text{--}3$ are strongly clustered and typically reside in dark-matter halos with masses of $M_{\text{halo,SMG}} = (6_{-5}^{+12}) \times 10^{12} M_{\odot}$ at $z = 2$.

The stellar masses, halo masses and the volume density of LESS SMGs at $z = 2\text{--}3$ are comparable to those of massive, passive galaxies at $z \sim 1\text{--}2$, and similarly the volume density of $z > 3$ SMGs is comparable to the limits on the numbers of massive galaxies at $z \sim 2\text{--}3$. Based in the remnant density of SMGs we calculate that $\sim 65\%$ of passive galaxies with $M^* > 10^{11} M_{\odot}$ at $z \sim 0$ underwent an SMG phase at $z = 1\text{--}3$ (the peak epoch of their activity). We also note that QSOs have comparable halo masses ($M_{\text{halo}} \sim 3 \times 10^{12} M_{\odot}$; Croom et al. 2005; Ross et al. 2009) to SMGs, and as we showed in Chapter 5 the peak epoch SMG activity corresponds to that of QSOs. This suggests that the activity in these two populations is related, and that they may be part of the same evolutionary sequence of high-redshift galaxies into massive, passive, cluster galaxies in the local Universe.

Chapter 7

Conclusions

In this thesis I have examined obscured active galaxies at high redshift, and considered the local population of massive, passive cluster galaxies, which may be the descendants of the high redshift starbursts. I conclude by summarising the main findings and discussing the remaining unanswered questions and potential avenues for further study.

7.1 Summary of main results

7.1.1 The galaxy populations in rich clusters at $z \sim 0.2$

We began this work by investigating the evolution of dwarf galaxies onto the colour-magnitude relation (CMR) in clusters at $z \sim 0.2$. By comparing the ratio of red-sequence dwarf-to-giant galaxies (RDGR) with published data we confirm the evolution of the RDGR from low values at high redshifts to high values locally. Similarly to previous authors, we interpret this evolution as evidence that increasing numbers of faint, blue, star-forming galaxies are being transformed onto the cluster red-sequence in recent times.

We statistically combine data from nine clusters at $z \sim 0.2$ to examine the variation of the RDGR with clustercentric radius and local giant galaxy density. In the outskirts of clusters, where the local density is typically low, there are relatively few galaxies on the CMR. The relative fraction of dwarf galaxies on the CMR increases towards the central higher-density regions and in the highest density, inner regions of the clusters the relative fraction of CMR dwarf-galaxies decreases. We interpret these trends as evidence that dwarf galaxies are transformed onto the red-sequence by the cluster environments, but that in the highest density, inner regions of the clusters the dwarf galaxies are dynamically disrupted. This disruption causes them to fade below our selection limits as luminous

material is stripped from them. We estimate that on average such interactions remove $\sim 17\%$ of the stellar mass from dwarf galaxies in the centres of clusters.

7.1.2 Searching for ULIRGs in a galaxy cluster at $z = 0.54$

We next use AzTEC 1.1-mm observations of the galaxy cluster MS 0451–03 at $z = 0.54$ to search for active star-forming galaxies within the cluster environment. We detect 36 sources with $S/N \geq 3.5$ in a 0.10 deg^2 map which is centered on the cluster. Counterparts to 18 sources (50%) are identified using radio, mid-infrared, *Spitzer* IRAC and Submillimeter Array data and we compile optical, near- and mid-infrared spectral energy distributions for the 14 of these galaxies with detectable counterparts. We use photometric redshifts to separate background galaxies from potential cluster members and test the reliability of this technique using archival observations of submillimetre galaxies. The photometric redshifts suggest that there are at most two cluster members, which, if they are both cluster galaxies have a combined star-formation rate (SFR) of $\sim 100 \text{ M}_{\odot} \text{ yr}^{-1}$ – a significant fraction of the SFR of all the other galaxies in MS 0451–03. If they are cluster members these galaxies will likely transform onto the cluster red-sequence as the starburst extinguishes.

We also examine the stacked rest-frame mid-infrared, millimetre and radio emission of cluster members below our AzTEC detection limit and find that the SFRs of mid-IR selected galaxies in the cluster and redshift-matched field populations are comparable. In contrast, the average SFR of the morphologically classified late-type cluster population is $\sim 3\times$ less than the corresponding redshift-matched field galaxies, suggesting that these galaxies may be in the process of being transformed on the red-sequence by the cluster environment. Our survey demonstrates that although the environment of MS 0451–03 appears to suppress star-formation in late-type galaxies, it can support active, dust-obscured mid-IR galaxies and potentially millimetre-detected LIRGs.

7.1.3 Properties of 870- μm selected SMGs

Finally, we use extensively tested photometric redshifts to investigate the properties of 126 SMGs selected at $870 \mu\text{m}$ by LABOCA observations in the Extended *Chandra* Deep Field South (ECDFS). The SMGs are identified from radio, $24 \mu\text{m}$ and *Spitzer* IRAC data, yielding 74 optically and near-infrared detected, robust counterparts to 68 of the 126 SMGs.

The median photometric redshift of identified SMGs is $z = 2.2 \pm 0.1$, with an interquartile range of $z = 1.8\text{--}2.7$, including 10 ($\sim 15\%$) high-redshift ($z \gtrsim 3$) SMGs. Using a statistical analysis of sources around unidentified SMGs we identify a population of likely counterparts with a redshift distribution peaking at $z = 2.5 \pm 0.3$, which likely comprises $\sim 60\%$ of the unidentified SMGs. This confirms that the bulk of the undetected SMGs are co-eval with those detected in the radio/mid-infrared. We conclude that at most $\sim 15\%$ of all the SMGs are below the flux limits of our IRAC observations and lie at $z \gtrsim 3$; hence around $\sim 30\%$ of all SMGs have $z \gtrsim 3$. We estimate that the full $S_{870\mu\text{m}} > 4$ mJy SMG population has a median redshift of 2.5 ± 0.6 .

We detect signatures of AGN activity in 20% of the SMGs, and find that it is necessary to use a range of methods to successfully identify all the potential AGN. SMGs with evidence of near-infrared power law emission, in the form of excess 8- μm flux compared to the best-fit SEDs, potentially contain AGN from which the the X-ray flux is significantly obscured. Using a single temperature modified blackbody fit with $\beta = 1.5$ we calculate that the median characteristic dust temperature of SMGs is 35.9 ± 1.4 K and the interquartile range is 28.5–43.3 K. The infrared luminosity function shows that SMGs at $z = 2\text{--}3$ typically have higher far-infrared luminosities and luminosity density than those at $z = 1\text{--}2$. This is mirrored in the evolution of the star-formation rate density (SFRD) for SMGs which peaks at $z \sim 2$. The maximum contribution of bright SMGs to the global SFRD ($\sim 5\%$ for SMGs with $S_{870\mu\text{m}} \gtrsim 4$ mJy; $\sim 50\%$ for SMGs with $S_{870\mu\text{m}} > 1$ mJy) also occurs at $z \sim 2$ – the same epoch as the peak of QSO activity.

The median stellar mass of the SMGs derived from SED fitting is $(9.2 \pm 0.9) \times 10^{10} M_{\odot}$, although we caution that uncertainties in the star-formation histories results in an additional factor of ~ 5 uncertainty in the stellar masses. The SMGs are strongly clustered, with dark-matter halo masses of $\sim 6 \times 10^{12} M_{\odot}$ at $z \sim 2$ – similar to that for QSOs. Consequently, as suggested by other authors, it appears that SMGs and QSOs may be different phases of the same evolutionary sequence at $z \sim 2$, which is most likely triggered by galaxy mergers. The high masses and strong clustering of SMGs and the space density of their descendants suggests that at the end of the starburst phase they evolve into massive early-type galaxies, eventually becoming the CMR galaxies observed in local clusters.

7.2 Remaining questions and future research

In this thesis we have used wide-field imaging to consider the populations of galaxies in low-redshift clusters, and their progenitor populations – LIRGs and ULIRGs, selected from millimetre and submillimetre data. Although we have made significant progress in understanding the evolution of these galaxies, as is typical of research many questions remain unanswered. For example:

Do clusters typically contain LIRGs and ULIRGs? How does their abundance evolve? Are they distributed evenly throughout the cluster environments? We

have shown that MS 0451–03 at $z = 0.54$ potentially contains two LIRGs; each is likely a merger-triggered starburst with $\text{SFR} \sim 50 M_{\odot} \text{yr}^{-1}$. Geach et al. (2006) showed that MS 0451–03 contains fewer 24- μm selected galaxies than expected and is underactive compared to other clusters at $z \sim 0.5$. Therefore, it is likely that other clusters may contain larger numbers of LIRGs and potentially more obscured star-formation activity. Submillimetre and millimetre surveys of larger numbers of clusters with a range of redshifts and spectroscopic confirmation of cluster members will enable us to much better examine these populations.

What are the conditions in the ISM of SMGs? How does this compare with local ULIRGs? CO emission from galaxies is a good tracer of H_2 gas and observations have shown that SMGs contain large reservoirs of H_2 gas that fuels the starburst. However, the extent, temperature, density and metallicity of the star-forming regions are not well understood. It is also currently unclear whether SMGs are simply scaled-up versions of local ULIRGs or whether the physical processes are different in the two populations. Submillimetre and millimetre emission lines of several species are required to constrain ISM models in the different populations.

What are the dynamics of SMGs? As we have discussed it is currently believed that SMGs are typically triggered by interactions and mergers, and fade as the starburst ends. Integral-field spectroscopy of statistically significant samples of SMGs will enable us to measure the dynamical masses of these galaxies and further investigate the distribution and kinematics of gas in these galaxies, to search for evidence of mergers, and AGN outflows that could quench the star-formation.

How are the currently unidentified SMGs different from those that are identified and have been studied? Currently, very little is known about the the 20–40% of SMGs that are not identified through their radio and mid-infrared emission. In Chapter 5

we presented tentative evidence that these SMGs have redshift distributions similar to the identified population, and therefore, likely contain more cold dust than the identified population. With the advent of new observatories and instrumentation (such as ALMA) comes the first opportunities to study these galaxies in detail and undertake comprehensive comparisons to radio and mid-infrared identified SMGs.

What are the properties of lower-luminosity obscured star-forming galaxies at high-redshift? The sensitivity of the current generation of millimetre and submillimetre cameras is such that only the most luminous examples of obscured high-redshift starbursts are detectable. With future advances in detector technology we will be able to begin to detect less luminous examples, potentially leading to a better understanding of their evolution.

How numerous were the earliest SMGs? Current galaxy formation models predict that ultraluminous starbursts at $z \gtrsim 4$ are rare, although increasing numbers of SMGs are being detected at $z = 4-5$, and the observed density is beginning to put pressure on the models. Therefore, the detection of numerous $z \gtrsim 4$ SMGs would add significant observational constraints to galaxy formation models and could provide a formation mechanism for the passive red galaxies that are observed at $z \sim 3$. The alternative picture of the major assembly period in these galaxies is through extended, less intense, star-formation events, which may be detectable with the next generation of far-infrared instruments.

Are SMGs and QSOs *really* different phases of an evolutionary sequence?

What fraction of SMGs undergo a QSOs and vice-versa? Circumstantial evidence is building that major mergers between gas-rich galaxies at high-redshift triggers a dusty starburst (the SMG phase), followed by a period of black-hole growth (the QSO phase). However, hard evidence is still lacking and it is also currently unclear what fraction of SMGs undergo a QSO phase, and what fraction of QSOs have had a period of SMG activity.

We are extremely privileged to be working at a time when so many new telescopes and instruments are being commissioned, which have the potential provide solutions to many of these problems, and undoubtedly produce many more.

SCUBA, on the James Clerk Maxwell Telescope (JCMT) was the first instrument to detect SMGs, and the arrival of its long-awaited successor, SCUBA-2, is imminent. With its full complement of science-grade arrays SCUBA-2 will be able to perform simultaneous observations at 450 and 850 μm , and thanks to increased sensitivity and areal coverage

is expected to be able to perform mapping observations $\sim 1000\times$ faster than SCUBA, making it ideally suited to performing large surveys. SCUBA-2 is most sensitive at 850- μm and will add many more galaxies to the samples of SMGs currently available. Indeed, the SCUBA-2 Cosmology Survey (S2CLS) aims to map ~ 50 -square degrees to $\sigma \sim 0.7$ mJy – significantly wider and deeper than previous work. This data will provide the largest sample of 850- μm selected SMGs to date and, amongst other things, enable us to measure the clustering of SMGs much more accurately, perform detailed analysis of sub-populations of SMGs, and identify examples of rare high-redshift (perhaps even beyond $z = 5$) SMGs. In addition, deep, wide-field observations such as these, enable stacking on sources that are not individually detected and with a survey of the area and sensitivity of that planned for S2CLS, stacking on subsets of populations (e.g. discriminated by redshift, luminosity, reddening etc.) is increasingly viable (e.g. Lutz et al. 2010).

The *Herschel Space Observatory* (*Herschel*) was launched in May 2009 and, at 3.5 m, has the largest primary mirror ever flown in space. *Herschel* is able to perform continuum surveys at 70-500 μm and is also equipped with spectrometers, which for the first time are enabling sensitive observations of far-infrared emission lines in extragalactic sources at cosmological distances. Since *Herschel* operates at shorter wavelengths than previous instruments it is sensitive to galaxies with different properties. Indeed, early *Herschel* results suggest that samples selected at 250-500 μm contain examples of “traditional” SMGs at $z \sim 2$ as well as populations of lower redshift, lower luminosity, active dusty galaxies, (e.g. Amblard et al. 2010). One major advantage of *Herschel* over existing facilities is that it can simultaneously map at 250, 350 and 500- μm , providing three distinct points on the far-infrared SED and far better constraints on the far-infrared luminosity and the characteristic dust temperature than is possible with just one measurement (e.g. Chapter 5). The spectrometers on *Herschel* also provide a new opportunity to study the chemical composition and evolution of the interstellar medium (ISM) of local LIRGs and ULIRGs, as well as SMGs.

The most highly anticipated submillimetre and millimetre facility in recent years is the Atacama Large Millimeter/submillimeter Array (ALMA). When completed (expected 2013) ALMA will consist of an array of at least 66 antennae of 6–12 m diameter; early-science, with 16 antennae is due to begin in 2011. ALMA is located at one of the driest sites on Earth – in the Chilean Andes at an altitude of 5000 m – meaning that it can operate effectively at wavelengths of 300 μm –9.6 mm. Baselines of 15 m–18 km are available, enabling unprecedented sub-arcsecond spatial resolution at millimetre and submillimetre

wavelengths. ALMA is such revolutionary facility that we cannot begin to imagine all the breakthroughs it will make in the coming years. Therefore, we shall limit this discussion to some of major contributions ALMA can make towards answering the questions introduced above.

ALMA is suited to pinpointing the counterparts of the submillimetre emission in SMGs, and its unprecedented sensitivity means that it will be much more efficient than existing facilities such as the Submillimeter Array (SMA). For example, ALMA could detect the faintest of the LESS SMGs in an exposure of just a few minutes, allowing us to identify counterparts to the 68 LESS SMGs that do not have robust radio, 24- μm or IRAC identifications (Chapter 5), in only a few hours. ALMA is also able to carry out blind-redshift surveys through the detection of multiple CO lines, and thus should be able to conclusively determine the redshift distribution of currently unidentified SMGs. Resolved observations of emission lines, harnessing the unique capabilities of ALMA will enable measurements of the dynamical masses of large numbers of SMGs, providing further constraints on the populations that evolve from SMGs (e.g. Chapter 6). Furthermore, unprecedented sensitivity of ALMA means that even late-type galaxies at $z \sim 3$ will be detectable. Indeed, one of the design goals of ALMA is to be able to detect CO or CII emission from a $z = 3$ galaxy with the star-formation properties similar to the Milky Way.

The next major new near- and mid-infrared space observatory is the James Webb Space Telescope (JWST). JWST has a 6.5 m diameter segmented primary mirror and is due for launch after 2014. The JWST combines much of the wavelength coverage of the *Spitzer Space Telescope (Spitzer)* and the *Hubble Space Telescope (HST)* into one telescope, with significantly improved sensitivity and resolution, thanks to the the large primary mirror. The JWST will be able to detect and resolve significantly fainter and smaller galaxies than is possible with any current instruments, and can help to identify and characterise many of the most dust obscured SMGs. It should also be able to identify and measure dust-obscured star-formation in galaxy clusters, and further determine the buildup of galaxies onto the CMR, even out to high redshifts.

Bibliography

- Abraham R. G., van den Bergh S., Glazebrook K., Ellis R. S., Santiago B. X., Surma P., Griffiths R. E., 1996, *ApJS*, 107, 1
- Alexander D. M., Bauer F. E., Brandt W. N., Hornschemeier A. E., Vignali C., Garmire G. P., Schneider D. P., et al. C., 2003, *AJ*, 125, 383
- Alexander D. M., Bauer F. E., Chapman S. C., Smail I., Blain A. W., Brandt W. N., Ivison R. J., 2005, *ApJ*, 632, 736
- Amblard A., Cooray A., Serra P., Temi P., Barton E., Negrello M., Auld R., et al. B., 2010, *A&A*, 518, L9+
- Andreon S., 2002, *A&A*, 382, 821
- Andreon S., Quintana H., Tajer M., Galaz G., Surdej J., 2006, *MNRAS*, 365, 915
- Aretxaga I., Hughes D. H., Chapin E. L., Gaztañaga E., Dunlop J. S., Ivison R. J., 2003, *MNRAS*, 342, 759
- Aretxaga I., Hughes D. H., Coppin K., Mortier A. M. J., Wagg J., Dunlop J. S., Chapin E. L., Eales et al., 2007, *MNRAS*, 379, 1571
- Arnaboldi M., Freeman K. C., Mendez R. H., Capaccioli M., Ciardullo R., Ford H., Gerhard O., et al. H., 1996, *ApJ*, 472, 145
- Ashby M. L. N., Dye S., Huang J.-S., Eales S., Willner S. P., Webb T. M. A., Barmby P., et al. R., 2006, *ApJ*, 644, 778
- Austermann J. E., Aretxaga I., Hughes D. H., Kang Y., Kim S., Lowenthal J. D., Perera T. A., et al. S., 2009, *MNRAS*, 393, 1573
- Austermann J. E., Dunlop J. S., Perera T. A., Scott K. S., Wilson G. W., Aretxaga I., Hughes D. H., Almaini et al., 2010, *MNRAS*, 401, 160

- Babbedge T. S. R., Rowan-Robinson M., Gonzalez-Solares E., Polletta M., Berta S., Pérez-Fournon I., Oliver S., et al. S., 2004, *MNRAS*, 353, 654
- Baldry I. K., Balogh M. L., Bower R. G., Glazebrook K., Nichol R. C., Bamford S. P., Budavari T., 2006, *MNRAS*, 373, 469
- Balestra I., Mainieri V., Popesso P., Dickinson M., Nonino M., Rosati P., Teimoorinia H., Vanzella et al., 2010, *A&A*, 512, A12+
- Banados E., Hung L., De Propriis R., West M., 2010, *astro-ph/1008.1082*
- Bardeau S., Soucail G., Kneib J., Czoske O., Ebeling H., Hudelot P., Smail I., Smith G. P., 2007, *A&A*, 470, 449
- Barger A. J., Cowie L. L., Sanders D. B., 1999, *ApJ*, 518, L5
- Barger A. J., Cowie L. L., Sanders D. B., Fulton E., Taniguchi Y., Sato Y., Kawara K., Okuda H., 1998, *Nature*, 394, 248
- Barkhouse W. A., Yee H. K. C., López-Cruz O., 2009, *ApJ*, 703, 2024
- Baugh C. M., Lacey C. G., Frenk C. S., Granato G. L., Silva L., Bressan A., Benson A. J., Cole S., 2005, *MNRAS*, 356, 1191
- Bell E. F., 2003, *ApJ*, 586, 794
- Benítez N., 2000, *ApJ*, 536, 571
- Bertin E., Arnouts S., 1996, *A&AS*, 117, 393
- Bertoldi F., Carilli C., Aravena M., Schinnerer E., Voss H., Smolcic V., Jahnke K., Scoville et al., 2007, *ApJS*, 172, 132
- Bertoldi F., Carilli C. L., Menten K. M., Owen F., Dey A., Gueth F., Graham J. R., Kreysa et al., 2000, *A&A*, 360, 92
- Best P. N., 2002, *MNRAS*, 336, 1293
- Biggs A. D., Ivison R. J., 2006, *MNRAS*, 371, 963
- Biggs A. D., Ivison R. J., Ibar E., Wardlow J. L., Dannerbauer H., Smail I., Walter F., Weiß et al., 2010, *MNRAS*, submitted
- Blain A. W., Barnard V. E., Chapman S. C., 2003, *MNRAS*, 338, 733

- Blain A. W., Chapman S. C., Smail I., Ivison R., 2004, *ApJ*, 611, 725
- Blain A. W., Longair M. S., 1993, *MNRAS*, 264, 509
- Blain A. W., Smail I., Ivison R. J., Kneib J., 1999, *MNRAS*, 302, 632
- Blain A. W., Smail I., Ivison R. J., Kneib J., Frayer D. T., 2002, *Phys. Rep.*, 369, 111
- Bolzonella M., Miralles J.-M., Pelló R., 2000a, *A&A*, 363, 476
- , 2000b, *HYPERZ v1.1 User's manual*
- Borys C., Chapman S., Donahue M., Fahlman G., Halpern M., Kneib J.-P., Newbury P., et al. S., 2004, *MNRAS*, 352, 759
- Borys C., Chapman S., Halpern M., Scott D., 2003, *MNRAS*, 344, 385
- Borys C., Smail I., Chapman S. C., Blain A. W., Alexander D. M., Ivison R. J., 2005, *ApJ*, 635, 853
- Bouwens R. J., Illingworth G. D., Franx M., Ford H., 2008, *ApJ*, 686, 230
- Bouwens R. J., Illingworth G. D., Gonzalez V., Labbe I., Franx M., Conselice C. J., Blakeslee J., et al. v., 2010a, *astro-ph/1003.1706*
- Bouwens R. J., Illingworth G. D., Oesch P. A., Stiavelli M., van Dokkum P., Trenti M., Magee D., et al. L., 2010b, *ApJ*, 709, L133
- Bower R. G., Lucey J. R., Ellis R. S., 1992, *MNRAS*, 254, 601
- Braglia F. G., Ade P. A. R., Bock J. J., Chapin E. L., Devlin M. J., Edge A., Griffin M., et al. G., 2010, *astro-ph/1003.2629*
- Brammer G. B., van Dokkum P. G., Coppi P., 2008, *ApJ*, 686, 1503
- Broadhurst T. J., Taylor A. N., Peacock J. A., 1995, *ApJ*, 438, 49
- Bruzual A. G., Charlot S., 1993, *ApJ*, 405, 538
- Bruzual G., 2007, in *Astronomical Society of the Pacific Conference Series*, Vol. 374, *From Stars to Galaxies: Building the Pieces to Build Up the Universe*, A. Vallenari, R. Tantalo, L. Portinari, & A. Moretti, ed., pp. 303–+
- Bundy K., Ellis R. S., Conselice C. J., 2005, *ApJ*, 625, 621

- Bunker A. J., Stanway E. R., Ellis R. S., McMahon R. G., McCarthy P. J., 2003, *MNRAS*, 342, L47
- Butcher H., Oemler Jr. A., 1984, *ApJ*, 285, 426
- Calzetti D., Armus L., Bohlin R. C., Kinney A. L., Koornneef J., Storchi-Bergmann T., 2000, *ApJ*, 533, 682
- Capak P., Cowie L. L., Hu E. M., Barger A. J., Dickinson M., Fernandez E., Giavalisco M., et al. K., 2004, *AJ*, 127, 180
- Carilli C. L., Yun M. S., 1999, *ApJ*, 513, L13
- , 2000, *ApJ*, 530, 618
- Casali M., Pirard J., Kissler-Patig M., Moorwood A., Bedin L., Biereichel P., Delabre B., Dorn et al., 2006, in *Society of Photo-Optical Instrumentation Engineers (SPIE) Conference Series*, Vol. 6269, *Society of Photo-Optical Instrumentation Engineers (SPIE) Conference Series*
- Casey C. M., Chapman S. C., Beswick R. J., Biggs A. D., Blain A. W., Hainline L. J., Ivison R. J., Muxlow et al., 2009, *MNRAS*, 399, 121
- Chabrier G., 2003, *PASP*, 115, 763
- Chapin E. L., Pope A., Scott D., Aretxaga I., Austermann J. E., Chary R., Coppin K., Halpern et al., 2009, *MNRAS*, 398, 1793
- Chapman S. C., Blain A. W., Ivison R. J., Smail I. R., 2003a, *Nature*, 422, 695
- Chapman S. C., Blain A. W., Smail I., Ivison R. J., 2005, *ApJ*, 622, 772
- Chapman S. C., Helou G., Lewis G. F., Dale D. A., 2003b, *ApJ*, 588, 186
- Chapman S. C., Scott D., Borys C., Fahlman G. G., 2002, *MNRAS*, 330, 92
- Chapman S. C., Smail I., Blain A. W., Ivison R. J., 2004a, *ApJ*, 614, 671
- Chapman S. C., Smail I., Windhorst R., Muxlow T., Ivison R. J., 2004b, *ApJ*, 611, 732
- Clements D. L., Vaccari M., Babbedge T., Oliver S., Rowan-Robinson M., Davoodi P., Ivison R., Farrah et al., 2008, *MNRAS*, 387, 247

- Colbert E. J. M., Heckman T. M., Ptak A. F., Strickland D. K., Weaver K. A., 2004, *ApJ*, 602, 231
- Cole S., Helly J., Frenk C. S., Parkinson H., 2008, *MNRAS*, 383, 546
- Collister A. A., Lahav O., 2004, *PASP*, 116, 345
- Condon J. J., 1992, *ARA&A*, 30, 575
- Cooray A., Amblard A., Wang L., Arumugam V., Auld R., Aussel H., Babbedge T., et al. B., 2010, *A&A*, 518, L22+
- Coppin K., Chapin E. L., Mortier A. M. J., Scott S. E., Borys C., Dunlop J. S., Halpern M., Hughes et al., 2006, *MNRAS*, 372, 1621
- Coppin K., Chapman S., Smail I., Swinbank M., Walter F., Wardlow J., Weiss A., Alexander et al., 2010a, *MNRAS*, 407, L103
- Coppin K., Pope A., Menéndez-Delmestre K., Alexander D. M., Dunlop J. S., Egami E., Gabor J., Ibar et al., 2010b, *ApJ*, 713, 503
- Coppin K. E. K., Smail I., Alexander D. M., Weiss A., Walter F., Swinbank A. M., Greve T. R., Kovacs et al., 2009, *MNRAS*, 395, 1905
- Cowie L. L., Barger A. J., Wang W.-H., Williams J. P., 2009, *ApJ*, 697, L122
- Cristiani S., Appenzeller I., Arnouts S., Nonino M., Aragón-Salamanca A., Benoist C., da Costa L., Dennefeld et al., 2000, *A&A*, 359, 489
- Croom S. M., Boyle B. J., Shanks T., Smith R. J., Miller L., Outram P. J., Loaring N. S., et al. H., 2005, *MNRAS*, 356, 415
- Croom S. M., Warren S. J., Glazebrook K., 2001, *MNRAS*, 328, 150
- Cypriano E. S., Sodr e Jr. L., Campusano L. E., Dale D. A., Hardy E., 2006, *AJ*, 131, 2417
- Czoske O., 2002, PhD thesis, Universit e Paul Sabatier, Toulouse
- Daddi E., Cimatti A., Renzini A., Fontana A., Mignoli M., Pozzetti L., Tozzi P., Zamorani G., 2004, *ApJ*, 617, 746
- Daddi E., Renzini A., Pirzkal N., Cimatti A., Malhotra S., Stiavelli M., Xu C., Pasquali et al., 2005, *ApJ*, 626, 680

- Dale D. A., Helou G., 2002, *ApJ*, 576, 159
- Damen M., Labbé I., Franx M., van Dokkum P. G., Taylor E. N., Gawiser E. J., 2009, *ApJ*, 690, 937
- Damen M., Labbé I., van Dokkum P. G., Franx M., Taylor E. N., Brandt W. N., Dickinson M., Gawiser et al., 2010, *ApJ*, submitted
- Dannerbauer H., Lehnert M. D., Lutz D., Tacconi L., Bertoldi F., Carilli C., Genzel R., Menten K., 2002, *ApJ*, 573, 473
- Dannerbauer H., Walter F., Morrison G., 2008, *ApJ*, 673, L127
- De Lucia G., Poggianti B. M., Aragón-Salamanca A., Clowe D., Halliday C., Jablonka P., Milvang-Jensen B., et al. P., 2004, *ApJ*, 610, L77
- De Lucia G., Poggianti B. M., Aragón-Salamanca A., White S. D. M., Zaritsky D., Clowe D., Halliday C., et al. J., 2007, *MNRAS*, 374, 809
- Devlin M. J., Ade P. A. R., Aretxaga I., Bock J. J., Chapin E. L., Griffin M., Gundersen J. O., Halpern et al., 2009, *Nature*, 458, 737
- Dickinson M., Stern D., Giavalisco M., Ferguson H. C., Tsvetanov Z., Chornock R., Cristiani S., Dawson et al., 2004, *ApJ*, 600, L99
- Doherty M., Bunker A. J., Ellis R. S., McCarthy P. J., 2005, *MNRAS*, 361, 525
- Donovan D. A. K., 2007, PhD thesis, University of Hawai'i at Manoa
- Downes A. J. B., Peacock J. A., Savage A., Carrie D. R., 1986, *MNRAS*, 218, 31
- Dressler A., 1980, *ApJ*, 236, 351
- Dressler A., Oemler A. J., Couch W. J., Smail I., Ellis R. S., Barger A., Butcher H., et al. P., 1997, *ApJ*, 490, 577
- Dunlop J. S., Ade P. A. R., Bock J. J., Chapin E. L., Cirasuolo M., Coppin K. E. K., Devlin M. J., et al G., 2009, *astro-ph/0910.3642*
- Dunne L., Eales S., Edmunds M., Ivison R., Alexander P., Clements D. L., 2000, *MNRAS*, 315, 115
- Dye S., Eales S. A., Aretxaga I., Serjeant S., Dunlop J. S., Babbedge T. S. R., Chapman S. C., Cirasuolo et al., 2008, *MNRAS*, 386, 1107

- Eales S., Lilly S., Gear W., Dunne L., Bond J. R., Hammer F., Le Fèvre O., Crampton D., 1999, *ApJ*, 515, 518
- Ebeling H., Voges W., Bohringer H., Edge A. C., Huchra J. P., Briel U. G., 1996, *MNRAS*, 281, 799
- Edge A. C., Ivison R. J., Smail I., Blain A. W., Kneib J.-P., 1999, *MNRAS*, 306, 599
- Elbaz D., Cesarsky C. J., 2003, *Science*, 300, 270
- Ellis R. S., Smail I., Dressler A., Couch W. J., Oemler Jr. A., Butcher H., Sharples R. M., 1997, *ApJ*, 483, 582
- Elvis M., Wilkes B. J., McDowell J. C., Green R. F., Bechtold J., Willner S. P., Oey M. S., et al. P., 1994, *ApJS*, 95, 1
- Faber S. M., Tremaine S., Ajhar E. A., Byun Y., Dressler A., Gebhardt K., Grillmair C., Kormendy J., Lauer T. R., Richstone D., 1997, *AJ*, 114, 1771
- Fazio G. G., Hora J. L., Allen L. E., Ashby M. L. N., Barmby P., Deutsch L. K., Huang J., et al. K., 2004, *ApJS*, 154, 10
- Feldmann R., Carollo C. M., Porciani C., Lilly S. J., Capak P., Taniguchi Y., Le Fèvre O., Renzini et al., 2006, *MNRAS*, 372, 565
- Ferguson H. C., Sandage A., 1991, *AJ*, 101, 765
- Frayer D. T., Ivison R. J., Smail I., Yun M. S., Armus L., 1999, *AJ*, 118, 139
- Gal-Yam A., Maoz D., Guhathakurta P., Filippenko A. V., 2003, *AJ*, 125, 1087
- Garrett M. A., 2002, *A&A*, 384, L19
- Gawiser E., van Dokkum P. G., Herrera D., Maza J., Castander F. J., Infante L., Lira P., Quadri et al., 2006, *ApJS*, 162, 1
- Geach J. E., Smail I., Best P. N., Kurk J., Casali M., Ivison R. J., Coppin K., 2008, *MNRAS*, 388, 1473
- Geach J. E., Smail I., Ellis R. S., Moran S. M., Smith G. P., Treu T., Kneib J.-P., et al. E., 2006, *ApJ*, 649, 661
- Geach J. E., Smail I., Moran S. M., Treu T., Ellis R. S., 2009, *ApJ*, 691, 783

- Gebhardt K., Bender R., Bower G., Dressler A., Faber S. M., Filippenko A. V., Green R., et al. G., 2000, *ApJ*, 539, L13
- Genzel R., Baker A. J., Tacconi L. J., Lutz D., Cox P., Guilleaume S., Omont A., 2003, *ApJ*, 584, 633
- Giacconi R., Zirm A., Wang J., Rosati P., Nonino M., Tozzi P., Gilli R., Mainieri et al., 2002, *ApJS*, 139, 369
- Giavalisco M., Ferguson H. C., Koekemoer A. M., Dickinson M., Alexander D. M., Bauer F. E., Bergeron J., Biagetti et al., 2004, *ApJ*, 600, L93
- Goto T., Takagi T., Matsuhara H., Takeuchi T. T., Pearson C., Wada T., Nakagawa T., et al. I., 2010, *A&A*, 514, A6+
- Grazian A., Fontana A., de Santis C., Nonino M., Salimbeni S., Giallongo E., Cristiani S., Galozzi et al., 2006, *A&A*, 449, 951
- Gregg M. D., West M. J., 1998, *Nature*, 396, 549
- Greve T. R., Bertoldi F., Smail I., Neri R., Chapman S. C., Blain A. W., Ivison R. J., Genzel et al., 2005, *MNRAS*, 359, 1165
- Gunn J. E., Gott III J. R., 1972, *ApJ*, 176, 1
- Güsten R., Nyman L. Å., Schilke P., Menten K., Cesarsky C., Booth R., 2006, *A&A*, 454, L13
- Gutermuth R. A., Megeath S. T., Myers P. C., Allen L. E., Pipher J. L., Fazio G. G., 2009, *ApJS*, 184, 18
- Haines C. P., Smith G. P., Egami E., Ellis R. S., Moran S. M., Sanderson A. J. R., Merluzzi P., Busarello G., Smith R. J., 2009, *ApJ*, 704, 126
- Haines C. P., Smith G. P., Pereira M. J., Egami E., Moran S. M., Hardegree-Ullman E., Rawle T. D., Rex M., 2010, *A&A*, 518, L19+
- Hainline L. J., Blain A. W., Smail I., Alexander D. M., Armus L., Chapman S. C., Ivison R. J., 2010, *astro-ph/1006.0238*
- Hainline L. J., Blain A. W., Smail I., Frayer D. T., Chapman S. C., Ivison R. J., Alexander D. M., 2009, *ApJ*, 699, 1610

- Hao C., Xia X., Shu-DeMao, Deng Z., Wu H., 2008, *CJAA*, 8, 12
- Helou G., Soifer B. T., Rowan-Robinson M., 1985, *ApJ*, 298, L7
- Hickox R. C., Jones C., Forman W. R., Murray S. S., Kochanek C. S., Eisenstein D., Jannuzi B. T., et al. D., 2009, *ApJ*, 696, 891
- Hildebrandt H., Arnouts S., Capak P., Moustakas L. A., Wolf C., Abdalla F. B., Assef R. J., et al. B., 2010, *astro-ph/1008.0658*
- Hill M. D., Shanks T., 2010, *ArXiv e-prints*
- Holden B. P., Franx M., Illingworth G. D., Postman M., van der Wel A., Kelson D. D., Blakeslee J. P., et al. F., 2009, *ApJ*, 693, 617
- Hopkins A. M., Beacom J. F., 2006, *ApJ*, 651, 142
- Hopkins P. F., Cox T. J., Kereš D., Hernquist L., 2008a, *ApJS*, 175, 390
- Hopkins P. F., Hernquist L., Cox T. J., Kereš D., 2008b, *ApJS*, 175, 356
- Hopkins P. F., Richards G. T., Hernquist L., 2007, *ApJ*, 654, 731
- Horesh A., Maoz D., Ebeling H., Seidel G., Bartelmann M., 2010, *MNRAS*, 406, 1318
- Hubble E. P., 1926, *ApJ*, 64, 321
- , 1929, *ApJ*, 69, 103
- Hughes D. H., Serjeant S., Dunlop J., Rowan-Robinson M., Blain A., Mann R. G., Ivison R., Peacock et al., 1998, *Nature*, 394, 241
- Iono D., Ho P. T. P., Yun M. S., Matsushita S., Peck A. B., Sakamoto K., 2004, *ApJ*, 616, L63
- Iono D., Peck A. B., Pope A., Borys C., Scott D., Wilner D. J., Gurwell M., et al. H., 2006, *ApJ*, 640, L1
- Isaak K. G., Priddey R. S., McMahon R. G., Omont A., Peroux C., Sharp R. G., Withington S., 2002, *MNRAS*, 329, 149
- Ivison R. J., Greve T. R., Dunlop J. S., Peacock J. A., Egami E., Smail I., Ibar E., van Kampen et al., 2007, *MNRAS*, 380, 199

- Iverson R. J., Greve T. R., Serjeant S., Bertoldi F., Egami E., Mortier A. M. J., Alonso-Herrero A., Barmby et al., 2004, *ApJS*, 154, 124
- Iverson R. J., Greve T. R., Smail I., Dunlop J. S., Roche N. D., Scott S. E., Page M. J., Stevens et al., 2002, *MNRAS*, 337, 1
- Iverson R. J., Magnelli B., Ibar E., Andreani P., Elbaz D., Altieri B., Amblard A., et al. A., 2010a, *astro-ph/1005.1072*
- Iverson R. J., Smail I., Barger A. J., Kneib J., Blain A. W., Owen F. N., Kerr T. H., Cowie L. L., 2000, *MNRAS*, 315, 209
- Iverson R. J., Smail I., Dunlop J. S., Greve T. R., Swinbank A. M., Stevens J. A., Mortier A. M. J., Serjeant et al., 2005, *MNRAS*, 364, 1025
- Iverson R. J., Smail I., Le Borgne J., Blain A. W., Kneib J., Bezecourt J., Kerr T. H., Davies J. K., 1998, *MNRAS*, 298, 583
- Iverson R. J., Smail I., Papadopoulos P. P., Wold I., Richard J., Swinbank A. M., Kneib J., Owen F. N., 2010b, *MNRAS*, 404, 198
- Iverson R. J., Swinbank A. M., Swinyard B., Smail I., Pearson C. P., Rigopoulou D., Polehampton E., et al. B., 2010c, *A&A*, 518, L35+
- Kennicutt Jr. R. C., 1998, *ARA&A*, 36, 189
- Kim D.-C., Veilleux S., Sanders D. B., 2002, *ApJS*, 143, 277
- King C. R., Ellis R. S., 1985, *ApJ*, 288, 456
- Kissler-Patig M., Pirard J., Casali M., Moorwood A., Ageorges N., Alves de Oliveira C., Baksai P., Bedin et al., 2008, *A&A*, 491, 941
- Knudsen K. K., Kneib J., Richard J., Petitpas G., Egami E., 2010, *ApJ*, 709, 210
- Knudsen K. K., van der Werf P. P., Kneib J., 2008, *MNRAS*, 384, 1611
- Kodama T., Tanaka M., Tamura T., Yahagi H., Nagashima M., Tanaka I., Arimoto N., et al. F., 2005, *PASJ*, 57, 309
- Kriek M., van Dokkum P. G., Franx M., Illingworth G. D., Marchesini D., Quadri R., Rudnick G., Taylor et al., 2008, *ApJ*, 677, 219

- Lacey C. G., Baugh C. M., Frenk C. S., Benson A. J., Orsi A., Silva L., Granato G. L., Bressan A., 2010, *MNRAS*, 405, 2
- Lacey C. G., Baugh C. M., Frenk C. S., Silva L., Granato G. L., Bressan A., 2008, *MNRAS*, 385, 1155
- Laird E. S., Nandra K., Pope A., Scott D., 2010, *MNRAS*, 401, 2763
- Landolt A. U., 1992, *AJ*, 104, 340
- Landsman W. B., 1993, in *Astronomical Society of the Pacific Conference Series*, Vol. 52, *Astronomical Data Analysis Software and Systems II*, R. J. Hanisch, R. J. V. Brissenden, & J. Barnes, ed., pp. 246–+
- Landy S. D., Szalay A. S., 1993, *ApJ*, 412, 64
- Larson R. B., Tinsley B. M., Caldwell C. N., 1980, *ApJ*, 237, 692
- Le Fèvre O., Vettolani G., Paltani S., Tresse L., Zamorani G., Le Brun V., Moreau C., Bottini et al., 2004, *A&A*, 428, 1043
- Le Floch E., Charmandaris V., Laurent O., Mirabel I. F., Gallais P., Sauvage M., Vigroux L., Cesarsky C., 2002, *A&A*, 391, 417
- Le Floch E., Papovich C., Dole H., Bell E. F., Lagache G., Rieke G. H., Egami E., et al. P., 2005, *ApJ*, 632, 169
- Lehmer B. D., Brandt W. N., Alexander D. M., Bauer F. E., Schneider D. P., Tozzi P., Bergeron J., Garmire et al., 2005, *ApJS*, 161, 21
- Leitherer C., Schaerer D., Goldader J. D., González Delgado R. M., Robert C., Kune D. F., de Mello D. F., Devost et al., 1999, *ApJS*, 123, 3
- Lobo C., Biviano A., Durret F., Gerbal D., Le Fevre O., Mazure A., Slezak E., 1997, *A&A*, 317, 385
- Lubin L. M., Postman M., Oke J. B., Ratnatunga K. U., Gunn J. E., Hoessel J. G., Schneider D. P., 1998, *AJ*, 116, 584
- Luo B., Bauer F. E., Brandt W. N., Alexander D. M., Lehmer B. D., Schneider D. P., Brusa M., Comastri et al., 2008, *ApJS*, 179, 19

- Luo B., Brandt W. N., Xue Y. Q., Brusa M., Alexander D. M., Bauer F. E., Comastri A., Koekemoer et al., 2010, *ApJS*, 187, 560
- Lutz D., Mainieri V., Rafferty D., Shao L., Hasinger G., Weiß A., Walter F., Smail et al., 2010, *ApJ*, 712, 1287
- Madau P., 1995, *ApJ*, 441, 18
- Magnelli B., Elbaz D., Chary R. R., Dickinson M., Le Borgne D., Frayer D. T., Willmer C. N. A., 2009, *A&A*, 496, 57
- Magnelli B., Lutz D., Berta S., Altieri B., Andreani P., Aussel H., Castaneda H., Cava et al., 2010, *astro-ph/1005.1154*
- Magorrian J., Tremaine S., Richstone D., Bender R., Bower G., Dressler A., Faber S. M., et al. G., 1998, *AJ*, 115, 2285
- Maiolino R., Salvati M., Bassani L., Dadina M., della Ceca R., Matt G., Risaliti G., Zamorani G., 1998, *A&A*, 338, 781
- Matsuda Y., Iono D., Ohta K., Yamada T., Kawabe R., Hayashino T., Peck A. B., Petitpas G. R., 2007, *ApJ*, 667, 667
- McCarthy P. J., Le Borgne D., Crampton D., Chen H., Abraham R. G., Glazebrook K., Savaglio S., et al. C., 2004, *ApJ*, 614, L9
- Menéndez-Delmestre K., Blain A. W., Alexander D. M., Smail I., Armus L., Chapman S. C., Frayer et al., 2007, *ApJ*, 655, L65
- Menéndez-Delmestre K., Blain A. W., Smail I., Alexander D. M., Chapman S. C., Armus L., Frayer D., Ivison et al., 2009, *ApJ*, 699, 667
- Mercurio A., Massarotti M., Merluzzi P., Girardi M., La Barbera F., Busarello G., 2003, *A&A*, 408, 57
- Mignoli M., Cimatti A., Zamorani G., Pozzetti L., Daddi E., Renzini A., Broadhurst T., Cristiani et al., 2005, *A&A*, 437, 883
- Miller N. A., Fomalont E. B., Kellermann K. I., Mainieri V., Norman C., Padovani P., Rosati P., Tozzi P., 2008, *ApJS*, 179, 114
- Molnar S. M., Hughes J. P., Donahue M., Joy M., 2002, *ApJ*, 573, L91

- Moore B., Katz N., Lake G., Dressler A., Oemler A., 1996, *Nature*, 379, 613
- Moran S. M., Ellis R. S., Treu T., Smith G. P., Rich R. M., Smail I., 2007a, *ApJ*, 671, 1503
- Moran S. M., Miller N., Treu T., Ellis R. S., Smith G. P., 2007b, *ApJ*, 659, 1138
- Morrissey P., Conrow T., Barlow T. A., Small T., Seibert M., Wyder T. K., Budavári T., Arnouts et al., 2007, *ApJS*, 173, 682
- Moster B. P., Somerville R. S., Maulbetsch C., van den Bosch F. C., Macciò A. V., Naab T., Oser L., 2010, *ApJ*, 710, 903
- Myers A. D., White M., Ball N. M., 2009, *MNRAS*, 399, 2279
- Nandra K., Pounds K. A., 1994, *MNRAS*, 268, 405
- Nonino M., Dickinson M., Rosati P., Grazian A., Reddy N., Cristiani S., Giavalisco M., Kuntschner et al., 2009, *ApJS*, 183, 244
- Oemler Jr. A., 1974, *ApJ*, 194, 1
- , 1976, *ApJ*, 209, 693
- Oke J. B., Korycansky D. G., 1982, *ApJ*, 255, 11
- Owen F. N., Keel W. C., Ledlow M. J., Morrison G. E., Windhorst R. A., 2005, *AJ*, 129, 26
- Page M. J., Stevens J. A., Mittaz J. P. D., Carrera F. J., 2001, *Science*, 294, 2516
- Pereira M. J., Haines C. P., Smith G. P., Egami E., Moran S. M., Finoguenov A., Hardegree-Ullman E., et al. O., 2010, *A&A*, 518, L40+
- Perera T. A., Chapin E. L., Austermann J. E., Scott K. S., Wilson G. W., Halpern M., Pope A., et al. S., 2008, *MNRAS*, 391, 1227
- Persic M., Rephaeli Y., Braito V., Cappi M., Della Ceca R., Franceschini A., Gruber D. E., 2004, *A&A*, 419, 849
- Pimblet K. A., Smail I., Edge A. C., O'Hely E., Couch W. J., Zabludoff A. I., 2006, *MNRAS*, 366, 645

- Pimblet K. A., Smail I., Kodama T., Couch W. J., Edge A. C., Zabludoff A. I., O'Hely E., 2002, *MNRAS*, 331, 333
- Pirard J., Kissler-Patig M., Moorwood A., Biereichel P., Delabre B., Dorn R., Finger G., Gojak et al., 2004, in *Society of Photo-Optical Instrumentation Engineers (SPIE) Conference Series*, Vol. 5492, Society of Photo-Optical Instrumentation Engineers (SPIE) Conference Series, A. F. M. Moorwood & M. Iye, ed., pp. 1763–1772
- Poggianti B. M., von der Linden A., De Lucia G., Desai V., Simard L., Halliday C., Aragón-Salamanca A., et al. B., 2006, *ApJ*, 642, 188
- Pope A., Borys C., Scott D., Conselice C., Dickinson M., Mobasher B., 2005, *MNRAS*, 358, 149
- Pope A., Chary R., Alexander D. M., Armus L., Dickinson M., Elbaz D., Frayer D., Scott et al., 2008, *ApJ*, 675, 1171
- Pope A., Scott D., Dickinson M., Chary R., Morrison G., Borys C., Sajina A., Alexander et al., 2006, *MNRAS*, 370, 1185
- Popesso P., Dickinson M., Nonino M., Vanzella E., Daddi E., Fosbury R. A. E., Kuntschner H., Mainieri et al., 2009, *A&A*, 494, 443
- Pracy M. B., De Propris R., Driver S. P., Couch W. J., Nulsen P. E. J., 2004, *MNRAS*, 352, 1135
- Priddey R. S., Ivison R. J., Isaak K. G., 2008, *MNRAS*, 383, 289
- Ravikumar C. D., Puech M., Flores H., Proust D., Hammer F., Lehnert M., Rawat A., Amram et al., 2007, *A&A*, 465, 1099
- Rawle T. D., Chung S. M., Fadda D., Rex M., Egami E., Pérez-González P. G., Altieri B., et al. B., 2010, *A&A*, 518, L14+
- Rieke G. H., Young E. T., Engelbracht C. W., Kelly D. M., Low F. J., Haller E. E., Beeman J. W., et al. G., 2004, *ApJS*, 154, 25
- Risaliti G., Maiolino R., Salvati M., 1999, *ApJ*, 522, 157
- Rodighiero G., Vaccari M., Franceschini A., Tresse L., Le Fevre O., Le Brun V., Mancini C., Matute et al., 2010, *A&A*, 515, A8+

- Rosa-González D., Terlevich E., Terlevich R., 2002, *MNRAS*, 332, 283
- Ross N. P., Shen Y., Strauss M. A., Vanden Berk D. E., Connolly A. J., Richards G. T., Schneider D. P., et al. W., 2009, *ApJ*, 697, 1634
- Rujopakarn W., Eisenstein D. J., Rieke G. H., Papovich C., Cool R. J., Moustakas J., Jannuzi B. T., et al. K., 2010, *ApJ*, 718, 1171
- Sandage A., Sandage M., Kristian J., 1975, *Galaxies and the Universe*, Sandage, A., Sandage, M., & Kristian, J., ed.
- Sanders D. B., Mirabel I. F., 1996, *ARA&A*, 34, 749
- Sanders D. B., Soifer B. T., Elias J. H., Madore B. F., Matthews K., Neugebauer G., Scoville N. Z., 1988a, *ApJ*, 325, 74
- Sanders D. B., Soifer B. T., Elias J. H., Neugebauer G., Matthews K., 1988b, *ApJ*, 328, L35
- Schechter P., 1976, *ApJ*, 203, 297
- Schlegel D. J., Finkbeiner D. P., Davis M., 1998, *ApJ*, 500, 525
- Scott K. S., Austermann J. E., Perera T. A., Wilson G. W., Aretxaga I., Bock J. J., Hughes D. H., et al. K., 2008, *MNRAS*, 385, 2225
- Scott S. E., Dunlop J. S., Serjeant S., 2006, *MNRAS*, 370, 1057
- Serjeant S., Dye S., Mortier A., Peacock J., Egami E., Cirasuolo M., Rieke G., Borys et al., 2008, *MNRAS*, 386, 1907
- Sheth R. K., Mo H. J., Tormen G., 2001, *MNRAS*, 323, 1
- Silva L., Granato G. L., Bressan A., Danese L., 1998, *ApJ*, 509, 103
- Siringo G., Kreysa E., Kovács A., Schuller F., Weiß A., Esch W., Gemünd H., Jethava et al., 2009, *A&A*, 497, 945
- Smail I., Chapman S. C., Blain A. W., Ivison R. J., 2004, *ApJ*, 616, 71
- Smail I., Edge A. C., Ellis R. S., Blandford R. D., 1998, *MNRAS*, 293, 124
- Smail I., Ivison R. J., Blain A. W., 1997, *ApJ*, 490, L5+

- Smail I., Ivison R. J., Kneib J., Cowie L. L., Blain A. W., Barger A. J., Owen F. N., Morrison G., 1999, MNRAS, 308, 1061
- Smail I., Ivison R. J., Owen F. N., Blain A. W., Kneib J.-P., 2000, ApJ, 528, 612
- Smith G. P., Haines C. P., Pereira M. J., Egami E., Moran S. M., Hardegree-Ullman E., Babul A., et al. R., 2010, A&A, 518, L18+
- Smith R. E., Peacock J. A., Jenkins A., White S. D. M., Frenk C. S., Pearce F. R., Thomas P. A., et al. E., 2003, MNRAS, 341, 1311
- Stanford S. A., Stern D., van Breugel W., De Breuck C., 2000, ApJS, 131, 185
- Stanway E. R., Bunker A. J., McMahon R. G., Ellis R. S., Treu T., McCarthy P. J., 2004, ApJ, 607, 704
- Steidel C. C., Shapley A. E., Pettini M., Adelberger K. L., Erb D. K., Reddy N. A., Hunt M. P., 2004, ApJ, 604, 534
- Stetson P. B., 2000, PASP, 112, 925
- Stott J. P., Smail I., Edge A. C., Ebeling H., Smith G. P., Kneib J.-P., Pimblet K. A., 2007, ApJ, 661, 95
- Strolger L., Riess A. G., Dahlen T., Livio M., Panagia N., Challis P., Tonry J. L., Filippenko et al., 2004, ApJ, 613, 200
- Surace J. A., Shupe D. L., Fang F., Lonsdale C. J., Gonzalez-Solares et al., 2005, <http://swire.ipac.caltech.edu/swire/astronomers/publications>
- Swinbank A. M., Chapman S. C., Smail I., Lindner C., Borys C., Blain A. W., Ivison R. J., Lewis G. F., 2006, MNRAS, 371, 465
- Swinbank A. M., Lacey C. G., Smail I., Baugh C. M., Frenk C. S., Blain A. W., Chapman S. C., Coppin et al., 2008, MNRAS, 391, 420
- Swinbank A. M., Smail I., Chapman S. C., Blain A. W., Ivison R. J., Keel W. C., 2004, ApJ, 617, 64
- Szokoly G. P., Bergeron J., Hasinger G., Lehmann I., Kewley L., Mainieri V., Nonino M., Rosati et al., 2004, ApJS, 155, 271

- Takata T., Sekiguchi K., Smail I., Chapman S. C., Geach J. E., Swinbank A. M., Blain A., Ivison R. J., 2006, *ApJ*, 651, 713
- Tanaka M., Kodama T., Arimoto N., Okamura S., Umetsu K., Shimasaku K., Tanaka I., Yamada T., 2005, *MNRAS*, 362, 268
- Taylor E. N., Franx M., van Dokkum P. G., Bell E. F., Brammer G. B., Rudnick G., Wuyts S., et al. G., 2009a, *ApJ*, 694, 1171
- Taylor E. N., Franx M., van Dokkum P. G., Quadri R. F., Gawiser E., Bell E. F., Barrientos L. F., Blanc et al., 2009b, *ApJS*, 183, 295
- Theuns T., Warren S. J., 1997, *MNRAS*, 284, L11
- Treister E., Virani S., Gawiser E., Urry C. M., Lira P., Francke H., Blanc G. A., Cardamone et al., 2009, *ApJ*, 693, 1713
- Trentham N., 1998, *MNRAS*, 295, 360
- Treu T., Auger M. W., Koopmans L. V. E., Gavazzi R., Marshall P. J., Bolton A. S., 2010, *ApJ*, 709, 1195
- Vaccari M., Marchetti L., Franceschini A., Altieri B., Amblard A., Arumugam V., Auld R., Aussel e. a., 2010, *astro-ph/1005.2187*
- van der Wel A., Franx M., van Dokkum P. G., Rix H., 2004, *ApJ*, 601, L5
- van Dokkum P. G., Franx M., 1996, *MNRAS*, 281, 985
- Vanzella E., Cristiani S., Dickinson M., Giavalisco M., Kuntschner H., Haase J., Nonino M., Rosati et al., 2008, *A&A*, 478, 83
- Vignali C., Brandt W. N., Fan X., Gunn J. E., Kaspi S., Schneider D. P., Strauss M. A., 2001, *AJ*, 122, 2143
- Visvanathan N., Sandage A., 1977, *ApJ*, 216, 214
- Wagg J., Owen F., Bertoldi F., Sawitzki M., Carilli C. L., Menten K. M., Voss H., 2009, *ApJ*, 699, 1843
- Wang W., Cowie L. L., van Saders J., Barger A. J., Williams J. P., 2007, *ApJ*, 670, L89
- Webb T. M., Eales S. A., Lilly S. J., Clements D. L., Dunne L., Gear W. K., Ivison R. J., et al. F., 2003, *ApJ*, 587, 41

- Webb T. M. A., Yee H. K. C., Ivison R. J., Hoekstra H., Gladders M. D., Barrientos L. F., Hsieh B. C., 2005, *ApJ*, 631, 187
- Wei A., Kovács A., Coppin K., Greve T. R., Walter F., Smail I., Dunlop J. S., Knudsen et al., 2009, *ApJ*, 707, 1201
- Wilson G. W., Austermann J. E., Perera T. A., Scott K. S., Ade P. A. R., Bock J. J., Glenn J., et al. G., 2008, *MNRAS*, 386, 807
- Wilson J. C., Eikenberry S. S., Henderson C. P., Hayward T. L., Carson J. C., Pirger B., Barry D. J., et al. B., 2003, in Presented at the Society of Photo-Optical Instrumentation Engineers (SPIE) Conference, Vol. 4841, Instrument Design and Performance for Optical/Infrared Ground-based Telescopes. Edited by Iye, Masanori; Moorwood, Alan F. M. Proceedings of the SPIE, Volume 4841, pp. 451-458 (2003)., Iye M., Moorwood A. F. M., eds., pp. 451–458
- Younger J. D., Fazio G. G., Huang J., Yun M. S., Wilson G. W., Ashby M. L. N., Gurwell M. A., Lai et al., 2007, *ApJ*, 671, 1531
- Younger J. D., Fazio G. G., Huang J., Yun M. S., Wilson G. W., Ashby M. L. N., Gurwell M. A., Peck et al., 2009, *ApJ*, 704, 803
- Yun M. S., Aretxaga I., Ashby M. L. N., Austermann J., Fazio G. G., Giavalisco M., Huang J.-S., et al. H., 2008, *MNRAS*, 389, 333
- Yun M. S., Carilli C. L., 2002, *ApJ*, 568, 88
- Zemcov M., Borys C., Halpern M., Mauskopf P., Scott D., 2007, *MNRAS*, 376, 1073
- Zhang Y., Finoguenov A., Böhringer H., Kneib J., Smith G. P., Kneissl R., Okabe N., Dahle H., 2008, *A&A*, 482, 451
- Zheng W., Mikles V. J., Mainieri V., Hasinger G., Rosati P., Wolf C., Norman C., Szokoly et al., 2004, *ApJS*, 155, 73
- Zibetti S., White S. D. M., Schneider D. P., Brinkmann J., 2005, *MNRAS*, 358, 949
- Zwicky F., 1951, *PASP*, 63, 61